Michael R. P. Ragazzon

Parameter Estimation in Atomic Force Microscopy

Nanomechanical Properties and High-speed Demodulation

Thesis for the degree of Philosophiae Doctor

Trondheim, April 2018

Norwegian University of Science and Technology
Faculty of Information Technology
and Electrical Engineering
Department of Engineering Cybernetics

NTNU
Norwegian University of
Science and Technology

NTNU
Norwegian University of Science and Technology

Thesis for the degree of Philosophiae Doctor

Faculty of Information Technology
and Electrical Engineering
Department of Engineering Cybernetics

ISBN 978-82-326-3082-0 (printed version)
ISBN 978-82-326-3083-7 (electronic version)
ISSN 1503-8181

ITK-report: 2018-4-W

Doctoral theses at NTNU, 2018:146

Printed by Skipnes Kommunikasjon as

Summary

Atomic force microscopy (AFM) has become a key enabling technology for high-precision study of materials and biological processes over the last few decades. Since its invention in 1986, it has undergone rapid developments and has been adapted for novel applications. High-speed AFM has enabled video-rate imaging, and the first ever direct evidence of several biological processes. Furthermore, its ability to mechanically interact with samples has enabled AFM to be used for revealing nanomechanical properties of samples. The rapidly developing field of multifrequency AFM has enabled fast acquisition times for nanomechanical properties. This thesis provides further contributions to these topics, in large part by the employment of online parameter identification techniques. The thesis is divided into three parts.

Part I presents a novel imaging method for revealing true topography and tip-sample interaction forces in dynamic mode atomic force microscopy. An observer-based approach is used to estimate the interaction force, while the true topography is obtained by inverting a nonlinear model of the tip-sample interaction force. Due to the nonlinear relationship between the force and the tip-sample distance, a nonlinear state- and parameter estimation approach is employed to guarantee near-global exponential stability of the error dynamics.

Part II concerns amplitude and phase demodulation for high-speed AFM. State-of-the-art techniques are compared and evaluated in terms of several performance criteria, including bandwidth, attenuation of noise, and rejection of frequency components away from the carrier frequency. The latter is particularly important for the application of demodulators to multifrequency AFM. A novel demodulator based on a Lyapunov estimator is proposed, and implemented experimentally. It achieves a particularly attractive combination of performance in terms of bandwidth and noise attenuation, low implementation complexity, and rejection of

frequency components away from the carrier frequency.

Part III introduces the model-based identification approach for resolving nanomechanical sample properties in AFM. This approach is particularly attractive compared to recent multifrequency AFM approaches, since it avoids complicated relationships between the observables and the properties to be determined. Instead of depending on stationary signals such as amplitude and phase, possibly at multiple frequencies, the model-based approach uses the entire transient information of the measured signals to directly identify the parameters of the sample model. This approach can be operated in two modes. The DIVE mode indents into the sample at regular intervals, while the SVE mode continuously scans the surface while modulating the cantilever. The DIVE mode is implemented experimentally and successfully resolves the mechanical properties of the samples investigated, including online identification of both elastic and viscous properties. The SVE mode can achieve higher imaging speeds than DIVE mode, possibly surpassing those of recent multifrequency AFM approaches as it does not rely on demodulated signals.

Contents

List of Figures vii

List of Tables xi

List of Abbreviations xiii

1 Introduction 1
- 1.1 Operating Modes in AFM . . . 2
- 1.2 Tip-Sample Interaction Models . . . 7
- 1.3 Objective I: Scanning Performance . . . 9
- 1.4 Objective II: Revealing Nanomechanical Properties . . . 13
- 1.5 Thesis Outline and Rationale . . . 15
- 1.6 Experimental Equipment . . . 17
- 1.7 Notation . . . 19

2 Recursive Parameter Identification: Preliminaries 21
- 2.1 Linear Parametric Model . . . 22
- 2.2 Estimation Model . . . 23
- 2.3 Gradient Estimator . . . 23
- 2.4 Lyapunov Estimator . . . 24
- 2.5 Least Squares Estimator . . . 26
- 2.6 Convergence of Parameters . . . 27

I Topography Estimation in AFM 29

3 Topography Estimation by Force Inversion 31
- 3.1 Introduction . . . 31
- 3.2 System Modeling . . . 33
- 3.3 State- and Parameter Estimator . . . 37
- 3.4 Simulation Setup . . . 43
- 3.5 Results . . . 43

3.6 Discussion 44
3.7 Conclusions 47

II Demodulation for High-Speed Dynamic Mode AFM 49

4 Amplitude and Phase Demodulation by Lyapunov Estimator 51
4.1 Introduction 52
4.2 Problem Formulation 54
4.3 Estimator Background 54
4.4 Lyapunov Amplitude and Phase Estimator 56
4.5 Tuning and Simulations 60
4.6 Experimental Results 62
4.7 Conclusions 69

5 Comparison of Demodulation Techniques in AFM 71
5.1 Introduction 71
5.2 Problem Formulation 73
5.3 Amplitude Estimation Techniques 74
5.4 Simulation Results 80
5.5 Making a Choice 88
5.6 Conclusions 91

III Mechanics of Cells and Soft Samples: Modeling and Identification by AFM 93

6 Cell Mechanics Modeling and Identification by AFM 95
6.1 Introduction 95
6.2 System Modeling 98
6.3 Modes of Operation 102
6.4 Parameter Identification 103
6.5 Simulation Results 109
6.6 Discussion 116
6.7 Conclusions 120

7 Convergence Time of Parameter Estimates 121
7.1 Introduction 122
7.2 Recursive Least Squares Estimation 123
7.3 Covariance Bounds and Lyapunov-Like Convergence 124
7.4 Convergence for Constant Parameters 128

7.5 Convergence for Time-Varying Parameters . . . 131
7.6 Case Study: Viscoelastic Identification in AFM . . . 133
7.7 Conclusions . . . 143

8 Model-Based Identification of Nanomechanical Properties: Experiments 145
8.1 Introduction . . . 145
8.2 System Modeling . . . 147
8.3 Parameter Identification . . . 153
8.4 Implementation . . . 157
8.5 System Identification and Tuning . . . 161
8.6 Experimental Results . . . 166
8.7 Conclusions . . . 173

9 Conclusions and Future Work 175
9.1 Part I . . . 175
9.2 Part II . . . 176
9.3 Part III . . . 176

A Total Integrated Noise 179

List of Figures

1.1 Working principles of AFM operating in static mode 3
1.2 AFM operating in dynamic mode. 5
1.3 Frequency response of the first three modes of a rectangular and uniform cantilever. 7
1.4 Vertical feedback loop in dynamic mode AFM 11
1.5 Lab equipment used for experiments. 18

3.1 Block diagram of the cantilever system. 34
3.2 Interaction between cantilever and sample, $D = x_1 + \theta$. 34
3.3 The tip-sample interaction force resulting from the Lennard-Jones potential between a half-sphere and a flat surface. 36
3.4 Structure of the state- and parameter estimator 38
3.5 Topography estimate. 45
3.6 Zoom of topography estimate. Position offset by 4.4 nm. 45
3.7 Topography estimate with output noise. 45
3.8 Closest tip-sample distance D each oscillation cycle with and without feedback control. 46
3.9 Topography estimate with output noise and feedback control . . . 46
3.10 Estimated interaction force ϕ with noise. 46

4.1 Amplitude modulated operating mode in AFM. 53
4.2 Block diagram of the estimator 57
4.3 Step response simulation 61
4.4 Lyapunov estimator simulated with a step in DC-offset at the input signal. 63
4.5 Amplitude tracking experiment using the lock-in-amplifier and Lyapunov estimator 64
4.6 Tracking response of Lyapunov estimator for increasing gain γ. . . 64
4.7 Measured total integrated noise of amplitude estimate from LIA and Lyapunov estimator, with curve fit, as a function of tracking bandwidth. 66
4.8 AFM scanning results over a $10 \times 10\,\mu m^2$ area of the sample 67

4.9 Multifrequency Lyapunov estimator implemented for phase demodulation used in an AFM imaging experiment. 68

5.1 Block diagram of test environment 81
5.2 Step response of the various amplitude estimation techniques. . . 82
5.3 Tracking frequency response to a modulated amplitude signal $A(t)$, performed at different bandwidth settings for each method. 84
5.4 Rejection of frequency components away from the carrier frequency 85
5.5 Bias as a function of tracking bandwidth, with a reference amplitude of 100 nm. 86
5.6 Total integrated noise versus demodulation bandwidth 87

6.1 The sample is modeled as spring-damper elements evenly spaced along the lateral axes. 99
6.2 Indentation of the tip into the sample. 99
6.3 Block diagram of the cantilever-sample dynamics and parameter estimator 100
6.4 The indentation depth is larger than the average of the element depths 108
6.5 Sample topography versus identified topography 112
6.6 Sample viscosity versus identified viscosity 112
6.7 Sample elasticity versus identified elasticity 113
6.8 Error plots of identified parameters. 114
6.9 Convergence of the identified parameters along the sample cross section 115
6.10 Spring force over depth during indentation. 116
6.11 Errors due to varying topography. 119

7.1 Upper-bound of V by an exponential function. 129
7.2 Notation for piecewise constant parameters. 131
7.3 Indentation of the cantilever tip into the sample 135
7.4 The exponential convergence rate λ, and multiplier a, as a function of β, p_0 of the least squares estimator. 137
7.5 Upper limit on convergence of parameter error 138
7.6 Time-varying parameters: Minimum estimation interval 138
7.7 Block diagram of the simulation setup, with cantilever-sample dynamics and parameter estimator. 139
7.8 Simulated parameter estimation with parameters changing at regular intervals *without* covariance reset 141
7.9 Simulated parameter estimation with parameters changing at regular intervals *with* covariance reset at the same intervals 142

8.1 AFM dynamic mode setup considered in this chapter. 148
8.2 Operation of DIVE mode in AFM 148
8.3 AFM cantilever interacting with sample 149
8.4 Plant dynamics and corresponding inputs and outputs 151
8.5 Block diagram of the control logic and parameter estimator. 158
8.6 State machine controlling the overall operation of the procedure. . 159
8.7 System identification 163
8.8 Minimum estimation time T which guarantees convergence of the parameter estimate error to within q fraction of the initial error. . 165
8.9 AFM experiment for a two-component polymer sample. 167
8.10 Tip position and parameter estimation during two subsequent indentations into the two-component polymer sample 168
8.11 Four AFM experiments demonstrating identification of spring constants versus elastic moduli, at different indentation depths on a homogeneous gel sample. 170
8.12 Time-varying parameter estimates 172

List of Tables

1.1 Characteristics of the first four modes of a rectangular cantilever . 6

3.1 Simulation Parameters 43

5.1 Characteristics of demodulation techniques. 80
5.2 Simulation parameters 81
5.3 Performance metrics of demodulation techniques 89

8.1 Depth versus elasticity. 169

A.1 TIN Ratio for nth vs. first order low-pass filter. 180

List of Abbreviations

AFM	atomic force microscopy	1
AM	amplitude modulation	63
AM-AFM	amplitude modulated atomic force microscopy	72
DIVE	dynamic indentation viscoelastic	97
DMT	Derjaguin-Muller-Toporov	8
FM	frequency modulation	63
JKR	Johnson-Kendall-Roberts	8
LIA	lock-in amplifier	51
LTI	linear time-invariant	134
MF-AFM	multifrequency atomic force microscopy	59
PE	persistently exciting	27
RLS	recursive least-squares	26
RMS	root mean square	65
STM	scanning tunneling microscope	1
SVE	scanning viscoelastic	97
TIN	total integrated noise	179

Preface

This thesis is the result of my doctoral studies at the Department of Engineering Cybernetics (ITK), at the Norwegian University of Science and Technology (NTNU). The work presented is undertaken from August 2013 to January 2018 for partial fulfillment of the degree of philosophiae doctor (PhD), under the supervision of Professor Jan Tommy Gravdahl (ITK, NTNU) and co-supervisor Professor Kristin Y. Pettersen (ITK, NTNU). Funding of my studies has been provided by an NTNU SO scholarship from the IME faculty through the Lighthouse Robotics Project. Travel grants have been provided by ITK and the Fund of the Norwegian Institute of Technology.

Acknowledgments

First of all, I would like to thank my supervisor Jan Tommy Gravdahl, for his support and encouragement during my studies. Always with a positive attitude and receptive of my ideas, his guidance has allowed me to find my own path through this exciting field of study. I would also like to thank my co-supervisor Kistin Y. Pettersen for her support. I have learned a lot from her feedback, and I feel much more confident in my work as a result.

I would also like to thank Arnfinn Eielsen for introducing me to the world of nanopositioning and atomic force microscopy, and happily taking the role as my tutor as I was still finding my way. Also, I want to thank Marialena Vagia and Saverio Messineo for their invaluable contributions and great discussions.

During my studies, I had the pleasure of an extended stay at the University of Newcastle, Australia, to visit Andrew J. Fleming and his group of researchers at the Precision Mechatronics Lab. My experiences from this visit has broadened

my perspectives, and led to a continued collaboration. I am grateful to have met and worked with you, Omid Tayefeh, Michael Ruppert, David Harcombe, Garth Berriman, and all the rest.

I would like to thank all of my fellow colleagues at the department, present and former – none mentioned, none forgotten. It has been great sharing cake, beer, and good times with you. I am happy to have had such great travel mates to explore the world with. Also, I want to thank our administrative staff for always bringing a smile along with their help, and the technical staff for helping out with the lab equipment.

A sincere thank you also goes to my friends who have helped me forget all about my work during these years, Martin, Jens, Fredric, Alf, Aili, Ole-Henrik, and Anders. It has been a great combination of bad jokes, board games, cabin trips, and travel.

Finally, to my family. I am happy for all the support and encouragement you have given me over all the years. Thank you for providing the best place to rest, the best food to eat, and all the care I could need.

Michael R. P. Ragazzon
Trondheim, January 2018

Publications

Journal Articles

[147] M. R. P. Ragazzon, J. T. Gravdahl, and K. Y. Pettersen. "Model-Based Identification of Nanomechanical Properties in Atomic Force Microscopy: Theory and Experiments." *IEEE Transactions on Control Systems Technology*, 2018. Provisionally accepted.

[75] D. M. Harcombe, M. G. Ruppert, M. R. P. Ragazzon, and A. J. Fleming. "Lyapunov estimation for high-speed demodulation in multifrequency atomic force microscopy." *Beilstein Journal of Nanotechnology*, 9(1):490–498, 2018.

[148] M. R. P. Ragazzon, M. G. Ruppert, D. M. Harcombe, A. J. Fleming, and J. T. Gravdahl. "Lyapunov Estimator for High-Speed Demodulation in Dynamic Mode Atomic Force Microscopy." *IEEE Transactions on Control Systems Technology*, 26(2):765–772, 2018.

[146] M. R. P. Ragazzon, J. T. Gravdahl, and M. Vagia. "Viscoelastic properties of cells: Modeling and identification by atomic force microscopy." *Mechatronics*, 2017. In press, available online.

[157] M. G. Ruppert, D. M. Harcombe, M. R. P. Ragazzon, S. O. R. Moheimani, and A. J. Fleming. "A review of demodulation techniques for amplitude-modulation atomic force microscopy." *Beilstein Journal of Nanotechnology*, 8(1):1407–1426, 2017.

Conference Papers

[144] M. R. P. Ragazzon, J. T. Gravdahl, and K. Y. Pettersen. "Exponential Convergence Bounds in Least Squares Estimation: Identification of Viscoelastic Properties in Atomic Force Microscopy." In *IEEE Conference on Control Technology and Applications*, Kohala Coast, Hawai'i, USA, 2017.

[74] D. M. Harcombe, M. G. Ruppert, M. R. P. Ragazzon, and A. J. Fleming. "Higher-harmonic AFM Imaging with a High-Bandwidth Multifrequency Lyapunov Filter." In *IEEE International Conference on Advanced Intelligent Mechatronics*, Munich, Germany, 2017.

[158] M. G. Ruppert, D. M. Harcombe, M. R. P. Ragazzon, S. O. R. Moheimani, and A. J. Fleming. "Frequency Domain Analysis of Robust Demodulators for High-Speed Atomic Force Microscopy." In *American Control Conference*, Seattle, USA, 2017.

[142] M. R. P. Ragazzon and J. T. Gravdahl. "Imaging Topography and Viscoelastic Properties by Constant Depth Atomic Force Microscopy." In *IEEE Multi-Conference on Systems and Control*, Buenos Aires, Argentina, 2016.

[149] M. R. P. Ragazzon, M. Vagia, and J. T. Gravdahl. "Cell Mechanics Modeling and Identification by Atomic Force Microscopy." In *7th IFAC Symposium on Mechatronic Systems*, Loughborough, UK, 2016.

[143] M. R. P. Ragazzon, J. T. Gravdahl, and A. J. Fleming. "On Amplitude Estimation for High-Speed Atomic Force Microscopy." In *American Control Conference*, Boston, USA, 2016.

[145] M. R. P. Ragazzon, J. T. Gravdahl, K. Y. Pettersen, and A. A. Eielsen. "Topography and force imaging in atomic force microscopy by state and parameter estimation." In *American Control Conference*, Chicago, USA, 2015.

Related Publications

Related publications which are not part of this thesis.

[125] S. Messineo, M. R. P. Ragazzon, F. Busnelli, and J. T. Gravdahl. "Nonlinear Analysis of PI-control for Atomic Force Microscopy in Contact Mode," 2018. In writing.

[187] J. Å. Stakvik, M. R. P. Ragazzon, A. A. Eielsen, and J. T. Gravdahl. "On Implementation of the Preisach Model: Identification and Inversion for Hysteresis Compensation." *Modeling, Identification and Control*, 36(3):133–

142, 2015.

[150] M. R. P. Ragazzon, A. A. Eielsen, and J. T. Gravdahl. "H∞ Reduced Order Control for Nanopositioning: Numerical Implementability." In *19th IFAC World Congress*, Cape Town, South-Africa, 2014.

Chapter 1

Introduction

Over the recent decades, there has been an explosive development of technologies and tools for studying and manipulating matter at the nanoscale. The results of this development can be widely observed in today's society; in particular, in fields such as materials and manufacturing, nanoelectronics, medicine, and healthcare [14, 194]. While still in its infancy, nanotechnology is expected to have a profound impact on our economy and society over the coming century.

One of the earliest tools for studying and manipulating matter at the nanoscale, was the scanning tunneling microscope (STM), invented in 1981 [17]. This was the first technology to enable true 3d topographic imaging at atomic resolutions, and is routinely being used for manipulation of individual atoms [83]. A major limitation of the STM is the necessity of the sample to be conductive. Later efforts in overcoming this limitation, spawned the invention of atomic force microscopy (AFM) in 1986 [16]. Together, STM and AFM can be considered the main innovations behind the birth of nanotechnology [28].

Since its invention, AFM has become one of the key enabling technologies for studying materials and biological processes at the nanoscale [3]. The technology is enjoying an ever-increasing number of applications, and a continuous expansion of capabilities. The high adoption of AFM can be attributed to the advantages it enjoys over comparable techniques. In particular, it has the ability to image the topography of most materials, including both insulators and conductors, at up to atomic resolutions. Additionally, it can measure interaction forces accurately at high spatial resolutions in most media, including air, water and solutions. It can also be employed in ultra-high vacuum, and at a wide range of temperatures. These attributes have made AFM the preferred tool for many applications, in particular in fields such as cell- and molecular biology, solid-state physics, and

surface chemistry [21, 73, 88, 128].

Some of the major active research efforts in the AFM community can be organized into two main objectives.

Improving the scanning performance. Due to the fundamental operating principles of AFM, typical imaging speeds require minutes or longer for a single image scan. There is an enduring ambition in the AFM community to increase the imaging speed [5].

Revealing nanomechanical sample properties. Due to the ability of AFM to apply forces to a sample and measure the resulting mechanical response, it has become one of the prime tools for studying nanomechanical sample properties at up to molecular resolutions. Recent innovations demonstrate increased image acquisition rates, while simultaneously allowing for increasingly number of characteristics of a material to be quantified [26, 112, 151].

In this thesis, several topics within AFM are covered, mainly concerning these two objectives.

In the remainder of this chapter, background material on the working principles of AFM in a variety of operating modes is given, and the interaction between the sample and cantilever tip is described. Then, an overview of recent efforts in the research community concerning the two stated objectives is provided. Finally, an outline on the thesis is given, relating the contributions to the proposed objectives.

1.1 Operating Modes in AFM

Since the invention of AFM, a variety of operating modes have been developed for different applications. A fundamental working principle is the feedback loop, which renders the microscope particularly interesting for control engineering. Its working principle is best described by the static mode, which serves as a foundation for the other modes.

1.1.1 Static Mode

The working principles of AFM [3] in static mode (or contact mode, constant-force mode) is shown in Fig. 1.1. A central component in AFM is the sharp tip attached to the end of a cantilever. The cantilever will deflect as soon as the tip is brought into contact with the sample, and this deflection can be measured in a photodetector setup at high precision. A feedback loop ensures that the deflection of the cantilever is kept constant by adjusting the vertical piezo actuator. The

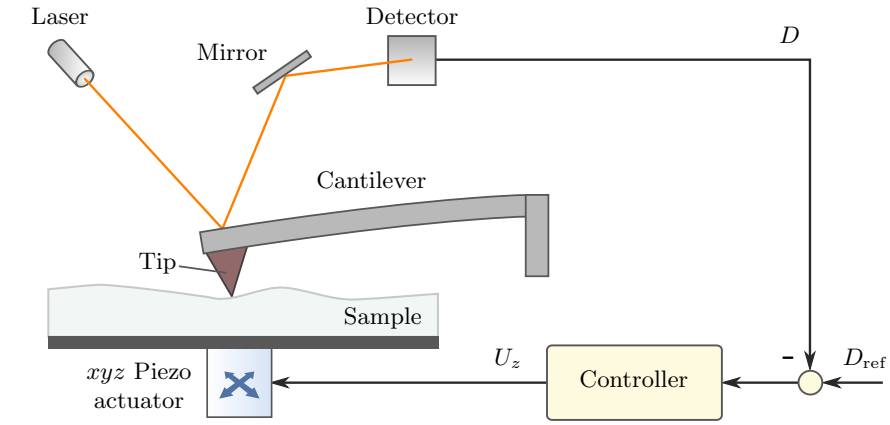

(a) AFM operating in static mode

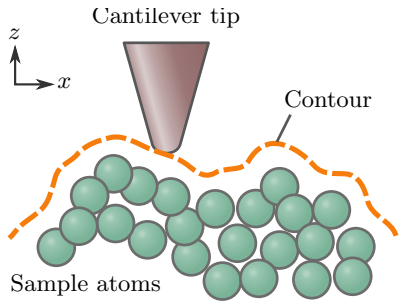

(b) Sample contour

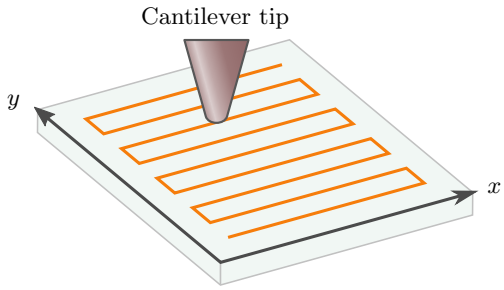

(c) Raster scan pattern

Figure 1.1: Working principles of AFM operating in static mode. **(a)** The cantilever deflection is kept constant in a feedback loop, such that **(b)** the tip follows the sample contour, while **(c)** the tip is scanned across the sample in a raster pattern.

sample is then scanned in the lateral directions, typically in a raster pattern. By keeping the deflection constant, the cantilever tip follows the contour of the sample surface. Thus, by mapping the vertical piezo position against the lateral position, the topography of the sample is revealed.

In the static sense, the cantilever deflection is proportional to the tip-sample interaction force in accordance with Hooke's law. Thus, the atomic force microscope acts as a highly precise force sensor interacting with the sample. By utilizing this principle, the nanomechanical properties of the sample can be determined by applying a force to the sample and measuring its response [21].

A challenge with the static mode is the large lateral forces (or frictional forces) arising during scanning, which can cause damage to the cantilever tip or the sample, especially for fragile samples such as in biology [36]. Furthermore, soft cantilevers may snap to the surface due to attractive tip-sample forces, creating an instability in the feedback loop [191]. These are the main motivations for the development of dynamic mode AFM [87].

1.1.2 Dynamic Mode

In dynamic mode AFM, the cantilever is oscillated typically using a dither piezo located at the base of the cantilever [55, 174], as seen in Fig. 1.2. The amplitude, phase, or frequency of the deflection will change as the cantilever is brought closer towards the sample. Thus, by demodulating the deflection signal, and keeping it constant in a feedback loop, the distance between the tip and the sample is maintained at some constant setpoint. As in the static mode, the sample is then typically scanned in a raster pattern, and the topography of the sample is revealed by mapping the vertical actuator position to the lateral position of the sample.

Dynamic mode AFM can be further classified. In tapping mode (or intermittent contact mode), the cantilever tip is oscillated at larger amplitudes, thereby crossing into both the attractive and repulsive force regions of the tip-sample interaction. In non-contact mode, smaller amplitudes are applied, and the tip is primarily located in the attractive force region at a small distance from the sample. In either mode, the tip-sample interaction and frictional forces are much lower than in static mode. For this reason, the dynamic modes of AFM are particularly well suited for studying soft biological materials [36, 87]. Over the last few decades it has increasingly been applied to studies of soft and biological matter at cellular and molecular scales [8, 197].

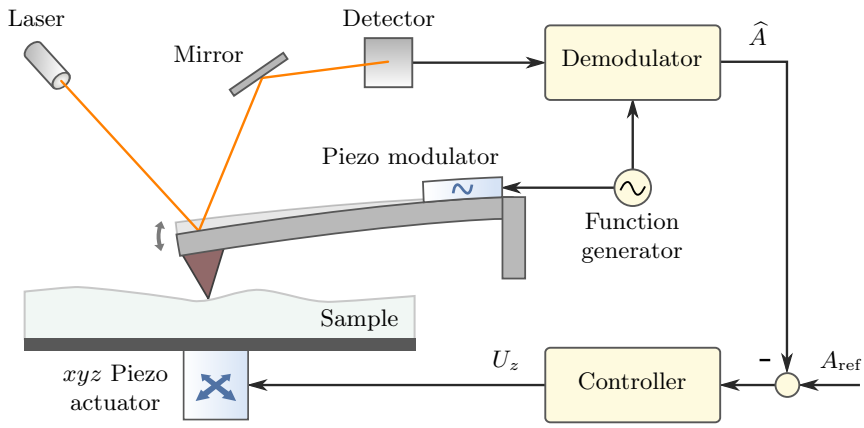

Figure 1.2: AFM operating in dynamic mode.

1.1.3 Multifrequency

In dynamic mode AFM, the cantilever is driven at a single frequency component, and its response measured at the same frequency. The dynamics of the cantilever are often approximated by a simple harmonic oscillator [55]. If the tip-sample interaction force is linear with respect to the distance, all information about the sample is contained in the driven frequency component. However, nature is more complicated; rather, in general the interaction force is highly nonlinear with respect to the sample, as discussed in the next section. This nonlinearity excites the cantilever motion at higher harmonics – that is, at multiples – of the driving frequency [189]. The interaction force can be time-resolved by considering all the higher harmonics [188]. Thus, by measuring the cantilever response only at a single frequency component, information about the sample is irreversibly lost. These insights spawned the field of *multifrequency AFM*, where the cantilever is driven or measured at multiple frequencies simultaneously [58].

For a full understanding of multifrequency AFM, the dynamics of the cantilever must be considered. The motion of the cantilever can be found using Euler-Bernoulli beam theory [39, 56, 140, 191]. An approximation can be found using a discrete lumped mass model of order n, whose transfer function from applied tip force F_{ts} to deflection D, for a beam fixed at one end. This gives the transfer function [41]

$$\frac{D}{F_{\text{ts}}}(s) = \frac{1}{M}\sum_{i=1}^{n}\frac{\beta_i}{s^2 + \frac{\omega_i}{Q_i}s + \omega_i^2} \tag{1.1}$$

where M is the cantilever mass, and ω_i, β_i, Q_i are the resonance frequency, gain determined by the modal shape function, and Q factor for each *mode* i, respec-

Table 1.1: Characteristics of the first four modes of a rectangular cantilever*.

Eigenmode i	Resonance frequency ω_i	Quality factor Q_i	Force constant k_i
1 (Fundamental)	ω_1	Q_1	k_1
2	$6.27\,\omega_1$	$6.27\,Q_1$	$39.3\,k_1$
3	$17.6\,\omega_1$	$17.6\,Q_1$	$308\,k_1$
4	$34.4\,\omega_1$	$34.4\,Q_1$	$1180\,k_1$

*Adapted from [56].

tively. For a co-located actuator and sensor placed at the freely oscillating end of the cantilever, $\beta_i = 4\,\forall i$. Relationships between the parameters of the first mode and higher modes can be found, a subset of which is given in Table 1.1 [56, 61, 152]. The frequency response of the cantilever dynamics from (1.1) is shown in Fig. 1.3. Note that the higher harmonic components arising from the nonlinear interaction force do not necessarily coincide with the modes of the cantilever. Thus, the cantilever will be more sensitive to some harmonic components than others.

An overview of the developments in multifrequency AFM is given in [57, 58, 116, 138, 172]. Early efforts were mainly concerned with measuring the amplitude and phase at higher harmonics, while driving the cantilever at a single frequency [63, 190]. Later, the bimodal multifrequency approach was introduced [120, 121, 139], where the cantilever is driven at the first two resonance modes, resulting in an increased imaging contrast compared to single-frequency excitation. A theoretical justification for the increased contrast was soon developed [116]. A host of imaging modes in multifrequency AFM rapidly followed. In intermodulation AFM [133], the cantilever frequency is driven at two frequencies in the vicinity of a resonance. In the band excitation approach [90], a band of frequencies is excited and detected simultaneously. In torsional harmonic AFM [162], special cantilevers are used to induce a flexural response, which can further enhance the ability to resolve the tip-sample interaction force.

The introduction of multifrequency AFM came with the realization that the key to a full understanding of the tip-sample interaction is located in the complex motion of the cantilever. With the introduction of new imaging methods, and new observable signals being available for measurement, the focus has shifted towards using these signals to reveal spatially resolved, nanomechanical properties of the sample. In particular, relating the multifrequency amplitude and phase components to the sample elasticity, viscosity, and their gradients along the vertical direction [26, 59, 151].

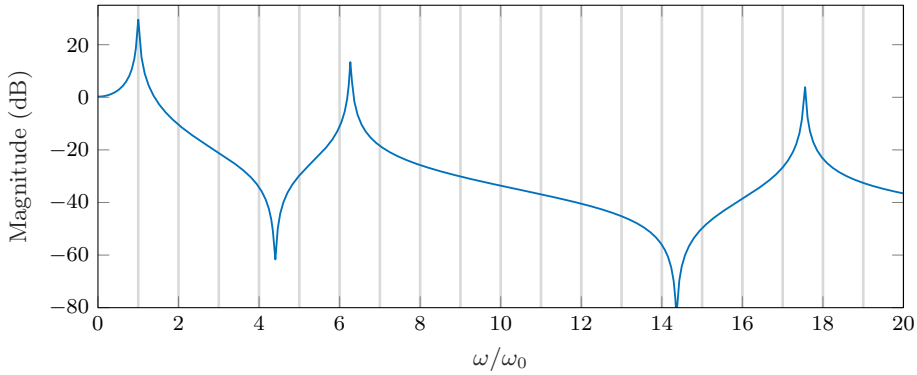

Figure 1.3: Frequency response of the first three modes of a rectangular and uniform cantilever. The harmonics of the fundamental frequency are marked by vertical lines.

1.2 Tip-Sample Interaction Models

The interaction between the cantilever tip and sample is an important consideration for several purposes in AFM, including simulations, theoretical understanding of the cantilever-sample interaction, and revealing nanomechanical properties of the sample. A variety of interaction models have been utilized in the AFM community. In general, the models commonly originate either from the study of inter-molecular forces [85], or from the field of contact mechanics [91]. The former is especially suitable when some distance between the tip and the sample is considered (non-contact), while the latter is suitable when an indentation occurs from the tip into the sample (contact). Thus, as the cantilever approaches the sample, one could consider two different regimes determining the nature of the tip-sample interaction. During approach of the tip onto the sample (non-contact), the interaction force can be described using the Lennard-Jones potential [85, 173]. As the tip comes in contact with the sample and starts indenting it, the mechanical response of the sample due to its deformation determines the interaction [91]. The various topics of this thesis considers either the contact, non-contact, or both regimes.

1.2.1 Non-Contact Model

The Lennard-Jones potential is typically used to describe the tip-sample interaction force for AFM operating in non-contact mode, or in general for rigid samples. Fundamentally, the potential describes the interaction between two molecules. It combines attractive van der Waals forces, with repulsive forces originating from

the Pauli exclusion principle preventing the collapse of the molecules. For application in AFM, the Lennard-Jones potential is typically summed over molecules in a half-sphere, representing the cantilever tip, and a half-space, representing the sample. By taking the distance-derivative of the summed energy potential, the interaction force between the tip and the sample in the non-contact regime is found to be [3, 173]

$$F_{\mathrm{LJ}}(d) = k_1 \left[\frac{\sigma^2}{d^2} - \frac{1}{30} \frac{\sigma^8}{d^8} \right], \tag{1.2}$$

where k_1, σ are physical parameters and d is the tip-sample distance.

1.2.2 Contact Models

A wide variety of contact models exist, incorporating physical phenomena such as elasticity, viscosity, adhesion and plasticity. Traditionally, the Hertz contact model has been widely used in the AFM community to describe elasticity of soft samples [24, 141]. This approach assumes small indentations, no friction, and continuous, non-conforming surfaces. For a spherical tip with radius R indenting into an elastic half-space, the contact force as a function of indentation δ is given by

$$F_{\mathrm{Hertz}}(\delta) = \tfrac{4}{3} E^* R^{\frac{1}{2}} \delta^{\frac{3}{2}} \tag{1.3}$$

where E^* is the reduced elastic modulus,

$$E^* = \left(\frac{1 - \nu_{\mathrm{tip}}^2}{E_{\mathrm{tip}}} + \frac{1 - \nu^2}{E} \right)^{-1} \tag{1.4}$$

and ν_{tip}, ν are the Poisson ratios of the tip and sample, respectively, and E_{tip}, E are the elastic moduli of the tip and sample. Since the cantilever tip is made of a stiff material, then, for soft samples it can safely be assumed that $E_{\mathrm{tip}} \gg E$, which simplifies (1.4) to

$$E^* = \frac{E}{1 - \nu^2}. \tag{1.5}$$

Extensions of the Hertz model often incorporate adhesion effects. Common models include the Derjaguin-Muller-Toporov (DMT) and Johnson-Kendall-Roberts (JKR) contact models [29, 92, 108, 195]. For the DMT model, the interaction force is modified by including a constant long-range adhesive force,

$$F_{\mathrm{DMT}}(\delta) = \tfrac{4}{3} E^* R^{\frac{1}{2}} \delta^{\frac{3}{2}} - 2\pi R \varpi \tag{1.6}$$

where ϖ is the work of adhesion. On the other hand, the JKR model introduces a surface energy term which describes the adhesion. However, in this case there

is no analytical solution for the interaction force, but it can be found numerically [35, 37, 113, 207]. Other variations include the Sneddon model [71, 183] which generalizes the Hertz model to additional tip geometries, thereby enabling the use of non-spherical cantilever tips.

These and related models are often used for top-down approaches for measuring cell mechanics and other biological applications in AFM [13, 24, 71, 72, 86, 185, 186], but can be used for any material that displays elasticity or adhesion.

As demonstrated by the given models, the tip-sample interaction force is nonlinear. For this reason, in dynamic mode AFM, the tip-sample interaction force will excite higher harmonics of the driven modulation frequency. In order to build a theoretical understanding of how the cantilever interacts with the sample, the provided nonlinear interaction models, or variations of them, are typically combined with a linear cantilever model [20, 54, 107, 161, 181, 191]. However, general interaction forces have also been considered [44].

Note that the two regimes considered here are not always clearly distinguishable. For instance, a stiff contact model with adhesion would behave similarly to the model based on the Lennard-Jones potential. They are also sometimes mixed, such as van der Waals attractive forces combined with the DMT model [107], or the Lennard-Jones potential combined with the Hertz model [175].

1.3 Objective I: Scanning Performance

In commercial atomic force microscopes, the imaging speeds typically require minutes or higher for a single complete scan. There has been an enduring effort in the research community to improve the imaging speed [7]. Some of the benefits of this objective, is the improved productivity of the operator, as well as the ability to image biological and chemical processes that occur at high speeds, and observe their changes as they occur over time [5]. This thesis aims to provide further contributions for improved performance in AFM. In the following, an overview of existing approaches on this topic is presented.

The challenges in scanning speeds are attributed to the fundamental working principles of AFM. In AFM, a physical probe must be moved over the entire sample and visit each point of the area of interest. This creates an immense demand on the bandwidth of every component involved in the scanning operation. The research in this area can be separated into bandwidth improvements for positioning in the lateral axes, and the feedback loop in the vertical axis.

1.3.1 Lateral Positioning

Achieving a high bandwidth in the lateral positioner is essential for high-speed AFM. In particular, considering the raster scan pattern shown in Fig. 1.1(c), the scanning rate can become very high along the fast-scanning direction. There is a desire to achieve the fastest possible bandwidth, however, at higher bandwidths, the challenges involved for control of the actuator becomes apparent, and can result in a severely distorted image due to inaccurate positioning.

Increasing the bandwidth in the lateral positioning has been the topic of a large amount of research on the topic of nanopositioning [31, 41, 49, 69]. The results are typically applicable to any scanning probe microscopy technique, including AFM, STM, and a wide range of related techniques [14]. Some of the challenges involved in nanopositioning include the vibration dynamics of the piezoelectric actuator, and its sensitivity to environmental changes such as temperature. These sensitivities introduce uncertainties in the model and associated parameters. Additionally, the piezoelectric actuator displays nonlinear effects such as hysteresis and creep.

Several approaches have been taken to overcome the preceding challenges. The mechanical design of the positioner is fundamental to achieving high resonance frequencies [203], which ultimately constraints the achievable bandwidth. Since the resonance frequency is typically dependent on the achievable range of the actuator, dual stacked actuators with distinct ranges, have been used to simultaneously achieve high bandwidth and long range [9, 104]. Several feedforward and feedback techniques have been proposed to increase the achievable bandwidth, with a particular emphasis on robustness due to the uncertainties in the model [27, 30, 40, 47, 48, 169, 175, 180, 198, 199]. The raster scanning approach is particularly demanding along the fast scanning axis. Since the typical triangle-shaped reference trajectory contains strong harmonic components, modifications to the reference trajectory can attenuate such higher frequency components [46, 177]. Alternatively, completely different reference trajectories such as spiral or Lissajous trajectories can be utilized [12, 118]. However, these approaches typically come at the expense of a higher lateral speed and thus higher demand on the vertical feedback loop [196]. For compensating creep and hysteresis, nonlinear feedforward approaches can be employed [42, 106, 126].

1.3.2 Vertical Feedback Loop

In order to ensure fast scanning speeds, every part of the vertical feedback loop in AFM, as shown in Fig. 1.4, needs to be developed for high bandwidths. In

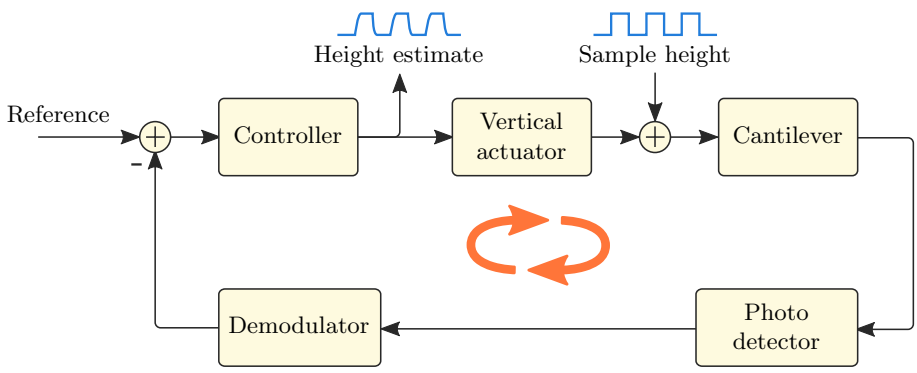

Figure 1.4: Vertical feedback loop in dynamic mode AFM. The scanning speed is limited by the slowest component in the loop. The sample height acts as an unknown disturbance to the system. Adapted from [3, 5].

static mode AFM, the scanning speed limit can be determined by the cantilever properties and sample stiffness, in addition to the vertical actuator bandwidth [23]. However, due to the high tip-sample forces arising in static mode, in particular high lateral forces, more recent high-speed applications utilize dynamic mode AFM [7].

In dynamic mode AFM, the bandwidth of the deflection sensor typically exceeds the other components [43, 51, 52], while the feedback controller, typically implemented by a PID controller, uses the highest possible gain while maintaining an acceptable imaging quality [7]. Thus, the main limitations for the closed loop bandwidth in dynamic mode AFM to be studied are the vertical actuator, cantilever, and demodulator.

Vertical Actuator

As in lateral positioning, the vertical actuator bandwidth is limited by its first resonance mode. Its mechanical design is therefore of high significance [176]. A counter-weight can be used to attenuate the first resonance mode [204], and dual-stage piezo actuators can be used for simultaneous long range and high bandwidth [98, 205]. The bandwidth of the vertical actuator can be bypassed altogether by operating the cantilever in constant height mode [23]. However, this sacrifices some flexibility, as the sample must lay very flat within the scanning area, and cannot display considerable topographic variability, unless large tip-sample interaction forces are acceptable.

Cantilever

The bandwidth of the cantilever is proportional to both its first mode resonance frequency and damping ratio [5]. Often the quality (Q) factor of the cantilever is reported, which is inversely proportional to the damping ratio. Thus, for high-speed dynamic mode AFM applications, the cantilever is constructed for high resonance frequencies and low Q factors. However, the Q factor needs to be considered carefully, as a lower Q factor results in a lower force sensitivity and higher tip-sample interaction forces which can cause damage to the sample [154, 174]. Due to these trade-offs, the Q factor can be modified through feedback control to suite the application [45, 124, 154, 193]. Current state-of-the-art in high-speed AFM has enabled the construction of cantilevers with a bandwidth near 100 kHz. It has been suggested that this is the upper limit, as going beyond must sacrifice the stiffness of the cantilever [5].

Another source of time delay in high-speed AFM is due to the *parachuting* effect [7]. This effect describes the event where the cantilever is lifted off from the sample surface, such as after a sudden drop in the topography. A dynamic PID controller can be used to mitigate this effect [100], where the gain is increased at downhill regions when the cantilever almost starts parachuting, and reduced at uphill regions in order to reduce the tip-sample force.

Demodulator

For demodulation in dynamic mode AFM, the lock-in amplifier has become widely adopted [3]. However, it is not suitable for high-speed applications, as its bandwidth is severely limited by a low-pass filter required to suppress the mixing products occurring at twice the resonance frequency of the cantilever. In [6], the peak-hold method was introduced, allowing a substantial improvement in bandwidth. However, this approach is very prone to measurement noise and unsuitable for multifrequency applications. To enable high-speed, low-noise, and multifrequency applications, the Kalman filter was adopted for demodulation [155, 159]. However, the Kalman filter is practically limited in terms of sampling times, due to its high implementation complexity.

Other approaches avoid the demodulator altogether by using observer-based approaches [95, 165, 167, 168, 178]. This makes it possible to increase imaging speeds by exploiting the transient behavior of the deflection signal, instead of using stationary signals such as amplitude, phase, and frequency. Typically, the tip-sample interaction force is estimated and used for feedback control.

Prospect

Clearly, high-speed AFM is a fairly mature field, and has achieved many notable results, including imaging speeds well beyond 10 frames per second [5, 6, 7]. A celebrated result is the video-rate imaging of walking myosin V [101], the first visual evidence for such molecular behavior in biology. However, these approaches require a very rigorous setup and do not seem to have been adopted in commercial AFM. Instead, it can be argued, that there is a need to improve performance under existing setups, by employing simple approaches which do not introduce additional constraints. Furthermore, the application of some of the high-speed approaches to novel imaging modes, such as multifrequency AFM, also needs to be studied.

1.4 Objective II: Revealing Nanomechanical Properties

Nanomechanical properties of samples are of wide interest to researchers in several fields, such as cell- and molecular biology, solid-state physics, and surface chemistry. In living cells, their elasticity and adhesion are important in several cellular processes [151]. In particular, cellular deformability can play a critical role in the development and progression of various diseases [111]. Furthermore, adhesion or stiffness maps can be used to visualize material contrast, such as for identification of materials, or for investigation of local properties of a given material [21].

Since the invention of the atomic force microscope, it has clearly proven itself to be one of the foremost tools for measuring sample topography at high resolutions [53, 131]. In addition, it is capable of measuring tip-sample interaction forces in the piconewton range, due to its highly sensitive laser-cantilever setup. The ability of the microscope to probe the sample during operation, and measure the mechanical response at high precision, has made it a prominent tool for determining nanomechanical sample properties [21].

The techniques for studying nanomechanical properties using AFM have been under immense development since its introduction, from traditional force-distance curves, to more recent multifrequency AFM approaches. This thesis aims to contribute to the topic, including new approaches for identification of nanomechanical properties using AFM. In the following, a brief overview of existing approaches is presented.

Force-Distance Curves

By Hooke's law, the static response of the cantilever deflection is proportional to the interaction force. This principle can be utilized for determining the properties of the sample, by slowly indenting the cantilever tip into the sample, while measuring the cantilever deflection. The elastic properties of the sample can then be revealed from the resulting force-distance curves, fitted to some contact model [21, 105, 123]. Recently, viscous properties can also be gathered in this approach by considering the time-history of the tip-sample interaction [19, 38]. In force-volume imaging mode [135, 185], indentations are repeated across the sample, which allows its elastic modulus to be spatially resolved along the lateral axes. A variation of force-volume imaging includes the peak-force quantitative nanomechanical mode, which forcibly oscillates the cantilever at below resonance frequency, allowing for faster and higher-resolution gathering of force-distance curves [35, 195].

Dynamic Mode Force-Distance Curves

In dynamic mode AFM, the interaction forces are typically lower, which makes it more suitable for fragile samples such as in biology. Early results demonstrated the correlations between amplitude and elasticity, and between phase and viscosity [141]. However, the observables in this mode, including amplitude and phase, are gathered over a single or several oscillation cycles. Thus, they cannot directly reveal force-distance curves [132]. Instead, by recording the amplitude and phase as a function of distance to the sample, the force-distance curve can be found [79, 80, 97]. Furthermore, by applying one of the tip-sample interaction models such as from Section 1.2, the elasticity of the sample can be revealed.

Multifrequency Nanomechanics

In order to speed up the gathering of the force-distance curves, a method for inverting the complete transient signal in dynamic mode AFM was sought. Then, the higher harmonics of the cantilever motion need to be considered [188]. This development made multifrequency AFM approaches closely associated with revealing nanomechanical properties. Typically, the observables in either single- or multifrequency dynamic modulation are related to the mechanical properties of the sample [25, 26, 59, 77, 151, 163]. However, these relations are often quite complicated and are still under development [36]. Furthermore, existing approaches are limited in terms of the properties that can be extracted from the sample, typically isolated to viscoelastic properties and their gradient along the depth axis.

Avoiding such complicated relations, and allowing for additional properties to be identified, would be beneficial.

Another challenge in multifrequency AFM, is the insensitivity of the cantilever to the higher harmonics. In the torsional harmonic approach [162], special cantilevers are used to induce a torsional response, allowing for a better sensitivity of the higher harmonics and effective reconstruction of force-distance curves. Recent approaches also allow for mapping frequency-dependent sample elasticity at a broad band of frequencies simultaneously [112].

1.5 Thesis Outline and Rationale

This thesis is divided into three separate parts. An overview of the thesis is given in this section, along with the rationale for each part. Chapter 2 is separated from the main parts and contains background information on recursive parameter identification, a concept which is used throughout the thesis. In closing of this thesis, conclusions and suggestions for future work are given in Chapter 9.

1.5.1 Part I: Topography Estimation in AFM

This part contains Chapter 3, where the non-contact regime in dynamic mode AFM is considered. In dynamic mode AFM, the topography image is gathered by ensuring that the demodulated signal, such as amplitude, is constant. However, as the sample properties may change across the scanning area, a constant amplitude image does not necessarily represent the true topography. Instead, we develop a method for recursive estimation of the time-resolved tip-sample interaction force and true topography in dynamic mode AFM.

In the presented method, the interaction force is estimated using observer techniques. The estimated force is simultaneously used to invert the force model of the sample, revealing its true topography. Furthermore, by utilizing the entire transient information of the cantilever deflection signal, it is not necessary to rely on stationary signals such as amplitude and phase, which may increase the imaging speed.

Two distinct observer approaches are provided as a solution to this problem. The first is based on a nonlinear state- and parameter estimator, which guarantees exponentially stable error dynamics. The second approach is based on an extended Kalman filter where the state-vector is augmented to include the parameters to be estimated. Numerical results demonstrate the feasibility of the technique using both observers, and their differences are outlined.

1.5.2 Part II: Demodulation for High-Speed Dynamic Mode AFM

In this part, the demodulator in dynamic mode AFM is considered. In order to improve the scanning performance in AFM, every component of the vertical feedback loop must be designed for high bandwidths, including the demodulator. Furthermore, due to the emerging field of multifrequency AFM, the demodulator should be able to isolate single frequency components for demodulation. Existing methods are either limited in terms of bandwidth, very sensitive to measurement noise, unable to operate on multifrequency signals, and/or complicated in terms of implementation complexity, thereby unable to operate in real-time in a high-speed setting.

In Chapter 4, the *Lyapunov estimator* is proposed for amplitude and phase demodulation in high-speed dynamic mode AFM. Implementation details are given, and the estimator is experimentally compared to a state-of-the-art lock-in amplifier (LIA) commonly used in AFM applications. In a high-speed setting, the Lyapunov estimator outperforms the LIA in terms of bandwidth and noise attenuation. Additionally, it allows for multifrequency applications, and is simple in terms of implementation complexity.

A comparison of state-of-the-art demodulation techniques in AFM, including the Lyapunov estimator, is given in Chapter 5. The various techniques are numerically compared in terms of bandwidth, sensitivity to noise, implementation complexity, and suitability for multifrequency AFM applications. Suggestions for choosing a particular technique are given for a variety of use-cases: low implementation complexity, low noise and high accuracy, and high imaging speed.

1.5.3 Part III: Mechanics of Cells and Soft Samples: Modeling and Identification by AFM

The use of AFM for identification of nanomechanical properties of samples is rapidly increasing, in part due to the development of multifrequency AFM. However, in multifrequency AFM, complicated relationships are necessary to relate the observables, such as amplitude and phase, to nanomechanical properties. Instead, we propose a *modeling and identification* approach to this problem. Here, the system dynamics are modeled, containing unknown parameters representing the sample properties. Then, a parameter estimation technique is employed, in order to recursively identify the unknown parameters, which represent nanomechanical properties such as elasticity and viscosity. This approach separates the observed signals and identified properties, thus, complicated relationships are avoided. Fur-

thermore, instead of relying on stationary signals such as amplitude and phase, the entire transient response of the signal is used. Thus, a faster imaging throughput may be achieved, while avoiding the additional complexity of employing and tuning a multifrequency demodulator.

In Chapter 6, the modeling and identification approach for revealing nanomechanical properties in AFM is presented, employing a recursive least squares estimator. Two distinct operation modes are developed for this approach, the dynamic indentation viscoelastic (DIVE) mode which resembles the operation in force volume imaging, and the scanning viscoelastic (SVE) mode which resembles the operation in recent multifrequency approaches. A simulation environment is constructed to evaluate the proposed approach.

In recursive parameter estimation, the time sufficient for convergence of the parameters are not typically evaluated. However, it would be highly beneficial to know exactly how fast the proposed modeling and identification approach can be operated, while being able to guarantee convergence of the parameters. A solution to this problem is given in Chapter 7, in the general framework of the recursive least squares estimator. The results are applied to the DIVE mode, and provides the sufficient operating time interval which guarantees the convergence of the parameters to any given degree of accuracy.

Finally, in Chapter 8, experimental results are provided for the modeling and identification approach in DIVE mode. Several aspects of the previous results in this thesis are employed, including the new Lyapunov demodulator, and the sufficient time interval for parameter convergence. Implementation considerations are given in detail, and the approach is employed on multiple samples. The method successfully reveals their nanomechanical properties, including elasticity and viscosity.

1.6 Experimental Equipment

Some of the experiments contained in this thesis were performed in the *Nanopositioning Lab* at the Dept. of Engineering Cybernetics, NTNU. A commercial atomic force microscope (Park Systems XE-70) is available, and all aspects of the microscope can be controlled with custom signals. A variety of supporting equipment is also available, some of which are shown in Fig. 1.5, including a programmable dSpace (DS1103) and an xPC target computer, as well as a variety of signal generators and filters. Other experiments of this thesis were performed at the *Precision Mechatronics Lab* at the University of Newcastle [136].

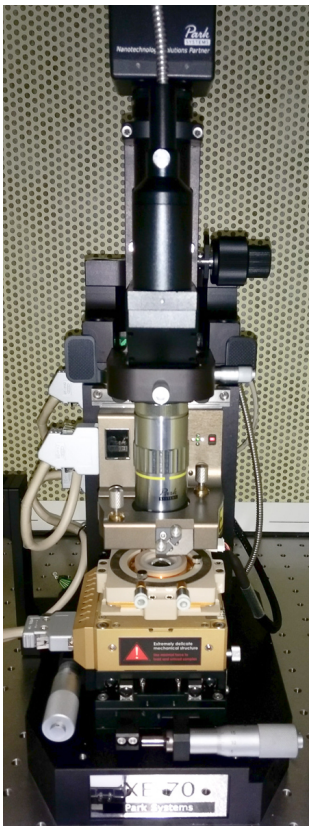

(a) Park Systems XE-70 AFM

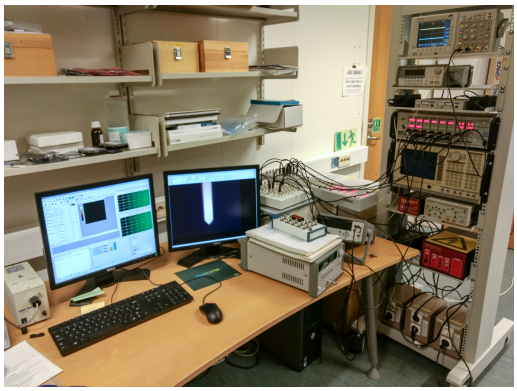

(b) Supporting equipment

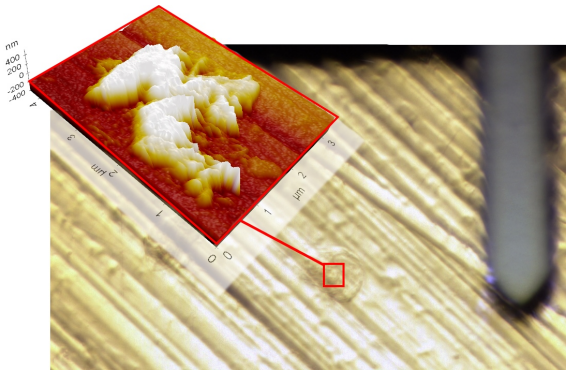

(c) AFM sample image

Figure 1.5: Lab equipment used for experiments.

1.7 Notation

The following notational conventions are used throughout the thesis. Filters and signals are occasionally mixed, e.g., the expression $w(t) = W(s)y(t)$ should be understood as $w(t) = \mathcal{L}^{-1}\left[W(s)\mathcal{L}(y(t))\right]$ where $\mathcal{L}$ is the Laplace transformation. The time-dependency of a signal is often not explicitly stated for ease of notation. Vector signals are given in italic bold such as $\boldsymbol{\theta}(t)$, while matrices are denoted uppercase bold, e.g. $\mathbf{A}$. Additionally, the Euclidean norm of a vector is written as $|\cdot|$, while $\mathrm{diag}(\cdot)$ and $\mathrm{col}(\cdot)$ denote a diagonal matrix and column vector of elements, respectively. The $\mathcal{L}_p$-norm of a signal $\boldsymbol{x}(t)$ for $1 \leq p \leq \infty$ is defined as

$$\|\boldsymbol{x}\|_p \triangleq \begin{cases} \left(\int_0^\infty |\boldsymbol{x}(\tau)|^p d\tau\right)^{1/p}, & 1 \leq p < \infty, \\ \sup_{t \geq 0} |\boldsymbol{x}(t)|, & p = \infty. \end{cases} \tag{1.7}$$

Furthermore, $\boldsymbol{x}(t)$ is said to belong to the $\mathcal{L}_p$-space – that is, $\boldsymbol{x}(t) \in \mathcal{L}_p$ – when $\|\boldsymbol{x}\|_p$ is finite.

Chapter 2

Recursive Parameter Identification: Preliminaries

A fundamental topic in science and engineering is the understanding of how a system behaves. Many physical systems can be described by a dynamic model. Typically, these models are expressed as a plant with inputs and outputs, corresponding to the actuators and sensors of the system. A situation often arises, where parts of the model contain unknown parameters. A *parameter estimator* can then be tasked with finding the unknown values, such that an equivalent input-output response as the physical plant is produced. However, sometimes multiple parameter values can produce the same observed input-output response. If the parameters themselves are of prime concern, it is necessary to guarantee that the parameter estimates are equivalent to those of the physical system. In this thesis, the term *parameter identification* is used to indicate that the parameter estimates are guaranteed to converge to their unique physical counterparts.

In this thesis, parameters are estimated by recursive methods. Employing a recursive estimator has several advantages over offline approaches. First, it makes it possible to use the parameter estimates in a feedback loop if desired. Secondly, even if the parameters are not used in a closed loop, it allows online identification of the parameters, enabling the operator to see real-time conditions. Finally, it allows the determination of time-varying changes of the parameters. Observing time-varying changes can be intrinsically useful; in addition, it can be used to reveal erroneous conditions or unmodeled dynamics, as such conditions may dramatically affect the estimated parameters over time.

In this chapter, a modeling framework suitable for parameter estimation is presented. Then, various parameter estimators are given. Finally, conditions for

identification of the estimated parameters are discussed, guaranteeing convergence to their real values. The material in this chapter is collated from [18, 39, 64, 84, 103, 114, 129].

2.1 Linear Parametric Model

A dynamic model often relates the inputs to the outputs of the plant. Examples of this is a transfer function, which relates the inputs to outputs in the frequency domain; or a state-space model, where the inputs, outputs and some internal state variables are related by first-order differential equations. In parameter estimation, a particularly useful structure is the linear parametric model (or linear regression model), given by

$$w' = \boldsymbol{\theta}^T \boldsymbol{\phi}', \tag{2.1}$$

where w' is a known signal, $\boldsymbol{\theta}$ is the parameter vector with unknown constant values, and $\boldsymbol{\phi}'$ is the signal (or regressor) vector. Note that, w' and $\boldsymbol{\phi}'$ are typically filtered versions of both the inputs and outputs of the plant. Thus, the linear parametric model often abstracts away the physical plant, as opposed to input-output descriptions such as transfer functions and state-space models. However, the system can often be transformed to the form (2.1), as long as the parameters appear linearly in the signals.

Remark 2.1. Even though the parameters appear linearly in the signal vector, the signals themselves can represent nonlinear dynamics.

Remark 2.2. The parameter vector is assumed constant for now. As time-varying parameters are of interest in this thesis, this case is discussed in Section 2.6.

An important implementation consideration concerns the case where derivatives of some signals, such as inputs or outputs, appear in w' or $\boldsymbol{\phi}'$. In order to avoid pure differentiation of the signals in (2.1), both sides of the equation can be filtered by a low-pass filter $1/\Lambda(s)$ of sufficiently high relative degree. Let the filtered signals be given by

$$w = \frac{w'}{\Lambda}, \quad \boldsymbol{\phi} = \frac{\boldsymbol{\phi}'}{\Lambda}. \tag{2.2}$$

Then, by applying the low-pass filter to each side of (2.1), we have

$$w = \boldsymbol{\theta}^T \boldsymbol{\phi}, \tag{2.3}$$

which is now suitable for implementation of the parameter estimators.

2.2 Estimation Model

In the subsequent sections, various recursive parameter estimators are presented for estimation of the unknown parameters $\boldsymbol{\theta}$. The vector of estimated parameters are denoted $\widehat{\boldsymbol{\theta}}$, and the estimation model used to generate a signal $\widehat{w}$, is given by

$$\widehat{w} = \widehat{\boldsymbol{\theta}}^T \boldsymbol{\phi}. \tag{2.4}$$

Furthermore, the estimation error ε is given by

$$\varepsilon = \frac{w - \widehat{w}}{m^2} \tag{2.5}$$

where m^2 is a normalization signal. The signal vector $\boldsymbol{\phi}$ may represent unstable dynamics or unbounded input signals. By using a normalization signal, the parameter estimates can be guaranteed to be bounded even in these conditions. One common normalization signal is given by

$$m^2 = 1 + \alpha \boldsymbol{\phi}^T \boldsymbol{\phi} \tag{2.6}$$

for some constant $\alpha > 0$, typically unity. If no normalization is needed, $m^2 = 1$ can be used. Furthermore, it will be used that the parameter estimate error is given by

$$\widetilde{\boldsymbol{\theta}} = \widehat{\boldsymbol{\theta}} - \boldsymbol{\theta}. \tag{2.7}$$

In the following sections, several estimation laws are presented for updating $\widehat{\boldsymbol{\theta}}$, such that the error ε becomes small in some sense as $t \to \infty$. Later it is discussed how to additionally guarantee that $|\widetilde{\boldsymbol{\theta}}| \to 0$ as $t \to \infty$, such that the parameters are identified.

2.3 Gradient Estimator

The gradient estimator (also called gradient method or steepest descent method) originates from optimization theory. Consider the quadratic cost function

$$J(\widehat{\boldsymbol{\theta}}) = \tfrac{1}{2}\varepsilon^2 m^2. \tag{2.8}$$

Since $J(\widehat{\boldsymbol{\theta}})$ is convex in $\widehat{\boldsymbol{\theta}}$, there is only a single global minimum corresponding to $\varepsilon = 0$. Thus, the optimal value can be approached by descending along the gradient of the cost function, that is

$$\dot{\widehat{\boldsymbol{\theta}}} = -\boldsymbol{\Gamma} \nabla J(\widehat{\boldsymbol{\theta}}) \tag{2.9}$$

for some constant, positive definite gain matrix $\boldsymbol{\Gamma}$. Solving (2.9) in terms of the observable signals, gives the update law

$$\dot{\widehat{\boldsymbol{\theta}}} = \boldsymbol{\Gamma}\varepsilon\boldsymbol{\phi}, \tag{2.10}$$

which can be implemented for estimation of the parameters.

Remark 2.3. Note that the gradient approach does not itself guarantee that the error $\varepsilon \to 0$ as $t \to \infty$. This can be explained by the situation where the estimate approaches the minimum of the cost function. Then, the error ε becomes small, which implies that $\dot{\widehat{\boldsymbol{\theta}}}$ also becomes small, such that any further convergence may stall. However, a Lyapunov analysis can be used to show that ε becomes small in some sense, as discussed in the following section.

2.4 Lyapunov Estimator

The Lyapunov estimator is a generalization of the gradient estimator where an additional strictly positive real (SPR) transfer function $W(s)$ is used in the linear parametric model. The modified parametric model is written as

$$w = W(s)\boldsymbol{\theta}^T\boldsymbol{\phi}, \tag{2.11}$$

where notation is kept consistent with the previous model for simplicity. The transfer function $W(s)$ can either represent a part of the plant such as a measuring device, or alternatively be implemented as a signal processing filter as part of the estimator, such as for noise attenuation. The filter can be assumed unitary $W(s) = 1$ if not desired.

The estimation model and normalization signal also need to be modified, such that

$$\widehat{w} = W(s)\widehat{\boldsymbol{\theta}}^T\boldsymbol{\phi}, \tag{2.12}$$

$$m^2 = 1 + \alpha W(s)\boldsymbol{\phi}^T\boldsymbol{\phi}, \tag{2.13}$$

or $m^2 = 1$ if normalization is not needed. The estimation error ε uses the same expression as previously, from (2.5).

A necessary condition for the stability of the estimator requires the transfer function $W(s)$ to be SPR. Positive realness of a transfer function is related to the passivity of a system. The SPR property can be stated by the following definitions:

Definition 2.1. A rational proper transfer function $W(s)$ is *positive real* (PR) if

- $W(s)$ is real for real s.
- $\mathrm{Re}\,[G(s)] \geq 0$ for all $\mathrm{Re}[s] > 0$.

Definition 2.2. Assume that $W(s)$ is not identically zero for all s. Then $W(s)$ is called *strictly positive real* if $W(s-\varepsilon)$ is PR for some $\varepsilon > 0$.

Remark 2.4. If the desired $W(s)$ is not SPR, it can be modified by introducing a transfer function $L(s)$ such that the new filter $W^*(s) = W(s)L(s)$ is SPR and replaces $W(s)$. If no proper $L(s)$ can be found, the signals w and $\boldsymbol{\phi}$ themselves can be filtered to allow the estimator to be realizable.

The update law for the Lyapunov estimator is given by

$$\dot{\widehat{\boldsymbol{\theta}}} = \boldsymbol{\Gamma}\varepsilon\boldsymbol{\phi}, \tag{2.14}$$

which is equivalent to the gradient estimator, except that the modified estimation model and normalization signal must be used (2.12)-(2.13).

The update law (2.14) applies for a wide range of problems and guarantees boundedness of the error ε and the estimate $\widehat{\boldsymbol{\theta}}$. The stability properties of the estimator can be shown using the Lyapunov-like function

$$V(\widetilde{\boldsymbol{\theta}}, \boldsymbol{e}) = \frac{\boldsymbol{e}^T\mathbf{P}_c\boldsymbol{e}}{2} + \frac{\widetilde{\boldsymbol{\theta}}^T\boldsymbol{\Gamma}^{-1}\widetilde{\boldsymbol{\theta}}}{2} \tag{2.15}$$

for some constant matrix $\mathbf{P}_c = \mathbf{P}_c^T > 0$. Additionally, $\boldsymbol{e}$ is the state vector for the state-space representation of the error signal, which can be written on the form $\varepsilon = W(s)u$ with $u = -\widetilde{\boldsymbol{\theta}}^T\boldsymbol{\phi} - \varepsilon\alpha\boldsymbol{\phi}^T\boldsymbol{\phi}$ applied as input. The SPR property of $W(s)$ is exploited in the derivation of the update law (2.14), canceling the indefinite terms of $\dot{V}$ such that it becomes negative semidefinite. This immediately guarantees boundedness – that is $\mathcal{L}_\infty$-stability of $\varepsilon, \widehat{\boldsymbol{\theta}}$, and $\mathcal{L}_2$-stability of $\varepsilon, \dot{\widehat{\boldsymbol{\theta}}}$. However, this does not yet guarantee convergence of the parameters which is essential for the parameter identification problem. An additional persistency of excitation property of the signal $\boldsymbol{\phi}$ is necessary, as discussed later.

Remark 2.5. Note that, by setting $W(s) = 1$, the Lyapunov analysis used here can be applied to the gradient estimator. Then, the first term in (2.15) can be omitted, and the stability properties of the Lyapunov estimator can be established for the gradient estimator.

2.5 Least Squares Estimator

Another popular technique is the recursive least squares (RLS) estimator. In this approach, the time-history of the error is considered, and minimized in a least-squares sense. As such, the estimator should perform better in conditions with noise and disturbances. Consider the quadratic cost function

$$J(\widehat{\boldsymbol{\theta}}) = \tfrac{1}{2}\int_0^t e^{-\beta(t-\tau)}\varepsilon^2(\tau)m^2(\tau)d\tau + \tfrac{1}{2}e^{-\beta t}(\widehat{\boldsymbol{\theta}} - \widehat{\boldsymbol{\theta}}_0)^T\mathbf{Q}_0(\widehat{\boldsymbol{\theta}} - \widehat{\boldsymbol{\theta}}_0), \tag{2.16}$$

where the first term involves an exponentially decreasing forgetting factor controlled by $\beta > 0$, and the second term involving $\mathbf{Q}_0 = \mathbf{Q}_0^T > 0$ provides a penalty on the initial estimate $\widehat{\boldsymbol{\theta}}_0$ of $\boldsymbol{\theta}$. Since $J(\widehat{\boldsymbol{\theta}})$ is a convex function in $\widehat{\boldsymbol{\theta}}$, the global minimum of the cost function satisfies

$$\nabla J(\widehat{\boldsymbol{\theta}}) = 0, \quad \forall\, t \geq 0 \tag{2.17}$$

which can be solved in both recursive and non-recursive form.

The solution to (2.17) in recursive form gives the update law for the least-squares estimator,

$$\dot{\widehat{\boldsymbol{\theta}}} = \mathbf{P}\varepsilon\boldsymbol{\phi}, \tag{2.18}$$

$$\dot{\mathbf{P}} = \beta\mathbf{P} - \frac{\mathbf{P}\boldsymbol{\phi}\boldsymbol{\phi}^T\mathbf{P}}{m^2}, \tag{2.19}$$

where $\mathbf{P}$ is called the covariance matrix, and $\mathbf{P}(0) = \mathbf{P}_0 = \mathbf{Q}_0^{-1}$. Additionally, $\beta > 0$ is the main tunable for the update speed of the estimator.

Note that, the last term in (2.19) may be negative semidefinite. Thus, since $\beta > 0$, then $\mathbf{P}$ may grow without bounds. In this case, the update law for the covariance matrix can be modified such that

$$\dot{\mathbf{P}} = \begin{cases} \beta\mathbf{P} - \mathbf{P}\frac{\boldsymbol{\phi}\boldsymbol{\phi}^T}{m^2}\mathbf{P}, & \text{if } \|\mathbf{P}\| \leq R_0 \\ 0, & \text{otherwise} \end{cases} \tag{2.20}$$

for some $R_0 > 0$. However, this modification is not necessary if $\boldsymbol{\phi}$ is persistently exciting, defined in the next section. Then, $\mathbf{P}$ is guaranteed to be bounded without modifications, since the time-integral of $\boldsymbol{\phi}\boldsymbol{\phi}^T$ is positive definite.

If $\beta = 0$, then the update law (2.18)-(2.19) is called the pure least squares estimator. In this situation, the covariance matrix $\mathbf{P}$ may become small after some time, slowing down the estimation rate. A solution in this case is to perform a covariance reset, that is

$$\mathbf{P}(t_r^+) = P_0 \tag{2.21}$$

at some time t_r, e.g. at regular intervals or when the smallest eigenvalue of $\mathbf{P}$ becomes smaller than some threshold. However, one should instead consider using $\beta > 0$ to ensure a more consistent update speed, especially if the time-varying nature of the parameters are of prime interest.

2.6 Convergence of Parameters

Although the three parameter estimators presented seem well motivated, they do not necessarily guarantee that the estimation error approaches zero. And even if this was the case, they would not necessarily guarantee the convergence of the parameter estimates $\widehat{\boldsymbol{\theta}}$ to the real parameters $\boldsymbol{\theta}$. The latter property is essential for identification of the parameters, which is the primary motivation for this thesis. The convergence of the parameters is discussed in this section.

First, some formal stability properties are provided for the three methods.

Theorem 2.1. *The update laws for the gradient estimator, Lyapunov estimator, and least squares estimator, given by* (2.10),(2.14),(2.18)-(2.19)*, respectfully, guarantee that*

(i) $\widehat{\boldsymbol{\theta}}, \varepsilon \in \mathcal{L}_\infty$,

(ii) $\dot{\widehat{\boldsymbol{\theta}}}, \varepsilon \in \mathcal{L}_2$.

Thus, the estimation error ε is bounded and becomes small in the $\mathcal{L}_2$-sense. However, the convergence of $\widehat{\boldsymbol{\theta}} \to \boldsymbol{\theta}$ has not yet been established, which is of prime importance in this thesis. In order to guarantee this property, the signal vector $\boldsymbol{\phi}$ needs to be *persistently exciting* (PE), defined next.

Definition 2.3 (Persistency of excitation)**.** The signal vector $\boldsymbol{\phi}$ is said to be PE if there exist constants, $\alpha_0, \alpha_1, T_\mathrm{p} > 0$ such that

$$\alpha_0 \mathbf{I} \leq \frac{1}{T_\mathrm{p}} \int_t^{t+T_\mathrm{p}} \boldsymbol{\phi}\boldsymbol{\phi}^T d\tau \leq \alpha_1 \mathbf{I}, \quad \forall t \geq 0, \tag{2.22}$$

where $\mathbf{I}$ is the identity matrix and α_0 is known as the level of excitation.

Now, the main result for convergence of the parameters can be stated.

Theorem 2.2. *Let* $\boldsymbol{\phi}$ *be PE, and* $\boldsymbol{\phi}, \dot{\boldsymbol{\phi}} \in \mathcal{L}_\infty$*. Then, the update laws for the gradient estimator, Lyapunov estimator, and least squares estimator, given by* (2.10),(2.14),(2.18)-(2.19)*, respectfully, guarantee that* $\widehat{\boldsymbol{\theta}} \to \boldsymbol{\theta}$ *exponentially fast.*

Consequently, a main consideration throughout this thesis is to establish the PE property of $\boldsymbol{\phi}$.

The results given in this chapter only consider a constant parameter vector. However, sometimes the time-varying properties of the parameters are of interest in this thesis. It is challenging to establish formal stability and convergence results in this case. However, as long as the conditions of Theorem 2.2 are satisfied, we have exponential convergence in the constant parameter case. In general, it can be established that exponential convergence in the constant parameter case, guarantees some degree of tracking for a sufficiently slowly-varying signal [4, 122]. Thus, the estimators presented can be used for tracking time-varying signals, typically as long as the parameters represent dynamics which are slower than the internal dynamics of the estimator.

Part I

Topography Estimation in AFM

Chapter 3

Topography Estimation by Force Inversion

A novel imaging method for revealing true topography and tip-sample interaction forces in dynamic mode atomic force microscopy is presented. The method utilizes observers for estimation of state and parameters. The cantilever dynamics are modeled as a linear system augmented by the tip-sample interaction force. The states of this augmented system are observed. The tip-sample force function is based on the Lennard-Jones potential with a nonlinearly parameterized unknown topography parameter. By estimating this parameter together with the tip-sample force using a nonlinear observer approach, the true topography of the sample can be found. The observer and parameter estimator is shown to be exponentially stable. A more conventional extended Kalman filter is also implemented for the same system, for comparison to the nonlinear observer. Numerical results are presented to demonstrate the approach.

Publications The material in this chapter is based on [145].

3.1 Introduction

Dynamic modes of AFM can be limited in terms of spatial resolution due to their dependency on steady-state signals, such as amplitude and phase. Instead, the error signal in the feedback loop of the vertical piezo scanner demonstrate an improved resolution, but the physical interpretation of the error signal is not immediately clear [7]. However, the error signal can been utilized together with the deflection signal and an observer in static mode for improved topography reconstruction [170, 171]. Some studies have used higher harmonics to exploit

additional information in the available signal [78, 163], and demonstrates an improved spatial resolution by utilizing the time-varying interaction force. Other studies try to exploit the transient response for more information [168]. Such methods are often observer-based, and can be used for directly controlling the interaction force [89], or for active Q-control [164, 165]. In active Q-control the cantilever stiffness – or quality factor – is virtually controlled. This can be exploited to reduce the time it takes for the transient to vanish, and allows for higher resolution and increased scanning bandwidth.

Furthermore, in dynamic mode AFM, the topography is typically mapped by ensuring that the demodulated deflection signal, such as the amplitude, remains constant in a feedback loop. However, since the chemical and mechanical properties of the sample are often spatially varying, a constant amplitude does not necessarily reveal the true topography of the sample [10, 99]. The true topography of the sample can be found through force-distance curves [202]. However, any new method for revealing the true topography in dynamic mode AFM would be beneficial, as it could enable improved resolution and imaging speed for true topography.

3.1.1 Contributions

In this chapter, a novel approach is used for topography imaging. The true topography and interaction force signals are estimated directly by using a state- and parameter estimator based on the results of Grip et al. [68], with guaranteed exponentially stable error dynamics. To achieve this, the linear cantilever dynamics is placed in a closed loop with a model of the tip-sample interaction force. This interaction force is described by the nonlinear Lennard-Jones potential, which depends on the position of the cantilever and the sample topography. Thus, the system can be described as a linear system augmented by a nonlinearly parameterized topography signal, which is applicable for the methodology in [68].

Similarly, an extended Kalman filter is also investigated for estimation of true topography and interaction force, for comparison to the nonlinear observer. However, it does not guarantee exponential stability, but rather demonstrates a lower sensitivity to measurement noise.

The presented method is designed for noncontact mode where the tip of the cantilever is located in the attractive region of the interaction force. This method does not rely on steady-state signals, thus, the transient information is exploited. Additionally, the presented scheme also provides an estimate of the interaction force, which can allow for more direct force feedback control such as in [89]. This force measurement can also be used for applications such as force spectroscopy

[127]. Estimation of interaction forces by use of observers has been investigated in optical probing systems [81], but to the authors' best knowledge no previous observer-based techniques for true topography estimation have included a model of the tip-sample interaction force.

3.1.2 Notation

The symbols used in this chapter are sometimes distinct from the rest of the thesis; rather, the notation in this chapter emphasizes an easy comparison to the notation and methodology used in [68].

3.1.3 Outline

This chapter is organized as follows. In Section 3.2 the modeling of the system is presented. The state- and parameter estimation scheme is presented in Section 3.3. The simulation setup is described in Section 3.4. In Section 3.5 the simulation results are presented. The overall imaging scheme is discussed in Section 3.6. Finally, conclusions are given in Section 3.7.

3.2 System Modeling

3.2.1 Cantilever Dynamics

The cantilever deflection subjected to the nonlinear interaction forces can be described by a Luré feedback system [179]. This model has proven effective for describing several properties – including stability – of the cantilever loop [181]. The model can be seen in Fig. 3.1, where F_{exc} controls the force applied to the cantilever for oscillation, F_{ts} is the tip-sample interaction force, and θ represents the topography of the sample.

The motion of the cantilever deflection can be described by a second-order harmonic oscillator [168] given by the transfer function

$$G(s) = \frac{\frac{1}{m}}{s^2 + 2\omega_0\zeta s + \omega_0^2} \tag{3.1}$$

where ω_0 is the resonance frequency, ζ is the damping ratio, and m is the effective mass of the cantilever.

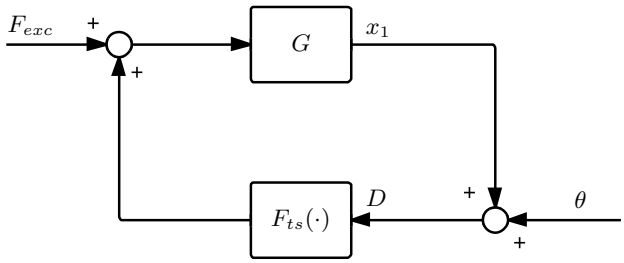

Figure 3.1: Block diagram of the cantilever system. F_{exc} is controllable, while the cantilever deflection x_1 is the only measurable signal. The sample topography is represented by the signal θ.

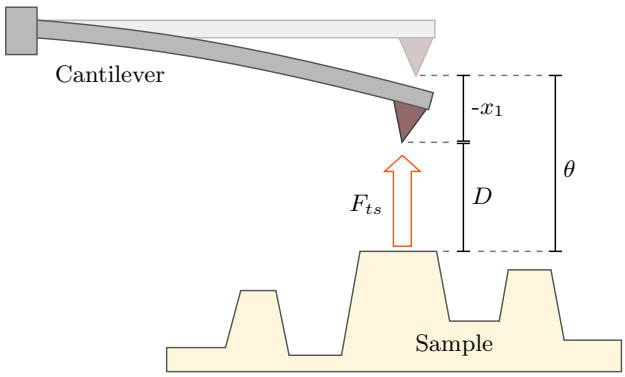

Figure 3.2: Interaction between cantilever and sample, $D = x_1 + \theta$.

3.2.2 Tip-Sample Interaction Force

The interaction force between the probe tip and sample surface is nonlinear. Additionally, it has both an attractive region at large distances due to van der Waals-forces, and a repulsive region at very short distances due to electrostatic forces [173]. The attractive force can lead to an undesirable effect where the tip suddenly jumps into contact with the repulsive region of the force [62].

The interaction force between tip and sample can be described using the Lennard-Jones potential [3]

$$F_{\text{ts}}(D) = k_1 \left[\frac{\sigma^2}{D^2} - \frac{1}{30} \frac{\sigma^8}{D^8} \right] \tag{3.2}$$

where $D \triangleq x_1 + \theta$ is the tip-sample distance, x_1 is the cantilever deflection, θ is the unknown topography to be estimated, and $k_1 < 0, \sigma$ are parameters which depend on the physical and geometrical properties of the tip and the sample assumed to be known. The cantilever interaction with the sample is illustrated in Fig. 3.2.

3.2.3 Noncontact Mode

As we operate the cantilever in noncontact mode, the following assumption introduces a monotonically increasing version of the Lennard-Jones potential, valid in this operating mode:

Assumption 3.1. The modified force profile g is given by

$$g(D) = \begin{cases} F_{\text{ts}}(D) & D > D_{cut} \\ S(D) & \text{otherwise} \end{cases} \tag{3.3}$$

$$S(D) = e^{r(D - D_{cut})} \left[F_{\text{ts}}(D_{cut}) - F_{\text{ts}}(D_0) \right] + F_{\text{ts}}(D_0) \tag{3.4}$$

where

$$\begin{aligned} D_0 &\triangleq \min_D F_{\text{ts}}(D) \\ &= \sigma \sqrt[6]{2/15} \end{aligned} \tag{3.5}$$

and $D_{cut} > D_0$ is a user-defined constant ideally set close to D_0.

To ensure sufficient smoothness of g, r needs to be solved from

$$\left. \frac{\partial S}{\partial D} \right|_{D_{cut}} = \left. \frac{\partial F_{\text{ts}}}{\partial D} \right|_{D_{cut}} \tag{3.6}$$

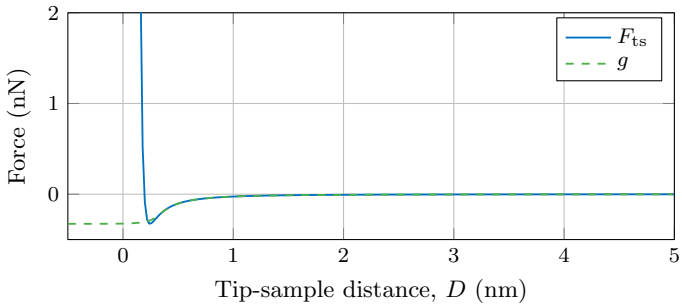

Figure 3.3: The tip-sample interaction force resulting from the Lennard-Jones potential between a half-sphere and a flat surface, plotted with the modified force profile g employed by the nonlinear observer in noncontact mode.

which gives

$$r = k_1 \frac{-2\sigma^2 D_{cut}^{-3} + \frac{8}{30}\sigma^8 D_{cut}^{-9}}{F_{\text{ts}}(D_{cut}) - F_{\text{ts}}(D_0)} \tag{3.7}$$

The interaction force F_{ts} is plotted with the modified force $g(D)$ in Fig. 3.3 as a function of tip-sample distance for a given set of parameters.

Remark 3.1. The purpose of introducing a monotonically increasing modified force profile is to guarantee exponential stability of the nonlinear observer according to Theorem 3.1. Function $S(D)$ in (3.4) was chosen to provide a monotonically increasing force profile in the contact regime with a smooth transition to the traditional Lennard-Jones force curve $F_{\text{ts}}(D)$ in (3.2).

The operation in noncontact mode can be achieved either by feedback control of the z-piezo in the AFM or by controlling the cantilever oscillation amplitude. Alternatively, one can assume sufficiently small changes in the topography. Employing feedback control is outside the scope of this work, but will be briefly presented in the simulations in Section 3.4–3.5. As such, we will make use of the following assumption:

Assumption 3.2. The topography is assumed to be bounded, that is, there exists a known $\bar{\Theta} \in [\theta_{\min}, \theta_{\max}]$ such that $\theta \in \bar{\Theta}$.

Additionally, the frequency of the driving signal for the cantilever oscillation should be set equal to or larger than the resonance frequency. When the tip approaches the surface, the attractive tip-sample force will effectively lower the resonance frequency of the cantilever. Thus, the amplitude will be reduced as the tip comes closer to the sample and is less inclined to approach the repulsive region [174].

3.3 State- and Parameter Estimator

3.3.1 Overview

We utilize the methodology in [68] for estimation of states and parameters. The system depicted in Fig. 3.1 can be written in an extended state-space form as

$$\begin{bmatrix} \dot{\boldsymbol{x}} \\ \dot{\phi} \end{bmatrix} = \begin{bmatrix} \mathbf{A} & \boldsymbol{E} \\ 0 & 0 \end{bmatrix} \begin{bmatrix} \boldsymbol{x} \\ \phi \end{bmatrix} + \begin{bmatrix} \boldsymbol{B} \\ 0 \end{bmatrix} u + \begin{bmatrix} \mathbf{0} \\ 1 \end{bmatrix} d \tag{3.8}$$

$$y = \boldsymbol{C}\boldsymbol{x} \tag{3.9}$$

where the interaction force $g(x_1 + \theta)$ has been introduced as a state ϕ and its time-derivative denoted as $d(\boldsymbol{x}, \theta) \triangleq \dot{\phi}$, the input u is the driving force of the cantilever, and $y = x_1$ as the only measurable signal.

The states $\boldsymbol{x} \triangleq (x_1, x_2)^T$ of the system represent the cantilever deflection and the deflection velocity respectively, and the system matrices are given by

$$\mathbf{A} = \begin{bmatrix} 0 & 1 \\ -\omega_0^2 & -2\zeta\omega_0 \end{bmatrix}, \; \boldsymbol{B} = \boldsymbol{E} = \begin{bmatrix} 0 \\ \frac{1}{m} \end{bmatrix}, \; \boldsymbol{C} = \begin{bmatrix} 1 & 0 \end{bmatrix}. \tag{3.10}$$

Let us also introduce the definition $\boldsymbol{\nu} \triangleq \mathrm{col}(u, y)$ to simplify notation. The time-derivative of the interaction force can be found as

$$d(\boldsymbol{x}, \theta) = \begin{cases} k_1 \left[-2\sigma^2 D^{-3} + \frac{8}{30}\sigma^8 D^{-9} \right] x_2 & D > D_{cut} \\ r e^{r(D - D_{cut})} \left[F_{\mathrm{ts}}(D_{cut}) - F_{\mathrm{ts}}(D_0) \right] x_2 & \text{otherwise} \end{cases} \tag{3.11}$$

where we have used $\dot{\theta} = 0$ which assumes that θ is slowly-varying compared to the rest of the dynamics. This will ultimately introduce a limitation to the lateral scanning speed that can be employed in order for the observer to properly track the topography. However, this will always be the case when imaging using any type of scanning probe microscope.

The modified high-gain observer of [68] is employed to estimate the states of this extended system, while the parameter estimator provides estimates for θ in (3.2) as depicted in Fig. 3.4. Estimates are denoted by a hat, e.g. $\widehat{\theta}$.

The estimation scheme in [68] contains several assumptions that must be satisfied in order to guarantee stability.

Assumption 3.3. The time derivative $\dot{u}$ is well defined and piecewise continuous; there exist compact sets $\boldsymbol{X} \in \mathbb{R}^n, U \subset \mathbb{R}^m$, and $U' \subset \mathbb{R}^m$ such that for all $t \geq 0, \boldsymbol{x} \in \boldsymbol{X}, u \in U$, and $\dot{u} \in U'$.

Assumption 3.4. The triple $(\boldsymbol{C}, \mathbf{A}, \boldsymbol{E})$ is left-invertible and minimum-phase.

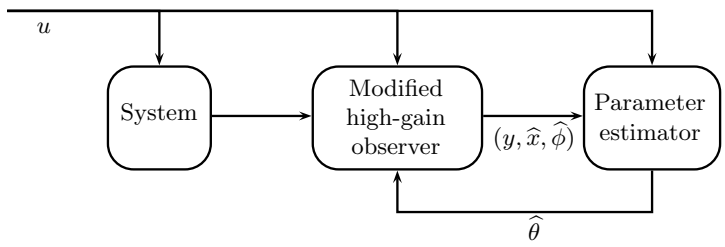

Figure 3.4: Structure of the state- and parameter estimator. Modified from [68].

Assumption 3.5. There exists a number $\beta > 0$ such that for all $(\boldsymbol{\nu}, \dot{\boldsymbol{\nu}}, \boldsymbol{x}, \theta, \phi) \in V \times V' \times X \times \Theta \times \Phi$ and for all $(\widehat{\boldsymbol{x}}, \widehat{\theta}, \widehat{\phi}) \in \mathbb{R}^n \times \Theta \times \mathbb{R}^k$,
$\left| d(\boldsymbol{\nu}, \dot{\boldsymbol{\nu}}, \boldsymbol{x}, \theta, \phi) - d(\boldsymbol{\nu}, \dot{\boldsymbol{\nu}}, \widehat{\boldsymbol{x}}, \widehat{\theta}, \widehat{\phi}) \right| \leq \beta \left| \mathrm{col}(\boldsymbol{x} - \widehat{\boldsymbol{x}}, \theta - \widehat{\theta}, \phi - \widehat{\phi}) \right|$.

The preceding assumptions are satisfied as follows:

- A sinusoidal input signal u will be employed for oscillating the cantilever. The states x_1, x_2 are bounded due to the damped nature of the cantilever dynamics (3.1). Thus, Assumption 3.3 is satisfied.
- The system $G(s)$ has no invariant zeros, so it is left-invertible and minimum-phase and Assumption 3.4 is satisfied.
- Due to the smooth saturation introduced on g in (3.3), d becomes globally Lipschitz in terms of both x_1 and θ. Additionally, x_2 appears only linearly in (3.11), thus Assumption 3.5 is satisfied.

3.3.2 Modified High-Gain Observer

By following the methodology in [68] a modified high-gain observer will be designed next where the estimated parameters are assumed to be available.

The observer is implemented as

$$\begin{aligned} \dot{\widehat{\boldsymbol{x}}} &= \mathbf{A}\widehat{\boldsymbol{x}} + \boldsymbol{B}u + \boldsymbol{E}\widehat{\phi} + \boldsymbol{K}_{\boldsymbol{x}}(\varepsilon)(y - \boldsymbol{C}\widehat{\boldsymbol{x}}) \\ \dot{z} &= -\frac{\partial g}{\partial \theta}\dot{\widehat{\theta}} - \frac{\partial g}{\partial \boldsymbol{x}}\boldsymbol{K}_{\boldsymbol{x}}(\varepsilon)(y - \boldsymbol{C}\widehat{\boldsymbol{x}}) + K_\phi(\varepsilon)(y - \boldsymbol{C}\widehat{\boldsymbol{x}}) \\ \widehat{\phi} &= g(\widehat{x}_1, \widehat{\theta}) + z \end{aligned} \tag{3.12}$$

where the gains $\boldsymbol{K}_{\boldsymbol{x}}(\varepsilon), K_\phi(\varepsilon)$ are to be determined. By defining the errors $\widetilde{\boldsymbol{x}} \triangleq \boldsymbol{x} - \widehat{\boldsymbol{x}}$, $\widetilde{\phi} \triangleq \phi - \widehat{\phi}$, we can find the error dynamics from (3.12). Our goal is to design the gains $\boldsymbol{K}(\varepsilon) \triangleq \mathrm{col}(\boldsymbol{K}_{\boldsymbol{x}}(\varepsilon), K_\phi(\varepsilon))$ such that for a sufficiently small ε the error dynamics are input-to-state stable with respect to $\widetilde{\theta} \triangleq \theta - \widehat{\theta}$.

The error dynamics are found as

$$\begin{bmatrix} \dot{\widetilde{\boldsymbol{x}}} \\ \dot{\widetilde{\phi}} \end{bmatrix} = \begin{bmatrix} 0 & 1 & 0 \\ 0 & 0 & 1 \\ 0 & -\omega_0^2 & -2\zeta\omega_0 \end{bmatrix} \begin{bmatrix} \widetilde{\boldsymbol{x}} \\ \widetilde{\phi} \end{bmatrix} + \begin{bmatrix} 0 \\ 0 \\ 1 \end{bmatrix} \widetilde{d} - \begin{bmatrix} \boldsymbol{K}_{\boldsymbol{x}}(\varepsilon) \\ K_\phi(\varepsilon) \end{bmatrix} \widetilde{y} \tag{3.13}$$

The error dynamics are then transformed to the special coordinate basis (SCB). The Maple program developed in [67] was used for this purpose, resulting in the transformation matrices

$$\boldsymbol{\Lambda}_1 = \begin{bmatrix} 1 & 0 & 0 \\ 0 & 1 & 0 \\ \omega_0^2 & 2\zeta\omega_0 & 1 \end{bmatrix}, \quad \Lambda_2 = [1], \quad \Lambda_3 = [m]$$

which transforms the system to the SCB in accordance with

$$\mathrm{col}(\widetilde{\boldsymbol{x}}, \widetilde{\phi}) = \boldsymbol{\Lambda}_1 \chi, \quad \widetilde{y} = \Lambda_2 \gamma, \quad \widetilde{d} = \Lambda_3 \delta$$

The observer gains can now be designed. Let $\bar{\boldsymbol{K}}_q = \mathrm{col}(\bar{K}_{q_1}, \ldots, \bar{K}_{q_3})$ be chosen such that the matrix

$$\mathbf{H} \triangleq \begin{bmatrix} 1 & 0 & 0 \\ 0 & 1 & 0 \\ 0 & 0 & 0 \end{bmatrix} - \bar{\boldsymbol{K}}_q \begin{bmatrix} 1 & 0 & 0 \end{bmatrix} \tag{3.14}$$

is Hurwitz using a pole-placement technique [68]. Then for our special case without any invariant zeros, the resulting gain is found from $\boldsymbol{K}_q(\varepsilon) = \mathrm{col}(\bar{K}_{q1}/\varepsilon, \ldots, \bar{K}_{q3}/\varepsilon^3)$ and the transformation $\boldsymbol{K}(\varepsilon) = \Lambda_1 \boldsymbol{K}_q(\varepsilon) \Lambda_2^{-1}$. The poles of $\mathbf{H}$ were placed at $-1 \pm 0.2i$ and -2, resulting in the gain

$$\boldsymbol{K}(\varepsilon) = \begin{bmatrix} 4.0\epsilon^{-1} \\ 5.04\epsilon^{-2} \\ 4.0\omega_0^2\epsilon^{-1} + 10.08\zeta\omega_0\epsilon^{-2} + 2.08\epsilon^{-3} \end{bmatrix} \tag{3.15}$$

The following Lemma from [68] ensures that this procedure for determining the gains will provide a stable estimate of the states with respect to $\widetilde{\theta}$:

Lemma 1. *Assuming $\widehat{\theta} \in \Theta$, there exists $0 < \varepsilon^* \leq 1$ such that for all $0 < \varepsilon \leq \varepsilon^*$, the error dynamics (3.13) are input-to-state stable with respect to $\widetilde{\theta}$.*

3.3.3 Parameter Estimator

In the previous section a high-gain observer was designed based on known parameters. Next, we will design a parameter estimator for the topography signal which

will be provided to the observer. An update law for the topography estimate $\widehat{\theta}$,

$$\dot{\widehat{\theta}} = u_\theta(\boldsymbol{\nu}, \widehat{\boldsymbol{x}}, \widehat{\phi}, \widehat{\theta}) \tag{3.16}$$

must be found satisfying the following assumption from [68]:

Assumption 3.6. There exist a differentiable function $V_u : \mathbb{R}_{\geq 0} \times (\Theta - \Theta) \to \mathbb{R}_{\geq 0}$ and positive constants $a_1, \ldots, a_4$ such that for all $(t, \widetilde{\theta}) \in \mathbb{R}_{\geq 0} \times (\Theta - \Theta)$,

$$\begin{aligned}
&a_1 \left|\widetilde{\theta}\right|^2 \leq V_u(t, \widetilde{\theta}) \leq a_2 \left|\widetilde{\theta}\right|^2 \\
&\frac{\partial V_u}{\partial t}(t, \widetilde{\theta}) - \frac{\partial V_u}{\partial \widetilde{\theta}}(t, \widetilde{\theta}) u_\theta(\boldsymbol{\nu}, \boldsymbol{x}, \phi, \theta - \widetilde{\theta}) \leq -a_3 \left|\widetilde{\theta}\right| \\
&\left|\frac{\partial V_u}{\partial \widetilde{\theta}}(t, \widetilde{\theta})\right| \leq a_4 \left|\widetilde{\theta}\right|
\end{aligned}$$

Furthermore, the update law (3.16) ensures that if $\widehat{\theta}(0) \in \Theta$, then for all $t \geq 0, \widehat{\theta} \in \Theta$.

Assumption 3.6 guarantees that the origin of the error dynamics

$$\dot{\widetilde{\theta}} = -u_\theta(\boldsymbol{\nu}, \widehat{\boldsymbol{x}}, \widehat{\phi}, \theta - \widetilde{\theta}) \tag{3.17}$$

where $\widetilde{\theta} \triangleq \theta - \widehat{\theta}$, is uniformly exponentially stable whenever $\widehat{\boldsymbol{x}} = \boldsymbol{x}$ and $\widehat{\phi} = \phi$.

In [66, Ch. 6], four propositions are stated in order to satisfy Assumption 6. Being a rational function with an 8th-degree polynomial in the denominator, it is difficult to solve $g(x_1 + \theta)$ in terms of θ. Instead, a numerical search is performed to find the solution. We restate the following proposition from [66]:

Proposition 3.1. *Suppose that there exist a positive-definite matrix P and a function $M : V \times \mathbb{R}^n \times \Theta \to \mathbb{R}^{p \times k}$, such that for all $(\boldsymbol{\nu}, \boldsymbol{x}) \in V \times \mathbb{R}^n$ and for all pairs $\theta_1, \theta_2 \in \Theta$,*

$$M(\boldsymbol{\nu}, \boldsymbol{x}, \theta_1) \frac{\partial g}{\partial \theta}(\boldsymbol{\nu}, \boldsymbol{x}, \theta_2) + \frac{\partial g}{\partial \theta}^T(\boldsymbol{\nu}, \boldsymbol{x}, \theta_2) M^T(\boldsymbol{\nu}, \boldsymbol{x}, \theta_1) \geq 2P \tag{3.18}$$

Then Assumption 3.6 is satisfied with the update law

$$u_\theta(\boldsymbol{\nu}, \widehat{\boldsymbol{x}}, \widehat{\phi}, \widehat{\theta}) = \mathrm{Proj}\left(\Gamma M(\boldsymbol{\nu}, \widehat{\boldsymbol{x}}, \widehat{\theta})(\widehat{\phi} - g(\boldsymbol{\nu}, \widehat{\boldsymbol{x}}, \widehat{\theta})\right), \tag{3.19}$$

where Γ is a symmetric, positive-definite gain matrix.

Next, we need to choose an M such that (3.18) is satisfied. Let $M(\widehat{D}) = M(\boldsymbol{\nu}, \widehat{\boldsymbol{x}}, \widehat{\theta})$ where $\widehat{D} \triangleq \widehat{x}_1 + \widehat{\theta}$. We then choose

$$M(\widehat{D}) = \tfrac{1}{2} M_{\max} \left[\tanh(M_{\mathrm{rate}}(\widehat{D} - D_M)) + 1\right] \tag{3.20}$$

where $M_{\max}, M_{\text{rate}}, D_M$ are tunable positive constants and $M(\widehat{D}) > 0$ for any finite value of $\widehat{D}$. Since our g and θ are scalar values, we have from (3.18),

$$2M(\boldsymbol{\nu}, \boldsymbol{x}, \theta_1)\frac{\partial g}{\partial \theta}(\boldsymbol{\nu}, \boldsymbol{x}, \theta_2) \geq 2P \tag{3.21}$$

To satisfy this inequality for some positive P, we want to show that $\partial g/\partial\theta$ is strictly positive in the domain of the arguments. We have

$$\frac{\partial g}{\partial \theta}(\boldsymbol{x}, \theta) = \begin{cases} k_1\left[-2\sigma^2 D^{-3} + \frac{8}{30}\sigma^8 D^{-9}\right] & D > D_{cut} \\ re^{r(D-D_{cut})}\left[F_{\text{ts}}(D_{cut}) - F_{\text{ts}}(D_0)\right] & \text{otherwise} \end{cases} \tag{3.22}$$

The first case in (3.22) has only one real, positive root at the point $D = D_0$. Thus, $\frac{\partial g}{\partial \theta}$ never switches sign in $D > D_{cut} > D_0$. Above this point the negative D^{-3} term dominates, and since $k_1 < 0$, the result is positive. For the second case, we have that $F_{\text{ts}}(D_{cut}) - F_{\text{ts}}(D_0) > 0$, the exponential function is positive for all real, finite values, and r has the same sign as in the first case as evident from (3.7). Additionally, $\frac{\partial g}{\partial \theta} \neq 0$ for any finite value of D, assuming $k_1, \sigma \neq 0$.

Thus, the conditions of Proposition 3.1 are satisfied, and we can use the update law (3.19)–(3.20). The projection function in (3.19) ensures that the parameters $\widehat{\theta}$ never leave Θ. For implementation details of this function we refer to [66].

Remark 3.2. Another feasible candidate for M is the choice $M = \frac{\partial g}{\partial \theta}$ as discussed in [66]. We found this choice to give wildly varying estimation speeds as the cantilever tip approached the sample. At the minimum tip-sample distance the update was very quick – limiting the update gain – while very slow anywhere else. The new choice of M in (3.20) gives a smoother transition of the estimation speed which allows us to increase the overall gain of the update law, providing better performance. Because the tip-sample force at large distances is very small, its detection will be dominated by noise. Thus, M is saturated by M_{max} to limit the update speed at large tip-sample distances.

3.3.4 Stability of Interconnected System

The interconnection between the modified high-gain observer (3.12) and the parameter estimator (3.16) also needs to be considered.

Assumption 3.7. The parameter update law $u_\theta(\boldsymbol{\nu}, \widehat{\boldsymbol{x}}, \widehat{\phi}, \widehat{\theta})$ is Lipschitz continuous in $(\widehat{\boldsymbol{x}}, \widehat{\phi})$, uniformly in $(\boldsymbol{\nu}, \widehat{\theta})$, on $V \times \mathbb{R}^n \times \mathbb{R}^k \times \Theta$.

This assumption can be satisfied as follows:

- Consider the update law (3.19). We have that M in (3.20) is a saturated Lipschitz continuous function because of its dependency on the $\tanh(\cdot)$-function. We also have that $\partial g/\partial x_1 = \partial g/\partial \theta$ given in (3.22) is continuous and bounded. Thus g is Lipschitz continuous both in terms of x_1 and θ. The projection function in the update law does not change the Lipschitz properties as discussed in [66]. Thus, Assumption 3.7 is satisfied.

Finally, the following theorem based on [68, Thm. 1] establishes the stability of the interconnected system:

Theorem 3.1. *If Assumption 3.1 – 3.7 are satisfied and $\widehat{\theta}(0) \in \Theta$, there exists $0 < \varepsilon^* \leq 1$ such that for all $0 < \varepsilon \leq \varepsilon^*$, the origin of the error dynamics of the observer (3.13) and parameter estimator (3.17) are exponentially stable.*

Remark 3.3. Note that the system is globally exponentially stable with respect to the observer error states, i.e. it is only the parameter estimates that have limitations on their initial values.

3.3.5 Extended Kalman Filter

In order to provide a more detailed discussion on the performance of the nonlinear approach, an extended Kalman filter (EKF) was implemented for comparison. EKF is a well-established method for estimating the states of a nonlinear system, see e.g. [182].

The system as described in Section 3.2 can be modeled by the following set of equations:

$$\begin{aligned} \dot{x}_1 &= x_2 \\ \dot{x}_2 &= -\omega_0^2 x_1 - 2\zeta\omega_0 x_2 + \tfrac{1}{m}u + \tfrac{1}{m}F_{\text{ts}}(D) \\ \dot{D} &= x_2 + w \\ y &= x_1 + v \end{aligned} \tag{3.23}$$

where the zero-mean white process noise w models the changes in topography with covariance Q, and v is zero-mean white measurement noise with covariance R.

The observer was implemented by using the continuous-time extended Kalman filter described in [182]. From the state estimates, the topography θ can be found from $\theta = D - x_1$ and the estimated interaction force is found by calculating $F_{\text{ts}}(D)$.

3.4 Simulation Setup

A simulation of the system has been set up with the system dynamics and estimation laws described in the previous sections. The parameters used in the simulation are given in Table 3.1. A sinusoidal input signal is used for the cantilever giving it a freely oscillating amplitude of 100 nm. An oscillating cantilever is chosen in order to avoid the jump-to-contact behavior thereby satisfying Assumption 1. Initial distance to the sample is set to 105 nm from the resting position of the cantilever, while the topography is modeled as a square-like wave. The interaction force parameters σ, k_1 in (3.2) are based on values and formulas from [173].

The cantilever position is only controlled by a feedforward signal. Thus, over cavities in the sample the tip-sample distance will increase, and ultimately reduce the interaction force. This does affect the performance of the observers. To compensate for this, one simulation was run with a feedback controller to illustrate some possibilities for actual implementation. The feedback controller uses the estimated tip-sample distance $\widehat{D} = \widehat{x}_1 + \widehat{\theta}$ to find the closest approach distance each cycle. A P-controller on the error between this signal and a reference distance is then used to control the amplitude of the cantilever oscillations.

Simulations were run both with and without additive white noise on the output of the cantilever deflection measurement, in order to discuss the effects of noise on the system. Note that the actual force F_{ts} in (3.2) is used in the plant dynamics to provide a more physically accurate simulation.

Table 3.1: Simulation Parameters

Param.	Value	Param.	Value
ω_0	$1000\,\text{Hz}$	M_{max}	10^{-5}
ζ	0.005	M_{rate}	5×10^4
m	$1.5728 \times 10^{-9}\,\text{kg}$	D_M	10^{-5}
σ	$3.41 \times 10^{-10}\,\text{m}$	D_{cut}	$D_0 + 10^{-10}\,\text{m}$
k_1	$-2.2242 \times 10^{-10}\,\text{N}$	Q	10^{-6}
ε	10^{-5}	R	10^{-16}
Γ	5×10^4	$u(t)$	$6.21 \times 10^{-11} \sin(\omega_0 t)\,[\text{N}]$

3.5 Results

The simulation results are plotted in Fig. 3.5 – Fig. 3.10.

Fig. 3.5 shows the estimated topography parameter $\widehat{\theta}$ plotted together with the

actual topography. It can be seen that the estimates from both the nonlinear observer and the extended Kalman filter (EKF) are reasonably accurate. In Fig. 3.6 it can be seen that the estimates have a staircase-like behavior. The steps occur when the cantilever position is at the bottom of its oscillation cycle, where the force interaction is the strongest. Far from the sample, the force field is so weak it does not provide any information on the distance.

After adding output noise to the simulations, we had to increase the ε-value and reduce the gain Γ of the nonlinear observer to give sufficiently accurate estimations. However, this resulted in some loss in performance as seen in Fig. 3.7, noticeable by the slightly slower response and small drifting when the cantilever oscillates far from the surface over the sample cavities. The closest tip-sample distance each oscillation cycle is plotted in Fig. 3.8, which varies with the topography due to the lack of feedback control.

With the feedback controller turned on the nonlinear observer regains some of its lost performance after adding output noise, as seen in Fig. 3.9. Both observers also provide an estimate of the tip-sample interaction force as seen in Fig. 3.10.

3.6 Discussion

The results demonstrate the efficiency of both the nonlinear observer (NLO) scheme and extended Kalman filter (EKF). The advantage of the NLO is its near-global exponential stability results as given in Theorem 3.1. The results suggest that the EKF provides a somewhat better trade-off between noise attenuation and response time. However, this could possibly be due to the tuning of the parameters.

The choice of M in (3.20) was based on an improvised approach after studying the observed characteristics of the NLO. Possibilities for further improvements to this function is considerable, as it is only required to be positive definite and to satisfy the Lipschitz conditions of Assumption 3.7.

For studying highly inhomogeneous samples the parameters in the Lennard-Jones potential in (3.2) would need to be estimated simultaneously. This can be achieved by including them in the parameter estimator of the nonlinear observer. This should be possible with relative ease, as a reformulation of these parameters will make them appear linearly in (3.2).

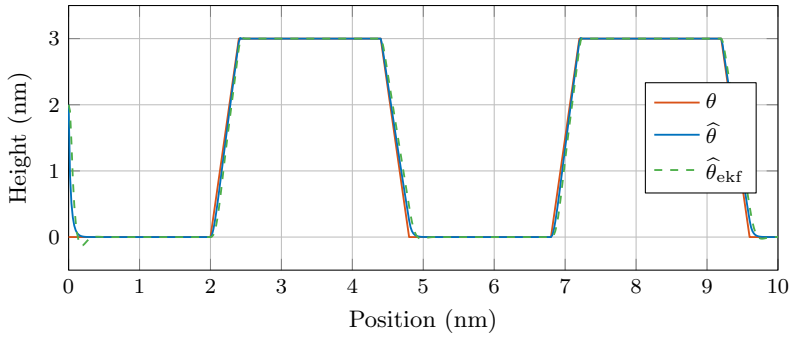

Figure 3.5: Topography estimate.

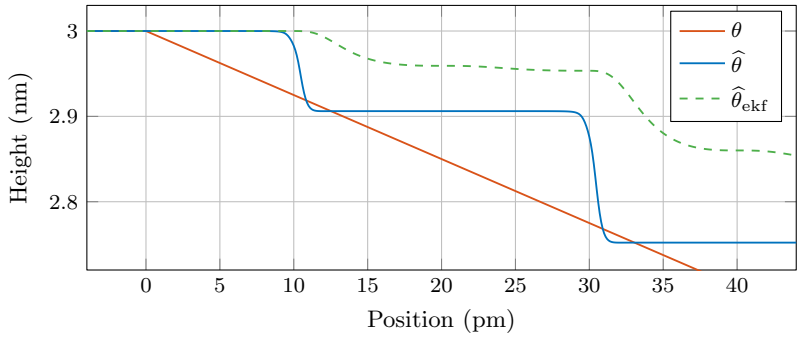

Figure 3.6: Zoom of topography estimate. Position offset by 4.4 nm.

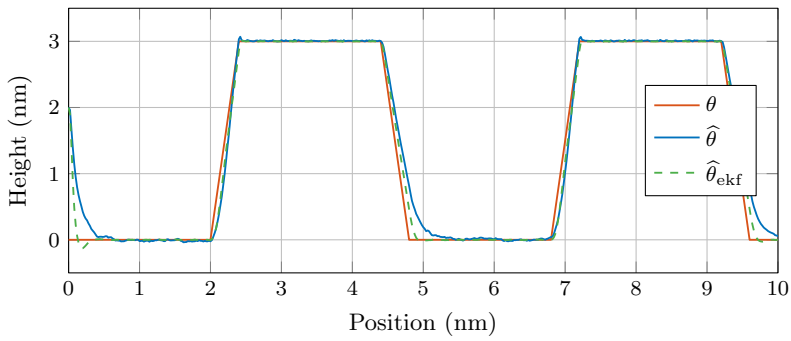

Figure 3.7: Topography estimate with output noise. To attenuate the effects of noise ϵ was increased by a factor of 15 and Γ reduced by a factor of 4, which results in a slower response especially at large tip-sample distances.

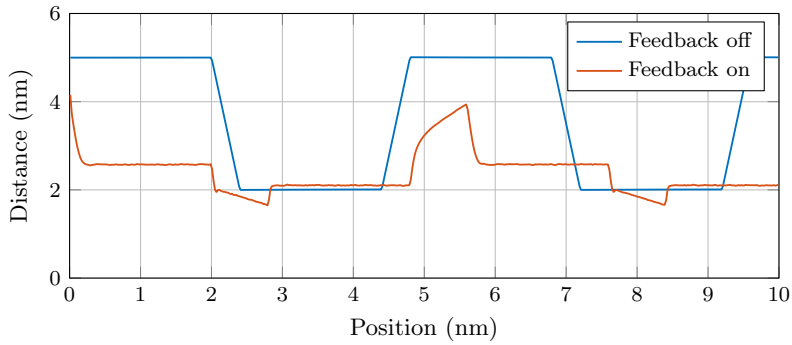

Figure 3.8: Closest tip-sample distance D each oscillation cycle with and without feedback control.

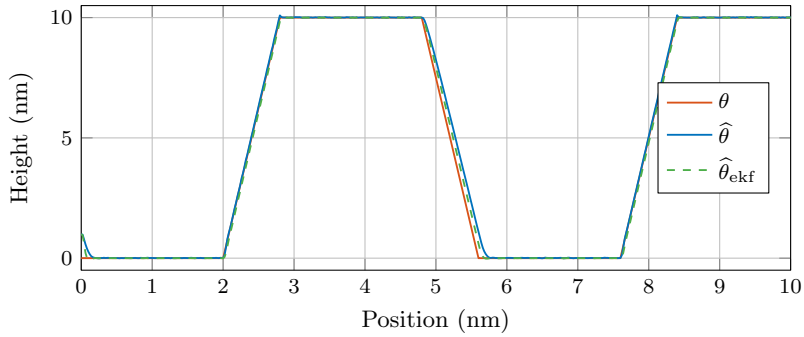

Figure 3.9: Topography estimate with output noise and feedback control. This allows for scanning larger height differences and reduced gains which attenuates some of the noise.

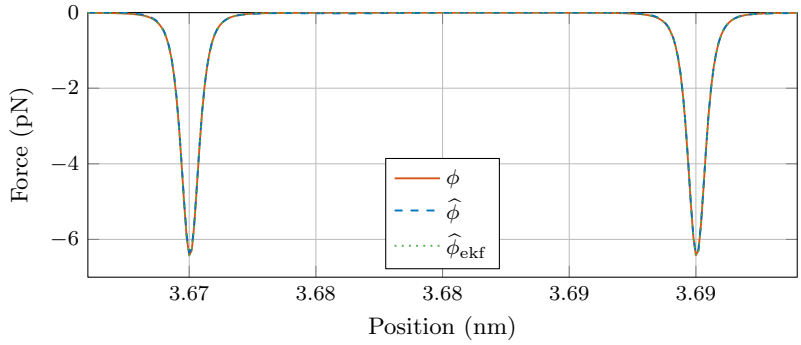

Figure 3.10: Estimated interaction force ϕ with noise.

3.7 Conclusions

In this chapter, a novel imaging technique for noncontact operation mode in AFM based on observers, is introduced. Two distinct observer schemes are presented to show the viability of this approach, both of which directly estimates the tip-sample interaction force and topography of the sample. The nonlinear observer shows well-defined exponential stability results. A simulation study confirms the stability and convergence properties of the analysis. The second observer, based on an extended Kalman filter, shows good performance in terms of accuracy and noise tolerance, but the nonlinear observer has stronger stability properties.

Part II

Demodulation for High-Speed Dynamic Mode AFM

Chapter 4

Amplitude and Phase Demodulation by Lyapunov Estimator

In dynamic mode atomic force microscopy (AFM), the imaging bandwidth is governed by the slowest component in the open-loop chain consisting of the vertical actuator, cantilever and demodulator. While the common demodulation method is to use a lock-in amplifier (LIA), its performance is ultimately bounded by the bandwidth of the post-mixing low-pass filters. This chapter proposes an amplitude and phase estimation method based on a strictly positive real Lyapunov design approach. The estimator is designed to be of low complexity while allowing for high bandwidth, and is suitable for multifrequency AFM applications. Additionally, suitable gains for high performance are suggested such that no tuning is necessary. The Lyapunov estimator is experimentally implemented for amplitude demodulation and shown to surpass the LIA in terms of tracking bandwidth and noise performance. High-speed AFM images are presented to corroborate the results.

Publications The material in this chapter is primarily based on [148]. The parts on multifrequency are based on [75].

4.1 Introduction

In dynamic mode AFM, the imaging bandwidth is limited by the slowest component in the control loop consisting of the vertical actuator, cantilever, and demodulator, as outlined in Chapter 1. A high bandwidth demodulator is necessary to complete the control loop, which is the primary focus of this chapter.

A typical imaging setup of a demodulator used in amplitude modulated AFM is shown in Fig. 4.1. The most common demodulator in AFM applications is the lock-in amplifier, which is a type of synchronous demodulator where the carrier reference signal is known. In their simplest form, these amplifiers consist of a multiplier followed by a low-pass filter [130]. Although lock-in amplifiers can provide a high noise rejection, the performance is ultimately limited by the bandwidth of the post-mixing low-pass filters.

Several high-bandwidth amplitude demodulation techniques have been proposed for increasing the overall imaging bandwidth. The high-speed AFM results presented in [6] introduce the peak hold method which measures the amplitude once or twice every oscillation cycle. However, this method is prone to noise and disturbances from unwanted harmonics. Thus, it cannot be used in multifrequency AFM applications since frequency components outside the vicinity of the modulating signal are not rejected.

Recent developments include the low-latency coherent demodulator [1], the high-bandwidth lock-in amplifier [93], and the Kalman filter [94, 159]. The latter has also been extended for multifrequency AFM imaging [155, 156]. Although the Kalman filter is shown to be effective in terms of performance, the complexity of implementing a complete Kalman filter in a high-speed setting can be challenging. In fact, the computational complexity of the update law can ultimately become a limiting factor in terms of allowable bandwidth. Additionally, with simpler update laws the sampling speed can be increased, which will reduce the overall noise floor of the system [117]. Thus, a simpler estimator is sought with similar performance characteristics.

4.1.1 Contributions

In this chapter, a new method for amplitude and phase demodulation in AFM is presented. The method employs an adaptive law based on a strictly positive real Lyapunov design approach [84], or Lyapunov estimator, and demonstrates a good balance between performance and complexity. This estimator can be seen as a simplification of the Kalman filter in terms of the update laws and computational complexity, without sacrificing significant performance.

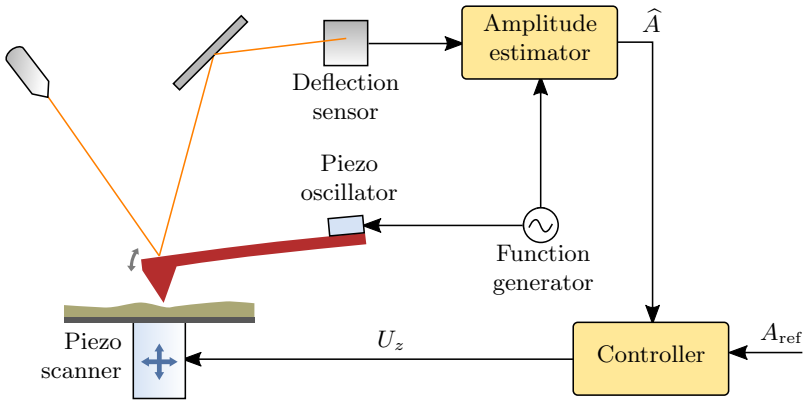

Figure 4.1: Amplitude modulated operating mode in AFM.

The Lyapunov estimator is described in detail, including convergence properties, implementation, and tuning details. Its relationship to the Kalman filter is outlined, demonstrating that the Kalman filter converges to the Lyapunov estimator for some special cases. The extension of the estimator to multifrequency applications is provided. The Lyapunov estimator is experimentally implemented and compared to a state-of-the-art lock-in amplifier, demonstrating an improved performance for high-speed demodulation. Furthermore, the Lyapunov estimator is used in a high-speed AFM imaging experiment, in addition to a multifrequency AFM imaging experiment for determination of higher harmonics phase components.

4.1.2 Outline

The remainder of the chapter proceeds as follows. In Section 4.2 the amplitude and phase estimation problem is formulated. Background material for the general Lyapunov estimator is provided in Section 4.3, and stability properties and convergence rates are established. In Section 4.4 the Lyapunov amplitude estimator is presented. Section 4.5 provides procedures for tuning the estimator. Experimental results are discussed in Section 4.6. Finally, conclusions are drawn in Section 4.7.

4.2 Problem Formulation

The problem can be formulated as estimating the amplitude $A(t)$ and phase $\varphi(t)$ using only past and present measurements of the signal

$$y(t) = A(t)\sin(\omega_0 t + \varphi(t)) + v(t), \tag{4.1}$$

where ω_0 is the known angular frequency and $v(t)$ represents a zero-mean noise process. Optionally, the signal is measured through a device or filtered through a transfer function $W(s)$ such that

$$w = W(s)y \tag{4.2}$$

where w is the input signal exposed to the estimator. Furthermore, $W(s)$ is strictly positive real (SPR) and can be used to describe a measuring device or alternatively, a signal processing filter for noise attenuation. The transfer function can be assumed unitary $W(s) = 1$ if not desired.

4.3 Estimator Background

In this section, the measurement signal is transformed to a model suitable for implementation of the Lyapunov estimator given in Chapter 2. Furthermore, for the given problem, it is shown that the estimator guarantees convergence of the parameter estimates in exponential time due to the persistently exciting (PE) property of the signal vector. Additionally, a conservative limit on the convergence speed of the method is found for the given signal vector. This allows easy tuning of the gain γ later.

4.3.1 Linear Parametric Model

The sinusoidal signal (4.1) can be written in terms of its in-phase and quadrature component by applying trigonometric identities such that

$$\begin{aligned} y &= A\sin(\omega_0 t + \varphi) && (4.3)\\ &= A\cos(\varphi)\sin(\omega_0 t) + A\sin(\varphi)\cos(\omega_0 t) && (4.4)\\ &= \boldsymbol{\phi}^T\boldsymbol{\theta}, && (4.5) \end{aligned}$$

where noise has been disregarded, and

$$\boldsymbol{\theta} = [\theta_1, \theta_2]^T = [A\cos(\varphi), A\sin(\varphi)]^T \tag{4.6}$$

$$\boldsymbol{\phi} = [\sin(\omega_0 t),\ \cos(\omega_0 t)]^T. \tag{4.7}$$

The system is now in a linear parametric form, which permits the direct application of estimation methods such as from Chapter 2. By comparing (4.4) and (4.5) the amplitude and phase can be recovered from

$$A = |\boldsymbol{\theta}|, \tag{4.8}$$

$$\varphi = \operatorname{atan2}(\theta_2, \theta_1), \tag{4.9}$$

where $\operatorname{atan2}(\cdot)$ is the four-quadrant tangent inverse function.

The linear parametric model (4.2),(4.5) is now in a form suitable for application of the Lyapunov estimator.

4.3.2 Persistency of Excitation

Although the Lyapunov estimator is guaranteed to be stable in some sense, an additional PE property of the signal vector $\boldsymbol{\phi}$ is required for convergence of the parameters. In the following, it is shown that $\boldsymbol{\phi}$ given in (4.7) is PE.

From Definition 2.3, the signal is PE if there exist constants $T_p, \alpha_0, \alpha_1 > 0$ such that

$$\alpha_1 \mathbf{I} \geq \mathbf{S} \triangleq \frac{1}{T_p} \int_t^{t+T_p} \boldsymbol{\phi}(\tau)\boldsymbol{\phi}^T(\tau) d\tau \geq \alpha_0 \mathbf{I} \quad \forall\, t \geq 0. \tag{4.10}$$

Evaluating $\mathbf{S}$ with $\boldsymbol{\phi}$ from (4.7) gives

$$\mathbf{S} = \frac{1}{4T_p\omega_0} \begin{bmatrix} 2\omega_0 T_p - \sin(2\omega_0(T_p+t)) + \sin(2\omega_0 t) & \\ -\cos(2\omega_0(T_p+t)) + \cos(2\omega_0 t) & \\ & -\cos(2\omega_0(T_p+t)) + \cos(2\omega_0 t) \\ & 2\omega_0 T_p + \sin(2\omega_0(T_p+t)) - \sin(2\omega_0 t) \end{bmatrix} \tag{4.11}$$

and choosing

$$T_p = \tfrac{1}{2} f_0^{-1} = \pi \omega_0^{-1} \tag{4.12}$$

results in

$$\mathbf{S} = \begin{bmatrix} \frac{1}{2} & 0 \\ 0 & \frac{1}{2} \end{bmatrix} = \tfrac{1}{2}\mathbf{I} \quad \forall\, t \geq 0 \tag{4.13}$$

with a level of excitation $\alpha_0 = \frac{1}{2}$. Thus, $\boldsymbol{\phi}$ from (4.7) is PE and guarantees exponential convergence of $\widehat{\boldsymbol{\theta}} \to \boldsymbol{\theta}$, as seen by applying Theorem 2.2.

4.3.3 Convergence Rate and Gain γ

Given the PE property of the signal vector $\boldsymbol{\phi}$, the parameter estimates are guaranteed to converge in exponential time. In fact, the rate of convergence can be found

in terms of the gain γ. An expression for γ can then be found which optimizes the rate of convergence as shown in the following.

For ease of analysis, assume here that $W(s) = 1$ which makes the update law (4.17)-(4.18) equivalent to the update law of the gradient estimator, given in Chapter 2, which can be considered a special case of the Lyapunov estimator. Then, the convergence of the parameter estimate error $\widetilde{\boldsymbol{\theta}}(t)$ is determined by [84]

$$\widetilde{\boldsymbol{\theta}}^T\widetilde{\boldsymbol{\theta}} \leq k^n\widetilde{\boldsymbol{\theta}}_0^T\widetilde{\boldsymbol{\theta}}_0, \quad \forall\, t \geq nT_p,\ n = 0, 1, \ldots \tag{4.14}$$

for $\widetilde{\boldsymbol{\theta}}_0 = \widetilde{\boldsymbol{\theta}}(0)$ and $0 < k < 1$ given by

$$k = 1 - \frac{2\alpha_0 T_p \gamma}{2 + \beta^4 T_p^2 \gamma^2} \tag{4.15}$$

where $\beta = \sup_t |\boldsymbol{\phi}(t)| = 1$ for $\boldsymbol{\phi}$ in (4.7). Thus, the convergence rate is given by k such that a smaller value gives faster convergence.

The gain γ minimizing k in (4.15) can now be found. Inserting for T_p from (4.12) and α_0 found from (4.13) results in

$$\arg\min_{\gamma} k = 2\sqrt{2} f_0. \tag{4.16}$$

This expression for γ reveals that the optimal gain is inherently tied to the carrier frequency f_0. The given value for γ in (4.16), serves as a suitable initial choice. However, since the convergence rate in (4.14) represents a conservative limit due to the inherent conservative nature of Lyapunov analysis, a faster solution may be found through simulations.

4.4 Lyapunov Amplitude and Phase Estimator

4.4.1 Update Law

The Lyapunov estimator allows the estimated parameters $\widehat{\boldsymbol{\theta}}$ to be found from the input signal w and the known signal vector $\boldsymbol{\phi}$. Since the signal vector is bounded, no normalization of the error is necessary. Then, by applying the estimator from Chapter 2 to the system (4.5)-(4.7), the update law can be written as

$$\dot{\widehat{\boldsymbol{\theta}}} = \gamma\boldsymbol{\phi}\left(w - \widehat{w}\right), \tag{4.17}$$

$$\widehat{w} = W(s)\boldsymbol{\phi}^T\widehat{\boldsymbol{\theta}} \tag{4.18}$$

where γ is a constant gain parameter. Finally, the estimated amplitude $\widehat{A}$ and phase $\widehat{\varphi}$ can be found by applying the parameter estimate $\widehat{\boldsymbol{\theta}}$ into (4.8)-(4.9).

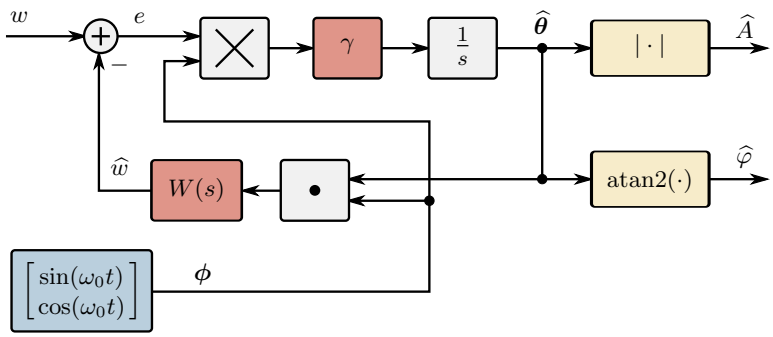

Figure 4.2: Block diagram of the estimator. The blocks '$\cdot$' and '$\times$' represent vector dot product and matrix multiplication respectively.

Since $\widehat{\boldsymbol{\theta}}$ converges in exponential time, it is clear that $(\widehat{A}, \widehat{\varphi}) \to (A, \varphi)$ in exponential time considering (4.8)-(4.9). Some implementations of atan2 may not be defined for $\widehat{\boldsymbol{\theta}} = 0$. However, because of the exponential convergence properties, the estimator cannot stay identically in $\widehat{\boldsymbol{\theta}} = 0$ unless $y \equiv 0$. Thus, the issue is resolved in finite time for a well-posed problem. A block-diagram of the update law is shown in Fig. 4.2.

4.4.2 Relationship to the Kalman filter

Under certain conditions the Kalman filter for amplitude estimation [159] is equivalent to the Lyapunov estimator, as will be demonstrated in the following. First, it is shown that the two methods are equivalent when the covariance matrix of the Kalman filter, $\mathbf{P}$, is constant. Then, certain conditions under which the covariance matrix approaches constant is given, thus showing equivalence.

With a system matrix $\mathbf{A} = 0$ and no input signal, $\mathbf{B} = 0$, the continuous-time Kalman filter can be written as

$$\dot{\widehat{\boldsymbol{\theta}}} = \mathbf{P}\boldsymbol{\phi}\mathbf{R}^{-1}(w - \boldsymbol{\phi}^T\widehat{\boldsymbol{\theta}}), \tag{4.19}$$

$$\dot{\mathbf{P}} = \mathbf{Q} - \mathbf{P}\boldsymbol{\phi}\mathbf{R}^{-1}\boldsymbol{\phi}^T\mathbf{P} \tag{4.20}$$

where the process covariance $\mathbf{Q}$ and measurement covariance $\mathbf{R}$ are assumed to be on the form $\mathbf{Q} = q\mathbf{I}, \mathbf{R} = r\mathbf{I}$ for some positive constants q, r.

Note that for $\dot{\mathbf{P}} = 0, \mathbf{P} = p\mathbf{I}$, the Kalman filter (4.19) is equivalent to the Lyapunov estimator (4.17)–(4.18) with $W(s) = 1$ and $\gamma = pr^{-1}$. Thus, in cases where $\mathbf{P}$ is constant, the Kalman filter can be reduced to the Lyapunov estimator with mathematical equivalency. In the following, solutions to the Kalman equations with constant $\mathbf{P}$ are found and investigated.

Consider a particular solution to (4.20) of the form

$$\mathbf{P} = \begin{bmatrix} A\sin(2\omega_0 t + \varphi) + C & A\cos(2\omega_0 t + \varphi) \\ A\cos(2\omega_0 t + \varphi) & -A\sin(2\omega_0 t + \varphi) + C \end{bmatrix} \tag{4.21}$$

for some constants A, C, φ. The real, positive solution to these constants in terms of ω_0, r, q are given by

$$A = \frac{q}{2\omega_0}, \tag{4.22}$$

$$C = \frac{\sqrt{q}\sqrt{q + 4\omega_0\sqrt{r^2\omega_0^2 + qr} + 4r\omega_0^2}}{2\omega_0}, \tag{4.23}$$

$$\varphi = 2\text{atan}\left(\sqrt{\frac{q - 4\omega_0\sqrt{r^2\omega_0^2 + qr} + 4r\omega_0^2}{q - 8r\omega_0^2}}\right). \tag{4.24}$$

In some cases the covariance matrix $\mathbf{P}$ approaches a constant, consider

$$\lim_{\omega_0 \to \infty} A/C = 0. \tag{4.25}$$

Thus, with increasing oscillation frequency the amplitude A in the covariance matrix is dominated by the constant offset term C and can be approximated by $\mathbf{P} = C\mathbf{I}$. In this case the Kalman filter can be simplified to the Lyapunov estimator with $W(s) = 1$ and

$$\gamma = C/r. \tag{4.26}$$

In fact, this equation can be used to tune the Lyapunov estimator if the measurement and process noise covariances are known. Additionally,

$$\lim_{q \to 0} A/C = 0, \tag{4.27}$$

$$\lim_{r \to \infty} A/C = 0. \tag{4.28}$$

Thus, the Kalman filter behaves identically to the Lyapunov estimator in the cases where

- the oscillation frequency ω_0 is large
- the process noise covariance q is small
- the measurement noise covariance r is large

In these cases, by replacing the Kalman filter with the Lyapunov estimator, the estimator can be run at higher update speeds possibly allowing for a higher bandwidth and improved noise response, due to the simpler implementation of the latter.

4.4.3 Multifrequency Lyapunov Estimator

Multifrequency AFM (MF-AFM) is a rapidly developing area of research. Here, it is shown how the Lyapunov estimator can be extended to multifrequency demodulation, for use in MF-AFM applications.

Consider a signal consisting of a sum of sinusoids,

$$y_m(t) = \sum_{i=1}^{n} A_i \sin(\omega_i t + \varphi_i) \tag{4.29}$$

where $i \in \{1, 2, \ldots, n\}$ denotes the ith modeled frequency. Then, through the same procedure as in Section 4.3, the signal (4.29) can be rewritten as the linear parametric model

$$y_m = \boldsymbol{\phi}_m^T \boldsymbol{\theta}_m \tag{4.30}$$

$$\boldsymbol{\theta}_m = [A_1 \cos(\varphi_1),\ A_1 \sin(\varphi_1),\ \ldots,\ A_n \cos(\varphi_n),\ A_n \sin(\varphi_n)]^T \tag{4.31}$$

$$\boldsymbol{\phi}_m = [\sin(\omega_1 t),\ \cos(\omega_1 t),\ \ldots,\ \sin(\omega_n t),\ \cos(\omega_n t)]^T . \tag{4.32}$$

By employing the Lyapunov estimator, the amplitudes A_i and phases φ_i can be estimated, strictly by the measurement of y_m. The estimator update law for this multifrequency model, for simplicity assuming $W(s) = 1$, is given by

$$\dot{\widehat{\boldsymbol{\theta}}}_m = \boldsymbol{\Gamma}_m \boldsymbol{\phi}_m \left(y_m - \widehat{y}_m\right) \tag{4.33}$$

$$\widehat{y}_m = \boldsymbol{\phi}_m^T \widehat{\boldsymbol{\theta}}_m \tag{4.34}$$

where $\widehat{\boldsymbol{\theta}}_m$ is the estimated parameter vector analogous to $\boldsymbol{\theta}_m$ in (4.31), and

$$\boldsymbol{\Gamma}_m = \operatorname{diag}(\gamma_1, \gamma_1, \ldots, \gamma_n, \gamma_n) \tag{4.35}$$

where γ_i determines the estimation tracking bandwidth for the ith sinusoid component.

The estimates of the amplitude and phase for each frequency component can then be retrieved from

$$\widehat{A}_i = \sqrt{\widehat{\theta}_{m,2i-1}^2 + \widehat{\theta}_{m,2i}^2} \tag{4.36}$$

$$\widehat{\varphi}_i = \operatorname{atan2}(\widehat{\theta}_{m,2i}, \widehat{\theta}_{m,2i-1}) \tag{4.37}$$

where $\widehat{\theta}_{m,j}$ is the jth element into the vector $\widehat{\boldsymbol{\theta}}_m$.

Remark 4.1. Even though additional parameters are estimated in the multifrequency Lyapunov estimator, it can be shown that $\boldsymbol{\phi}_m$ is PE as long as the frequency components are distinct. Thus, the multifrequency estimator retains the exponential convergence properties of the single frequency Lyapunov estimator.

4.5 Tuning and Simulations

4.5.1 Simulation Results

Simulations for both amplitude and phase demodulation are plotted in Fig. 4.3 for different values of γ, measurement noise, and low-pass filter $W(s)$, implemented at a sampling rate of 4 MHz. In general, it can be seen that for higher values of γ the estimator converges faster but at some point it starts to overshoot. When noise is added in Fig. 4.3(b) it can be seen that high values of γ are more prone to noise. However, by applying a low-pass filter for $W(s)$ on the measured signal $y(t)$, some of the high-frequency noise is attenuated even at high γ values. The performance of the phase demodulation closely follows that of the amplitude demodulation, which is expected as they are both immediate calculations from the same estimated in-phase and quadrature components ($\widehat{\boldsymbol{\theta}}$). Thus, the dynamics of the two demodulation modes should be equivalent.

4.5.2 Choosing the Transfer Function $W(s)$

The strictly positive real transfer function $W(s)$ can either represent any device or system between the sinusoidal signal $y(t)$ as in (4.1) and the estimator, and/or be designed as a post-measurement filter for reducing high-frequency noise. Otherwise, it can be assumed that the measurement $w(t)$ closely resembles that of the signal $y(t)$ by setting $W(s) = 1$. If instead, a low-pass filter is used, the bandwidth should be set high enough such that the oscillation frequency of the sinusoid in $y(t)$ is not attenuated.

4.5.3 Choosing the Gain γ

With an initial estimate of γ given by (4.16), further adjustments can be made by investigating the transient effect in the step response simulations in Fig. 4.3. It can be seen that for the highest value of the gain, $\gamma = 24f_0$ the transient overshoots considerably, while at $\gamma = 9f_0$ (red) it is seemingly close to critically damped. For lower values of γ the convergence rate is noticeably slower. The simulations thus suggest a value of

$$\gamma = 9f_0 \tag{4.38}$$

which, as expected, is slightly higher than the initial conservative estimate from (4.16).

Note that this evaluation is based on finding a gain primarily for achieving the highest possible estimation bandwidth. In some cases this may result in a noisy

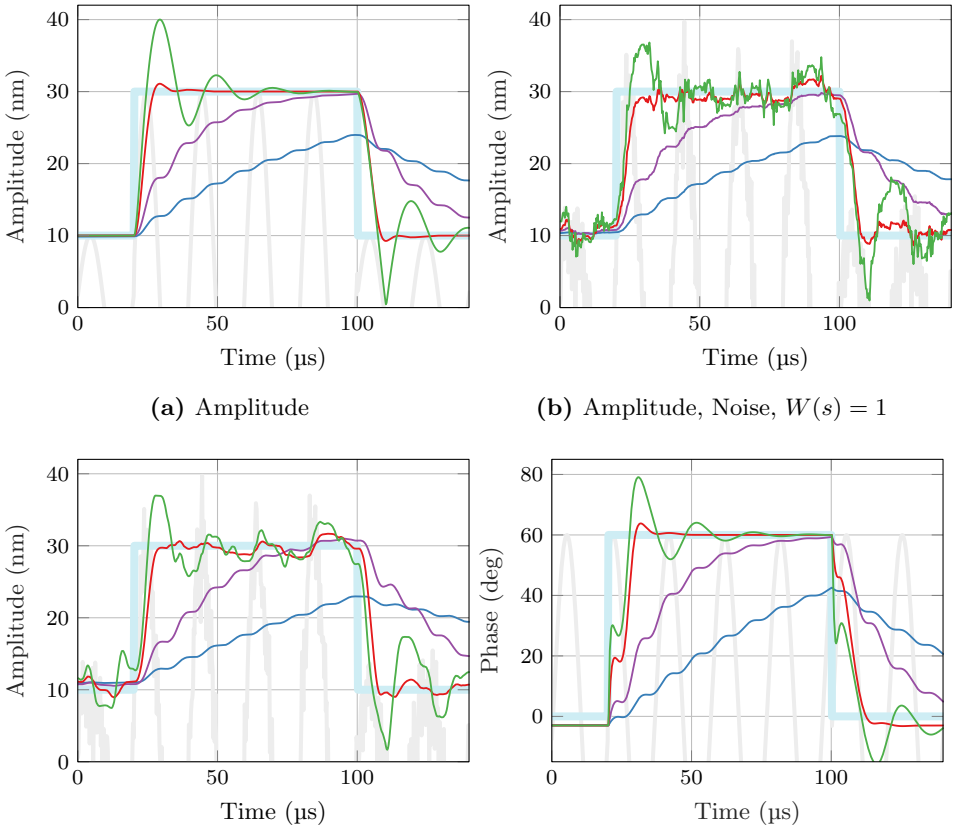

(a) Amplitude

(b) Amplitude, Noise, $W(s) = 1$

(c) Amplitude, Noise, $W(s) = W_{\mathrm{LP}}(s)$

(d) Phase

Figure 4.3: Step response simulation of the Lyapunov estimator for amplitude demodulation (a)-(c) and phase demodulation (d), with carrier frequency $f_0 = 50\,\mathrm{kHz}$. Measurement noise with RMS $= 4\,\mathrm{nm}$ added to (b)-(c) demonstrating difference in $W(s)$ filters, where $W_{\mathrm{LP}}(s) = 1/(0.8\omega_0^{-1}s + 1)$. Real amplitude/phase ( ), input signal ( ), demodulated amplitude $\widehat{A}$ or phase $\widehat{\varphi}$ with $\gamma = 0.6f_0$ (—), $\gamma = 2f_0$ (—), $\gamma = 9f_0$ (—), $\gamma = 24f_0$ (—).

amplitude estimate. As demonstrated in the simulation results, by reducing the value of γ the estimator essentially acts as a low-pass filter on the noise, improving the noise rejection.

4.5.4 DC-Offset

In dynamic mode AFM there is typically a DC-offset in the measured cantilever deflection. A constant offset in the input signal w can affect the output response of the estimator, as demonstrated in Fig. 4.4. In general, this problem is most prominent at higher demodulator bandwidths. One solution for handling this is to use AC-coupling on the experimental measurement equipment, or equivalently adding a high-pass filter at the measured input signal. Another solution is to augment the Lyapunov estimator to simultaneously estimate the offset. This can be performed by adding a third state in $\widehat{\boldsymbol{\theta}}$ representing estimated offset, and adding a third constant element to $\boldsymbol{\phi}$ – typically 1. Finally, γ is modified to accept a different gain for the offset than for the amplitude/phase estimates, replacing it with the diagonal matrix

$$\boldsymbol{\Gamma} = \mathrm{diag}(\gamma, \gamma, \gamma_{DC}) \tag{4.39}$$

where γ_{DC} is the DC-offset update gain, and (4.17) now assumes matrix multiplication. Since the offset is by definition slowly-varying, the DC-gain can be set relatively low to avoid affecting the performance of the demodulated signals. This implementation is demonstrated in Fig. 4.4 (purple line). It is seen that the oscillations in tracking response introduced with the DC-step is reduced once the DC-estimate converges. Conversely, the amplitude estimate of the original Lyapunov estimator continues with standing oscillations after the DC-offset is introduced.

4.6 Experimental Results

4.6.1 Implementation Details

The Lyapunov estimator was implemented on a National Instruments USB-7855R with Kintex-7 70T FPGA using dedicated DSP blocks, achieving a sample frequency of 300 kHz. The performance of the implemented Lyapunov estimator was experimentally assessed and compared with a state-of-the-art lock-in amplifier (LIA, Zürich Instruments HF2LI) which provides flexible post-mixing low-pass filter (LPF) settings.

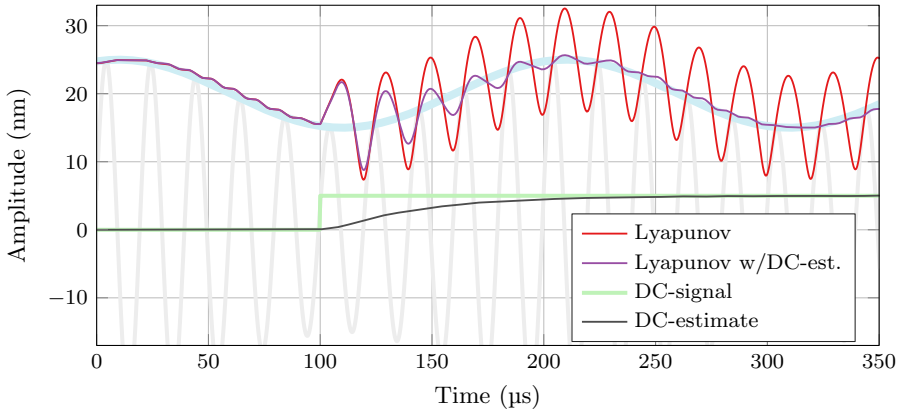

Figure 4.4: Lyapunov estimator simulated with a step in DC-offset at the input signal, with carrier frequency $f_0 = 50\,\text{kHz}$, gain $\gamma = 9f_0$, and DC-gain $\gamma_{DC} = 20\,\text{k}$ for the augmented Lyapunov estimator with DC-estimation.

4.6.2 Amplitude Tracking Bandwidth

To determine the amplitude tracking bandwidth, a laboratory function generator (Agilent 33521A) is employed, providing a carrier frequency of 50 kHz amplitude modulated by a swept sine signal. This FM-AM concept directly reveals the LPF characteristic of the Lyapunov estimator and of the post-mixing filters of the LIA and allows for a direct extraction of the −3 dB tracking bandwidth.

The tracking bandwidth frequency responses of a slow LIA with LPF cut-off frequency $f_c = 500\,\text{Hz}$, fast LIA with $f_c = 50\,\text{kHz}$, slow Lyapunov estimator with $\gamma = 20\,\text{k}$ and fast Lyapunov estimator with $\gamma = 700\,\text{k}$ are shown in Fig. 4.5(a). The slow settings achieve a −3 dB bandwidth of around 500 Hz for both the LIA and Lyapunov estimator, while the fast settings achieve a −3 dB bandwidth of 48.2 kHz and 50.0 kHz for the LIA and Lyapunov estimator, respectively.

Note, that the fast LIA shows significant spikes at $2f_0$ and $4f_0$ due to insufficient filtering of the mixing products. To further highlight this point, time-domain tracking experiments of a square-modulated sine wave are shown in Fig. 4.5(b). Using the fast bandwidth setting for both demodulators, the LIA amplitude estimate is dominated by $2f_0$ oscillations, making this demodulator impractical at these tracking bandwidths.

The results emphasize the fact that the Lyapunov estimator is superior to the LIA when carrier frequencies are small compared to the necessary tracking bandwidth. While the tracking bandwidth of the LIA can be increased by choosing a large LPF cut-off frequency, the amplitude estimate becomes increasingly distorted by

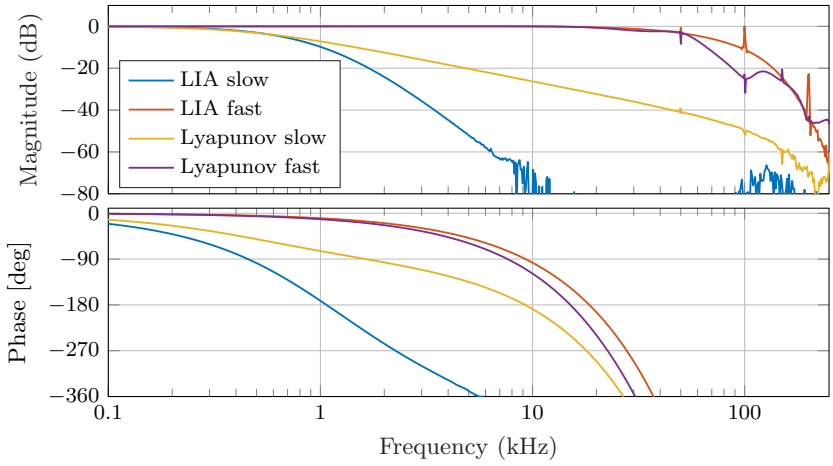

(a) Frequency response

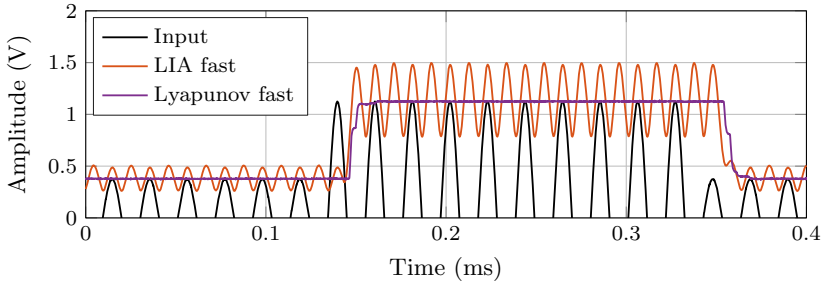

(b) Time-domain tracking

Figure 4.5: Amplitude tracking experiment using the lock-in-amplifier and Lyapunov estimator with a carrier frequency of 50 kHz. (a) Frequency response at different bandwidth settings. (b) Time-domain tracking of a square-modulated sine wave.

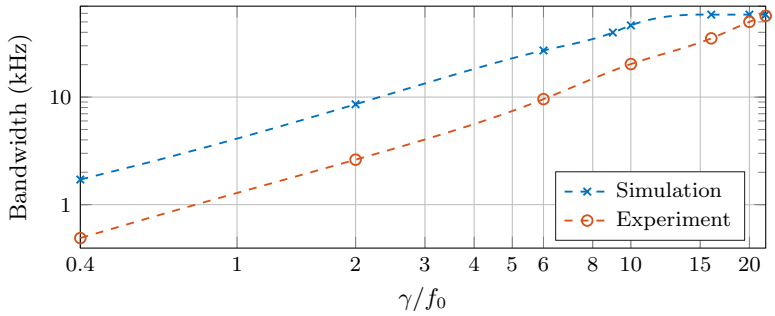

Figure 4.6: Tracking response of Lyapunov estimator for increasing gain γ.

the mixing products.

The $-3\,\mathrm{dB}$ tracking bandwidth of the Lyapunov estimator is plotted against the gain γ in Fig. 4.6, and compared to simulated values. The bandwidth increases approximately linearly with increasing γ until the bandwidth approaches the cantilever oscillation frequency f_0. There is a constant gain discrepancy between simulations and experiments, this can possibly be attributed to internal gains in the experimental setup not accounted for.

4.6.3 Noise Analysis

In this experiment, the RMS noise of the amplitude estimate of the Lyapunov estimator and LIA is evaluated as a function of tracking bandwidth. For this purpose, the four channel acquisition front-end of a micro system analyzer (Polytec MSA-050-3D) is used to capture time-domain data passed through a high order anti-aliasing LPF with cut-off frequency of 1.2 MHz and sampled at $f_s = 2.56\,\mathrm{MHz}$ for $T = 13.11\,\mathrm{s}$. We use the total integrated noise (TIN) (see Appendix A) as the performance metric which is obtained by integrating the noise density estimate from DC to $f_s/2$ using Welch's method [137] without averaging nor overlap.

The total integrated noise of the amplitude estimate obtained from the Lyapunov estimator is compared with the demodulated amplitude of the LIA as a function of the tracking bandwidth in Fig. 4.7. The RMS noise of the Lyapunov estimator estimate only increases slightly from 1.21 mV for the smallest bandwidth of 500 Hz to 5.6 mV for the largest bandwidth of 50 kHz. In contrast, the RMS noise of the demodulated amplitude using a LIA, increases exponentially when the LPF cut-off frequency is increased above approximately 10 kHz. While the LIA is better at very low bandwidths, above 7 kHz the Lyapunov estimator shows significantly lower noise. In other words, for the same TIN of 5.6 mV, the LIA only achieves a 10 kHz bandwidth compared to almost 50 kHz achieved by the Lyapunov estimator. Thus, during high-speed experiments, the Lyapunov estimator could either track at the same bandwidth for a lower total integrated noise compared to the LIA – or at higher bandwidths for the same total integrated noise.

The improved LIA noise response at low bandwidths can be attributed to its higher order low-pass filtering. In fact, the Lyapunov estimator can be seen to act as a first-order LPF in the 1–10 kHz range based on its 20 dB/decade roll-off in Fig. 4.5(a), while the commercial LIA employs a fourth order Butterworth filter. As shown in Appendix A, the TIN of the LIA is expected to be ~ 0.56 times the TIN of the Lyapunov estimator purely due to the different filter orders, while the experimental TIN ratio was measured to be 0.73. This may suggest that the Lyapunov estimator would outperform the LIA at the same filter order. However,

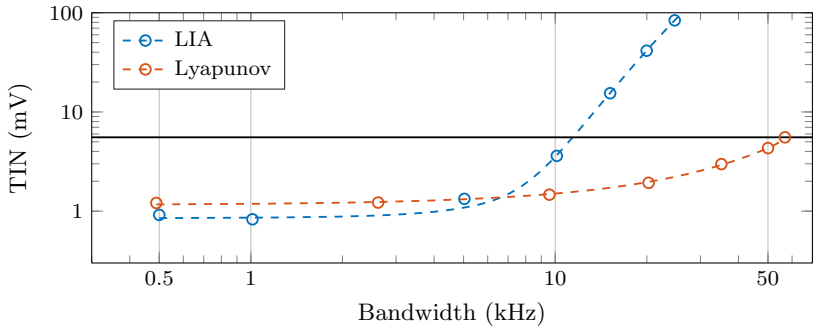

Figure 4.7: Measured total integrated noise of amplitude estimate from LIA and Lyapunov estimator, with curve fit, as a function of tracking bandwidth.

other sources for the difference should be considered, including noise not being completely white, or measurement noise at higher frequencies not being filtered out. Additionally, the LIA has a fixed sampling rate about 3 orders of magnitude faster than the Lyapunov estimator, and the two estimators use different signal input ranges. This will in total result in some differences partly attributable to the experimental setup.

4.6.4 High-Speed AFM Imaging

Finally, the Lyapunov estimator and LIA is used in a high-speed constant-height tapping-mode AFM experiment for demonstrating the effect of increased demodulator bandwidth. The common z-axis actuator bandwidth limitation is circumvented by reducing the z-axis controller bandwidth to the point where the sample features during scanning entirely appear in the amplitude error image, thus reducing the bandwidth-limiting components of the AFM z-axis feedback loop to the cantilever and demodulator exclusively.

The cantilever bandwidth is limited by its resonance frequency f_0 and quality (Q) factor by $f_0/(2Q)$ [7]. In order to render the demodulator the bottleneck of the open-loop AFM chain, a fast cantilever is necessary. Due to the sample frequency limitation of the Labview FPGA, we employ a cantilever with fundamental resonance frequency of $f_0 \approx 50\,\mathrm{kHz}$. The piezoelectric integrated actuation of the cantilever allows for model-based Q factor control to reduce the Q factor to $Q_0 = 8$ [160], resulting in an experimentally verified tracking bandwidth of 3.3 kHz (not shown) which adequately matches the first order approximation $f_0/(2Q_0)$.

AFM images of a calibration grating (NT-MDT TGZ3) with periodic features of heights $h = 520 \pm 3\,\mathrm{nm}$ were obtained on an NT-MDT NTEGRA AFM. The

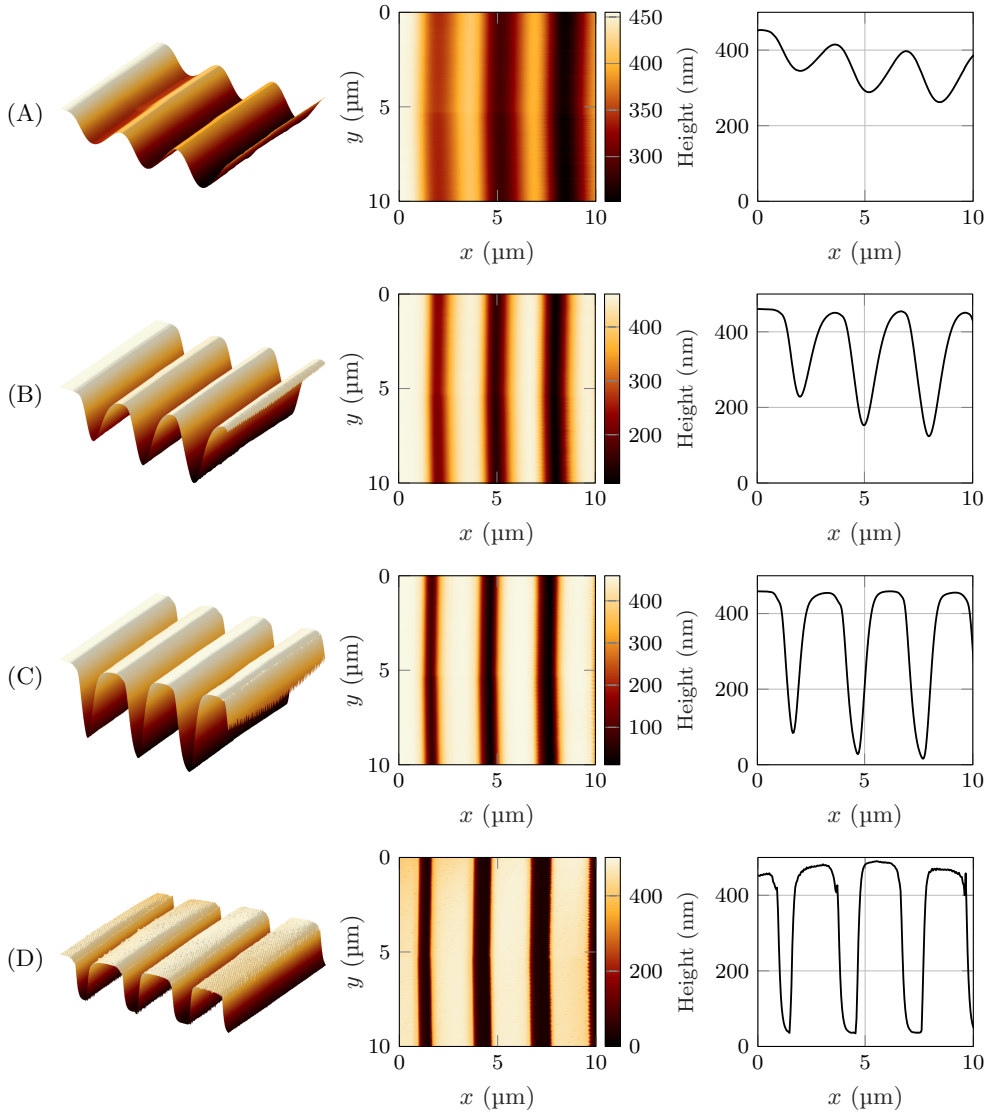

(a) 3D Image **(b)** 2D Image **(c)** Cross-section

Figure 4.8: AFM scanning results over a $10 \times 10\,\mu m^2$ area of the sample. (A) LIA with $f_c = 100\,Hz$, (B) LIA with $f_c = 200\,Hz$, (C) LIA with $f_c = 400\,Hz$ and (D) Lyapunov estimator with $\gamma = 60 \times 10^3$, providing a tracking bandwidth of $\sim$1.6 kHz.

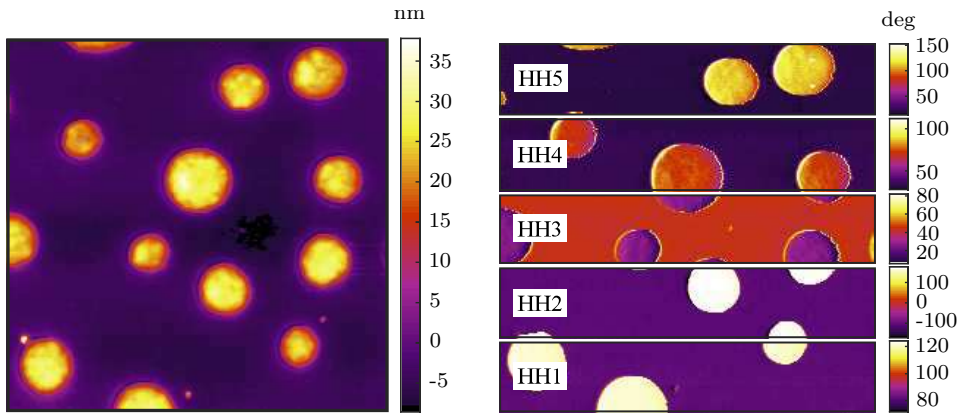

(a) Topography **(b)** Higher harmonics phase

Figure 4.9: Multifrequency Lyapunov estimator implemented for phase demodulation used in an AFM imaging experiment. The phase is demodulated at the first five harmonic frequencies of the cantilever.

sample was scanned at a speed of 627.45 µm/s in a $10 \times 10\,\mu m^2$ area at a scanner rate of 31.37 Hz and resolution of 256×256 pixels, while recording the amplitude estimates of the LIA and the Lyapunov estimator in parallel. As only the forward trajectory is recorded, the entire image is acquired in 8.16 seconds.

The γ of the Lyapunov estimator could have been set according to (4.38) for the highest demodulator bandwidth. However, this initial value allows the Lyapunov estimator to track the amplitude at a much higher bandwidth than that of the cantilever tracking bandwidth. Instead, γ was reduced in order to improve the overall noise response of the system. The resulting gain was set to $\gamma = 1.2 f_0$ which results in a -3 dB bandwidth at approximately 1.6 kHz.

The high-speed constant height imaging results are presented in Fig. 4.8. Every experiment is performed at the same imaging speed, and each row represents increasing demodulator bandwidths. By setting a larger demodulator bandwidth, the sharp sample features are more accurately tracked as demonstrated by the consecutive rows, with the highest bandwidth here performed by the Lyapunov estimator in the last row.

4.6.5 Multifrequency Phase Imaging

In order to demonstrate the multifrequency Lyapunov estimator, AFM phase images were obtained from the first five harmonics of the cantilever simultaneously. The experiment was implemented on an NT-MDT NTEGRA AFM, using

a Bruker DMASP cantilever with resonance frequency 46.1 kHz. A two-component polymer sample (PS-LDPE-12M) was used, due to its highly contrasting material properties between the two polymers. The multifrequency Lyapunov estimator (4.29)–(4.35) was implemented for demodulation at five frequencies, on a high-speed FPGA (Xilinx Kintex-7 KC705) achieving a sampling rate of 3.5 MHz.

The result of the higher harmonics phase imaging is shown in Fig. 4.9. Both the topography, and phase of the first five harmonics of the cantilever, are shown. The contrasting elements of the sample are clearly visible. A detailed analysis of the performance characteristics of the multifrequency Lyapunov estimator is given in [75].

4.7 Conclusions

In this chapter, an amplitude and phase estimator designed for use in high-speed dynamic mode atomic force microscopy has been introduced. The Lyapunov estimator is designed for high-bandwidth, yet low complexity for ease of implementation, and is suitable for multifrequency applications. It requires no tuning by using the suggested gain for high-bandwidth performance in (4.38). However, the noise response can be improved by reducing the gain, such as by matching the resulting demodulator bandwidth to the bandwidth of the cantilever or z-axis actuator. It has also been demonstrated that the Kalman filter reduces to the Lyapunov estimator under certain conditions. Experimental results, including AFM imaging with the estimator used for amplitude demodulation, demonstrate the high-bandwidth performance of the method.

Chapter 5

Comparison of Demodulation Techniques in AFM

Amplitude estimation, or demodulation, plays a vital part in the control loop of dynamic mode high-speed atomic force microscopy (AFM). The closed-loop bandwidth is limited by the convergence rate of the estimator. Recent developments have introduced new approaches for demodulation of the measured deflection signal. This chapter reviews and compares state-of-the-art techniques for AFM amplitude demodulation. The performance of the techniques is discussed in terms of bandwidth, convergence time, rejection of other frequency components, bias, noise attenuation, and implementation complexity. Based on the results, recommendations for the most appropriate technique are given for various criteria.

Publications The material in this chapter is based on [143]. However, all numerical results are new, with additional performance metrics based on [148, 157, 158]. The new simulations provide additional insights into the performance of each method, and the recommendations provided for various desired properties have been updated to reflect the new results. Additionally, another method is implemented for comparison (mean absolute deviation). Experimental results based on the original work have been presented in [157, 158].

5.1 Introduction

Increasing the imaging rate has been an enduring ambition in the AFM community [7]. Several strategies have been proposed for increasing the imaging rate, ranging from improvements to mechanical design [98], virtually controlling the stiffness of the cantilever with active Q-control [45, 193], to improving the feedback controller

[100].

Amplitude modulated AFM (AM-AFM) is well suited for imaging biological samples since the interaction forces generated can be very small, preventing damage to the sample [5]. However, AM-AFM has generally been slower than traditional contact mode. By increasing the bandwidth of the amplitude estimator, it is possible to increase the bandwidth of the entire closed-loop system and ultimately allow for faster imaging speeds. Additionally, by improving the estimator's noise response and attenuation of unwanted frequency components, the resulting image can be improved.

Traditionally, amplitude estimation has been performed by mean absolute deviation or lock-in amplifier techniques, requiring up to ten carrier wave periods to converge. The high-speed AFM results presented in [6] introduce the much faster peak hold method which converges in half an oscillation cycle. However, this method is prone to noise and disturbances from unwanted harmonics. Recent developments include the high-bandwidth lock-in amplifier [93], Kalman filter [94, 159], and coherent demodulator [1]. Additionally, the Lyapunov estimator from Chapter 4 is also included for comparison.

5.1.1 Contributions

In this chapter, common online demodulators for amplitude estimation in dynamic mode AFM, as well as recent state state-of-the-art developments, are numerically implemented and compared. Using these results and a properly defined set of performance indicators, recommendations are provided on the most suitable method for various application scenarios.

Recommendations are given for the following scenarios: low implementation complexity, low noise and high accuracy, and high imaging speed. In order to make proper recommendations, the various demodulators are compared in several aspects. Due to the inherent nonlinearity of demodulation, a step response plot gives a qualitative insight into the behavior of each method. The methods are compared in the frequency domain, and their bandwidths are measured. The rejection of frequency components away from the carrier frequency is essential for multifrequency AFM, and the methods are also compared in this aspect. Then, for accuracy, the bias of each method is given as a function of bandwidth. Finally, the methods are compared in terms of their total integrated noise against their bandwidth, which indicates their true practical bandwidth for implementation in high-speed AFM.

5.1.2 Outline

The chapter is organized as follows. In Section 5.2 the amplitude estimation problem is presented and performance indicators for comparing such estimators are suggested. Section 5.3 introduces the various estimation techniques that have been implemented for comparison. In Section 5.4 simulation results are presented. Considering these results, the proper choice of a method for various scenarios is discussed in Section 5.5, before concluding in Section 5.6.

5.2 Problem Formulation

The goal is to track the amplitude modulation signal $A(t)$, considering the measured time-varying signal

$$y(t) = A(t)\sin(\omega_0 t + \varphi) + v(t), \tag{5.1}$$

where ω_0 is a known angular carrier frequency, φ is an unknown phase contribution, and $v(t)$ is a noise process representing measurement noise. Additionally, it will be used that $f_0 = \omega_0/(2\pi)$ is the carrier frequency, and $T_0 = f_0^{-1}$ is the period of the carrier wave.

The performance of the various amplitude estimation techniques are evaluated in terms of the following performance indicators:

Bandwidth In dynamic mode high-speed AFM applications, every part of the closed-loop cycle must maintain a large bandwidth, including the amplitude estimator. The amplitude tracking bandwidth can be determined from the magnitude response plotted against the frequency of the modulation signal.

Convergence time The various estimation schemes are very different in their behavior, and due to the nonlinearity of the problem, the magnitude plot needs to be supplemented with a description of qualitative behavior. Some methods converge in finite time, others in exponential time. This will be discussed in addition to a helpful step response plot.

Bias and noise rejection Measurement noise is a limiting factor in the resolution of the deflection measurement, and is dominated by thermal noise [22]. Accurate measurements of amplitude require a low bias and low noise. There is typically a trade-off between these metrics and tracking bandwidth, as such, measurements of bias and total integrated noise are provided as a function of bandwidth.

Rejection of other frequency components Due to the nonlinear nature of the interaction force between the cantilever and sample while imaging, fre-

quencies other than the carrier frequency will also be excited. This interaction can excite higher harmonics or higher modes of the cantilever dynamics, and ultimately affect the resulting amplitude estimate. Furthermore, in multifrequency and multi-harmonic AFM, the demodulator must be able to demodulate each harmonic frequency component separately. Thus, the off-mode frequency components of the signal must be rejected.

Complexity Since speed is emphasized in AFM, the complexity must be kept low enough for the method to be implementable. Some methods can be implemented in simple analog circuits while others require digital implementations with computationally demanding arithmetics. In general, by using a simpler method the sample rate can be increased, which will reduce the overall noise floor of the system [117].

In the rest of this chapter, various estimation techniques are implemented for comparison of these performance metrics. The performance indicators are quantified, such that we can make recommendations for different scenarios.

5.3 Amplitude Estimation Techniques

In this section traditional and recent methods for amplitude estimation will be briefly introduced, with emphasis on those used in the AFM field. The purpose here is to introduce their mode of operation, with a brief overview of their implementation. All methods are implementable online, preferably with short convergence time. Traditional offline amplitude estimation methods such as least squares [192] are not suitable for feedback control and are not discussed here. Note that the naming convention for the various methods is not always consistent across the literature.

Notation

For the sake of clarity, in this chapter, methods are described in either a continuous or discrete form depending on their most suitable method of implementation. Discrete signals are written as u_k, defined by

$$u_k \triangleq u(kT_s) = u(t), \quad \text{for } kT_s \leq t < (k+1)T_s \tag{5.2}$$

where T_s is the sampling time. Discrete filters are denoted using the z-transform transfer function $H(z)$ while continuous filters are described by a transfer function $H(s)$ where s is the Laplace-variable. Furthermore, the amplitude estimate is given by $\widehat{A}(t)$.

Quadrature Based Methods

Before presenting the various methods, a concept shared among several techniques will be introduced here. These amplitude estimation methods are based on the multiplication of an in-phase and a quadrature sinusoidal signal

$$y(t) = A(t)\sin(\omega_0 t + \varphi) + v(t) \tag{5.3}$$
$$I(t) = y(t)\sin(\omega_0 t) \tag{5.4}$$
$$Q(t) = y(t)\cos(\omega_0 t). \tag{5.5}$$

By disregarding the noise term for now by setting $v = 0$, the following relations can be found using trigonometric identities

$$I(t) = \tfrac{A}{2}\left[\cos\varphi - \cos(2\omega_0 t + \varphi)\right] \tag{5.6}$$
$$Q(t) = \tfrac{A}{2}\left[\sin\varphi + \sin(2\omega_0 t + \varphi)\right]. \tag{5.7}$$

By attenuating or removing the $2\omega_0$ contribution in (5.6)-(5.7), the amplitude can be recovered from

$$i(t) = \tfrac{A}{2}\cos\varphi \tag{5.8}$$
$$q(t) = \tfrac{A}{2}\sin\varphi \tag{5.9}$$
$$\widehat{A}(t) = 2\sqrt{i(t)^2 + q(t)^2} = A(t). \tag{5.10}$$

5.3.1 Mean Absolute Deviation

Mean absolute deviation is possibly the simplest method to implement, and has been used for amplitude demodulation in the AFM literature [7]. It can be constructed using a rectifier circuit, low-pass filter, and scaling factor, such that

$$\widehat{A}_k = \frac{\pi}{2} H_{lp}(z)\left|y_k\right|, \tag{5.11}$$

where $H_{lp}(z)$ is a low-pass filter with unit gain. The chosen bandwidth of the low-pass filter determines the trade-off between bandwidth and noise attenuation. In our implementation, a 4th-order Butterworth filter is employed.

5.3.2 Peak Detector

A variation to the mean absolute deviation method is the peak detector. It uses a rectifier circuit in combination with a leaking low-pass filter in feedback loop. This approach is characterized by a slowly reducing estimate, and then quickly rising as

the measured signal becomes larger than the current estimate. Thus, increasing amplitudes are captured faster than decreasing amplitudes. The method can be written as

$$x_k = \max\left(|y_k|\,,\, \widehat{A}_{k-1}\right) \tag{5.12}$$

$$\widehat{A}_k = H_{lp}(z)x_k, \tag{5.13}$$

where $H_{lp}(z)$ is a low-pass filter with gain $0 \ll K < 1$.

5.3.3 RMS-to-DC

The amplitude of a sinusoidal signal is related to its root mean square (RMS) y_{rms} by the relation $A = \sqrt{2}y_{\text{rms}}$, assuming that the RMS is taken over any integer number of half-periods of the signal. By utilizing this relationship, the amplitude can easily be found. Both analog and digital implementations are commercially available, which are typically made to remove DC-offset. Our implementation is given by

$$\widehat{A}_k = \sqrt{\frac{2}{MN}\sum_{n=0}^{MN-1} y_{k-n}^2}, \tag{5.14}$$

where N is the number of samples in one half-period, and M is the number of half-periods. The choice of M will be a trade-off between bandwidth and noise attenuation.

5.3.4 Peak Hold

This method was presented in [6] to enable high-speed imaging in dynamic mode AFM. The signal is sampled as it reaches its peak, allowing one or even two samples per oscillation period. It works by introducing a 90° phase-delay to the measured signal which is then used to trigger a sample and hold. The method can be described by

$$x_k = \text{SH}(|y_k|\,,\, y_{k\perp}) \tag{5.15}$$

$$\widehat{A}_k = H_{lp}(z)x_k, \tag{5.16}$$

where $y_{k\perp}$ is a 90° phase-shifted version of y_k, $\text{SH}(\cdot,\cdot)$ is a sample and hold function where the first argument is the output and the second argument triggers a new sample on crossing zero, and $H_{lp}(z)$ is a high-bandwidth low-pass filter used to smooth out the noise from the triggering.

5.3.5 Coherent Demodulator

This is a quadrature based method utilizing the definite integral of $I(\cdot), Q(\cdot)$ from (5.6)-(5.7) over one or multiple periods to remove the $2\omega_0$ frequency component,

$$i(t) = \int_{t-T_0}^{t} I(\tau)d\tau \tag{5.17}$$

$$q(t) = \int_{t-T_0}^{t} Q(\tau)d\tau \tag{5.18}$$

$$\widehat{A}(t) = 2\sqrt{i(t)^2 + q(t)^2}. \tag{5.19}$$

Accurate knowledge of the oscillation period and timing is required. In [1, 2] these equations are implemented using the trapezoidal integration method, and it is discussed how to handle the case where the sampling frequency is not an exact integer multiple of the carrier frequency. This technique is also referred to as the Fourier method [102] as it is equivalent to determining the first coefficients from the Fourier series.

5.3.6 Lock-in Amplifier

The second quadrature-based method uses a low-pass filter with bandwidth $\omega_c \ll \omega_0$ to suppress the frequency component at $2\omega_0$ from (5.6)-(5.7). It is simpler to implement than the coherent demodulator since accurate timing is not needed and it can be implemented using analog circuitry. However, the method is limited in terms of bandwidth due to the necessary low-pass filter. The method is given as

$$i_k = H_{lp}(z)I_k \tag{5.20}$$

$$q_k = H_{lp}(z)Q_k \tag{5.21}$$

$$\widehat{A}_k = 2\sqrt{i_k^2 + q_k^2}, \tag{5.22}$$

where $H_{lp}(z)$ is a low-pass filter with unit gain and bandwidth $\omega_c \ll \omega_0$. A 4th-order Butterworth filter is used in our implementation of the technique.

5.3.7 High-Bandwidth Lock-in Amplifier

The bandwidth of the lock-in amplifier is severely limited by the $2\omega_0$ frequency-components contributions seen in (5.6)-(5.7), as this requires a low-pass filter with a bandwidth significantly lower than the carrier frequency in order to attenuate

these components. The high-bandwidth lock-in amplifier was introduced in [93] where the $2\omega_0$ components are eliminated by phase cancellation allowing for a much larger bandwidth on the low-pass filter.

A 90° phase-shift is introduced to the measured signal y, denoted by $y_\perp$. This is equivalent to switching the $\sin(\cdot)$ with a $\cos(\cdot)$ in (5.3). By repeating the steps of (5.3)-(5.7) with the phase-shifted signal $y_\perp$ the relations

$$I_\perp = \tfrac{A}{2}\left[\sin(2\omega_0 t + \varphi) - \sin\varphi\right] \tag{5.23}$$
$$Q_\perp = \tfrac{A}{2}\left[\cos(2\omega_0 t + \varphi) + \cos\varphi\right] \tag{5.24}$$

are found, where the time-dependency has been dropped for simplicity. By phase cancellation and trigonometric identities this results in

$$I + Q_\perp = A\cos(\varphi) \tag{5.25}$$
$$Q - I_\perp = A\sin(\varphi) \tag{5.26}$$
$$\widehat{A} = \sqrt{(I + Q_\perp)^2 + (Q - I_\perp)^2} = A. \tag{5.27}$$

In practice the phase-cancellation will not be perfect and a low-pass filter is still necessary to remove the resulting residues. However, these residues will be severely reduced compared to the lock-in amplifier which allows for a much greater bandwidth on the low-pass filter. A 4th-order Butterworth filter is again used for this purpose.

5.3.8 Kalman Filter

Recent studies have investigated the use of a Kalman filter for amplitude estimation [94, 159] with promising results. The states are modeled as the amplitude of in-phase and quadrature sinusoidal signals. The state-space model is given by

$$\boldsymbol{x}_k = \boldsymbol{x}_{k-1} + \boldsymbol{w}_{k-1} \tag{5.28}$$
$$y_k = \boldsymbol{c}_k \boldsymbol{x}_k + v_k \tag{5.29}$$
$$\boldsymbol{c}_k = \left[\sin(\omega_0 k T_s),\, \cos(\omega_0 k T_s)\right], \tag{5.30}$$

where $\boldsymbol{x}_k$ is the state vector, y_k is the measured variable, $\boldsymbol{w}_k$ is white noise with covariance $\mathbf{Q}$ describing how fast the amplitude changes, and v_k is white measurement noise with covariance $\mathbf{R}$.

The well-established Kalman filter equations [182] are used for estimation of the

states, rewritten here for convenience and simplified for the problem at hand:

$$\boldsymbol{x}_k^- = \boldsymbol{x}_{k-1} \tag{5.31}$$
$$\mathbf{P}_k^- = \mathbf{P}_{k-1} + \mathbf{Q} \tag{5.32}$$
$$\mathbf{K}_k = \mathbf{P}_k^- \boldsymbol{c}_k^T (\boldsymbol{c}_k \mathbf{P}_k^- \boldsymbol{c}_k^T + \mathbf{R})^{-1} \tag{5.33}$$
$$\boldsymbol{x}_k = \boldsymbol{x}_k^- + \mathbf{K}_k (y_k - \boldsymbol{c}_k \boldsymbol{x}_k^-) \tag{5.34}$$
$$\mathbf{P}_k = (\mathbf{I} - \mathbf{K}_k \boldsymbol{c}_k) \mathbf{P}_k^- (\mathbf{I} - \mathbf{K}_k \boldsymbol{c}_k)^T + \mathbf{K}_k \mathbf{R} \mathbf{K}_k^T \tag{5.35}$$
$$\widehat{A}_k = |\boldsymbol{x}_k|. \tag{5.36}$$

The Kalman filter is the optimal linear state estimator given white, uncorrelated noise [182]. However, the process noise is unlikely to be white since this will depend on the sample being scanned and overall feedback loop. Additionally, in this case the modeled states are the amplitude of the quadrature sinusoidal signals, not the unknown amplitude itself. The amplitude is found through a nonlinear transformation. Thus, optimality cannot easily be concluded.

5.3.9 Lyapunov Estimator

Finally, the Lyapunov estimator from Chapter 4 is implemented for comparison to the other methods. The method is implemented using a unitary filter $W(s) = 1$, which results in the update law

$$\dot{\widehat{\boldsymbol{\theta}}} = \gamma \boldsymbol{\phi} \left(y - \widehat{y} \right), \tag{5.37}$$
$$\widehat{y} = \boldsymbol{\phi}^T \widehat{\boldsymbol{\theta}}, \tag{5.38}$$

where $\boldsymbol{\phi} = [\sin(\omega_0 t), \cos(\omega_0 t)]^T$, and γ is a tuning parameter which determines the bandwidth of the estimator. Finally, the amplitude can be recovered from

$$\widehat{A} = |\boldsymbol{\theta}|. \tag{5.39}$$

The method can easily be tuned either to emphasize low noise (small γ) or high bandwidth (large γ).

Summary

A summary of the characteristics of each method is given in Table 5.1. The various techniques can broadly be categorized into *rectification* approaches, or *mixing* approaches where synchronous reference sinusoids are mixed with the measured signal. The latter class can further be divided into open-loop or closed-loop, depending on how the mixing products are eliminated.

Table 5.1: Characteristics of demodulation techniques.

Technique	Classification	Phase est.	Reference sines required	Accurate timing necessary
Mean abs. dev.	Rectification	No	No	No
Peak detector	Rectification	No	No	No
RMS-to-DC	Rectification	No	No	Yes
Peak hold	Rectification	No	No	Yes
Coherent	Mixing (open-loop)	Yes	Yes	Yes
Lock-in amp.	Mixing (open-loop)	Yes	Yes	No
HB Lock-in amp.	Mixing (open-loop)	Yes	Yes	No
Lyapunov	Mixing (closed-loop)	Yes	Yes	No
Kalman filter	Mixing (closed-loop)	Yes	Yes	No

5.4 Simulation Results

The methods described in the previous section have been implemented in Simulink for simulation. A test environment has been setup according to Fig. 5.1 with parameters given in Table 5.2. The phase shift and amplitude A represent the cantilever deflection response as the tip interacts with the sample, or any general plant. For simulation purposes, the amplitude is modulated such that

$$A(t) = A_0 + \bar{A}(t), \tag{5.40}$$

where the constant $A_0 > 0$ represents the baseline amplitude, and $\bar{A}(t)$ represents the modulation signal.

Several simulation results are presented in order to evaluate the performance of each demodulation technique, by the criteria stated in Section 5.2. For readability, the various methods are divided into two groups corresponding to their classification category. In the presentation of the results, each group is plotted separately.

5.4.1 Step Response

Since the demodulation techniques are inherently nonlinear, their estimates can display different qualitative behavior as a function of time. A step response plot demonstrates this. The results from a step-up and step-down amplitude change are plotted in Fig. 5.2. It can be observed that the methods converge fastest near the peaks of the measured signal (twice per period T_0). Most of the information

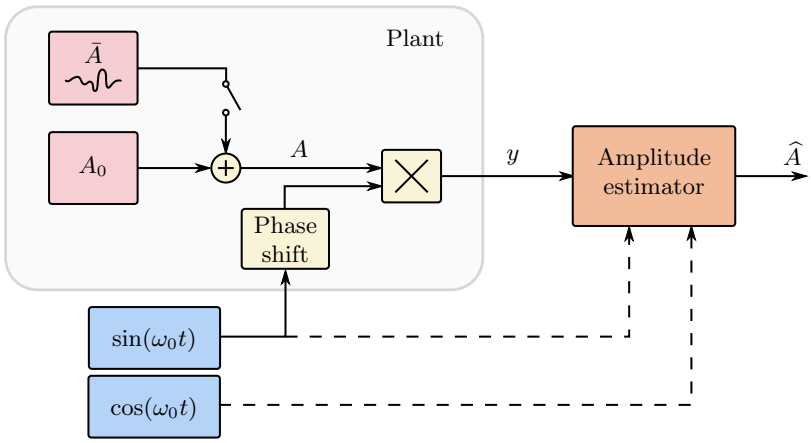

Figure 5.1: Block diagram of test environment. The objective of the amplitude estimator is to recover a constant or time-varying A from the measurement of y, in the presence of noise and harmonics of the carrier frequency.

Table 5.2: Simulation parameters

Carrier frequency	f_0	50 kHz
Signal phase	φ	15°
Reference amplitude	A_0	100 nm
Sampling rate	F_s	2.4 MHz

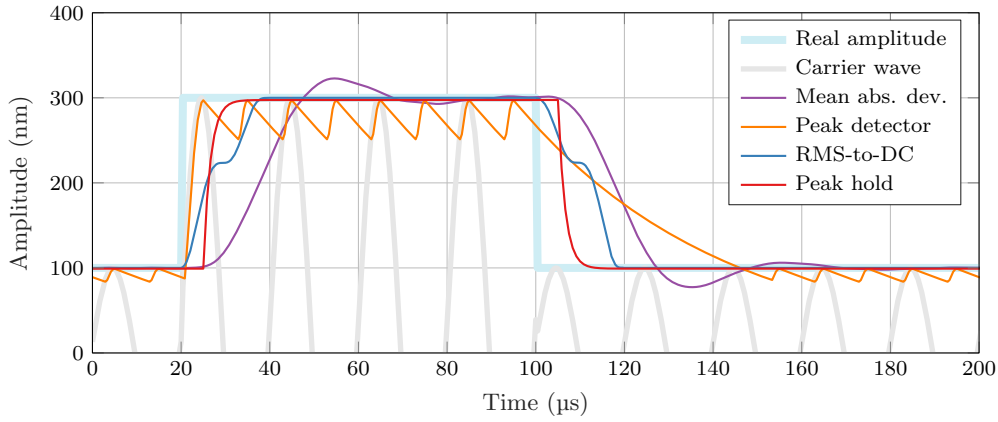

(a)

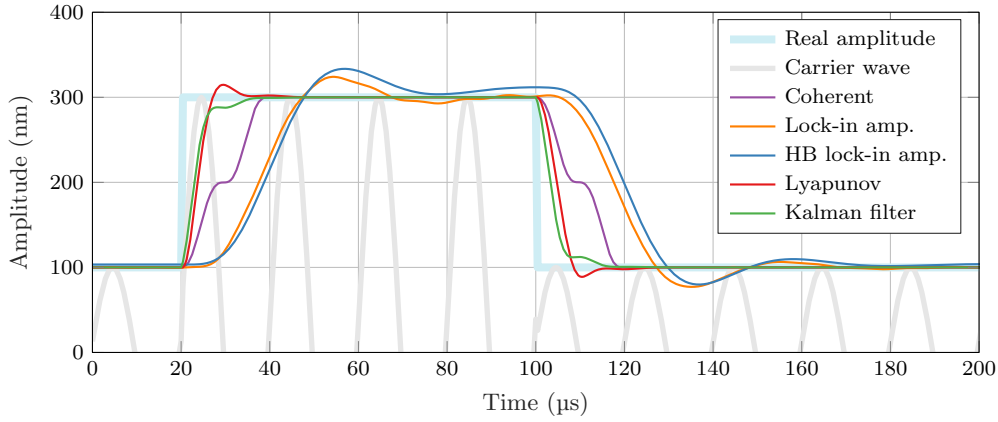

(b)

Figure 5.2: Step response of the various amplitude estimation techniques.

in the signal is located at these points, because the error between two sinusoidal signals of different amplitudes will be greatest here. This will ultimately limit the convergence rate of any amplitude estimator to one half-period, unless a great influence from the measurement noise is acceptable.

5.4.2 Tracking Frequency Response

The tracking bandwidth of each method can be determined by the frequency response of the estimates to the modulation signal $\bar{A}(t)$. Since the various demodulation techniques involves nonlinear operations, system identification techniques based on white noise or chirp signal excitation are rendered less usable. Instead,

the modulation signal is implemented as a single sinusoid at step-wise increasing frequency. Between each step-change, we let the transients come to rest in order to measure the stationary behavior of the demodulation techniques. Finally, the response at a given frequency is determined by the Goertzel algorithm [137], which resolves the discrete Fourier transform at the given frequency.

The results for two different bandwidth settings of each demodulator are given by Fig. 5.3. At the high bandwidth setting several methods display a sharp magnitude rise at $2f_0$, which severely limits their usability at this bandwidth setting. This occurs due to insufficient attenuation of the $2\omega_0$-components arising from either mixing of the signals (lock-in amplifier), or the absolute value operation (mean absolute deviation, peak detection). The other mixing techniques either use feedback to cancel the $2\omega_0$-components (Kalman filter, Lyapunov estimator), phase cancellation (high-bandwidth lock-in amplifier), or accurate timing (coherent demodulator). At lower bandwidth settings the peaks are effectively filtered out for all methods.

5.4.3 Rejection of Other Frequency Components

In multi-frequency or multi-harmonic AFM, several frequency components in a single signal are demodulated simultaneously. It is then necessary to attenuate frequency components other than the one of interest. In order to evaluate this for every technique, the carrier wave frequency was swept from low to high frequencies, while the mixing signals (ϕ) stayed at 50kHz. Then, the magnitude of the response was recorded at each carrier frequency. The tracking bandwidth was set to near 1 kHz.

The results are shown in Fig. 5.4. The ideal filter would rejection all components outside the 1 kHz bandwidth window. The rectification methods, which are all shown in Fig. 5.4(a), demonstrate a near-flat response. Thus, these methods are unsuitable when rejection of other frequency components is an important consideration. The mixing methods, as seen in Fig. 5.4(b), all perform rejection, but at different rates. Due to the 4th-order low-pass filter used in the lock-in- and high-bandwidth lock-in amplifier, they have a very sharp drop-off near f_0 and overlap each other. The Kalman filter, Lyapunov estimator, and coherent demodulator all act as a first-order filter, and drops off by similar rates. The difference between the Kalman filter and Lyapunov estimator could be attributed to small differences in tracking bandwidth settings.

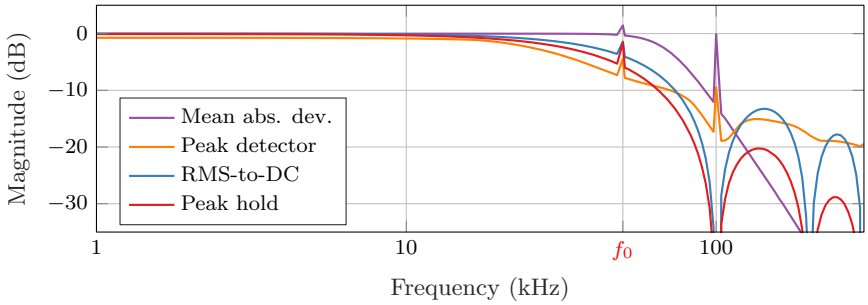

(a) High bandwidth (1/2)

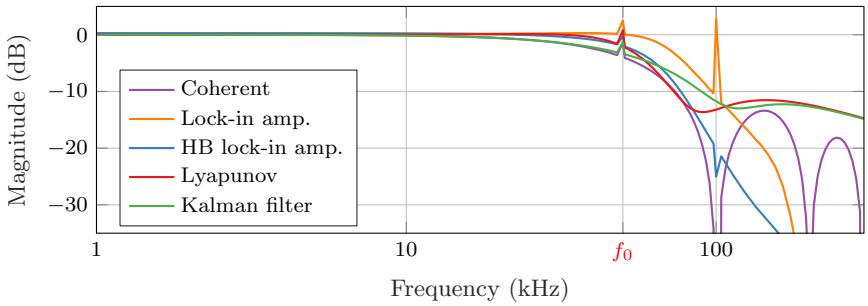

(b) High bandwidth (2/2)

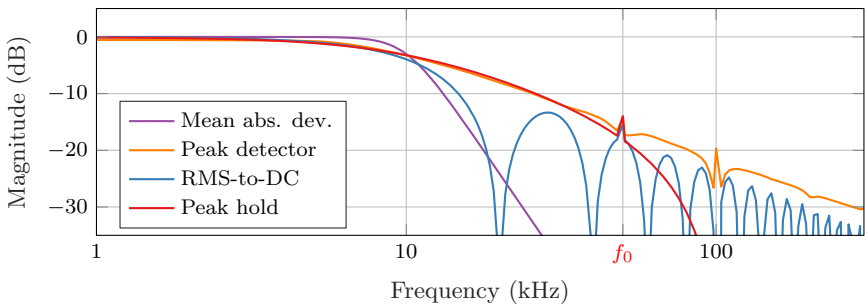

(c) Low bandwidth (1/2)

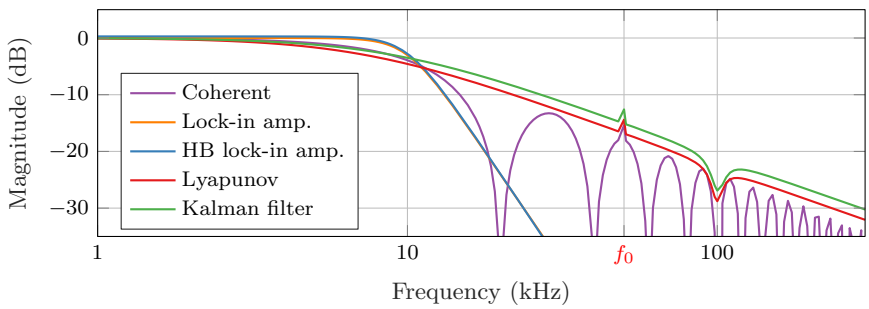

(d) Low bandwidth (2/2)

Figure 5.3: Tracking frequency response to a modulated amplitude signal $A(t)$, performed at different bandwidth settings for each method. (a)-(b) High bandwidth ∼50 kHz. (c)-(d) Low bandwidth ∼10 kHz.

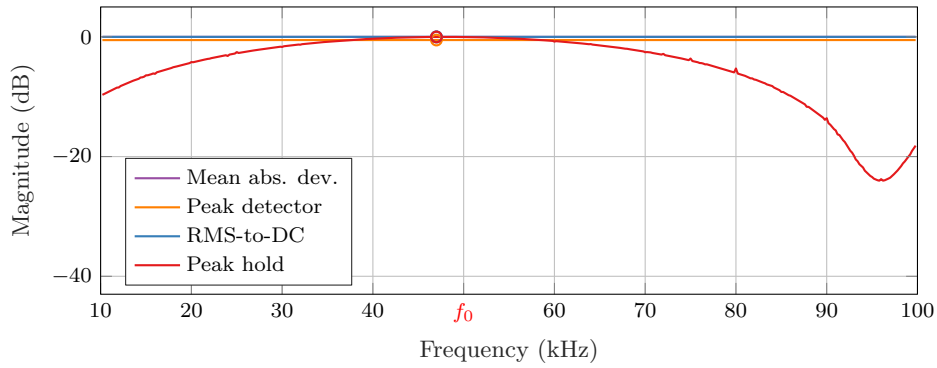

(a)

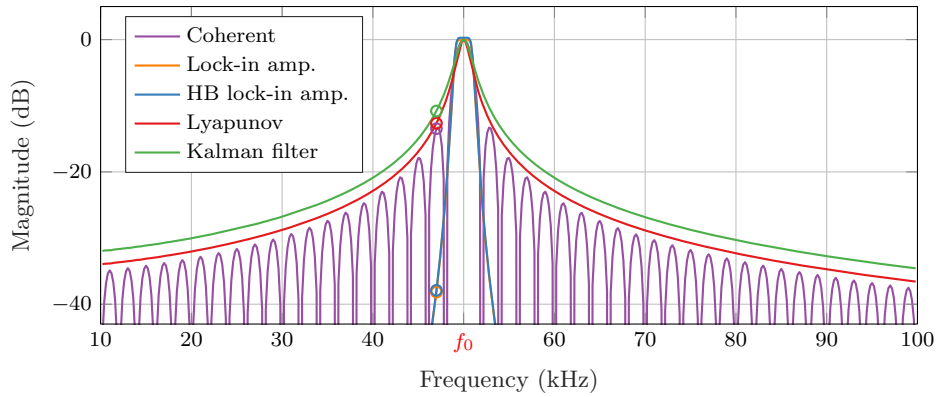

(b)

Figure 5.4: Rejection of frequency components away from the carrier frequency $f_0 = 50\,\text{kHz}$, where each technique is tuned to a tracking bandwidth of approximately 1 kHz. The circles mark the magnitude at 47 kHz.

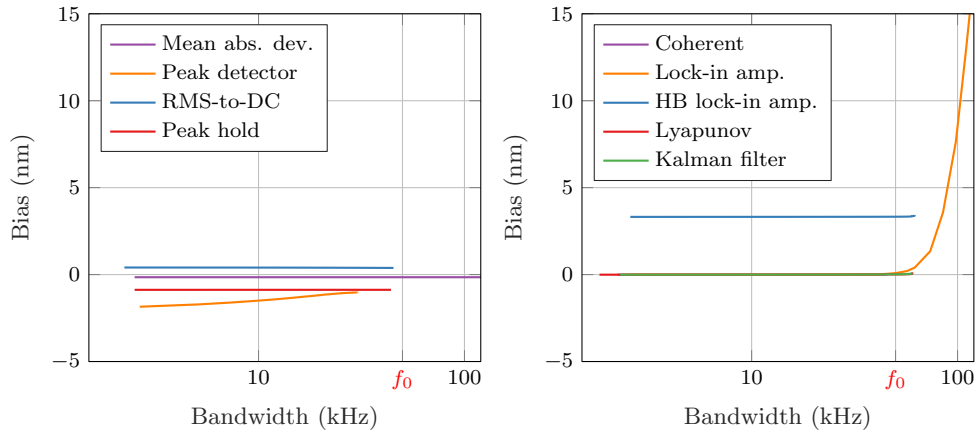

Figure 5.5: Bias as a function of tracking bandwidth, with a reference amplitude of 100 nm.

5.4.4 Bias and Noise Analysis

For accurate determination of the amplitude, the amplitude estimate should be unbiased. The bias was gathered for each method, at various tracking bandwidth settings. The bias is plotted as a function of bandwidth in Fig. 5.5.

Finally, in order to provide an accurate and low-noise amplitude estimate, the estimator should attenuate the noise as much as possible. A study for determining the response of the demodulators to noise was performed. Here, band-limited white noise was used as the modulation signal $\bar{A}(t)$. The resulting total integrated noise (TIN) of the estimated amplitude is used as a performance metric, after subtracting the baseline amplitude A_0. A large TIN value describes a lack of noise attenuation, thus a lower value is beneficial. The TIN is related to the RMS value, and further described in Appendix A. The TIN for each technique over increasing bandwidth settings, is shown in Fig. 5.6. The methods are compared to an ideal filter, modeled as a second-order low-pass filter directly connected to the noise.

Generally, the TIN increases with increased bandwidth. The mean absolute deviation technique and lock-in amplifier demonstrates very low TIN at lower bandwidths. This can be attributed primarily to the implementation using a 4th-order low-pass filter, which attenuates noise at higher frequencies more effectively than lower-order filters. However, at higher bandwidths, the $2\omega_0$-components starts getting mixed with the signal, and the resulting TIN increases rapidly. This ul-

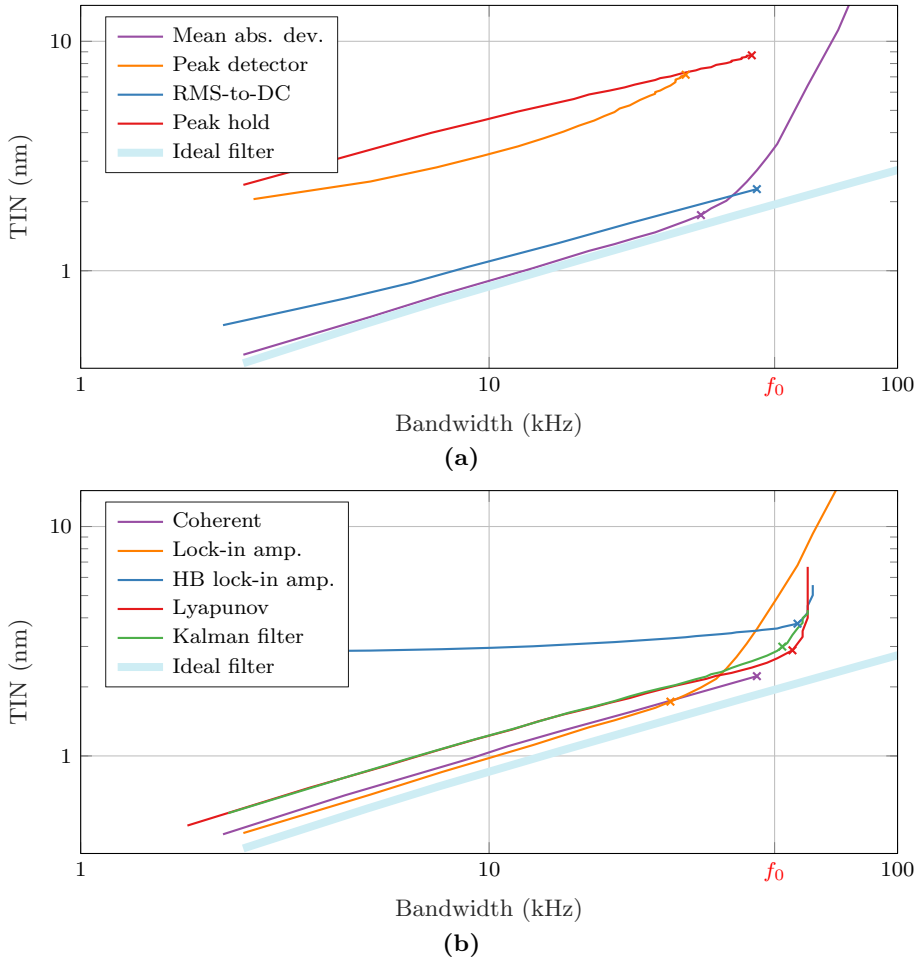

Figure 5.6: Total integrated noise versus demodulation bandwidth. The maximum practical bandwidth is marked by '×'.

timately limits the usable bandwidth. For these reasons, the reported maximum bandwidths of each method is recorded just before a rapid increase in TIN is observed, as marked in Fig. 5.6.

The peak detector and peak hold method effectively takes very few samples per carrier period. Thus, very little filtering is done, and the resulting TIN values are large. The high-bandwidth lock-in amplifier also uses a 4th-order low-pass filter. Nevertheless, it demonstrates a large TIN at lower bandwidths. This can primarily be attributed to its large bias as seen in Fig. 5.5, which ultimately increases the TIN value.

Finally, a summary of the observed performance properties of each method is given in Table 5.3. The convergence time of each method can be determined from their update laws, as well from knowledge on how their filters need to be tuned if appropriate.

5.5 Making a Choice

Based on the simulation results and general advantages and disadvantages of each method, the following suggestions can be made for the desired properties:

5.5.1 Low Implementation Complexity

The mean absolute deviation method and peak detector distinguishes themselves by not requiring reference sinusoidal signals or accurate timing information. This makes them simple to implement and suitable for analog implementation. The RMS-to-DC implementation in this work requires accurate knowledge of the carrier wave period, although simpler implementations of this method are possible. However, simpler implementations will need to average for longer thus decreasing the bandwidth.

If a simple estimator with high bandwidth is desired, the peak hold method is a suitable candidate. However, if digital implementations are available, the Lyapunov estimator is also simple to implement and achieves a much better response to noise and off-mode rejection. If accuracy and low noise is preferable, the mean absolute deviation method or lock-in amplifier can be used at lower bandwidths. Otherwise a simpler RMS-to-DC method with longer averaging is suitable. Peak detector is one of the simpler methods to implement, but is not suitable for feedback control due to its oscillatory nature from peak to peak, and very low convergence rate as the amplitude decreases. This will magnify the problem of *parachuting* in dynamic mode AFM which is already a challenge for high scanning

Table 5.3: Performance metrics of demodulation techniques*.

Technique	Convergence time	BW (kHz)	Off-mode mag. (dB)	TIN Low BW (nm)	TIN High BW (nm)	Bias (nm)
Mean abs. dev.	Exponential (slow)	33.0	0.0	0.9	4.8	−0.2
Peak detector	Exponential (fast up/slow down)	30.3	−0.5	3.2	—	−1.5
RMS-to-DC	Finite time (T_0)	45.2	0.0	1.1	—	0.4
Peak hold	Exponential (fast) + Constant ($\frac{1}{2}T_0$)	44.0	0.0	4.6	—	−0.9
Coherent	Finite time (T_0)	45.2	−13.4	1.0	—	0.0
Lock-in amp.	Exponential (slow)	27.8	−38.2	1.0	6.3	0.0
HB Lock-in amp.	Exponential (fast)	56.9	−37.9	3.0	3.7	3.3
Lyapunov	Exponential (fast)	55.3	−12.7	1.2	2.9	0.0
Kalman filter	Exponential (fast)	52.2	−10.8	1.2	3.4	0.0

*Bandwidth (BW) determined using a carrier frequency of 50 kHz, and chosen either at maximum bandwidth or where TIN rises sharply, see Fig. 5.6. Off-mode magnitude measured at 47 kHz, as seen in Fig. 5.4. TIN measured at low (10 kHz) and high (55 kHz) bandwidths, respectively. Bias measured at a bandwidth of 10 kHz, with a 100 nm reference amplitude. Exponential fast/slow: approximated time constant smaller/larger than one carrier wave period.

speeds [7].

5.5.2 Low Noise and High Accuracy

If a non-biased estimator is desired, the peak detector and the high-bandwidth lock-in amplifier should be avoided. However, for closed-loop control this is rarely a major concern. Attenuation of noise on the other hand will affect the complete control loop. From Table 5.3 it can be seen that the mean absolute deviation method, coherent demodulator, and lock-in amplifier have the smallest TIN at lower bandwidths.

At high bandwidths, the amplitude estimates from the mean absolute deviation method and lock-in amplifier is affected by the $2\omega_0$ components, severely limiting their usability and resulting in high TIN values. Instead, the Lyapunov estimator and Kalman filter have the lowest TIN values at high bandwidths. Of the two, the Lyapunov estimator is less computationally demanding, which allows it to run at faster sampling rates. This is an advantage since it will reduce the overall noise floor of the system [117].

Due to the nonlinear interaction forces occurring in AFM, higher harmonics of the

carrier frequency will also be excited, even in the case where only one frequency component is applied for modulation. Such higher modes should be rejected in order to provide an accurate amplitude at the given carrier frequency. All techniques based on rectification provide no rejection of other frequency components, and should be avoided. The lock-in amplifier and high-bandwidth lock-in amplifier provide the strongest rejection, which can be attributed to their 4th-order low-pass filter implementations. Thus, these methods are highly suitable for multifrequency demodulation.

5.5.3 High Imaging Speed

Only a selection of the techniques are able to reach the highest bandwidths. Furthermore, at very high bandwidths, the estimates may become very noisy and practically unusable. This is certainly true for the lock-in amplifier and mean absolute deviation method. The high-bandwidth lock-in amplifier provides a better noise response at high bandwidths. However, in practice it may struggle with non-perfect phase cancellation resulting in a frequency component most prominently at $2\omega_0$. Thus a low-pass filter is needed to attenuate this component, limiting its bandwidth in practice.

The Lyapunov estimator and Kalman filter provides the lowest noise at the highest bandwidths. The arithmetics involved in the Lyapunov estimator is a lot simpler than the Kalman filter, since it does not need to calculate the covariance matrix and Kalman gain. This should allow for a faster sampling rate which may lead to better noise response and higher bandwidth in practice.

The Kalman filter and the high-bandwidth lock-in amplifier represent state-of-the art for high-bandwidth amplitude estimation. The Lyapunov estimator is comparable in terms of performance with the additional benefit of ease of implementation. In fact, these three methods seem to be at the limit of what is attainable in terms of bandwidth. Most of the amplitude information in the measured signal is located around the signal peak since the error between two sinusoidal signals of different amplitudes will be greatest here. As a result, the estimation techniques generally converge faster near the peak than near zero values of the signal. Thus, a bandwidth of greater than $2\omega_0$ will be difficult if not impossible to achieve. It is then preferable to add a low-pass filter or otherwise reduce gains in order to attenuate high-frequency measurement noise and disturbances from higher harmonics.

5.6 Conclusions

Several traditional and state-of-the-art techniques for amplitude estimation have been implemented and compared. The results allow us to provide clear suggestions for choice of method based on emphasis for either low complexity, high accuracy, or high imaging speeds. The various methods display vast differences in the metrics being measured.

In general there is a clear trade-off between the bandwidth and noise attenuation of the amplitude estimation methods. At the very highest bandwidths, the Kalman filter and Lyapunov estimator provides the best performance in terms of noise attenuation. Of these two methods, the Lyapunov estimator is the simplest to implement. At lower bandwidths, the coherent demodulator, lock-in amplifier, and mean absolute deviation method give the best performance. Of these three techniques, the lock-in amplifier provides the strongest rejection of unwanted frequency components.

Part III

Mechanics of Cells and Soft Samples: Modeling and Identification by AFM

Chapter 6

Cell Mechanics Modeling and Identification by AFM

Identification of mechanical properties of cells has previously been shown to have a great potential and effectiveness on medical diagnosis. As a result, it has gathered increasing interest of researchers over the recent years. Atomic force microscopy (AFM) has become one of the prime technologies for obtaining such properties. Traditionally, local variations in elasticity has been obtained by mapping contact force during sample indentation to static Hertzian contact models. More recently, multifrequency AFM has allowed for both viscous and elastic measurements of soft samples. In this chapter, a new technique is presented based on dynamic modeling and identification of the sample. Essentially, the measured signals are mapped to the sample properties of the model in a least-square sense. This approach allows for easy extensibility beyond pure viscoelastic measurements. Furthermore, an iterative modeling approach can be used to best describe the measured data. The technique can be operated in either dynamic indentation viscoelastic mode, or scanning viscoelastic mode. First, a dynamic, viscoelastic model of the sample is presented. Then, the parameter identification method is described, showing exponential convergence of the parameters. Numerical results demonstrate the effectiveness of the approach in both modes of operation.

Publications The material in this chapter is based on [142, 146, 149].

6.1 Introduction

In the beginning, AFM was applied almost exclusively to characterize the surfaces of nonbiological materials [65], and even today, its major applications are

still in the visualization of microcircuits, material sciences and nanotechnology [153]. However, application of AFM to biological and biomedical research has increased exponentially during the recent years [197], since AFM enjoys several advantages over conventional optical microscopes and electron microscopes, especially concerning studies of biological samples [200].

The main beneficial feature of AFM in the study of biological samples is its ability to study the objects directly in their natural conditions. Other advantages include: [184] 1) AFM can get information about surfaces in situ and in vitro, if not in vivo, in air, in water, buffers and other ambient media, 2) it has an extremely high scanning resolution, up to nanometer (molecular) resolution, and up to 0.01 nm vertical resolution, 3) it provides true 3D surface topographical information, 4) it can scan with a wide range of forces, starting from virtually zero to large destructive forces, 5) it allows measuring various biophysical properties of materials including elasticity, adhesion, hardness, and friction.

In order to improve early diagnosis of cancer there is an urgent need to increase understanding of cancer biology on a cellular level. Single cell deformability has been studied for a long time using various techniques. The driving force for such studies is the assumption that, depending on disease type, the altered cellular deformability should play a critical role in the development and progression of various diseases [111]. So far, several approaches have been investigated, including methods such as micro-pipette manipulation [34], magnetic bead twisting [11], and optical tweezers [70]. With these techniques, local variations in the viscoelastic power law parameters have been observed [76].

Several recent efforts are trying to discover the potential of AFM in cancer detection [13, 32, 76, 109, 110, 111, 184, 197, 200]. Any research result that would provide the possibility of an early and easy diagnosis of carcinoid cells with accuracy is of extreme interest to specialists that deal with the diagnosis and cure of the disease. In [134], AFM measurements of the human breast biopsies reveal unique mechanical fingerprints that help define the stages of cancer progression. High-resolution stiffness mapping shows that in addition to matrix stiffening, tumor progression is due to softening of the tumor cells.

Clearly, mechanical properties of cells and other samples are of high interest to the research community. The usage of AFM for identifying such properties has matured over the recent years, as outlined in Chapter 1. Several techniques are available, such as force-distance curves and multifrequency AFM. However, force-distance curves [21] are typically only able to determine static properties of the sample, such as elasticity. Additionally, the gathering of such curves is a very slow process. On the other hand, multifrequency approaches can resolve nanomechanical properties at high acquisition rates [26]. However, they require the use of

complicated relationships between the observables and the nanomechanical properties of the sample, which are still under development [36]. Furthermore, they typically depend on stationary signals such as amplitude and phase at higher harmonics or higher modes. Instead, utilizing the entire transient information of the signal could potentially increase the acquisition rates further and possibly be less susceptible to measurement noise.

6.1.1 Contributions

In this chapter, a new technique for the identification of viscoelastic properties of soft samples in AFM is presented. Here, the sample is modeled as a dynamic model with unknown parameters, in terms of a laterally spaced grid of spring constants and damping coefficients. The parameters are identified from the measurable signals, using tools from the control literature. Essentially, the measurable signals are mapped to the parameters of the sample model recursively in a least squares sense, making it possible to observe changes over time. The estimated parameters are guaranteed to converge to the real values exponentially fast provided a suitable control input is chosen.

Two distinct modes are suggested for the operation of the approach taken in this chapter. In dynamic indentation viscoelastic (DIVE) mode, mechanical properties of the sample are identified at a discrete number of points by indenting in and out of the sample. In the scanning viscoelastic (SVE) mode, viscoelastic properties are gathered in a continuous fashion as the sample is scanned along the lateral axes at constant depth.

A simulation environment is constructed to evaluate the effectiveness of the proposed technique, for both modes of operation. The simulation results demonstrate the feasibility of the approach.

6.1.2 Outline

This chapter is organized as follows. In Section 6.2 a system model description of the viscoelastic sample is designed, suitable for parameter identification. The two modes of operation, DIVE and SVE, are presented in Section 6.3. Next, Section 6.4 presents the identification techniques for the unknown parameters of the system. Results are given in Section 6.5. In Section 6.6 the technique is discussed in the context of previous approaches and future considerations, and in Section 6.7 final conclusions are reached.

6.2 System Modeling

In this section, the system modeling is presented. This includes the dynamics of the sample, the cantilever dynamics, the geometry of the tip and their combinations, in order to acquire a full system description. The purpose of the modeling is to provide a description of the interaction between the cantilever and a general viscoelastic sample material, while allowing for identification of the model parameters by the usage of an atomic force microscope.

6.2.1 Sample Dynamics

The modeled sample is considered as a system of discrete spring-damper elements, as illustration in Fig. 6.1. The elements are evenly distributed in the lateral xy-axes, and can be compressed in the vertical z-direction.

The interaction between the AFM cantilever and the sample is analytically presented, and illustrated in Fig. 6.2. The position of the tip along the xyz-axes is denoted by (X, Y, Z). The vertical tip position Z, the cantilever deflection D, and the controllable cantilever base position U_z are related by

$$Z = U_z + D. \tag{6.1}$$

Since the deflection D is measurable and U_z is controllable, all three signals are assumed to be available.

The dynamics between the cantilever and the sample can be described by three main components as seen in Fig. 6.3. The cantilever dynamics are subject to an external sample force which generates a deflection along the vertical axis. The tip geometry and position is then used to determine the (possibly compressed) positions of each sample spring-damper element. The compressed elements in turn creates a restoration force acting on the cantilever tip. The details of each of these components will be described in the following.

6.2.2 Cantilever Dynamics

The cantilever dynamics can be approximated by its first resonance mode [166], resulting in the spring-damper system

$$M\ddot{Z} + KD + C\dot{D} = F_{\text{ts}} \tag{6.2}$$

where M is the effective mass of the cantilever [15], K, C are the cantilever spring and damping constants respectively, and F_{ts} is the force from the sample acting on the cantilever tip.

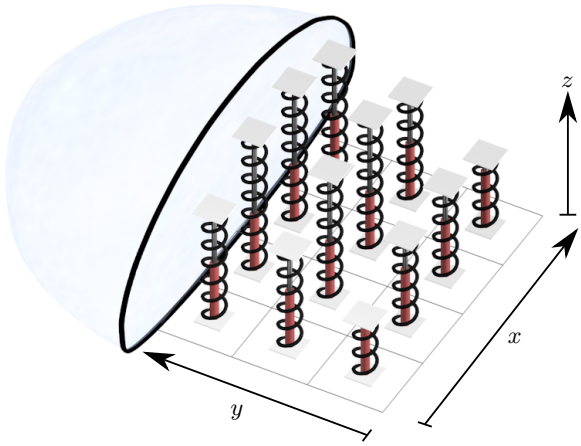

Figure 6.1: The sample is modeled as spring-damper elements evenly spaced along the lateral axes.

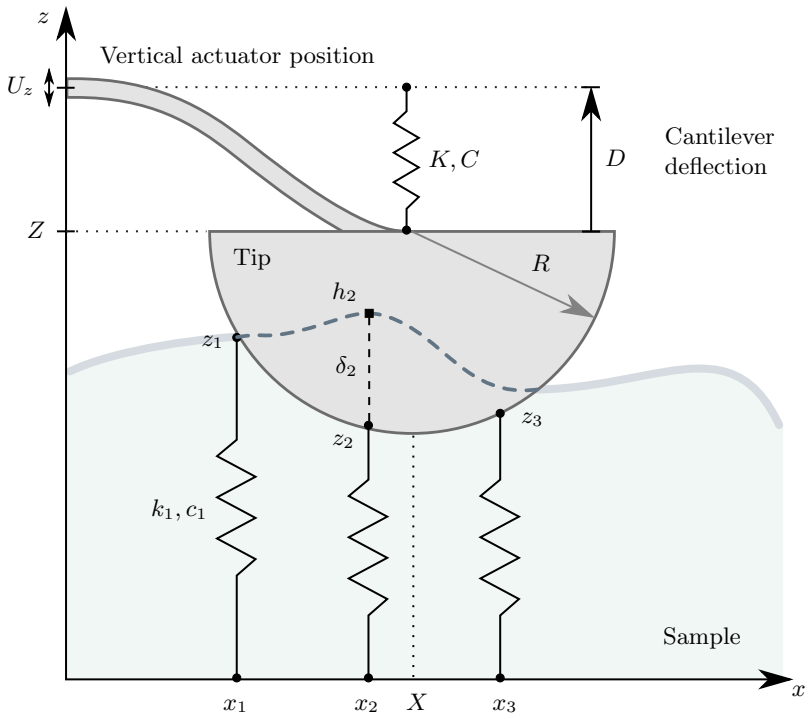

Figure 6.2: Indentation of the tip into the sample.

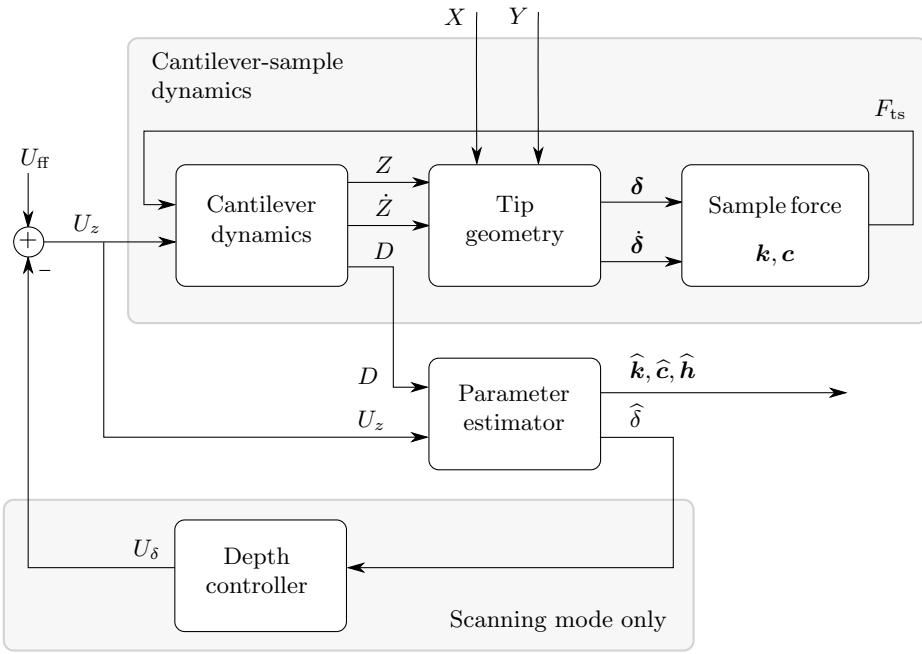

Figure 6.3: Block diagram of the cantilever-sample dynamics and parameter estimator. The parameter estimates are based solely on measurements of the deflection output D and the vertical position control input U_z.

6.2.3 Tip Geometry

The cantilever tip is modeled as a sphere with tip radius R. The vertical position z_i of the spring-damper element i in contact with the tip is then given by

$$z_i = Z - \sqrt{R^2 - (X - x_i)^2 - (Y - y_i)^2} \tag{6.3}$$

$$\dot{z}_i = \dot{Z} \tag{6.4}$$

where x_i, y_i are the position of the element along the lateral axes, and $\dot{z}_i$ is the element velocity. It has been assumed that $\dot{X}$ and $\dot{Y}$ are much smaller than $\dot{Z}$. This is justified by the fact that the cantilever is oscillated at a high frequency near resonance resulting in a significant rate of change in Z, while the sample is scanned comparatively slow in the lateral directions.

A spherical tip can be advantageous in use with soft, fragile samples [185], although if desired the equations (6.3)-(6.4) can be modified to handle different tip geometries. The tip geometry is only necessary for simulation purposes, as the parameter identification scheme does not require a tip model. However, the scaling of the identified parameters are dependent on the tip. Thus, if the radius or geometry is not known, the identified values will be scaled inaccurately. However, this inaccuracy will be consistent across the sample.

6.2.4 Sample Force

The sample is modeled by viscoelastic elements. Thus, each element in contact with the tip provides spring and damping forces. The force from element i can be described by

$$F_i = k_i \delta_i + c_i \dot{\delta}_i \tag{6.5}$$

where k_i is the spring constant of element i, c_i is the damping coefficient, and δ_i is the indentation of the tip into the element,

$$\delta_i = h_i - z_i \tag{6.6}$$

where h_i is the rest-position of the element, or equivalently the sample height (topography) at the position of the element. The sample is assumed not to display permanent deformations. Thus, $\dot{\delta}_i = -\dot{z}_i$ since the sample height is constant.

The sample elements in contact with the tip is denoted by the active set $\mathcal{W}(X, Y, Z)$ which changes as the tip scans over the sample,

$$\mathcal{W} = \left\{ i \,:\, \delta_i > 0 \,\wedge\, (X - x_i)^2 + (Y - y_i)^2 < R^2 \right\}. \tag{6.7}$$

The element i is thus only added to the active set if the tip is indenting it. This method could be extended to model the attractive forces near the surface by including elements with a small negative value of δ_i.

The sum of the forces acting on the cantilever tip from the sample is then given by

$$F_{\text{ts}} = \sum_{i \in \mathcal{W}} F_i. \tag{6.8}$$

In the following, the vectors $\boldsymbol{k}, \boldsymbol{c}, \boldsymbol{h}$ are used to refer to the family of elements, e.g. $\boldsymbol{k} = \{k_1, ..., k_m\}$ where m is the number of spring-damper elements in the sample.

6.3 Modes of Operation

The modeling and identification approach described in this chapter can be operated in two distinct modes, both of which identify the unknown sample parameters of the dynamic sample model.

6.3.1 Dynamic Indentation Viscoelastic Mode

In DIVE mode, the cantilever moves across the sample surface without contact. At discrete points in space, the lateral movement is paused and the tip is lowered into the sample and identifies the sample properties at this single point. The cantilever is then raised and the procedure is repeated across the sample to form an $N \times N$ grid of identified parameters.

In this mode, the tip is lowered sufficiently such that the entire tip is submerged into the sample. This is not strictly necessary, although for consistent measurements the scaling of the parameters, as discussed later, would need to be revised to account for this case.

6.3.2 Scanning Viscoelastic Mode

In SVE mode, the cantilever is always in contact with the sample, scanning continuously at constant depth across the surface of the sample in a raster pattern. The sample parameters are identified continuously resulting in an $N \times M$ grid of resolved parameters, where N is the number of discrete lines and M is the number of samples of the continuous signal at each line.

6.4 Parameter Identification

In this section it is shown how the unknown parameters of the system, $\boldsymbol{k}, \boldsymbol{c}, \boldsymbol{h}$, can be estimated. As seen in Fig. 6.3 the parameter estimator is separated from the system and only the cantilever deflection D and vertical control input signal U_z is assumed available for measurement.

6.4.1 Parametric System Model

The system equations needs to be on a form suitable for parameter identification. Rewriting (6.2) and inserting for (6.5),(6.8) gives

$$M\ddot{Z} + KD + C\dot{D} = \sum_{i \in \mathcal{W}} k_i \delta_i + c_i \dot{\delta}_i \tag{6.9}$$

where the signals on the left hand side are known, and the right hand side contains the parameters to be estimated. It would be very challenging to determine all the sample parameters of each element individually. The problem is therefore simplified by rather trying to estimate the aggregated spring constant k and damping constant c at the current tip position. The system can thus be approximated by

$$M\ddot{Z} + KD + C\dot{D} = k\delta + c\dot{\delta} \tag{6.10}$$

where c, k are now slowly-varying parameters as a function of the current lateral tip position (X, Y). By continuously estimating and logging c, k as the tip is scanned or tapped across the sample, the local viscoelastic properties of the sample are determined.

The indentation depth of the tip into the sample is given by

$$\delta = h - Z \tag{6.11}$$

where h is the unknown sample topography at the current tip position.

In DIVE mode, the topography h can be found from a simplified approach by recording the first point of contact during a tap, thus δ is assumed known in this mode. However, in SVE mode this approach does not work because the cantilever moves in the lateral directions while being indented. Thus, the topography parameter h will change after first point of contact.

Due to the difference in assumption of known δ, the parametric system model will have to differ between the two modes.

DIVE Mode System

The system equations (6.10) can be rearranged and rewritten in the complex s-domain as

$$Ms^2Z + CsD + KD = (cs + k)\,\delta \tag{6.12}$$

which can be formulated as

$$w'_{\mathrm{D}} = \begin{bmatrix} c \\ k \end{bmatrix}^T \begin{bmatrix} s\delta \\ \delta \end{bmatrix} \tag{6.13}$$

$$= \boldsymbol{\theta}_{\mathrm{D}}^T \boldsymbol{\phi}'_{\mathrm{D}} \tag{6.14}$$

where the known w'_{D} is the left hand side of (6.12), $\boldsymbol{\theta}_{\mathrm{D}}$ is the unknown parameter vector to be estimated, and $\boldsymbol{\phi}_{\mathrm{D}}$ is the known signal vector.

SVE Mode System

Using (6.10), and inserting for (6.1) and (6.11), the system equations can be rewritten as

$$Z(Ms^2 + Cs + K) - U_z(Cs + K) = k(h - Z) - csZ \tag{6.15}$$

where it has been used that h is a slowly-varying parameter, thus $\dot{h}$ can be approximated by zero. The parametric system equations can now be represented by

$$w'_{\mathrm{S}} = \begin{bmatrix} c \\ k \\ kh \end{bmatrix}^T \begin{bmatrix} -sZ \\ -Z \\ 1 \end{bmatrix} \tag{6.16}$$

$$= \boldsymbol{\theta}_{\mathrm{S}}^T \boldsymbol{\phi}'_{\mathrm{S}} \tag{6.17}$$

where w'_{S} is the left hand side of (6.15), and $\boldsymbol{\theta}_{\mathrm{S}}, \boldsymbol{\phi}_{\mathrm{S}}$ are the parameter and signal vector respectively.

Filtered System Equations

In order to avoid pure differentiation of the signals in (6.13),(6.16), both sides of each equation is filtered by a second-order low-pass filter such as $1/\Lambda(s) = 1/(\lambda s + 1)^2$,

$$\frac{w'_\jmath}{\Lambda} = \boldsymbol{\theta}_\jmath^T \frac{\boldsymbol{\phi}'_\jmath}{\Lambda} \tag{6.18}$$

$$w_\jmath = \boldsymbol{\theta}_\jmath^T \boldsymbol{\phi}_\jmath. \tag{6.19}$$

for $\jmath \in \{\mathrm{D}, \mathrm{S}\}$.

This linear-in-the-parameters form is suitable for implementation of various parameter estimation methods such as given in [84]. The objective of the estimator is thus to find the unknown $\boldsymbol{\theta}_\jmath$ given the signals $w_\jmath$ and $\boldsymbol{\phi}_\jmath$.

6.4.2 Parameter Estimator

Several estimation methods for the system (6.19) can be employed with similar stability and convergence properties, as outlined in Chapter 2. We have chosen the least squares estimator with forgetting factor. Due to the slowly varying nature of the parameters, a forgetting factor is useful. The method is restated here for completeness,

$$\widehat{w}_\jmath = \widehat{\boldsymbol{\theta}}_\jmath^T \boldsymbol{\phi}_\jmath \tag{6.20}$$

$$\varepsilon_\jmath = (w_\jmath - \widehat{w}_\jmath)/m_\jmath^2 \tag{6.21}$$

$$m_\jmath^2 = 1 + \alpha \boldsymbol{\phi}_\jmath^T \boldsymbol{\phi}_\jmath \tag{6.22}$$

$$\dot{\widehat{\boldsymbol{\theta}}}_\jmath = \mathbf{P}_\jmath \varepsilon_\jmath \boldsymbol{\phi}_\jmath \tag{6.23}$$

$$\dot{\mathbf{P}}_\jmath = \beta \mathbf{P}_\jmath - \mathbf{P}_\jmath \frac{\boldsymbol{\phi}_\jmath \boldsymbol{\phi}_\jmath^T}{m_\jmath^2} \mathbf{P}_\jmath \tag{6.24}$$

$$\mathbf{P}_\jmath(0) = \mathbf{P}_{\jmath,0} \tag{6.25}$$

for $\jmath \in \{\mathrm{D}, \mathrm{S}\}$, where α, β, R_0 are positive constants, and $\mathbf{P}_\mathrm{D} \in \mathbb{R}^{2\times 2}, \mathbf{P}_\mathrm{S} \in \mathbb{R}^{3\times 3}$ are the covariance matrices.

This method guarantees convergence of the error $\varepsilon_\jmath$ to zero given constant parameters $\boldsymbol{\theta}_\jmath$ as in DIVE mode. The parameters in SVE mode are slowly-varying, but the error can be made arbitrarily small by reducing the scanning speed.

For the parameter vector $\widehat{\boldsymbol{\theta}}_\jmath$ to converge to $\boldsymbol{\theta}_\jmath$, the signal vector $\boldsymbol{\phi}_\jmath$ needs to be persistently exciting (PE) [84]. Indeed, this is a sufficient condition for exponential convergence of $\widehat{\boldsymbol{\theta}}_\jmath \to \boldsymbol{\theta}_\jmath$, by Theorem 2.2. The following theorem provides conditions for PE and exponential convergence in DIVE mode. Equivalent conditions can be shown in the case of SVE mode.

Theorem 6.1 (Exponential convergence)**.** *Apply the cantilever input signal*

$$U_z = U_0 + A \sin(\omega_0 t) \tag{6.26}$$

for any positive constants A, ω_0, and let the constant U_0 be small enough for the cantilever tip to be in contact with the surface, i.e. $\delta > 0, \forall t$. Then $\boldsymbol{\phi}_\mathrm{D}$ is persistently exciting (PE) and $\widehat{\boldsymbol{\theta}}_\mathrm{D} \to \boldsymbol{\theta}_\mathrm{D}$ exponentially fast.

Proof. Expand the signal vector $\boldsymbol{\phi}_{\mathrm{D}}$ such that

$$\boldsymbol{\phi}_{\mathrm{D}} = \mathbf{H}(s)\delta, \quad \mathbf{H}(s) = \begin{bmatrix} \frac{s}{(1+\lambda s)^2} \\ \frac{1}{(1+\lambda s)^2} \end{bmatrix}.$$

Define the matrix $\mathbf{A}$ such that

$$\mathbf{A}(j\omega_1, j\omega_2) \triangleq \left[\mathbf{H}(j\omega_1)\, \mathbf{H}(j\omega_2)\right] = \begin{bmatrix} \frac{j\omega_1}{(1+\lambda j\omega_1)^2} & \frac{j\omega_2}{(1+\lambda j\omega_2)^2} \\ \frac{1}{(1+\lambda j\omega_1)^2} & \frac{1}{(1+\lambda j\omega_2)^2} \end{bmatrix}.$$

Taking the determinant of $\mathbf{A}$ gives

$$\begin{aligned} |\mathbf{A}(j\omega_1, j\omega_2)| &= \frac{1}{(1+\lambda j\omega_1)^2(1+\lambda j\omega_2)^2}\,(j\omega_1 - j\omega_2) \\ &\neq 0 \,\forall\, \{\omega_1, \omega_2 \in \mathbb{R} \,:\, \omega_1 \neq \omega_2\}. \end{aligned}$$

Thus $\mathbf{H}(j\omega_1), \mathbf{H}(j\omega_2)$ are linearly independent on $\mathbb{C}^2 \,\forall\, \{\omega_1, \omega_2 \in \mathbb{R} \,:\, \omega_1 \neq \omega_2\}$. By Theorem 5.2.1 in [84] $\boldsymbol{\phi}_{\mathrm{D}}$ is then PE if and only if δ is sufficiently rich of order 2.

By Definition 5.2.1 in [84] the signal $U_z = U_0 + A\sin(\omega_0 t)$ is sufficiently rich of order 2. The transformation from U_z to δ is seen to be linear and stable by considering (6.1),(6.11),(6.12), which means that a sinusoidal input on U_z results in a sinusoidal output on δ with amplitude $\left|\frac{\delta}{U_z}(j\omega_0)\right|$, phase $\angle\frac{\delta}{U_z}(j\omega_0)$ and frequency ω_0. The signal δ is thus sufficiently rich of order 2. Thus, $\boldsymbol{\phi}_{\mathrm{D}}$ is PE. Additionally, $\boldsymbol{\phi}_{\mathrm{D}}$ is bounded since $\dot{U}_z$ is bounded and $\mathbf{H}(s)$, $\frac{\delta}{U_z}(s)$ are stable. Then, by Corollary 4.3.1 in [84] the parameter vector $\widehat{\boldsymbol{\theta}}_{\mathrm{D}} \to \boldsymbol{\theta}_{\mathrm{D}}$ exponentially fast. ■

Although exponential convergence of $\widehat{\boldsymbol{\theta}}_{\mathrm{D}} \to \boldsymbol{\theta}_{\mathrm{D}}$ is guaranteed, some error is expected in the identified parameters at a given point because of the model approximation from (6.9) to (6.10).

6.4.3 Indentation Depth and Topography

As discussed earlier in this section, the two modes differ in how the identified topography $\widehat{h}$ is found. However, for each mode, when $\widehat{h}$ is found, the depth is given by

$$\widehat{\delta} = \widehat{h} - Z. \tag{6.27}$$

In the following, identification of the topography is described for each mode.

DIVE Mode

In the identification scheme for DIVE mode, the depth was assumed known in (6.12). This signal can be generated by identifying $\widehat{h}$ at each tap and using (6.27) during the tap. The procedure is described in the following.

As the tip enters the sample the cantilever will start to deflect. This point is recorded and used as the topography estimate $\widehat{h}$ at the current tip position. The topography estimate is stored after each tap ℓ, generating the estimate of the complete sample topography $\widehat{h}_\ell \, \forall \, \ell$. Additionally, a low-pass filter G_{lp} for attenuation of measurement noise and a hysteresis loop for avoiding retriggering during sample penetration is used in the implementation. The procedure is summarized as follows:

- Record the time $t_1 = t$ at rising edge of the boolean signal $G_{lp}D > \gamma$, for some positive constant γ.
- Create a hysteresis loop for t_1 by disabling retriggering until $G_{lp}D > \gamma_+$ where $\gamma_+ > \gamma$.
- Then $\widehat{h} = Z(t_1)$ and $\widehat{\delta}(t) = \widehat{h} - Z(t)$, where as previously $Z(t) = U_z(t) + D(t)$.
- Store $\widehat{h}_\ell = \widehat{h}$ for the current tap ℓ.

SVE Mode

In SVE mode, the topography is estimated as part of the identification scheme as seen in (6.16). The topography $\widehat{h}$ is found after division by $\widehat{k}$ in $\widehat{\theta}_{\mathrm{S},3}$. As such, the estimator should make sure $\widehat{k}$ does not become zero. Since k is known to be strictly positive, a projection function such as from [103] can be used in the update law (6.23) to ensure $\widehat{k}$ stays within provided limits.

6.4.4 Depth Controller

In SVE mode, an additional depth controller is required. Due to the spherical nature of the tip geometry, the submerged parts of the tip into the sample will vary based on the depth of the tip. The spring and damping forces are effectively nonlinear functions of depth. Thus, constant depth is necessary to enforce consistent measurements across the sample. For this reason, a depth controller has been designed.

A simple I-controller is used to maintain desired depth δ_{ref}, given by

$$U_\delta = k_i \int_0^t \left(\delta_{\mathrm{ref}} - \widehat{\delta}(\tau) \right) d\tau. \tag{6.28}$$

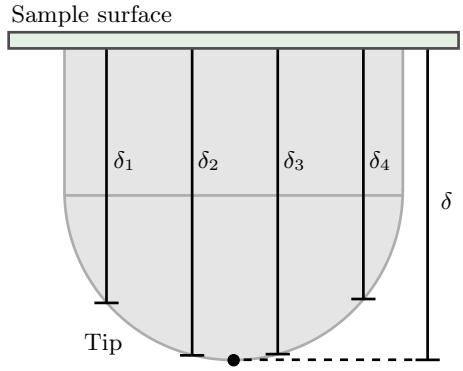

Figure 6.4: The indentation depth δ is larger than the average of the element depths, δ_i. This introduces a bias in the identified spring constant, which can be corrected for in post-processing.

This signal is applied to the system according to Fig. 6.3.

Note that due to the soft, heterogeneous sample material, traditional scanning approaches such as amplitude modulated AFM is not sufficient for constant depth. This is because the varying spring and damping parameters will ultimately affect the amplitude response of the cantilever. Thus, by controlling for constant amplitude, changes in the material properties is indistinguishable from changes in depth. This would ultimately lead to errors in the identified parameters.

6.4.5 Corrected Spring Constant

The indentation of the tip into the sample, δ, is defined as the distance from the edge of the tip to the surface. However, the indentation of each sample element δ_i is smaller or equal to δ as seen in Fig. 6.4. This creates a discrepancy between the sum of the spring force of each element, and the spring force identified in the approximated model for parameter identification. In the following, it is shown how to correct for this discrepancy.

Assuming homogeneous spring constants, $k_i \equiv k_0$, and completely submerged tip as in DIVE mode, $\delta \geq R$. From (6.5),(6.8) the total spring force acting on the tip is then given by

$$F_k = \sum_i k_0 \delta_i = k\delta \tag{6.29}$$

where k is the aggregate spring constant from the approximated model (6.10), and δ from (6.11) is the depth into the sample measured at the end of the tip.

The scaling between k_0 and k can then be found as

$$\begin{aligned} k_0 &= \frac{\delta}{\sum_i \delta_i} k \\ &= \frac{\delta}{n\delta - (\sum_i \delta - \delta_i)} k \end{aligned} \tag{6.30}$$

where $n = |\mathcal{W}|$ is the number of elements under the tip. An expression for the summation term can be found by considering the spherical tip geometry:

$$\begin{aligned} \frac{1}{n}\sum_i \delta - \delta_i &= R - \frac{1}{n}\sum_i \sqrt{R^2 - (X - x_i)^2 - (Y - y_i)^2} \\ &\approx R - \frac{1}{\pi R^2}\int_0^{2\pi}\int_0^R \rho\sqrt{R^2 - \rho^2}\, d\rho d\theta \\ &= R - \frac{2}{3}R \\ &= \frac{1}{3}R. \end{aligned} \tag{6.31}$$

The only approximation is due to moving from the discrete case to the continuous case. Inserting the last line into (6.30) gives

$$k_0 \approx \frac{1}{n}\frac{\delta}{\delta - \frac{1}{3}R} k$$

Since k and δ are not available, they can be replaced by their identified versions. In summary, the corrected spring constant for a completely submerged tip is given by

$$\widehat{k}_c = \frac{1}{n}\frac{\widehat{\delta}}{\widehat{\delta} - \frac{1}{3}R}\widehat{k} \tag{6.32}$$

6.5 Simulation Results

6.5.1 Setup

Simulations have been setup according to Fig. 6.3 for the DIVE and SVE modes respectively. The cantilever dynamics and sample properties are identical in both modes for the purpose of comparing the results.

The sample properties have been defined over a grid of $5 \times 5\,\mu m^2$ with 50×50 evenly spaced elements. The number of grid elements determines the smoothness

of the force versus depth-response of the cantilever as it indents the sample. A high number gives a smooth curve, while a low number gives a piecewise linear approximation to the curve. On the other hand, a high number of elements is more computationally demanding. The 50×50 grid results in a fairly smooth curve as seen in Fig. 6.10 at reasonable computation times. The number of elements should be scaled by the area the cantilever tip covers for consistent results.

Each grid element i is represented by its topography h_i, damping coefficient c_i, and spring constant k_i. The given sample properties plotted over the spatial domain can be seen in Figs. 6.5(a), 6.6(a) and 6.7(a) respectively. The properties have been designed to resemble a cell, but could represent any soft sample material.

A cantilever with a resonance frequency of 20 kHz was chosen with a spring constant 0.18 N/m, a damping coefficient 1.48×10^{-8} Ns/m, an effective mass 1.18×10^{-11} kg, and tip a radius 300 nm. This equates to a quality (Q) factor of 100.

DIVE mode was setup to perform a total of 20×20 indentations evenly spaced across the grid, with 0.2 s spent during each indentation for a total imaging time of 80 s. The sample parameters were recorded once towards the end of each tap.

In SVE mode, a total of 20 scanlines were performed across the sample, with a periodicity of 2 s for a total imaging time of 40 s. The sample properties were continuously sampled across the fast scanning direction, and resampled in post-processing to generate a 50×20 resolution image. A horizontal resolution of 50 was chosen to correspond to the number of defined elements. Due to phase-lag of the parameter identification scheme, the values across a backward and forward scan were averaged. Otherwise each consecutive line would appear slightly offset from the previous line.

Although the input signal from (6.26) is sufficient for PE conditions, the following excitation signal was implemented for both modes,

$$U_{\text{exc}} = U_0 + A_1 \sin(f_1 2\pi t) + A_2 \sin(f_2 2\pi t) \tag{6.33}$$

where U_0, A_1, A_2 are suitably chosen constants, f_1 is near resonance frequency of the cantilever, and f_2 is below resonance frequency. The last term is used to provide additional excitation of the signal vector for faster parameter convergence.

In DIVE mode, the excitation amplitudes A_1, A_2 were set to oscillate the cantilever tip with amplitudes of 100 nm and 25 nm respectively. The total vertical positioning signal is then given by $U_z = U_{\text{exc}} + U_{\text{in}}$, where U_{in} is a repeated signal actually performing the indentation.

In SVE mode, small oscillation amplitudes are used. This avoids exciting the nonlinearities of the interaction force arising due to the spherical tip geometry.

Additionally, in the case of lateral friction (not implemented) the tip would more easily move across the surface. The amplitudes A_1, A_2 in this case are set to oscillate the cantilever at 5 nm and 8 nm respectively. The reference depth δ_{ref} for the feedback controller is set to 150 nm. The input signal in this mode is given by $U_z = U_{\text{exc}} + U_\delta$.

6.5.2 Scaling the Parameters

The identified spring and damping constants are aggregate parameters, that is, they are the sum of the individual spring-damper elements which the tip is in contact with. Thus, they need to be scaled by the number of elements the tip covers. That is, the corrected parameters are given by

$$\widehat{k}_c = \widehat{k}/n, \tag{6.34}$$

$$\widehat{c}_c = \widehat{c}/n. \tag{6.35}$$

where $n = |\mathcal{W}|$ is the number of elements in the set $\mathcal{W}$, or equivalently, the number of sample elements the tip is in contact with.

Additionally, the non-flat tip geometry means that the indentation of individual elements will vary across the tip, even in the case of flat topography. Ultimately, this will affect the measurements of the spring constants.

In SVE mode only a small part of the tip is submerged. Thus, the error due to the spherical tip geometry is small. Additionally, due to the constant depth the error is consistent across the sample. For these reasons, the spring constant has been left uncorrected.

On the other hand, in DIVE mode the tip is completely submerged and the depth varies between each tap. In this case, the corrected spring constant is found by applying (6.32) to the estimated parameters.

These corrections as discussed have been applied to the results. The subscripts of the corrected parameters have been omitted for the sake of readability.

6.5.3 Results

Comparison of the identified topography for each mode to the given topography is seen in Fig. 6.5. The identified damping coefficients are seen in Fig. 6.6, and the identified spring constants are given in Fig. 6.7.

The error plots of the identified properties are given in Fig. 6.8. The errors are given in percentages of the maximum value of each property, that is, $h_{\max} = 0.3\,\mu\text{m}$, $c_{\max} = 8 \times 10^{-7}\,\text{Ns/m}$, and $k_{\max} = 5 \times 10^{-3}\,\text{N/m}$ respectively.

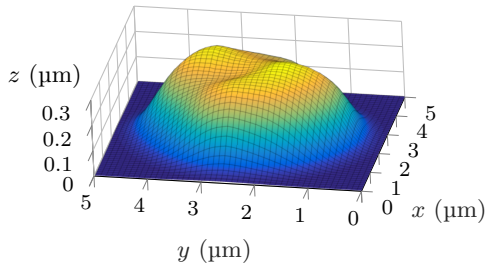

(a) Given values, $\boldsymbol{h}$

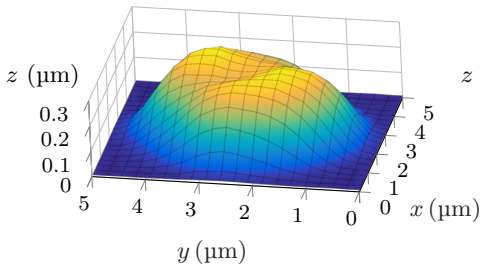

(b) DIVE mode, $\widehat{\boldsymbol{h}}_{\mathrm{D}}$

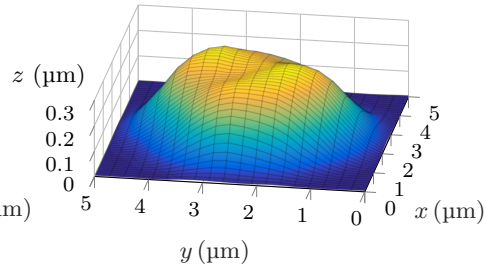

(c) SVE mode, $\widehat{\boldsymbol{h}}_{\mathrm{S}}$

Figure 6.5: Sample topography (a), versus identified topography (b)-(c).

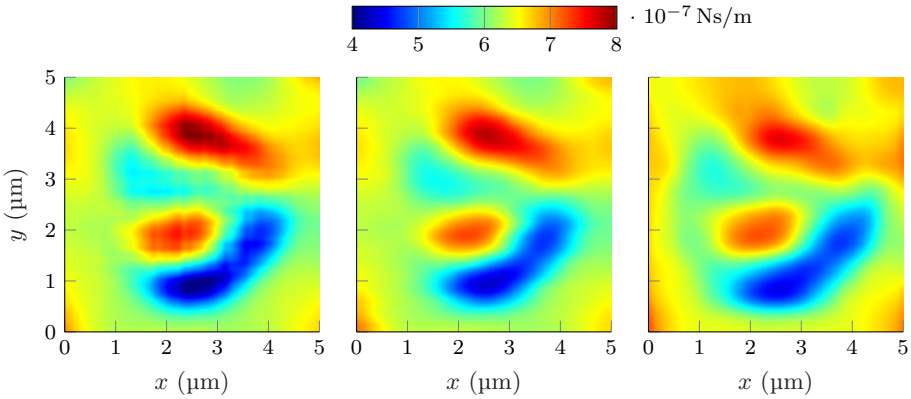

(a) Given values, $\boldsymbol{c}$ **(b)** DIVE, $\widehat{\boldsymbol{c}}_{\mathrm{D}}$ **(c)** SVE, $\widehat{\boldsymbol{c}}_{\mathrm{S}}$

Figure 6.6: Sample viscosity (a), versus identified viscosity (b)-(c).

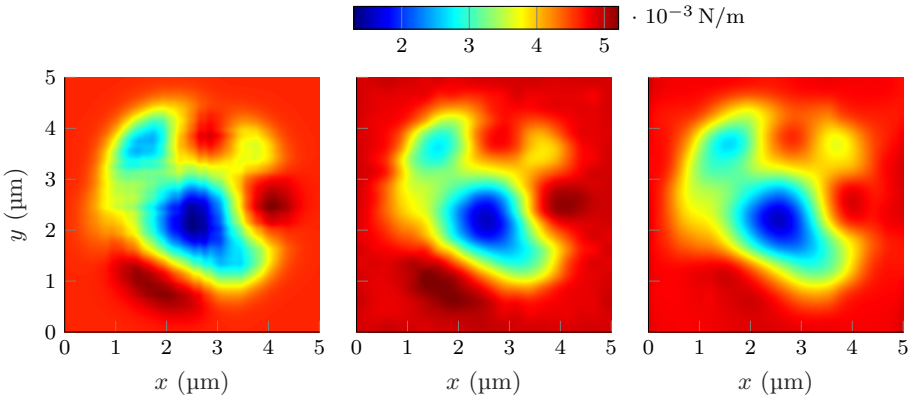

(a) Given values, $\boldsymbol{k}$ **(b)** DIVE, $\widehat{\boldsymbol{k}}_{\mathrm{D}}$ **(c)** SVE, $\widehat{\boldsymbol{k}}_{\mathrm{S}}$

Figure 6.7: Sample elasticity (a), versus identified elasticity (b)-(c).

In general, it is seen that both modes quite accurately represent the real sample properties. The real properties have small details that are not captured by any of the operating modes. This is expected for two reasons:

1. The large tip radius covers several sample elements essentially acting as an averaging filter. Details smaller than the radius will be less distinguishable.
2. The resolution is essentially limited by the number of indentations (DIVE mode) or scanlines (SVE mode), thus obfuscating high-resolution details.

From the error plots it can be seen that in general the errors are larger in the cases where the topography gradient is large. This effect and other biases are discussed in the next section.

Fig. 6.9 demonstrates the differences between the two modes of operation. For each mode it is seen how the parameter identification scheme approaches the real values across a complete cross section of the sample. Additionally, the vertical positioning input U_z is plotted to further demonstrate the differences between the modes.

The parameters presented in Fig. 6.9(b) experience a high-frequency oscillation. This is possibly due to the forced high-frequency oscillation of the cantilever, possibly combined with high gains in the parameter estimator. The frequencies are higher than the horizontal resolution of the image and the number of defined elements, thus the oscillations are not visible after resampling and anti-aliasing.

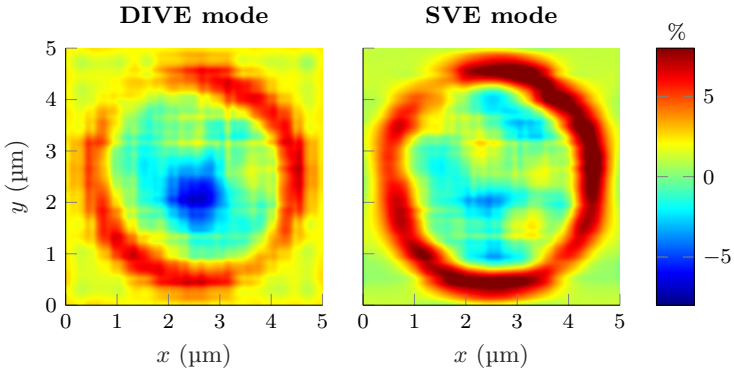

(a) Topography, $\widehat{\boldsymbol{h}} - \boldsymbol{h}$

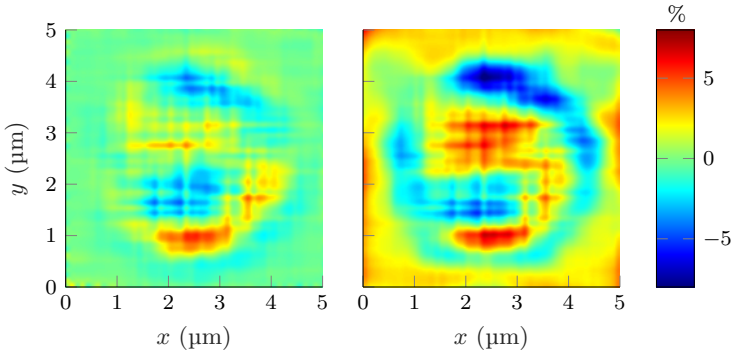

(b) Viscosity, $\widehat{\boldsymbol{c}} - \boldsymbol{c}$

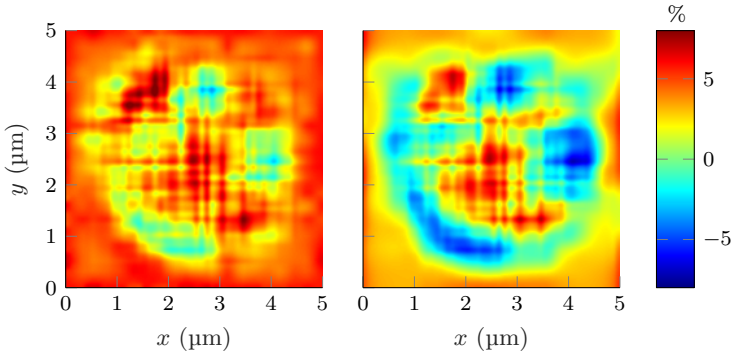

(c) Elasticity, $\widehat{\boldsymbol{k}} - \boldsymbol{k}$

Figure 6.8: Error plots of identified parameters.

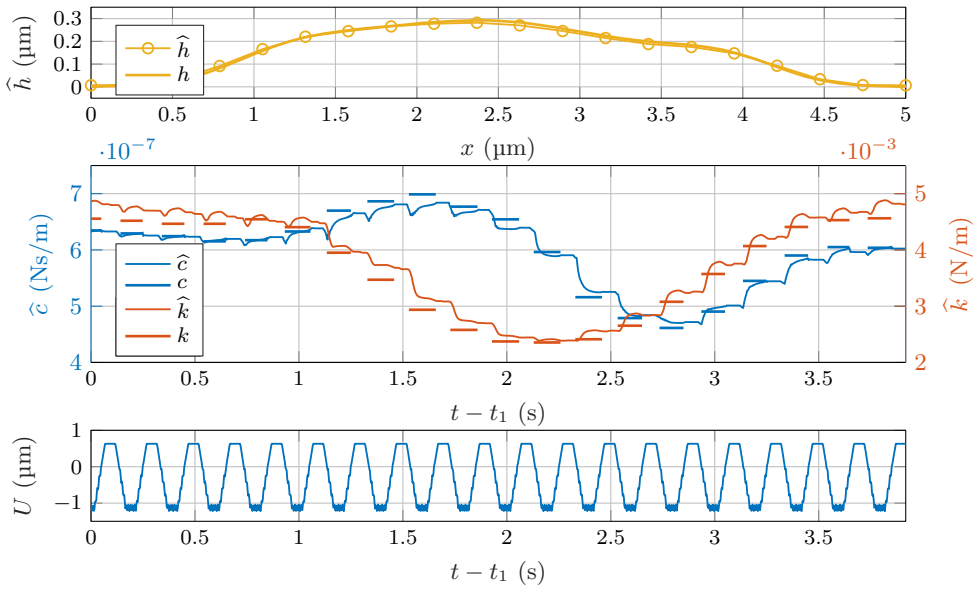

(a) DIVE mode

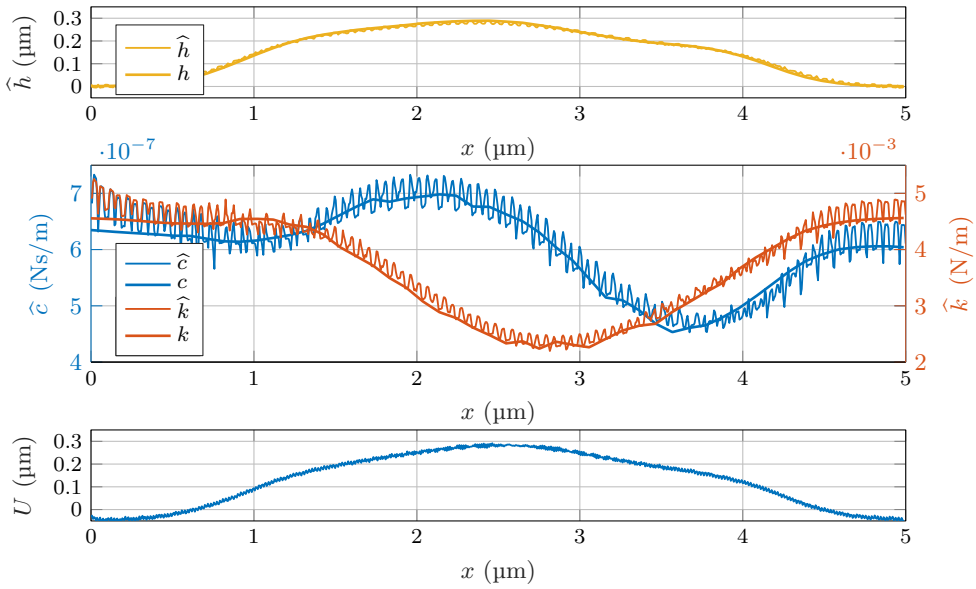

(b) SVE mode

Figure 6.9: Convergence of the identified parameters along the sample cross section at $y = 0.158\,\mu\text{m}$. In DIVE mode (a) lateral positioning of the tip pauses during each indentation, thus the properties are shown in the time domain. In SVE mode (b) the lateral tip speed is constant, thus all plots can be mapped to the spatial domain.

6.6 Discussion

6.6.1 Comparison to Existing Techniques

Sample Modeling

The modeling approach presented in this chapter should be examined to evaluate how it compares to previous experiments. In traditional Hertzian contact models the indentation depth is correlated to the loading force F_k by $F_k \propto \delta^{1.5}$ for a spherical indenter. Experiments have shown exponents ranging between 1.5 and 2.0 depending on the bluntness of the tip [24]. In Fig. 6.10 it is seen that during an indentation in our model the exponent is 1.72 which fits well within the range of previous experiments.

Although classical Hertzian contact mechanics seems to correlate well with experimental observations [105], it is based on some inherently strong assumptions. This includes small strains (indentations), homogeneous sample elasticity, and frictionless surfaces [91, 185]. The model presented in this chapter however is not inherently restricted by these limitations, or is easily extendable to account for them.

- Longer indentation ranges can be accounted for, e.g. by introducing nonlinear springs.
- The presented model allows for local variations in the elasticity at any spatial resolution.
- Friction can easily be added to the model by forces.

In some cases, models based on horizontal coupled linear springs have been used to describe the nanomechanics of lipid bilayers with a good fit to experimental data

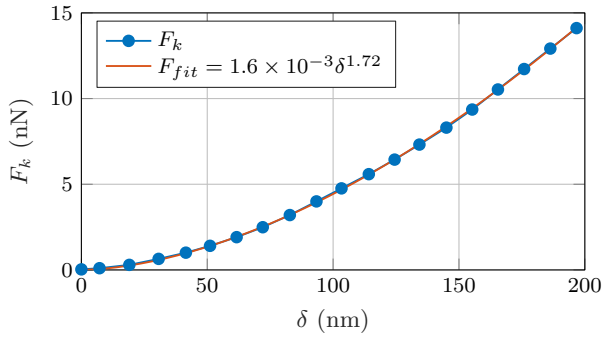

Figure 6.10: Spring force over depth during indentation.

[50, 60]. Such models could be a good fit for implementation with the approach presented in this chapter.

In static Hertzian contact mechanics, identifying dynamic phenomena such as damping is not possible or relevant. Since our presented model is dynamic in nature, such phenomena appear effortlessly in the model. Other dynamic phenomena can also be included in the model such as plasticity and hysteresis [187]. However, this will require some additional effort for identifying the relevant parameters.

Identification of Mechanical Properties

Recently, approaches based on multifrequency AFM have become increasingly popular. In these approaches, the frequency components of the cantilever's response to interaction with the sample surface is mapped to the mechanical properties of the sample. The operation of the SVE mode is related to the operation in multifrequency AFM. Both approaches scan across the surface at some indentation level with forced oscillations. However, the differences are clear when it comes to mapping the measured signals to mechanical properties. The multifrequency approaches evaluate several of the first few Fourier coefficients of the conservative and dissipative parts of the tip-sample interaction force [151]. Then, these coefficients are mapped to local material properties through a Taylor expansion of the interaction force around the indentation point.

Instead, in both modes presented in this chapter, the measured signals are mapped to a dynamic model of the sample in a least square sense, using traditional parameter estimation techniques from the control literature. This approach has several advantages:

1. The sample model can easily be extended for measurements of additional sample properties. Even certain nonlinearities can easily be implemented in the sample model and parameter estimator.
2. Errors in the dynamic model after mapping the parameters can easily be seen. This allows the user to see how well the measured properties matches the reality of the physical sample. Furthermore, these errors can be used to improve the model in an iterative approach, possibly using a data-driven modeling approach.
3. Such a dynamic model allows for predictive behavior of the material, and, it can be argued, leads to a more intuitive description of how the sample behaves.

DIVE mode can be considered a hybrid between the SVE mode and force-volume

imaging. It is similar to the latter in how it indents into the sample at discrete points along the lateral axes. However, it retains the advantages of SVE mode as it excites the sample at higher frequencies and exploits this for measuring dynamic properties of the sample.

6.6.2 DIVE Mode versus SVE Mode

The two modes of operation are both shown to be feasible candidates for identifying mechanical properties of a soft sample. However, there are certain differences between the two modes that should be emphasized.

DIVE mode indents deeper into the sample and assumes a completely submerged tip. However, with revised scaling of the parameters this mode could also tap at smaller indentation ranges. The pixel throughput of the two modes favors the SVE method with twice the number of pixels at half the time.

Earlier studies have demonstrated a difference between elasticity measurements in traditional force-distance curves and more recent multifrequency techniques, by up to an order of magnitude [151]. Materials such as cells can display variable elasticity and possibly damping as a function of both depth and frequency. Due to the differences in indentation depth and operation of the two modes in this chapter, they may essentially measure different physical properties of the sample. As such, the two modes supplement each other.

In SVE mode, an additional depth controller was proposed. This controller has a potential of replacing the traditional amplitude estimation feedback when scanning soft materials. The viscoelastic measurements are known to change with depth. By scanning at constant depth, consistency of the results is maintained.

6.6.3 Sources of Error

Some errors in the measured topography, viscosity, and elasticity can be explained by considering how the tip intersects with a sample of varying topography, see Fig. 6.11. A flat topography is the ideal case, in which the measured and actual height is equivalent. When the tip is placed over the highest point of a concave topography, the measured height will be correct. However, since the submerged volume of the tip is smaller than in the ideal case, an error will be introduced in the measured viscosity and elasticity. Lastly, in the case of steep topography, the side of the tip will touch the sample first. Additionally, only small parts of the tip will be submerged as the tip descends. This introduces errors in measured topography (ε_h), elasticity, and viscosity.

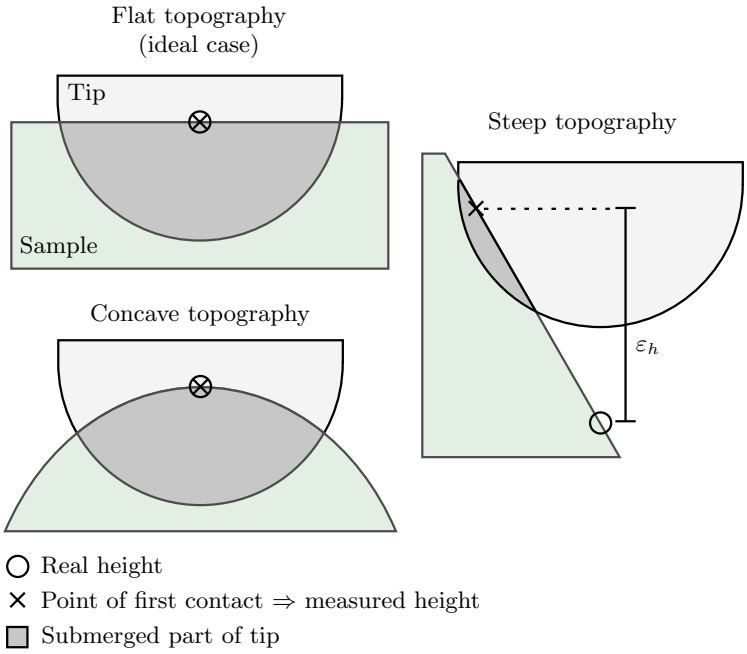

Figure 6.11: Errors due to varying topography.

These errors can be mitigated by using a tip with a smaller radius. Additionally, the errors will be reduced when the gradient of the sample topography is smaller.

6.6.4 Implementability for Experiments

For experimental implementation, only the parameter estimator needs to be considered. The sample modeling part does not need to be considered, as its primary purpose is to provide a foundation for design and analysis of the parameter estimator, as well as simulation implementations.

Some complications may arise during experiments. DIVE mode registers the height at the first point of contact, but some materials may not have a clearly defined edge, i.e. h, because of varying and possibly attractive tip-sample forces near the surface. If such forces are different between indentation points it may influence the measurements, especially for topography and spring constants.

The DIVE mode assumes a completely submerged tip. Depending on the softness and properties of the material being investigated, this may induce large stresses and possibly permanently deform the sample. A possible solution is to reduce the indentation depth and scale the measured parameters accordingly.

DIVE mode should be simple to implement because only a feedforward signal needs to be implemented online. The parameter estimator can be run offline as a post-processing technique of the measured signals. However, in SVE mode, the parameter estimator is used for depth estimation and feedback control. Thus, at least parts of the parameter estimator need to run online. If issues arise due to online implementability, the complexity of the solution could be reduced by implementing the pre-filters for $\widehat{\phi}$ and $\widehat{w}$ in analog circuitry and use the gradient estimator for the parameter estimation. This would reduce the digital implementation to a few arithmetic operations plus an integrator, in addition to the I-controller.

6.7 Conclusions

A new technique based on modeling and parameter estimation for simultaneously identifying the topography, damping coefficients, and spring constants of soft samples has been presented. The technique can be operated in two distinct modes, both of which share advantages over existing approaches. The advantages of such a modeling and identification approach include:

i) The transient signals are used directly, and do not rely on stationary signals such as amplitude and phase. Thus, faster imaging throughput may be achieved compared to existing approaches. Furthermore, no multifrequency demodulators are necessary, thereby avoiding additional tuning and complexity.

ii) The relationships between the observables and identified properties are easily recognized, and directly follows the dynamic modeling.

iii) The cantilever and contact models employed can easily be swapped for other models with minor modifications. Thus, a model could be found which more effectively explains the data for a given setup, such as to account for additional physical phenomena including nonlinear springs.

iv) Since a dynamic model of the sample is obtained, the behavior of the material can be predicted through simulations of the obtained model after experiments.

The two modes of operation, DIVE and SVE mode, are compared and evaluated. Both modes are shown to be feasible in simulation studies, and they could supplement each other in experiments. DIVE mode may be easier to implement, as it does not require any feedback signal from the parameter estimator. However, SVE mode displays a faster pixel throughput.

Chapter 7

Convergence Time of Parameter Estimates

In the previous chapter, recursive least squares estimation is used to identify the viscoelastic properties of a sample in AFM. As long as the signal vector is persistently exciting (PE), exponential convergence of the parameters to be identified can be guaranteed. However, even exponential convergence can be slow. In this chapter, upper bounds on the convergence rate of the estimated parameters are found, completely determined by the PE properties and least squares update law parameters. The results are developed in the general framework for recursive least squares estimation. Furthermore, for a parameter vector which is piecewise constant at regular intervals, the time interval sufficient for the error to converge to any specified upper limit is determined. For a soft sample in AFM, the viscoelastic properties can be spatially inhomogeneous. These properties can be spatially resolved by periodically tapping at discrete points along the sample, such as in the DIVE mode presented in the previous chapter. The results of this chapter then allow us to determine the time interval sufficient at each tap, in order to guarantee convergence to any specified fraction of the step-change in the parameters. Simulation results are presented, demonstrating the applicability of the approach.

Publications The material in this chapter is based on [144] with additional results from [147]. Furthermore, new numerical results are provided, in order to aid a more thorough discussion on the parameter convergence rate, specifically, when a covariance reset is applied at regular intervals.

7.1 Introduction

In Chapter 6, the DIVE mode for imaging viscoelastic properties of soft matter using AFM is presented. The approach is based on modeling and parameter identification by a recursive least squares (RLS) estimator with forgetting factor, as given in Chapter 2. The sample is then modeled as a spatially distributed grid of spring-damper elements to be identified. In DIVE mode, an oscillating cantilever is employed. Then, the cantilever is periodically indented into the sample, at discrete points across the scanning region to be examined.

In RLS, exponential convergence of the parameters can be guaranteed as long as the signal vector is persistently exciting (PE). However, even exponential convergence can be slow. Thus, for practical implementations, knowledge of a guaranteed upper bound on the convergence rate is highly beneficial to the user. Furthermore, such an upper bound would be a helpful tool in aiding the choice of update law parameters. In this chapter, an upper bound is presented which depends only on the PE properties and chosen update law parameters.

Another common practical consideration – often the reason for using recursive estimation approaches – is the time-varying nature of parameters and its effect on the parameter estimates. In general, exponential convergence in the constant parameter case, guarantees some degree of tracking for a sufficiently slowly-varying signal [4, 122]. The topic of time-varying parameters has been the focus of several studies [33, 115, 201, 208]. In DIVE mode identification using AFM, the viscoelastic properties of the sample are considered spatially inhomogeneous but constant in time. Accordingly, during each tap the parameters are constant, but for subsequent taps they can attain different constant values. Furthermore, the time interval between taps can be specified by the operator. Thus, a situation arises where the parameters are time-varying, piecewise constant, at a user-defined constant interval. In this chapter, by exploiting the exponential bounds that are derived for a constant parameter vector, the time interval sufficient to converge to any specified upper limit of the error is determined. The results are applicable to any similar problem with a time-varying, piecewise constant parameter vector.

7.1.1 Contributions

In this chapter, the general framework for RLS is considered. An upper bound on the exponential convergence rate of the parameter estimates are developed for the constant parameters case. The bound strictly depends on the PE properties of the signal vector, and chosen update law parameters. Furthermore, a sufficient time interval in order to guarantee that the parameter error has been reduced to

any given fraction of the initial error is found.

Then, the case where the parameters take on new constant values at regular intervals is considered. An upper bound on the estimation error is given in this case, which depends on the maximum step-change of the parameters at the regular intervals. Additionally, a sufficient time interval for the error to be reduced to any given fraction of the maximum step-change is found, in the case of piecewise constant parameters.

The results are applied to the DIVE mode for identification of viscoelastic properties in AFM. Then, the sufficient time interval between each indentation into the sample is found, in order to guarantee convergence to any specified value. The choice of update law parameters is then discussed, using the upper bound on the convergence error to ensure a fast convergence. Simulations results are given, which demonstrate that the parameters converge within the time interval found apriori. The usage of a covariance reset between intervals is also demonstrated, which allows for tighter bounds on the convergence rate.

7.1.2 Outline

The chapter is organized as follows. First, the general framework for RLS is briefly restated in Section 7.2. Intermediary results for parameter convergence are given in Section 7.3. These results are used to provide an upper-bound on the exponential convergence rate in the constant parameter case in Section 7.4, and in the piecewise constant parameter case in Section 7.5. Additionally, a sufficient time interval in order for the parameter estimation error to be reduced to any desired degree, is given for both cases. The theoretical results are applied to the viscoelastic identification problem in Section 7.6, before conclusions are given in Section 7.7.

7.2 Recursive Least Squares Estimation

In this section, the general framework for RLS estimation is briefly summarized from Chapter 2. The RLS estimator is applicable to a wide range of estimation problems. By adhering to the following setup of the plant model, RLS can easily be applied for estimation of the parameters. The described framework will be used as the foundation for the results of this chapter.

7.2.1 Parametric And Estimation Model

The system model is described by the linearly parametrized system

$$w = \boldsymbol{\theta}^T \boldsymbol{\phi}, \tag{7.1}$$

where $w \in \mathbb{R}$ is the input signal, $\boldsymbol{\theta} \in \mathbb{R}^n$ is the vector of n unknown parameters, and $\boldsymbol{\phi} \in \mathbb{R}^n$ is the known signal vector. Furthermore, the estimation model is given by

$$\widehat{w} = \widehat{\boldsymbol{\theta}}^T \boldsymbol{\phi}, \tag{7.2}$$

where $\widehat{w} \in \mathbb{R}$ is the estimated input signal, and $\widehat{\boldsymbol{\theta}} \in \mathbb{R}^n$ is the vector of estimated parameters. Furthermore, let the parameter estimation error be given by $\widetilde{\boldsymbol{\theta}} = \widehat{\boldsymbol{\theta}} - \boldsymbol{\theta}$.

7.2.2 Least Squares Estimator

Several methods exist for parameter estimation in models such as (7.1). The results of this chapter focus on the least squares estimator as described in the following. First consider the estimation error ε given by

$$\varepsilon = \frac{w - \widehat{w}}{m^2} \tag{7.3}$$

$$m^2 = 1 + \alpha \boldsymbol{\phi}^T \boldsymbol{\phi} \tag{7.4}$$

where m^2 is a normalization signal which guarantees boundedness of the error, and $\alpha > 0$ is a design constant, typically unity.

The update law of the least squares estimator with forgetting factor is given by

$$\dot{\widehat{\boldsymbol{\theta}}} = \mathbf{P} \varepsilon \boldsymbol{\phi} \tag{7.5}$$

$$\dot{\mathbf{P}} = \beta \mathbf{P} - \frac{\mathbf{P} \boldsymbol{\phi} \boldsymbol{\phi}^T \mathbf{P}}{m^2} \tag{7.6}$$

for some chosen value $\beta > 0$ and $\mathbf{P}(0) = \mathbf{P}_0 = \mathbf{P}_0^T > 0$. Additionally, the definitions of $\alpha_0, \alpha_1, T_\mathrm{p}$ from Definition 2.3 are used in this chapter.

7.3 Covariance Bounds and Lyapunov-Like Convergence

In this section, intermediate results are presented which are used to prove exponential stability of the parameters later in this chapter. In particular, upper and

lower bounds on $\mathbf{P}(t)$ are derived which depend only on the PE properties and the chosen update law parameters. Then, these bounds are used to prove exponential convergence of a Lyapunov-like function. In the subsequent sections, these results are used to prove an exponential convergence rate of the parameter estimates in the case of constant parameters and piecewise-constant parameters, respectively.

Lemma 7.1 (Bounds on $\mathbf{P}(t)$)**.** *If $m, \boldsymbol{\phi} \in \mathcal{L}_\infty$, $\boldsymbol{\phi}$ is PE, and $\boldsymbol{\theta}$ is constant, then the least squares estimator given by (7.3)-(7.6) guarantees the following bounds on $\mathbf{P}(t)$:*

$$\gamma_1 \mathbf{I} \leq \mathbf{P}(t) \leq \gamma_2 \mathbf{I}, \quad \forall t \geq 0 \tag{7.7}$$

with

$$\gamma_1 = \left(\lambda_{\min}(\mathbf{P}_0)^{-1} + (\alpha\beta)^{-1}\right)^{-1} \tag{7.8}$$

$$\gamma_2 = \max\left\{\frac{\bar{m}^2}{\alpha_0 T_p}, \lambda_{\max}(\mathbf{P}_0)\right\} e^{\beta T_p} \tag{7.9}$$

where $\bar{m}^2 = \sup_t m^2(t)$ and $\lambda_{\min}(\cdot), \lambda_{\max}(\cdot)$ denotes the minimum and maximum eigenvalue, respectively.

Proof. The proof closely follows the proof of [84, Cor. 4.3.2]. However, the bounds are here described in terms of $\mathbf{P}(t)$ instead of $\mathbf{Q}$, and completely described by the constants of the framework in Section 7.2. Specifically, (7.17) through (7.22) is new.

Denote $\mathbf{Q} = \mathbf{P}^{-1}(t)$. Then, it can be shown that

$$\dot{\mathbf{Q}} = -\beta \mathbf{Q} + \frac{\boldsymbol{\phi}\boldsymbol{\phi}^T}{m^2}, \quad \mathbf{Q}(0) = \mathbf{Q}^T(0) = \mathbf{Q}_0 = \mathbf{P}_0^{-1} \tag{7.10}$$

which gives

$$\mathbf{Q}(t) = e^{-\beta t}\mathbf{Q}_0 + \int_0^t e^{-\beta(t-\tau)} \frac{\boldsymbol{\phi}(\tau)\boldsymbol{\phi}(\tau)^T}{m^2(\tau)} d\tau. \tag{7.11}$$

Using the PE conditions stated in Definition 2.3 for $\boldsymbol{\phi}$, and $m \in \mathcal{L}_\infty$, we have for $t \geq T_p$,

$$\begin{aligned}
\mathbf{Q}(t) &\geq \int_0^t e^{-\beta(t-\tau)} \frac{\boldsymbol{\phi}(\tau)\boldsymbol{\phi}(\tau)^T}{m^2(\tau)} d\tau \\
&= \int_{t-T_p}^t e^{-\beta(t-\tau)} \frac{\boldsymbol{\phi}(\tau)\boldsymbol{\phi}(\tau)^T}{m^2(\tau)} d\tau \\
&\quad + \int_0^{t-T_p} e^{-\beta(t-\tau)} \frac{\boldsymbol{\phi}(\tau)\boldsymbol{\phi}(\tau)^T}{m^2(\tau)} d\tau \qquad (7.12) \\
&\geq e^{-\beta T_p} \frac{\alpha_0 T_p}{\bar{m}^2} \mathbf{I}. \qquad (7.13)
\end{aligned}$$

For $t \leq T_p$, we have

$$\mathbf{Q}(t) \geq e^{-\beta T_p}\mathbf{Q}_0 \geq \lambda_{\min}(\mathbf{Q}_0)e^{-\beta T_p}\mathbf{I}. \tag{7.14}$$

Then, combining (7.13)-(7.14), the lower bound is given by

$$\mathbf{Q}(t) \geq \eta_1 \mathbf{I}, \quad \forall t \geq 0 \tag{7.15}$$

$$\eta_1 \triangleq \min\left\{\frac{\alpha_0 T_p}{\bar{m}^2}, \lambda_{\min}(\mathbf{Q}_0)\right\} e^{-\beta T_p}. \tag{7.16}$$

Next, an upper bound on $\mathbf{Q}(t)$ is sought. First, consider

$$\begin{aligned}\frac{\boldsymbol{\phi}\boldsymbol{\phi}^T}{m^2} &\leq \frac{\lambda_{\max}\left(\boldsymbol{\phi}\boldsymbol{\phi}^T\right)}{1+\alpha\boldsymbol{\phi}^T\boldsymbol{\phi}}\mathbf{I} \\ &= \frac{\boldsymbol{\phi}^T\boldsymbol{\phi}}{1+\alpha\boldsymbol{\phi}^T\boldsymbol{\phi}}\mathbf{I} \\ &\leq \frac{1}{\alpha}\mathbf{I},\end{aligned} \tag{7.17}$$

where $\lambda_{\max}\left(\boldsymbol{\phi}\boldsymbol{\phi}^T\right) = \boldsymbol{\phi}^T\boldsymbol{\phi}$ because $\boldsymbol{\phi}\boldsymbol{\phi}^T$ is a rank one matrix with an eigenvector given by $\boldsymbol{\phi}$, and the single eigenvalue follows. Combining (7.11) and (7.17) gives

$$\begin{aligned}\mathbf{Q}(t) &\leq \mathbf{Q}_0 + \int_0^t e^{-\beta(t-\tau)}\frac{1}{\alpha}\mathbf{I}d\tau \\ &\leq \lambda_{\max}(\mathbf{Q}_0)\mathbf{I} + \frac{1}{\alpha\beta}\mathbf{I} \\ &= \eta_2\mathbf{I}\end{aligned} \tag{7.18}$$

where $\eta_2 \triangleq \lambda_{\max}(\mathbf{Q}_0) + \frac{1}{\alpha\beta}$.

Combining (7.15) and (7.18), gives

$$\eta_1\mathbf{I} \leq \mathbf{Q}(t) \leq \eta_2\mathbf{I} \tag{7.19}$$

$$\Updownarrow$$

$$\gamma_1\mathbf{I} \leq \mathbf{P}(t) \leq \gamma_2\mathbf{I} \tag{7.20}$$

where

$$\gamma_1 = \eta_2^{-1} = \left(\lambda_{\min}(\mathbf{P}_0)^{-1} + (\alpha\beta)^{-1}\right)^{-1} \tag{7.21}$$

$$\gamma_2 = \eta_1^{-1} = \max\left\{\frac{\bar{m}^2}{\alpha_0 T_p}, \lambda_{\max}(\mathbf{P}_0)\right\} e^{\beta T_p} \tag{7.22}$$

which concludes the proof. ■

In the following, the bounds on $\mathbf{P}(t)$ derived in Lemma 7.1 are used to prove exponential convergence of the Lyapunov-like function

$$V = \frac{\widetilde{\boldsymbol{\theta}}^T \mathbf{Q} \widetilde{\boldsymbol{\theta}}}{2}. \tag{7.23}$$

Please recall that $\widetilde{\boldsymbol{\theta}} \triangleq \widehat{\boldsymbol{\theta}} - \boldsymbol{\theta}$ and $\mathbf{Q} = \mathbf{P}^{-1}(t)$.

Lemma 7.2 (Exponential convergence)**.** *If $m, \boldsymbol{\phi} \in \mathcal{L}_\infty$, $\boldsymbol{\phi}$ is PE, and $\boldsymbol{\theta}$ is constant, then the least squares estimator given by (7.5)-(7.6) guarantees that V from (7.23) decreases according to*

$$V(t + T_p) \leq \gamma V(t), \quad \forall t \geq 0 \tag{7.24}$$

with $0 < \gamma < 1$, where

$$\gamma = \frac{1 - \mu}{1 + \beta T_p} \tag{7.25}$$

$$\mu = \frac{\alpha_0 T_p \gamma_1}{2\bar{m}^2 + \bar{\boldsymbol{\phi}}^4 T_p^2 \gamma_2^2} \tag{7.26}$$

and $\bar{\boldsymbol{\phi}} = \sup_t |\boldsymbol{\phi}|$.

Proof. In [84, Sec. 4.8.3], the case of constant $\mathbf{Q}$ was solved to find (7.24) with a different expression for γ. Here, the results are generalized to a time-varying $\mathbf{Q}$ following a similar approach.

From the system description (7.1)-(7.4), the following relationships can be found

$$\varepsilon = \frac{w - \widehat{w}}{m^2} = \frac{\boldsymbol{\theta}^T \boldsymbol{\phi} - \widehat{\boldsymbol{\theta}}^T \boldsymbol{\phi}}{m^2} = -\frac{\widetilde{\boldsymbol{\theta}}^T \boldsymbol{\phi}}{m^2} \tag{7.27}$$

such that

$$\varepsilon^2 m^2 = \frac{1}{m^2} \left(\widetilde{\boldsymbol{\theta}}^T \boldsymbol{\phi} \right)^2. \tag{7.28}$$

Using V from (7.23) it can be shown that for a time-varying $\mathbf{Q}$ [84, p. 199],

$$\dot{V} = -\frac{\varepsilon^2 m^2}{2} - \frac{\beta}{2} \widetilde{\boldsymbol{\theta}}^T \mathbf{Q} \widetilde{\boldsymbol{\theta}}. \tag{7.29}$$

Now, inserting for (7.23) and (7.28) into (7.29) gives

$$\dot{V} = -\frac{1}{2m^2} \left(\widetilde{\boldsymbol{\theta}}^T \boldsymbol{\phi} \right)^2 - \beta V. \tag{7.30}$$

Now, we have

$$V(t+T) = V(t) - \int_t^{t+T} \left[\frac{(\widetilde{\boldsymbol{\theta}}(\tau)^T \boldsymbol{\phi}(\tau))^2}{2m^2(\tau)} + \beta V(\tau) \right] d\tau. \tag{7.31}$$

Following the same procedure as for the constant $\mathbf{Q}$ case [84, Sec. 4.8.3], but replacing the constant $\mathbf{Q}$ by the bounds of Lemma 7.1 as appropriate, we have that the first term of the integral with $T = T_p$ is bounded by

$$\begin{aligned} \int_t^{t+T_p} \frac{(\widetilde{\boldsymbol{\theta}}(\tau)^T \boldsymbol{\phi}(\tau))^2}{2m^2(\tau)} d\tau &\geq \frac{\alpha_0 T_p \gamma_1}{2\bar{m}^2 + \bar{\boldsymbol{\phi}}^4 T_p^2 \gamma_2^2} V(t) \\ &\triangleq \mu V(t). \end{aligned} \tag{7.32}$$

Since $V(t)$ is a non-increasing function, as seen from (7.29) with $\mathbf{Q}$ positive definite, the second term of the integral (7.31) is bounded by

$$\int_t^{t+T} \beta V(\tau) d\tau \geq \beta T V(t+T). \tag{7.33}$$

Inserting (7.32) and (7.33) with $T = T_p$ into (7.31), we find

$$V(t+T_p) \leq V(t) - \mu V(t) - \beta T_p V(t+T_p) \tag{7.34}$$

$$V(t+T_p) \leq \frac{1-\mu}{1+\beta T_p} V(t) \tag{7.35}$$

$$= \gamma V(t) \tag{7.36}$$

which concludes the proof. Since $\mu, \beta, T_p > 0$ and $V(t) \geq 0$, it follows that $0 < \gamma < 1$. ■

7.4 Convergence for Constant Parameters

In this section, the exponential convergence rate in the case of constant parameters is established. Furthermore, a time interval can then be found such that the parameter error is reduced to any fraction of the initial error.

Since $\mathbf{Q} > 0$ and V decreases exponentially by Lemma 7.1–7.2, it follows that the parameter estimation error $\widetilde{\boldsymbol{\theta}}$ also decreases exponentially, as will be properly established in the following result.

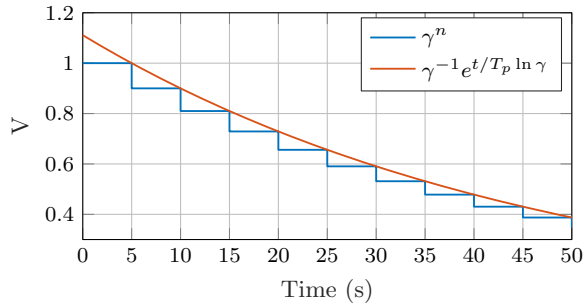

Figure 7.1: Upper-bound of V by an exponential function.

Theorem 7.1 (Convergence rate for constant parameters)**.** *Let $m, \boldsymbol{\phi} \in \mathcal{L}_\infty$, $\boldsymbol{\phi}$ be PE, and $\boldsymbol{\theta}$ constant. Then, the least squares estimator guarantees*

$$\left|\widetilde{\boldsymbol{\theta}}(t)\right| \leq ae^{-\lambda(t-t_0)}\left|\widetilde{\boldsymbol{\theta}}(t_0)\right|, \quad \forall t \geq t_0 \tag{7.37}$$

for any $t_0 \geq 0$, where the constants $a > 1, \lambda > 0$ are given by

$$a = a_1 \triangleq \sqrt{\frac{\gamma_2}{\gamma\gamma_1}}, \quad \lambda = -\frac{\ln \gamma}{2T_p}. \tag{7.38}$$

Furthermore, if $t_0 = 0$, or a covariance reset is performed at time t_0, a tighter bound is given by

$$a = a_0 \triangleq \sqrt{\frac{\gamma_2}{\gamma\lambda_{\min}(\mathbf{P}_0)}}. \tag{7.39}$$

Proof. By recursively applying (7.24) it is clear that

$$V(t+t_0) \leq V(nT_p + t_0) \leq \gamma^n V(t_0), \quad \forall t \geq nT_p, \;\; n = 0, 1, \ldots \tag{7.40}$$

for any $t_0 \geq 0$. Now, it can be shown that the discrete γ^n can be upper bounded by the continuous expression

$$\gamma^n \leq \gamma^{-1}e^{t/T_p \cdot \ln \gamma}, \tag{7.41}$$

as seen in Fig. 7.1. The discrete and continuous expression intersect at the points $t = (n+1)T_p, \forall n \in \mathbb{N}$. Thus,

$$V(t+t_0) \leq \gamma^{-1}e^{t/T_p \cdot \ln \gamma} V(t_0). \tag{7.42}$$

Furthermore, using Lemma 7.1, consider

$$V = \frac{\widetilde{\boldsymbol{\theta}}^T \mathbf{Q} \widetilde{\boldsymbol{\theta}}}{2} \geq \tfrac{1}{2}\eta_1 \widetilde{\boldsymbol{\theta}}^T \widetilde{\boldsymbol{\theta}} = \tfrac{1}{2}\eta_1 \left|\widetilde{\boldsymbol{\theta}}\right|^2. \tag{7.43}$$

Then, isolating $|\widetilde{\boldsymbol{\theta}}|$ and using (7.42) gives

$$\left|\widetilde{\boldsymbol{\theta}}(t'+t_0)\right| \leq \sqrt{2\eta_1^{-1}V(t'+t_0)} \tag{7.44}$$

$$\leq \sqrt{2\gamma_2\gamma^{-1}e^{t'/T_p\cdot\ln\gamma}V(t_0)} \tag{7.45}$$

$$\leq \sqrt{2\gamma_2\gamma^{-1}e^{t'/T_p\cdot\ln\gamma}\tfrac{1}{2}\widetilde{\boldsymbol{\theta}}(t_0)^T\eta_2\widetilde{\boldsymbol{\theta}}(t_0)} \tag{7.46}$$

$$= \sqrt{\gamma_2\gamma^{-1}\gamma_1^{-1}}e^{t'/(2T_p)\cdot\ln\gamma}\left|\widetilde{\boldsymbol{\theta}}(t_0)\right| \tag{7.47}$$

$$= a_1e^{-\lambda t'}\left|\widetilde{\boldsymbol{\theta}}(t_0)\right|, \tag{7.48}$$

where a_1, λ is given by (7.38). A change of coordinates by $t = t' + t_0$ gives (7.37). If $t_0 = 0$, or $\mathbf{P}(t_0^+) = \mathbf{P}_0$ then η_2 in (7.46) can be replaced by $\lambda_{\max}(\mathbf{Q}_0)$ and the tighter bound of a_0 in (7.39) follows. Since $0 < \gamma < 1$, we have $\ln\gamma < 0$ and in turn $\lambda > 0$. Furthermore, since $\gamma_1 \leq \gamma_2, \gamma < 1$ then $a > 1$. ■

Using the previous theorem, a time interval T can then be found such that the parameter error is guaranteed to be reduced to some fraction q of the initial error.

Corollary 7.1 (Time interval for constant parameters)**.** *Given that the assumptions of Theorem 7.1 are satisfied. Then, for any $0 < q < 1$, the recursive least squares estimator guarantees that within the time interval*

$$T = \frac{1}{\lambda}\ln\frac{a}{q} \tag{7.49}$$

the parameter error has been reduced to the fraction q, that is

$$\left|\widetilde{\boldsymbol{\theta}}(T+t_0)\right| \leq q\left|\widetilde{\boldsymbol{\theta}}(t_0)\right|. \tag{7.50}$$

Proof. Let $T = t - t_0$, and rewrite (7.37) as

$$\left|\widetilde{\boldsymbol{\theta}}(T+t_0)\right| \leq ae^{-\lambda T}\left|\widetilde{\boldsymbol{\theta}}(t_0)\right|, \quad \forall\, T \geq 0. \tag{7.51}$$

Note that, since $a > q$ and $\lambda > 0$, we have $T > 0$ using (7.49), thus, the condition $T \geq 0$ in (7.51) is automatically satisfied. Now, inserting for T from (7.49) gives

$$\left|\widetilde{\boldsymbol{\theta}}(T+t_0)\right| \leq ae^{-\lambda\frac{1}{\lambda}\ln\frac{a}{q}}\left|\widetilde{\boldsymbol{\theta}}(t_0)\right| \tag{7.52}$$

$$\leq a\tfrac{q}{a}\left|\widetilde{\boldsymbol{\theta}}(t_0)\right| \tag{7.53}$$

$$\leq q\left|\widetilde{\boldsymbol{\theta}}(t_0)\right|. \tag{7.54}$$

which confirms (7.50). ■

As long as the PE parameters are known, specifically α_0, T_p from Definition 2.3, then it is straightforward to find the time interval T using (7.38) and (7.49).

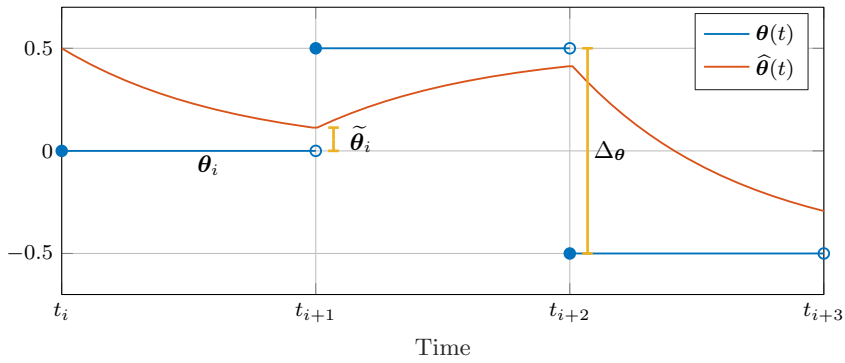

Figure 7.2: Notation for piecewise constant parameters.

7.5 Convergence for Time-Varying Parameters

The exponential convergence of a constant parameter vector at an arbitrary initial time was established in Theorem 7.1. In the viscoelastic identification in AFM [149], the parameter vector is instead piecewise constant at regular intervals $\bar{T}$. Convergence properties of the parameter estimates in this case, as well as insights for determining the interval, is desired and established in the following.

The parameter vector can now be described by

$$\boldsymbol{\theta}(t) = \boldsymbol{\theta}_i, \quad \forall \{t, i\} \, : \, t \in [t_i, t_{i+1}) \, , i \in \mathbb{N}, t_i = i\bar{T} \tag{7.55}$$

vectors $\boldsymbol{\theta}_i$. The change between successive values of $\boldsymbol{\theta}_i$ is assumed to be bounded by some constant $\Delta_{\boldsymbol{\theta}}$,

$$|\boldsymbol{\theta}_i - \boldsymbol{\theta}_{i-1}| \leq \Delta_{\boldsymbol{\theta}}, \quad \forall i. \tag{7.56}$$

Furthermore, the estimation error for $\boldsymbol{\theta}_i$ is defined by

$$\widetilde{\boldsymbol{\theta}}_i \triangleq \widehat{\boldsymbol{\theta}}(t_i + \bar{T}) - \boldsymbol{\theta}_i \tag{7.57}$$

which is motivated by $\widehat{\boldsymbol{\theta}}(t_i + \bar{T})$ being the last value estimated for $\boldsymbol{\theta}(t) = \boldsymbol{\theta}_i$. An example illustrating the notation used in this section is presented for a scalar case in Fig. 7.2.

Theorem 7.2 (Convergence rate for piecewise constant parameters)**.** *Let $m, \boldsymbol{\phi} \in \mathcal{L}_\infty$, $\boldsymbol{\phi}$ be PE, and the parameter vector $\boldsymbol{\theta}(t)$ be described by (7.55) and satisfy (7.56). Then, the least squares estimator guarantees*

$$\left|\widetilde{\boldsymbol{\theta}}_i\right| \leq \left(ae^{-\lambda\bar{T}}\right)^{i+1} \left|\widetilde{\boldsymbol{\theta}}(0)\right| + \frac{\left(ae^{-\lambda\bar{T}}\right)^{i} - 1}{ae^{-\lambda\bar{T}} - 1} ae^{-\lambda\bar{T}} \Delta_{\boldsymbol{\theta}}, \ \forall i \in \mathbb{N}. \tag{7.58}$$

Furthermore, if $ae^{-\lambda\bar{T}} < 1$*, then, for large* i*,*

$$\left|\widetilde{\boldsymbol{\theta}}_i\right| \leq r\Delta_{\boldsymbol{\theta}} \tag{7.59}$$

where

$$r = \frac{ae^{-\lambda\bar{T}}}{1 - ae^{-\lambda\bar{T}}}. \tag{7.60}$$

Proof. Using (7.37) in the intervals for which $\boldsymbol{\theta}(t)$ is constant,

$$\left|\widetilde{\boldsymbol{\theta}}(t_i + \bar{T})\right| \leq ae^{-\lambda\bar{T}} \left|\widetilde{\boldsymbol{\theta}}(t_i)\right|, \quad \forall i \tag{7.61}$$

which can be applied recursively as in the following. For ease of notation let $\widehat{\boldsymbol{\theta}}_i \triangleq \widehat{\boldsymbol{\theta}}(t_i)$,

$$\begin{aligned}
\left|\widetilde{\boldsymbol{\theta}}_i\right| &= \left|\widehat{\boldsymbol{\theta}}_{i+1} - \boldsymbol{\theta}_i\right| \\
&\leq ae^{-\lambda\bar{T}} \left|\widehat{\boldsymbol{\theta}}_i - \boldsymbol{\theta}_i\right|, \\
&= ae^{-\lambda\bar{T}} \left|\widehat{\boldsymbol{\theta}}_i - \boldsymbol{\theta}_{i-1} + \boldsymbol{\theta}_{i-1} - \boldsymbol{\theta}_i\right| \\
&\leq ae^{-\lambda\bar{T}} \left|\left|\widehat{\boldsymbol{\theta}}_i - \boldsymbol{\theta}_{i-1}\right| + |\Delta_{\boldsymbol{\theta}}|\right| \\
&\leq ae^{-\lambda\bar{T}} \left|ae^{-\lambda\bar{T}} \left|\widehat{\boldsymbol{\theta}}_{i-1} - \boldsymbol{\theta}_{i-1}\right| + \Delta_{\boldsymbol{\theta}}\right| \\
&\leq ae^{-\lambda\bar{T}} \left|ae^{-\lambda\bar{T}} \left(\left|\widehat{\boldsymbol{\theta}}_{i-1} - \boldsymbol{\theta}_{i-2}\right| + \Delta\boldsymbol{\theta}\right) + \Delta\boldsymbol{\theta}\right| \\
&= ae^{-\lambda\bar{T}} \left|ae^{-\lambda\bar{T}} \left|\widehat{\boldsymbol{\theta}}_{i-1} - \boldsymbol{\theta}_{i-2}\right| + \left(1 + ae^{-\lambda\bar{T}}\right) \Delta_{\boldsymbol{\theta}}\right| \\
&= a^2 e^{-2\lambda\bar{T}} \left|\widetilde{\boldsymbol{\theta}}_{i-2}\right| + \left(ae^{-\lambda\bar{T}} + a^2 e^{-2\lambda\bar{T}}\right) \Delta_{\boldsymbol{\theta}}
\end{aligned} \tag{7.62}$$

Recursively applying this n times until the initial condition $\left|\widehat{\boldsymbol{\theta}}_0 - \boldsymbol{\theta}_0\right| = \left|\widetilde{\boldsymbol{\theta}}(0)\right|$ appears and using the sum formula for the geometric series, gives

$$\left|\widetilde{\boldsymbol{\theta}}_i\right| \leq a^{n+1} e^{-(n+1)\lambda\bar{T}} \left|\widetilde{\boldsymbol{\theta}}(0)\right| + \frac{a^n e^{-\lambda n T} - 1}{ae^{-\lambda\bar{T}} - 1} ae^{-\lambda\bar{T}} \Delta_{\boldsymbol{\theta}}, \tag{7.63}$$

which confirms (7.58). Furthermore, if $ae^{-\lambda\bar{T}} < 1$, and by letting $n \to \infty$ such that the initial condition vanishes,

$$\left|\widetilde{\boldsymbol{\theta}}_n\right| \leq e^{-\infty} \left|\widehat{\boldsymbol{\theta}}(t_0) - \boldsymbol{\theta}_0\right| + \frac{ae^{-\lambda\bar{T}}}{1 - ae^{-\lambda\bar{T}}} \Delta_{\boldsymbol{\theta}} \tag{7.64}$$

$$= \frac{ae^{-\lambda\bar{T}}}{1 - ae^{-\lambda\bar{T}}} \Delta_{\boldsymbol{\theta}} \tag{7.65}$$

$$\triangleq r\Delta_{\boldsymbol{\theta}} \tag{7.66}$$

where $r = ae^{-\lambda\bar{T}}/(1 - ae^{-\lambda\bar{T}})$. ■

Notably, for a sufficiently large interval $\bar{T}$, the initial condition vanishes to zero after a sufficiently long time. Additionally, the estimation error reduces toward zero as $\bar{T}$ is increased.

The following converse result is particularly useful for implementation when the time interval $\bar{T}$ can be set by the operator.

Corollary 7.2 (Time interval for piecewise constant parameters)**.** *Given that the assumptions of Theorem 7.2 are satisfied. Furthermore, for any $r > 0$, let the time interval between subsequent values of $\boldsymbol{\theta}_i$ be given by*

$$\bar{T} = \lambda^{-1} \ln \frac{a\,(r+1)}{r}. \tag{7.67}$$

Then, the recursive least squares estimator guarantees that, for large i,

$$\left|\widetilde{\boldsymbol{\theta}}_i\right| \leq r\Delta_{\boldsymbol{\theta}}. \tag{7.68}$$

Proof. It can be shown that $\bar{T}$ given by (7.67) automatically satisfies $ae^{-\lambda\bar{T}} = r/(r+1) < 1$, such that (7.59) can be used. Then, (7.67) follows immediately from solving (7.60) for $\bar{T}$. ■

Thus, if $\bar{T}$ can be controlled, the estimate for each $\boldsymbol{\theta}_i$ can be guaranteed to stay within any given fraction r of the maximum parameter step size.

Remark 7.1. Note that, by performing a covariance reset between each change of parameters, that is $\mathbf{P}(n\bar{T}^+) = \mathbf{P}_0$, $n \in \mathbb{N}$, then, the less conservative version of $a = a_0$ from (7.39) can be used in (7.67).

7.6 Case Study: Viscoelastic Identification in AFM

7.6.1 Problem Description

The primary motivation for developing the theory in the previous sections was for use in identification of viscoelastic sample properties in AFM operating in DIVE mode, as detailed in Chapter 6. The sample properties are modeled as laterally spaced spring-damper elements to be identified. The sample is tapped into by the AFM tip at incrementing spatial coordinates, see Fig. 7.3, covering the entire sample grid by the end of the scan. Each tap is being performed at a constant lateral position for some chosen interval $\bar{T}$. The problem reduces to estimating

a time-varying, piecewise constant single pair of spring constant and damping coefficient.

In the following, the system dynamics are presented. The PE conditions for the system are developed, and following the theory developed in Sections 7.3 to 7.5, the choice of update law parameters for the least squares estimator is discussed. Furthermore, the interval $\bar{T}$ sufficient to guarantee convergence of the parameters are presented as a function of the update law parameters.

7.6.2 System

Following Chapter 6, the system can be described by

$$Ms^2Z + CsD + KD = (cs + k)\,\delta, \tag{7.69}$$

where M, C, K are the effective mass, damping coefficient and spring constant of the cantilever, respectively, and c, k are the unknown, piecewise constant parameters to be estimated. Furthermore,

$$Z = U_z + D, \quad \delta = h - Z \tag{7.70}$$

where Z is the vertical position of the cantilever tip, U_z is the vertical control input, D is the deflection of the cantilever, δ is the indentation of the tip into the sample, and h is the topography height at the current lateral position of the cantilever tip (X, Y). The symbols are illustrated in Fig. 7.3. Additionally, there is a linear time-invariant (LTI) transformation from U_z to δ,

$$\delta(s) = -\frac{Cs + K}{Ms^2 + (C + c)\,s + (K + k)} U_z(s) \tag{7.71}$$

The parametric system (7.1) can now be set up as follows,

$$\boldsymbol{\theta} = \begin{bmatrix} c & k \end{bmatrix}^T \tag{7.72}$$

$$\boldsymbol{\phi} = \begin{bmatrix} s\delta & \delta \end{bmatrix}^T / \Lambda(s) \tag{7.73}$$

$$w = \left(Ms^2Z + CsD + KD\right) / \Lambda(s) \tag{7.74}$$

$$1/\Lambda(s) = 1/\left(\omega_c^{-1}s + 1\right)^2 \tag{7.75}$$

where $1/\Lambda(s)$ is a second-order low-pass filter with cut-off frequency ω_c introduced to make $w, \boldsymbol{\phi}$ proper. Furthermore, U_z is a feedforward signal providing excitation to the system according to

$$U_z(t) = A' \sin(\omega_0 t) + U_0, \tag{7.76}$$

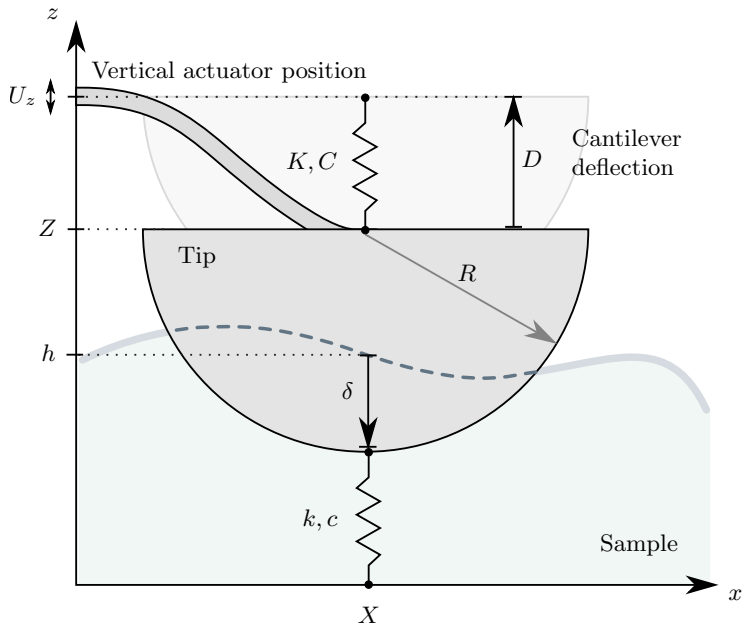

Figure 7.3: Indentation of the cantilever tip into the sample. The tip size is exaggerated for illustration purposes.

for some constants U_0 and $A', \omega_0 > 0$. For simplicity, in the following analysis it will be assumed that the contribution of U_0 to the PE conditions is negligible, and thus we use $U_0 = 0$.

Remark 7.2. The general case with a constant offset U_0 is properly accounted for in the experimental results presented in Chapter 8.

Using (7.71), (7.73), (7.75) it is seen that $\frac{\phi}{U_z}(s)$ is LTI and strictly proper. Thus, by using the excitation signal (7.76), there exist some constants A, φ such that

$$\delta/\Lambda = A \sin(\omega_0 t + \varphi) \tag{7.77}$$
$$s\delta/\Lambda = A\omega_0 \cos(\omega_0 t + \varphi) \tag{7.78}$$

where $A = \left|\frac{\phi_2}{U_z}(j\omega_0)\right| A'$ and $\varphi = \angle\frac{\phi_2}{U_z}(j\omega_0)$. Thus,

$$\boldsymbol{\phi} = \begin{bmatrix} A\omega_0 \cos(\omega_0 t + \varphi) & A \sin(\omega_0 t + \varphi) \end{bmatrix}^T. \tag{7.79}$$

7.6.3 Persistency of Excitation

First, consider the PE expression from Definition 2.3, and define

$$\mathbf{S} \triangleq \frac{1}{T_p} \int_t^{t+T_p} \boldsymbol{\phi}\boldsymbol{\phi}^T d\tau. \tag{7.80}$$

By choosing

$$T_p = \pi\omega_0^{-1} \tag{7.81}$$

and using (7.79), it can be shown that the solution to (7.80) is given by

$$\mathbf{S} = \begin{bmatrix} \frac{1}{2}A^2\omega_0^2 & 0 \\ 0 & \frac{1}{2}A^2 \end{bmatrix}. \tag{7.82}$$

Thus, $\boldsymbol{\phi}$ is PE with level of excitation α_0 and α_1 given by

$$\alpha_0 = \tfrac{1}{2}A^2 \min\left\{\omega_0^2, 1\right\} \tag{7.83}$$

$$\alpha_1 = \tfrac{1}{2}A^2 \max\left\{\omega_0^2, 1\right\} \tag{7.84}$$

which satisfies the PE condition

$$\alpha_0\mathbf{I} \leq \mathbf{S} \leq \alpha_1\mathbf{I}. \tag{7.85}$$

7.6.4 Tuning and Convergence Rate

The RLS estimator (7.3)-(7.6) is implemented for the described system. Since $\boldsymbol{\phi}$ is PE, exponential convergence of the parameters is guaranteed. By employing the theoretical results from Sections 7.3 to 7.5, the rate of convergence will be investigated in the following. We choose

$$\alpha = 1, \quad \mathbf{P}_0 = p_0\mathbf{I}, \tag{7.86}$$

and will further investigate the choice of β and p_0 in the following. First, the following properties can be determined already, considering $\boldsymbol{\phi}$ from (7.79)

$$\bar{\phi} = A\sqrt{\omega_0^2 + 1}, \;\; \bar{m}^2 = 1 + \bar{\phi}^2, \;\; \lambda_{\min}(\mathbf{P}_0) = \lambda_{\max}(\mathbf{P}_0) = p_0. \tag{7.87}$$

Inserting these values and the constants from the PE conditions into (7.25),(7.26), (7.38), the upper bound on the exponential convergence λ and a can be found in terms of β, p_0, A, ω_0.

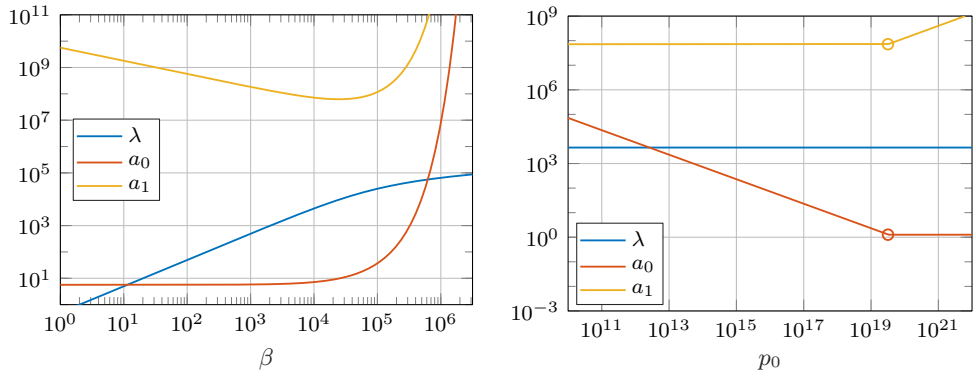

(a) β (with $p_0 = 10^{18}$) **(b)** p_0 (with $\beta = 10^4$)

Figure 7.4: The exponential convergence rate λ, and multiplier a, as a function of β, p_0 of the least squares estimator.

Remark 7.3. Note that A is implicitly a function of the system coefficients and transfer functions, including the unknown sample parameters. However, since A is measurable through demodulation of the deflection signal D, and $A \propto A'$ with A' being operator-defined, it can be controlled to any desired value.

In the following, the upper limit of the convergence rate determined by a, λ will be investigated by the parameter estimator constants β, p_0. It will be used that $A = 50\,\text{nm}$, and $\omega_0 = 2\pi f_0$ where $f_0 = 20\,\text{kHz}$, corresponding to the setup in Chapter 6.

In Fig. 7.4, the exponential convergence rate λ and multiplier a are plotted in terms of β, p_0. This gives valuable information into how the RLS estimator behaves. In the long run, the exponential rate λ will dominate the multiplier a and determine how fast the system converges. However, for a shorter run, a can in several cases become very large and thus lead to slow convergence. In both plots, a is plotted both for the conservative case a_1 (any initial time) and less conservative case a_0 (initial time zero), corresponding to (7.38),(7.39) respectively. In the former case, a_1 does not go lower than approximately 10^8, a very high number which can be attributed to the necessity of considering the largest range in the bounds of $\mathbf{P}(t)$. In the initial time zero a_0 case, the lower bound can be controlled by p_0, allowing for a decreasing range in the bounds of $\mathbf{P}(t)$ and thus a smaller value of a_0 with increasing p_0, as evident from Fig. 7.4(b). In fact, a becomes very close to unity for large values of p_0 and small values of β.

The plots in Fig. 7.4 can quickly be used to determine appropriate values of β, p_0.

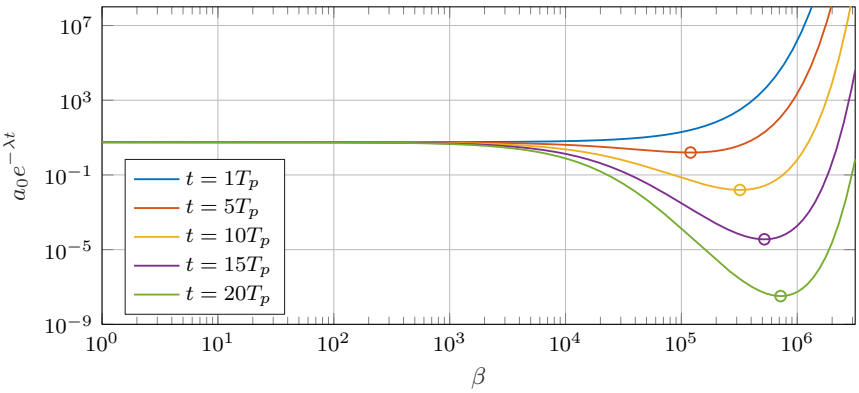

Figure 7.5: Upper limit on convergence of parameter error after $t = nT_p$, as a function of β, with $t_0 = 0, p_0 = 10^{18}$. Circles mark minimum points.

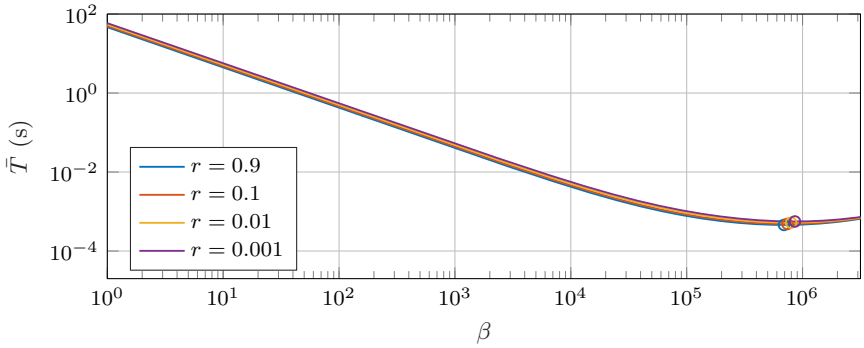

(a) $\bar{T}$

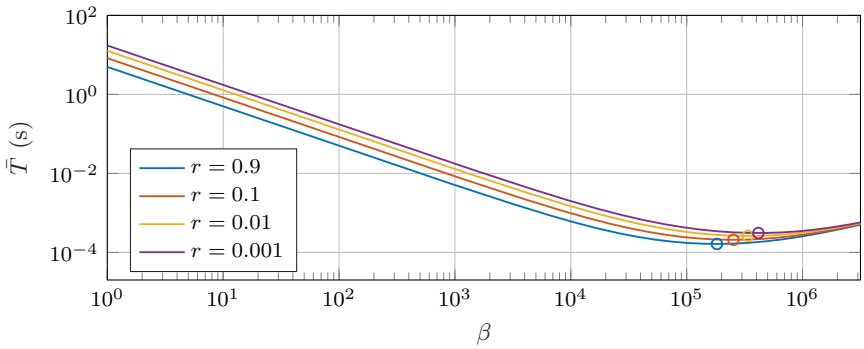

(b) $\bar{T}$ with covariance reset

Figure 7.6: Time-varying parameters: Minimum estimation interval $\bar{T}$ sufficient to guarantee parameter estimate to within $r\Delta_{\boldsymbol{\theta}}$ of real parameters, as a function of β. With covariance reset at the regular intervals, tighter bounds can be guaranteed.

In general, λ increases with increasing β, but at some point, around $\beta = 10^4$, a_0, a_1 starts to rapidly increase. On the other hand, λ does not change with p_0, but a_0 reaches its minimum at $p_0 = \bar{m}^2/(\alpha_0 T_p) \approx 3 \times 10^{19}$. Thus, $\beta = 10^4, p_0 = 3 \times 10^{19}$ are appropriate choices for this problem.

In Fig. 7.5, the upper limit of the parameter error relative to the initial condition, or $a_0 e^{-\lambda t}$ from (7.37), is plotted as a function of β. Due to the rapid increase in a_0 for large values of β, but λ increasing for large β, there exists an optimal point for β providing the fastest convergence after a given time. E.g. at $t = 10T_p$, the error has reached about 1% of the initial error with $\beta = 3 \times 10^5$.

For the piecewise constant parameter case, the time interval needed for reaching a given fraction r of the maximum parameter step size $\Delta_{\boldsymbol{\theta}}$ can be plotted as in Fig. 7.6(a). E.g., for $\beta = 10^2$, the time interval needed to reach 0.1% of $\Delta_{\boldsymbol{\theta}}$ is $\bar{T} \approx 0.55\,\mathrm{s}$. If a covariance reset is performed and coincide with the regular intervals $\bar{T}$, then the sufficient time interval is reduced due to the tighter bounds of a_0 in Theorem 7.1. Again at $\beta = 10^2, r = 0.01$, the time interval needed is now only $\bar{T} \approx 0.13\,\mathrm{s}$ as seen in Fig. 7.6(b).

7.6.5 Simulations

Simulations are performed in order to evaluate the results of Sections 7.3 to 7.5. Since the presented convergence bounds are based on an inherently conservative approach, a simulation can establish how the actual performance compares to the upper bounds. The convergence of the parameter estimates is evaluated in the case of piecewise constant parameters. Two simulations were performed, one *without* covariance reset, and another *with* covariance reset at regular intervals, that is, $\mathbf{P}(n\bar{T}^+) = \mathbf{P}_0$, $n \in \mathbb{N}$.

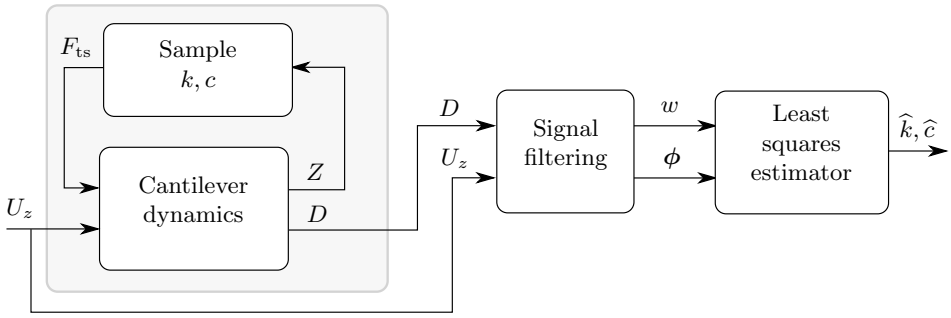

Figure 7.7: Block diagram of the simulation setup, with cantilever-sample dynamics and parameter estimator.

The simulations were setup according to Fig. 7.7. The cantilever-sample dynamics were modeled by (7.69), with physical parameters from Chapter 6. That is, $M = 1.2 \times 10^{-11}\,\text{kg}$, $C = 1.5 \times 10^{-8}\,\text{Ns/m}$, and $K = 0.19\,\text{N/m}$, corresponding to a resonance frequency of 20 kHz. The cantilever oscillations were performed at a depth of 100 nm into the sample. The unknown spring constant and damping coefficient of the sample to be estimated, were implemented as piecewise constant corresponding to the lateral placement of the cantilever, with $\Delta_{\boldsymbol{\theta}} = 0.01$. Only the vertical positioning U_z and deflection D were assumed available for measurement, corresponding to an actual AFM experiment.

A practical experiment would need to take into account noise when determining β. A very high value of β makes the estimator very sensitive to noise, since this leads to a larger value of $\mathbf{P}(t)$ in general. To be representative of an experiment, a relatively low value was chosen with $\beta = 100$. For the initial state of the covariance matrix, we chose $p_0 = 10^{10}$. From Fig. 7.6(a), and by choosing $r = 0.001$, the time interval between taps needs to be at least 0.55 s for the simulation without covariance reset. We chose $\bar{T} = 0.6\,\text{s}$ for the nearest round number, and for comparison, the same time interval was used in the simulation with covariance reset. This should guarantee $|\widetilde{\boldsymbol{\theta}}_i| \leq 0.001\Delta_{\boldsymbol{\theta}}$ by Theorem 7.2 in both cases. The resulting convergence parameters for the two setups are then given by

$$a_0 = 5.6 \times 10^4, \quad a_1 = 5.6 \times 10^8, \quad \lambda = 49.9. \tag{7.88}$$

The results of the simulation without covariance reset are shown in Fig. 7.8, and with covariance reset in Fig. 7.9. The parameter estimation of $\widehat{c}$ and $\widehat{k}$ compared to their real values, demonstrates the exponential convergence after each step-change in the parameters. Additionally, they are seen to converge within the given time interval $\bar{T}$.

In Fig. 7.8(c) the parameter error norm is plotted, and compared to the upper limit between intervals as given by Theorem 7.1. It is seen that at the end of each interval, the upper bound reaches below $r\Delta_{\boldsymbol{\theta}}$, in correspondence with Theorem 7.2. It is also seen that the real error stays below the upper bound, by a large offset. This can predominantly be attributed to the large value of a_1, which gives a very large offset at the beginning of each interval.

With covariance reset however, the upper bound is much tighter due to its lower value of a_0, as seen in Fig. 7.9(c). Note also that the convergence rates of $\widehat{c}, \widehat{k}$ are highly different. This suggests that the initial covariance matrix $\mathbf{P}_0$ should use distinct values along its diagonal, to control the initial convergence rate individually for the two parameters.

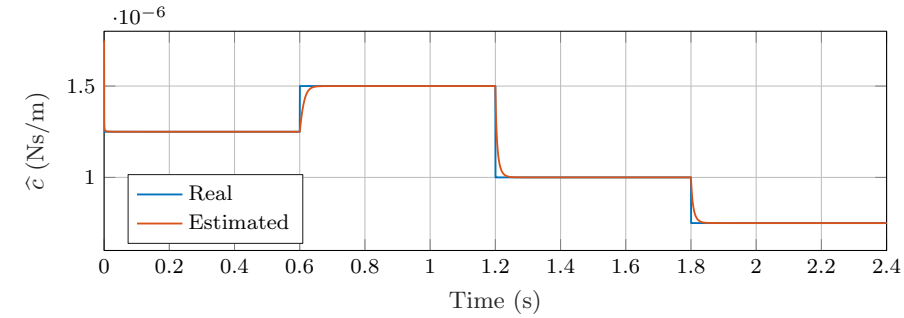

(a) $\widehat{c}$

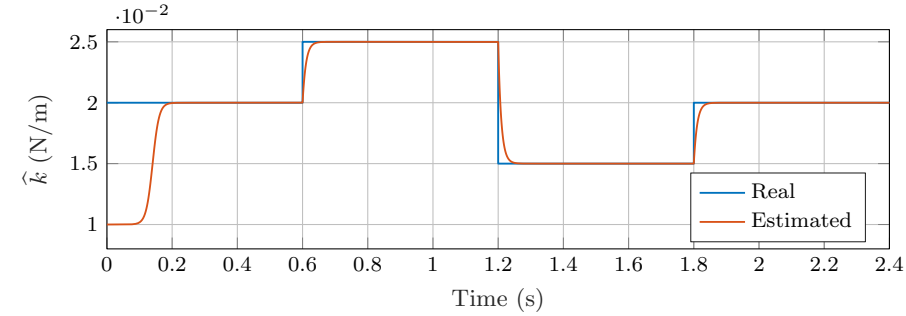

(b) $\widehat{k}$

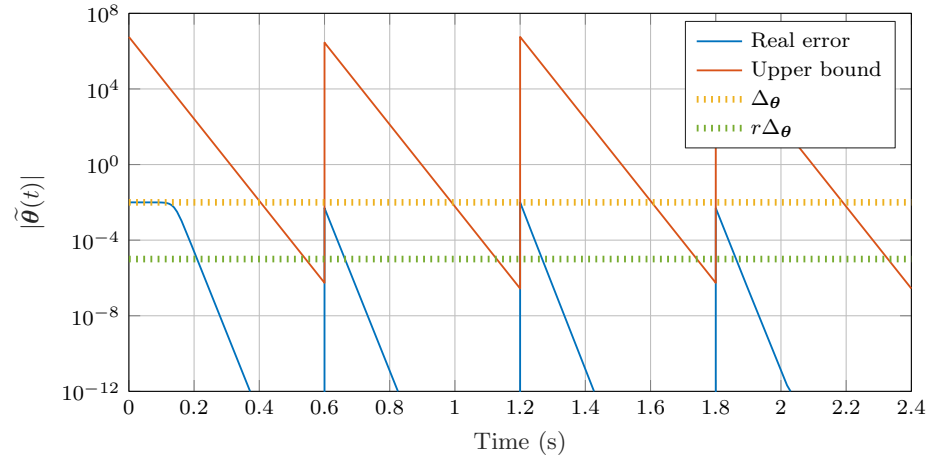

(c) Estimation error and upper bound

Figure 7.8: Simulated parameter estimation with parameters changing at regular intervals *without* covariance reset. (a)-(b) Estimated parameters. (c) After each interval, the upper bound guarantees convergence to less than $r\Delta_{\boldsymbol{\theta}}$ with $r = 0.001$.

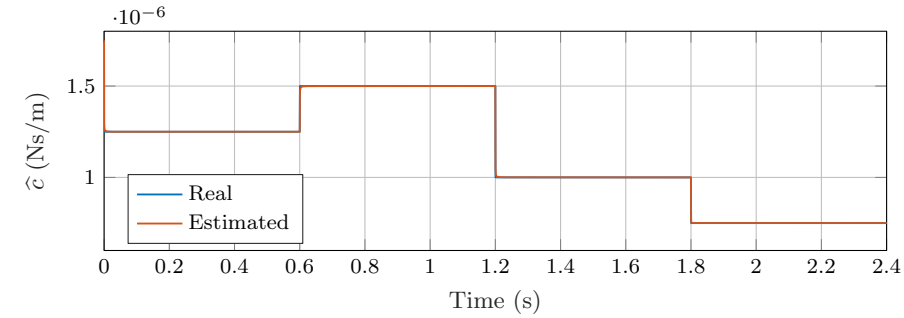

(a) $\widehat{c}$

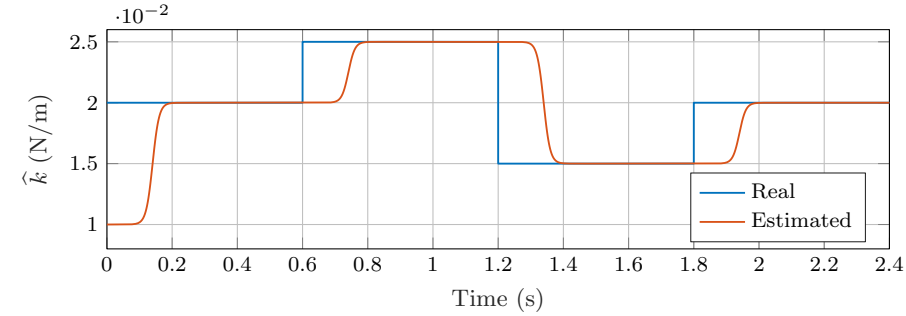

(b) $\widehat{k}$

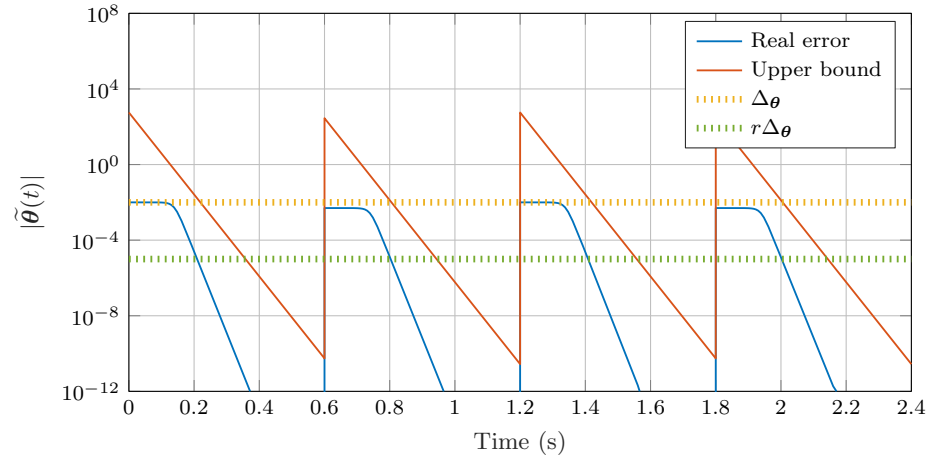

(c) Estimation error and upper bound

Figure 7.9: Simulated parameter estimation with parameters changing at regular intervals *with* covariance reset at the same intervals. (a)-(b) Estimated parameters. (c) After each interval, the upper bound guarantees convergence to less than $r\Delta_{\boldsymbol{\theta}}$ with $r = 0.001$.

7.7 Conclusions

In this chapter, the recursive least squares (RLS) estimator with forgetting factor is investigated. Upper bounds on the exponential convergence of the parameter estimation error is found – completely determined by the RLS parameters and the level of excitation of the signal vector. First, the upper bound is found in the case of constant parameters. Then, the case of piecewise constant parameter vector at regular intervals is considered. An upper bound in this case relates the initial parameter error and maximum parameter step-size, to the parameter error.

Furthermore, for the constant parameter case, a sufficient time interval is given such that the parameters are guaranteed to be reduced to any fraction of the initial error. For the piecewise constant parameters case, a sufficient time interval for the parameters to converge to any given fraction of the maximum parameter step-change is found.

Finally, the theoretical results are applied to the problem of identification of viscoelastic properties using AFM in DIVE mode. Choices of RLS parameters are discussed in terms of the convergence rate, and the minimum time interval sufficient for guaranteed convergence to some specified value is found. It is demonstrated that by performing covariance reset at regular intervals, tighter upper bounds can be found. However, tighter bounds do not necessarily mean faster convergence in practice, due to the inherently conservative nature of the Lyapunov approach taken in this chapter. Simulations corroborate the results and demonstrate the applicability of the approach.

Chapter 8

Model-Based Identification of Nanomechanical Properties: Experiments

In Chapter 6, the DIVE mode was presented, a model-based identification technique for resolving nanomechanical properties in AFM. Both the sample and cantilever are represented by dynamic models. A recursive least squares estimator is employed to identify the unknown parameters of the sample model, thus revealing its nanomechanical properties. In this chapter, the method is expanded upon and implemented experimentally. Two sample models are presented here, demonstrating the ability to swap sample models to best suit the material being studied. The method has been experimentally implemented on a commercial AFM for online estimation of elastic moduli, spring constants and damping coefficients. Additionally, the experimental results demonstrate the capability of measuring time- or space-varying parameters using the presented approach.

Publications The material in this chapter is based on [147].

8.1 Introduction

Using AFM to resolve nanomechanical properties has already opened up a new window into studying soft samples at the nano- to microscale. However, there is clearly room for improvements. In Chapter 6, the dynamic indentation viscoelastic (DIVE) mode was introduced. In DIVE mode, both the sample and cantilever are represented by separate dynamic models. By employing identification techniques

from the control literature, the parameters of the dynamic sample model can be identified from the observable signals. The observables are mapped to the sample parameters using a recursive least squares estimator.

In order to spatially resolve nanomechanical properties, DIVE mode operates by indenting into the sample at regular intervals laterally spaced across the scanning region. Between each indentation, the cantilever is raised and moved in a raster pattern to the next indentation point, until the entire sample is covered. During indentation, the cantilever tip is modulated in order to gain dynamic information from the sample.

The modeling and identification approach taken by the DIVE mode, enjoys several advantages over comparable techniques. Because the sample and cantilever dynamics are separated, the complicated relationships between the observables and the sample properties are circumvented. Instead, the observable signals are fit to the sample model in a least squares sense. Furthermore, this separation makes it easy to swap out, or expand, the sample model for one which could better match the material, as demonstrated in this chapter. Additionally, since the technique employs a recursive method, it can be implemented online and allows for observing time- or space-varying changes of the parameters.

8.1.1 Contributions

In Chapter 6, the demonstration of DIVE mode was restricted to numerical results with the sample modeled as spring-damper elements. In this chapter, several aspects of DIVE mode are expanded upon and experimental results are presented. In particular, (i) improvements are introduced to the system model, making it suitable for experiments. (ii) An additional sample model is introduced based on the Hertz contact model, allowing for online estimation of elastic moduli. (iii) A sufficient time interval during each indentation for guaranteed convergence of the sample parameters to any accuracy, developed in Chapter 7, is employed, demonstrating its practicability. (iv) In order to implement the experiments, the parameter estimator is combined with the demodulator from Chapter 4, an XYZ controller, and novel control logic implemented by a state machine. (v) Experimental results demonstrate the feasibility of the approach, using either of the two sample models, allowing for online estimation of spring constants, damping coefficients, and elastic moduli. Finally, (vi) experimental results additionally demonstrate identification of time-varying sample parameters using the presented approach.

8.1.2 Outline

The chapter is organized as follows. In Section 8.2 the cantilever and sample dynamics are modeled. The estimation procedure for the unknown sample parameters is presented in Section 8.3. Implementation details of the approach are given in Section 8.4. System identification of the cantilever model and tuning of the parameter estimator is demonstrated in Section 8.5. Experimental results are presented in Section 8.6. Finally, conclusions are drawn in Section 8.7.

8.2 System Modeling

In this section, the dynamics governing the AFM cantilever interacting with the sample are established. This is later used for developing appropriate parameter identification laws for the sample mechanical properties.

The following is based on Chapter 6. However, previously, modulation of the cantilever was generated by modulating the z-scanner. In a typical AFM setup, this scanner is severely bandwidth-limited, and unable to oscillate the cantilever near its resonance frequency. In this chapter, modifications are introduced by instead employing the piezo modulator typically used in dynamic modes of AFM. Additionally, in Chapter 6, only a spring-damper model was used to describe the sample. In this work, contact mechanics are considered, resulting in a second, nonlinear dynamic sample model.

8.2.1 System Overview

The AFM setup considered in this work is shown in Fig. 8.1, and the operating procedure for DIVE mode is illustrated in Fig. 8.2. The coordinate system in the xz-plane of the cantilever and sample is shown in Fig. 8.3. The position of the tip along the xyz-axes is denoted by (X, Y, Z). The vertical tip position Z, the cantilever deflection D, and the cantilever tip rest position Z_0 are related by

$$Z = Z_0 + D. \tag{8.1}$$

The deflection D is typically measured through a photodetector setup, and assumed available. The signal is positive along the z-direction with its origin placed at Z_0.

The interaction between the various components of the system is shown in Fig. 8.4, with corresponding inputs and outputs assumed available. The cantilever dynamics are subject to an external tip-sample interaction force F_{ts}, as well as a

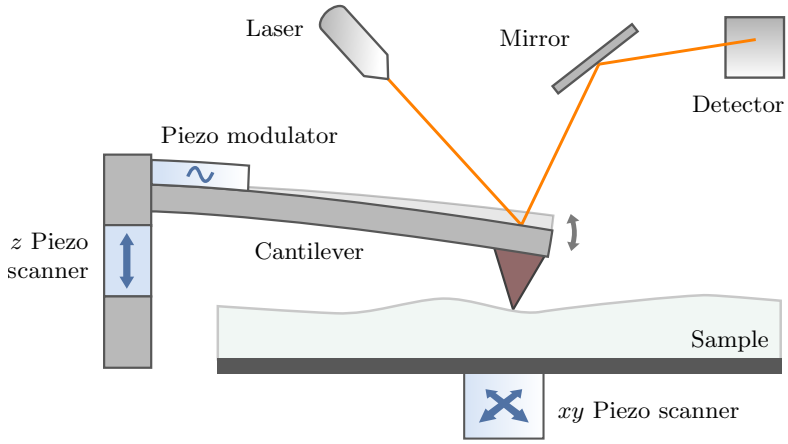

Figure 8.1: AFM dynamic mode setup considered in this chapter.

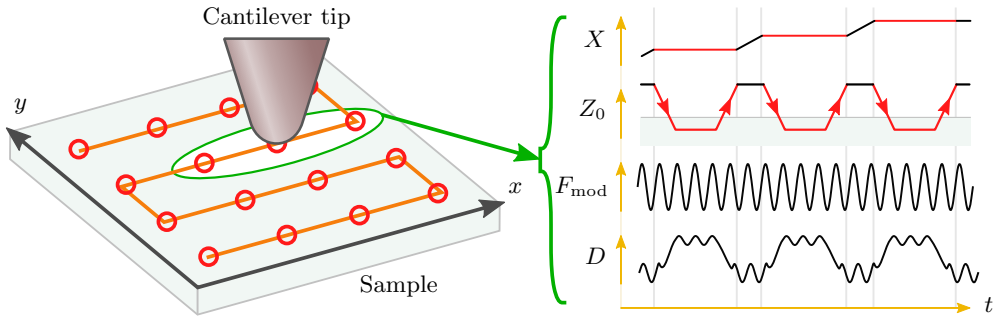

Figure 8.2: Operation of DIVE mode in AFM, for a 4×4-resolution image. The tip is indented into the sample at each red circle. The lateral movement is paused during indentation. During the entire procedure, the cantilever is oscillated using the piezo modulator, which enables identification of dynamical properties such as viscosity.

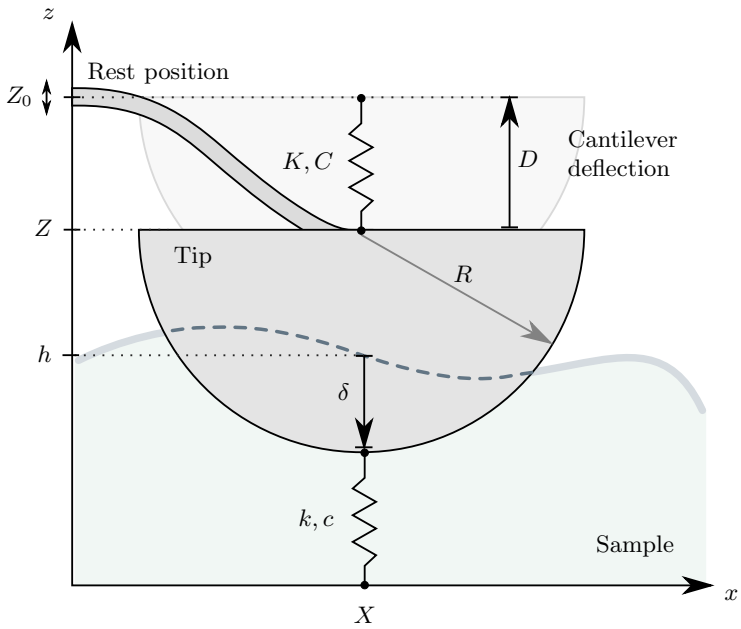

Figure 8.3: AFM cantilever interacting with sample. The tip size and cantilever deflection is exaggerated for illustration purposes.

modulating input force F_{mod}. The resulting cantilever deflection, as well as the z-actuator position, determines the tip position Z. As the tip indents the sample at depth δ, restoration and viscous forces from the sample are acting on the tip. The cantilever dynamics and contact forces are discussed in the following sections.

The xy- and z-actuators are often implemented by piezo scanners along each axis, as illustrated in Fig. 8.1. These actuators typically display vibration dynamics as well as nonlinear effects, such as creep and hysteresis [31, 42, 187]. However, these dynamics are not considered in this chapter, instead, any disturbances are assumed suppressed through feedback control. Such control schemes have been the topic of a large amount of research [40, 49, 180, 206]. The signals X, Y, Z_0 are considered measurable and controllable through actuators on each axis, by the signals U_x, U_y, U_z, respectively.

Remark 8.1. In Chapters 6 and 7, it was assumed that the cantilever rest position was controlled directly, thus, U_z was used directly in the development of the system model. In this chapter, a distinction is made between the applied actuator input U_z, and the response from the z-actuator dynamics Z_0. For practical considerations, this distinction is beneficial due to the inherent dynamics displayed by the actuator.

8.2.2 Cantilever Dynamics

The cantilever dynamics can be approximated by its first resonance mode [55], resulting in the spring-damper system

$$M\ddot{D} + KD + C\dot{D} = F_{\text{mod}} + F_{\text{ts}} \tag{8.2}$$

where M is the effective mass of the cantilever [15], K, C are the cantilever spring and damping constants respectively, F_{mod} is the modulation force, and F_{ts} is the force from the sample acting on the cantilever tip. Furthermore, the cantilever resonance frequency is denoted by ω_0.

8.2.3 Indentation Depth

The indentation depth of the tip δ can be determined during the approach phase for each indentation into the sample. The indentation is given by

$$\delta = h - Z \tag{8.3}$$

where h is the sample topography at the current tip position. As the origin of the topography is arbitrarily placed along the z-axis, any constant terms, such as

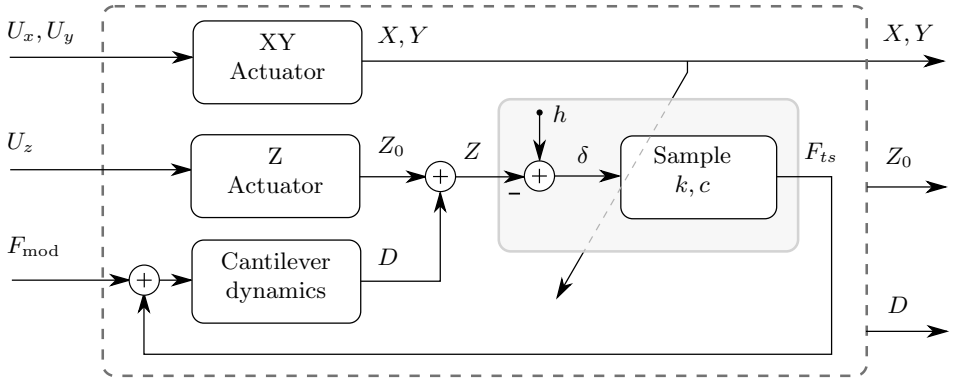

Figure 8.4: Plant dynamics and corresponding inputs and outputs. The sample properties – here k, c, h – are to be identified from the available signals.

the tip radius and height, can safely be disregarded. The topography h is found by measuring and recording the first point of contact during approach, thus δ is assumed known. Once contact is detected, the topography h at the current indentation is set and used in the relevant computations.

8.2.4 Contact Mechanics

As the cantilever approaches the sample, two different regimes determine the nature of the tip-sample interaction, as outlined in Chapter 1. During approach (non-contact), the interaction force can be described using the Lennard-Jones potential [173]. As the tip comes in contact with the sample and starts indenting it, the mechanical response of the sample due to its deformation determines the interaction. The latter interaction is of main interest in this chapter.

Traditionally, the Hertz contact model has been widely used in the AFM community to describe elasticity of soft samples [24, 141]. This approach assumes small indentations, no friction, and continuous, non-conforming surfaces. For a spherical tip with radius R indenting into an elastic half-space, the contact force as a function of indentation δ is given by

$$F_{\text{Hertz}} = \tfrac{4}{3} E^* R^{\frac{1}{2}} \delta^{\frac{3}{2}} \tag{8.4}$$

where

$$E^* = \left(\frac{1 - \nu_{\text{tip}}^2}{E_{\text{tip}}} + \frac{1 - \nu^2}{E} \right)^{-1} \tag{8.5}$$

and ν_{tip}, ν are the Poisson ratios of the tip and sample, respectively, and E_{tip}, E are the elastic moduli of the tip and sample. Since the cantilever tip is made of a stiff material, it can safely be assumed that $E_{\text{tip}} \gg E$, which simplifies (8.5) to

$$E^* = \frac{E}{1-\nu^2}. \tag{8.6}$$

In the following, two separate models are presented for modeling the sample. The first one is the linear spring-damper model considered in Chapter 6, while the second is based on the nonlinear Hertz model with an additional viscous term. Using two such models demonstrate that the presented approach can operate with various material descriptions, from a simple one which emphasizes implementation simplicity, to increasingly complex descriptions emphasizing accuracy.

8.2.5 Sample Model $\mathcal{A}$: Spring-Damper

A simplified approach to the sample interaction is achieved through modeling the sample by a spring-restoration force and a damper. This is equivalent to the Kelvin-Voigt model, considered one of the simpler models for viscoelasticity [73]. This model effectively captures viscoelastic effects such as creep, but may result in widely varying parameters due to being dependent on the frequency or time scale of the experiment. Additionally, due to the linearity of the elastic component of the model, the spring constant will change with depth, as well as the radius of the tip. The advantage of this approach is the simplicity of the equations, especially with regards to the linearity in terms of the indentation depth. The interaction force is given by

$$F_{\text{ts}}^{\mathcal{A}} = k\delta + c\dot{\delta} \tag{8.7}$$

where k is the spring constant, c is the damping coefficient, and δ is the indentation of the tip into the sample.

In the context of the Hertz contact model, the spring constant will change with the indentation depth, thus $k = k(\delta)$. If the spring constant is already known, the elastic modulus can be found offline by using (8.4), (8.6) and Hooke's law $F_{\text{Hooke}} = k\delta$, which gives

$$E = \tfrac{3}{4}k(1-\nu^2)R^{-\frac{1}{2}}\delta^{-\frac{1}{2}}. \tag{8.8}$$

8.2.6 Sample Model $\mathcal{B}$: Modified Hertz Model

An alternative implementation of the sample model is obtained by directly using the Hertz contact model (8.4),(8.6). By supplementing this approach with a linear

damping force as in the Kelvin-Voigt model, a viscoelastic model of the sample is obtained. The resulting tip-sample interaction force is given by

$$F_{\text{ts}}^{\mathcal{B}} = E'\delta^{\frac{3}{2}} + c\dot{\delta} \tag{8.9}$$

$$E = \tfrac{3}{4}R^{-\frac{1}{2}}(1-\nu^2)E' \tag{8.10}$$

where E is the elastic modulus of the sample, E' is the variable identified by the parameter estimator and proportional to the elastic modulus, R is the cantilever tip radius, and ν is the Poisson ratio of the sample – typically $\nu = 0.5$ for soft and biological samples [96]. The elastic modulus found by this approach should be invariant in terms of indentation depth, as long as the assumptions of the Hertz contact model hold.

8.3 Parameter Identification

In this section, an online estimation scheme for identification of the unknown parameters of the system, k, c, E, is established. The approach follows the identification approach presented in Chapter 6. However, the new models given in the previous section are employed.

First, the system dynamics are rewritten in a parametric form, suitable for estimation. Here, the two sample models $\mathcal{A}$ and $\mathcal{B}$ are treated separately. The two models are then applied in a generic recursive least squares estimator for identifying the unknown parameters. Finally, convergence of the parameter estimates is discussed.

8.3.1 Parametric System Model

For the spring-damper model $\mathcal{A}$, by applying the interaction force (8.7) to the cantilever model (8.2), the equations can be rearranged and rewritten in the complex s-domain as

$$Ms^2D + CsD + KD - F_{\text{mod}} = (cs + k)\,\delta. \tag{8.11}$$

Defining

$$w' \triangleq Ms^2D + CsD + KD - F_{\text{mod}} \tag{8.12}$$

the system (8.11) can be rewritten in parametric form as

$$w' = \begin{bmatrix} c \\ k \end{bmatrix}^T \begin{bmatrix} s\delta \\ \delta \end{bmatrix} \tag{8.13}$$

$$= \boldsymbol{\theta}_{\mathcal{A}}^T \boldsymbol{\phi}'_{\mathcal{A}} \tag{8.14}$$

where $\boldsymbol{\theta}_{\mathcal{A}}$ is the unknown parameter vector to be estimated and $\boldsymbol{\phi}_{\mathcal{A}}$ is the known signal vector.

By following the same procedure for the Hertz model $\mathcal{B}$, the interaction force (8.7) and cantilever model (8.2) can be written as

$$Ms^2D + CsD + KD - F_{\text{mod}} = cs\delta + E'\delta^{1.5}. \tag{8.15}$$

By using (8.12), the system can be written as

$$w' = \begin{bmatrix} c \\ E' \end{bmatrix}^T \begin{bmatrix} s\delta \\ \delta^{1.5} \end{bmatrix} \tag{8.16}$$

$$= \boldsymbol{\theta}_{\mathcal{B}}^T \boldsymbol{\phi}'_{\mathcal{B}} \tag{8.17}$$

which gives the parametric formulation of the second sample model.

8.3.2 Filtered System Equations

In order to avoid pure differentiation of the signals $w', \boldsymbol{\phi}'_i$ in (8.14), (8.17), both sides of each equation are filtered by a second-order low-pass filter such as $1/\Lambda(s) = 1/(\tau s + 1)^2$,

$$\frac{w'}{\Lambda} = \boldsymbol{\theta}_i^T \frac{\boldsymbol{\phi}'_i}{\Lambda} \tag{8.18}$$

$$w = \boldsymbol{\theta}_i^T \boldsymbol{\phi}_i \tag{8.19}$$

for $i \in \{\mathcal{A}, \mathcal{B}\}$. Since w' is of degree two, and $\boldsymbol{\phi}'_i$ is of degree one, using a second-order low-pass filter makes the transfer functions $w, \boldsymbol{\phi}_i$ proper and thus implementable.

This linear parametric form is suitable for implementation of various parameter estimation schemes, such as given in Chapter 2. The objective of the estimator is thus to find the unknown $\boldsymbol{\theta}_i$ given the known signals w and $\boldsymbol{\phi}_i$.

8.3.3 Parameter Estimator

Several estimation methods for the systems (8.14),(8.17) can be employed with similar stability and convergence properties. We have chosen the least squares estimator from Chapter 2 with forgetting factor, due to its greater ability to suppress measurement noise over many comparable techniques. Furthermore, because of the slowly varying nature of the parameters, a forgetting factor is

useful. The estimator is restated here for convenience,

$$\widehat{w} = \widehat{\boldsymbol{\theta}}^T \boldsymbol{\phi} \tag{8.20}$$

$$\varepsilon = (w - \widehat{w})/m^2 \tag{8.21}$$

$$m^2 = 1 + \alpha \boldsymbol{\phi}^T \boldsymbol{\phi} \tag{8.22}$$

$$\dot{\widehat{\boldsymbol{\theta}}} = \mathbf{P}\varepsilon\boldsymbol{\phi} \tag{8.23}$$

$$\dot{\mathbf{P}} = \beta\mathbf{P} - \mathbf{P}\frac{\boldsymbol{\phi}\boldsymbol{\phi}^T}{m^2}\mathbf{P} \tag{8.24}$$

$$\mathbf{P}(0) = \mathbf{P}_0 \tag{8.25}$$

where the parameter estimate vector $\widehat{\boldsymbol{\theta}} = \widehat{\boldsymbol{\theta}}_i$, and signal vector $\boldsymbol{\phi} = \boldsymbol{\phi}_i$ are implemented for some $i \in \{\mathcal{A}, \mathcal{B}\}$. Additionally, α is a positive constant, typically unity, $\beta > 0$ is the main tunable for the convergence speed of the estimates, and $\mathbf{P} \in \mathbb{R}^{2\times 2}$ is the covariance matrix.

8.3.4 Convergence of Parameters

The least squares estimator guarantees that the estimation error ε becomes small in some sense, given constant parameters $\boldsymbol{\theta}$. However, for the parameter vector $\widehat{\boldsymbol{\theta}}$ to converge to $\boldsymbol{\theta}$, which is of prime importance in parameter identification, the signal vector $\boldsymbol{\phi}$ needs to be persistently exciting (PE), as defined in Definition 2.3. Indeed, this is a sufficient condition for exponential convergence of $\widehat{\boldsymbol{\theta}} \to \boldsymbol{\theta}$.

For a modulating cantilever, that is, by using a sinusoidal input signal

$$F_{\text{mod}} = A' \sin(\omega_0 t) \tag{8.26}$$

for some amplitude A', the signal vector is PE as is demonstrated later. Thus, in dynamic mode AFM the parameters will convergence in exponential time.

The estimation scheme guarantees exponential convergence only for constant parameters. However, exponential convergence in the constant parameter case, guarantees some degree of tracking even for slowly-varying parameters, as discussed in Chapter 2. Thus, the estimation scheme can be used to track sample mechanical changes over time, or as a function of another signal, such as the indentation depth.

8.3.5 Estimation Time Interval for Convergence

Although the PE property guarantees exponential convergence of the parameters, even exponential convergence can be slow. In Chapter 7 the rate of convergence of

the parameters was investigated, specifically, when the parameters can be assumed to take on new constant values at regular intervals. This is the case in DIVE mode AFM, where new constant values are given from one indentation to the next.

By employing Theorem 7.1, we can establish the convergence rate of the parameter estimates, given the PE properties and tuning values for an implementation of the least squares estimator. In this chapter, we employ a covariance reset between each indentation, which allows the use of tighter bounds on the upper limit of the convergence error and thus faster guaranteed convergence time.

Remark 8.2. In Chapter 7, convergence rates and sufficient estimation times were provided both in the cases where, (i) the error was described in terms of the initial estimation error, and (ii) the error was described in terms of the maximum step-change of the parameters. In this chapter, the results for the first case (i) are used so that assumptions on the maximum step-change can be omitted.

The following theorem is a summary and reformulation of Theorem 7.1 for the specific case of covariance reset performed at the initial time t_0. The theorem provides an upper bound on the parameter error. Let the parameter estimation error be given by $\widetilde{\boldsymbol{\theta}} = \widehat{\boldsymbol{\theta}} - \boldsymbol{\theta}$.

Theorem 8.1. *Let $m, \boldsymbol{\phi} \in \mathcal{L}_\infty$, $\boldsymbol{\phi}$ be PE, and $\boldsymbol{\theta}$ constant. Then, by a covariance reset at time t_0 such that $\mathbf{P}(t_0) = \mathbf{P}_0$, the least squares algorithm guarantees*

$$\left|\widetilde{\boldsymbol{\theta}}(t)\right| \leq a_0 e^{-\lambda(t-t_0)} \left|\widetilde{\boldsymbol{\theta}}(t_0)\right|, \quad \forall t \geq t_0 \tag{8.27}$$

for any $t_0 \geq 0$, where the constants $a_0 > 1, \lambda > 0$ are given by

$$a_0 = \sqrt{\frac{\gamma_2}{\gamma \lambda_{\min}(\mathbf{P}_0)}}, \quad \lambda = -\frac{\ln \gamma}{2T_p}, \tag{8.28}$$

and where

$$\gamma = \frac{1-\mu}{1+\beta T_p} \tag{8.29}$$

$$\mu = \frac{\alpha_0 T_p \gamma_1}{2\bar{m}^2 + \bar{\phi}^4 T_p^2 \gamma_2^2} \tag{8.30}$$

$$\gamma_1 = \left(\lambda_{\min}(\mathbf{P}_0)^{-1} + (\alpha\beta)^{-1}\right)^{-1} \tag{8.31}$$

$$\gamma_2 = \max\left\{\frac{\bar{m}^2}{\alpha_0 T_p}, \lambda_{\max}(\mathbf{P}_0)\right\} e^{\beta T_p}. \tag{8.32}$$

Additionally, $\bar{m}^2 = \sup_t m^2(t)$, $\bar{\phi} = \sup_t |\boldsymbol{\phi}|$ and $\lambda_{\min}(\cdot)$, $\lambda_{\max}(\cdot)$ denote the minimum and maximum eigenvalue, respectively.

Proof. This theorem is a reformulation of Theorem 7.1. ■

A sufficient time interval T can then be found such that the parameter error is guaranteed to be reduced to some fraction q of the initial error, as shown in Corollary 7.1. The corollary is restated here.

Corollary 8.1. *Given that the assumptions of Theorem 8.1 are satisfied. Then, for any $0 < q < 1$, the recursive least squares estimator guarantees that within the time interval*

$$T = \frac{1}{\lambda} \ln \frac{a_0}{q} \tag{8.33}$$

the parameter error has been reduced to the fraction q, that is

$$\left| \widetilde{\boldsymbol{\theta}}(T + t_0) \right| \leq q \left| \widetilde{\boldsymbol{\theta}}(t_0) \right|. \tag{8.34}$$

Proof. This corollary is a reformulation of Corollary 7.1. ■

As long as the PE parameters are known, specifically α_0, T_p from Definition 2.3, then the time interval T can be found using (8.28) and (8.33).

8.4 Implementation

The control logic and parameter estimator is implemented according to the block diagram shown in Fig. 8.5. The implementation details of the various components are discussed in the following.

8.4.1 State Machine and Parameter Estimator

The state machine controls the logic of the operation. Its procedure is summarized in Fig. 8.6 and the following:

1. Lower the cantilever until indenting into the sample, and record the initial point of contact h (topography).
2. Pause the vertical movement of the cantilever when the mean deflection reaches some D_max.
3. Enable the parameter estimator. The duration of this step should be sufficient to guarantee convergence of the parameters as discussed later.
4. Raise the cantilever until it is free from the sample.
5. Move the cantilever in the lateral directions to the next indentation coordinate.

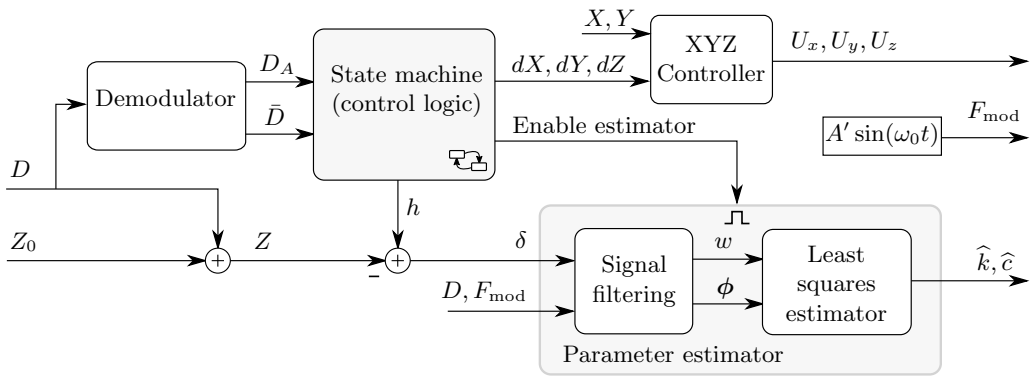

Figure 8.5: Block diagram of the control logic and parameter estimator.

The above procedure is repeated $n \times n$ times for each indentation laterally spaced across the sample, where n determines the resolution of the resolved nanomechanical properties. The parameter estimator implements (8.20)–(8.25) for either sample model $\mathcal{A}$ or $\mathcal{B}$. Between each indentation, all internal states of the parameter estimator are reset.

8.4.2 Demodulator

The cantilever deflection signal is demodulated using the Lyapunov estimator with DC-estimation from Chapter 4, which provides the amplitude, phase and mean of the signal. This demodulator was compared to state-of-the-art techniques and demonstrates a high performance with simplicity of implementation in Chapter 5.

The demodulator is exclusively used for:

- Determination of the initial point of contact with the sample during the approach phase – that is, the topography.
- Acquisition of the amplitude and phase for offline data analysis purposes.

Thus, only the state machine makes use of the demodulated signals. Contrarily, the parameter estimator rather uses the oscillating signals directly. Therefore, the performance of the demodulator does not directly influence the identified parameters.

A new notation for the demodulator is used in this chapter, in order to avoid confusion with the estimation of the sample parameters. Furthermore, it is used

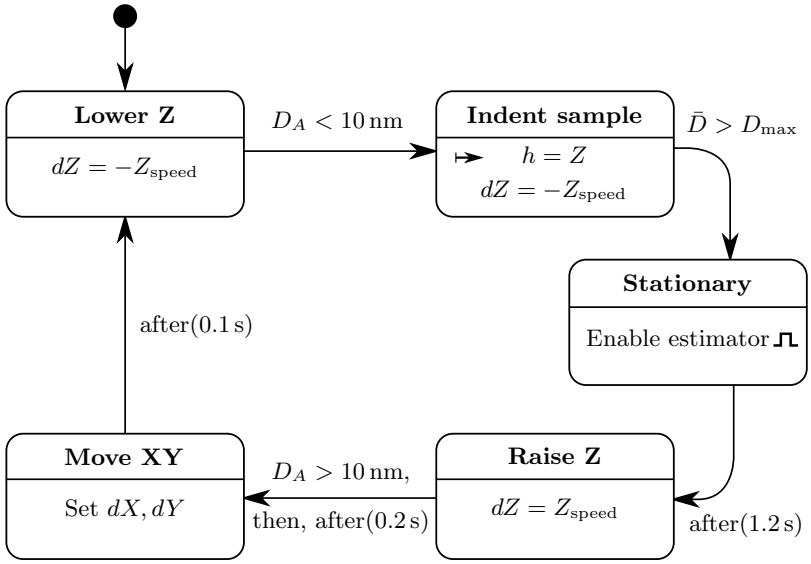

Figure 8.6: State machine controlling the overall operation of the procedure. One cycle represents a single indentation and is repeated for each pixel across the sample. The initial state is given by '•', while '↦' represents entry action. For other actions, their signals are reset to zero at state exit.

that $W(s) = 1$. Then, the demodulator from Chapter 4 can be implemented as

$$\dot{\widehat{\boldsymbol{x}}} = \boldsymbol{\Gamma c}(D - \widehat{D}), \tag{8.35}$$

$$\widehat{D} = \boldsymbol{c}^T \widehat{\boldsymbol{x}}, \tag{8.36}$$

where the constant diagonal matrix $\boldsymbol{\Gamma} = \mathrm{diag}(\gamma_a, \gamma_a, \gamma_b)$, and $\gamma_a, \gamma_b > 0$ determine the bandwidth of the demodulation and the mean estimate, respectively. Furthermore, the state vector $\widehat{\boldsymbol{x}}$ and quadrature signal vector $\boldsymbol{c}$ are given by

$$\widehat{\boldsymbol{x}} = [\widehat{x}_1, \widehat{x}_2, \widehat{x}_3]^T, \tag{8.37}$$

$$\boldsymbol{c} = [\sin(\omega_0 t), \cos(\omega_0 t)]^T. \tag{8.38}$$

The deflection amplitude D_A, phase D_φ, and mean $\bar{D}$ can then be recovered from

$$D_A = \sqrt{\widehat{x}_1^2 + \widehat{x}_2^2}, \tag{8.39}$$

$$D_\varphi = \mathrm{atan2}\left(\widehat{x}_2, \widehat{x}_1\right), \tag{8.40}$$

$$\bar{D} = \widehat{x}_3, \tag{8.41}$$

where atan2$(\cdot)$ is the four-quadrant inverse tangent function.

The Lyapunov estimator requires an exact knowledge of the frequency ω_0 of the modulated signal. The frequency is determined by the applied modulation signal F_{mod} from (8.26). Thus, by feeding this signal into the demodulator, the frequency will match trivially.

8.4.3 XYZ Controller

The XYZ controller positions the cantilever as commanded by the state machine. The controller takes the rate of movement along each axis, dX, dY, dZ, as reference, and positions the cantilever/sample accordingly.

Hysteresis and creep in the lateral piezoscanners can negatively influence the results. E.g., if the tip moves toward an area of higher topography during an indentation in DIVE mode, the value of the initial contact point would become invalid, and result in lower or even negative indentation depth values. This would introduce an error or completely invalidate the estimated parameters, especially for stiff samples and steep topography. In order to suppress such occurrences, a feedback PI-controller is implemented for accurate positioning along the lateral axes.

The vertical (z-axis) scanner on the other hand, is implemented using feedforward only. This scanner also displays hysteresis and creep. However, the effects along

this axis are negligible as the recorded initial contact point is still valid. This leads to a correct measurement of indentation depth, and the estimated parameters remain valid even when the sample creeps in the vertical direction.

8.4.4 Other Considerations

Contact point detection In order to determine the depth of the cantilever during indentation, first the point of contact with the sample must be detected. This additionally serves as a measurement of the topography h at the current lateral position. A rigorous contact point detection can be challenging, especially for soft samples with strong surface forces [21]. During approach, attractive forces can result in a jump to contact, possibly causing sample indentation in addition to adhesion forces. For these reasons, there is no simple solution to determining the contact point. In our experiments the contact point was determined by the deflection amplitude becoming less than some predetermined value, chosen as $D_A < 10\,\text{nm}$. When this condition is reached, the topography is determined from the current vertical tip position.

Calibration All signals are converted to SI units. For accurate indentation values, the deflection and vertical positioning need to be well calibrated. The vertical positioning can be calibrated by performing a scan over a rigid sample with a known step height. The deflection can be calibrated by performing an indentation into a rigid sample with the same cantilever as used in the experiment, and comparing this to the previously calibrated vertical positioning.

Deflection creep It was observed that the resting, static deflection point of the cantilever creeped slowly over time. This also appeared to change the deflection calibration over time. This is believed to be due to temperature changes, in particular from the reflective coating on the cantilever, which can result in bending of the cantilever [21]. This effect was mitigated by turning on the equipment some time before performing experiments, which let the thermals come to equilibrium in operating conditions. Additionally, the deflection zero-level was reset between each subsequent indentation.

8.5 System Identification and Tuning

In order to implement the parameter estimator, the cantilever dynamics (8.2) need to be known. In particular, the system parameters M, K, C need to be identified

in order to implement w using (8.12).

The experiments were implemented on a commercial AFM (Park Systems XE-70) using a spherical carbon tip cantilever with 40 nm tip radius (B40_CONTR).

8.5.1 System Identification

The cantilever spring constant K was calibrated by the thermal noise method [82] with modifications from [21]. In this method, first, the power spectral density of the cantilever is recorded without any applied force. The spectral density is then fit to a Cauchy distribution near the first resonance mode. The mean square deflection $\langle D^2 \rangle$ can then be found through integration of the fit. Finally, the spring constant is found by using

$$K = \beta^* \frac{k_B T}{\langle D^2 \rangle} \tag{8.42}$$

where $\beta^* = 0.817$ is a correction factor, k_B is the Boltzmann constant and T is the absolute temperature of the cantilever. The fit of the spectral density to the Cauchy distribution, from our experiments, can be seen in Fig. 8.7(a).

In order to identify the cantilever effective mass and damping coefficient, the frequency response of the cantilever deflection was found by applying white noise to the piezo modulator. The resonance frequency of the first mode, ω_0, was then identified at peak magnitude. Furthermore, the effective mass was found using the relationship

$$M = \frac{K}{\omega_0^2}. \tag{8.43}$$

Finally, the transfer function was fitted to the frequency response data by adjusting C. A good fit near the resonance peak was emphasized, and the result is seen in Fig. 8.7(b). Note that the cantilever is actuated from the base of the cantilever fixture, which excites additional dynamics. Self-actuated cantilevers are also available resulting in a cleaner frequency response [119].

The resulting system parameters are given by

$$K = 0.816\,\mathrm{N/m}, \qquad C = 7.86 \times 10^{-8}\,\mathrm{Ns/m},$$
$$M = 8.42 \times 10^{-11}\,\mathrm{kg}, \qquad f_0 = 15.7\,\mathrm{kHz}$$

with $\omega_0 = 2\pi f_0$.

Additionally, a calibration for the piezo modulator voltage-to-force ratio need to be determined. This was performed by applying a sinusoidal signal at cantilever resonance frequency and comparing the deflection response with the expected output from the previously found transfer function.

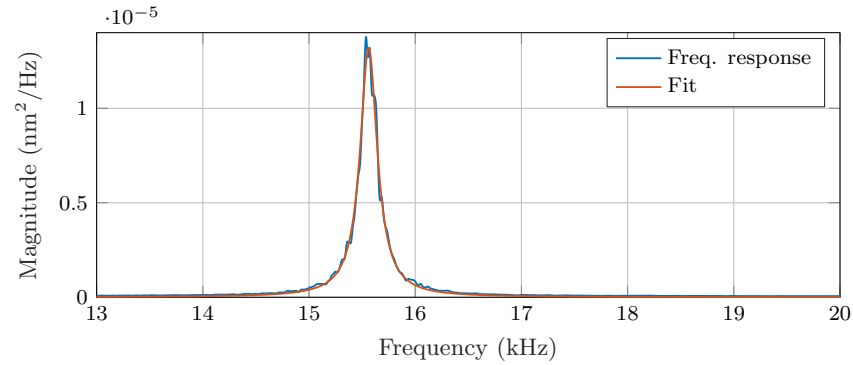

(a)

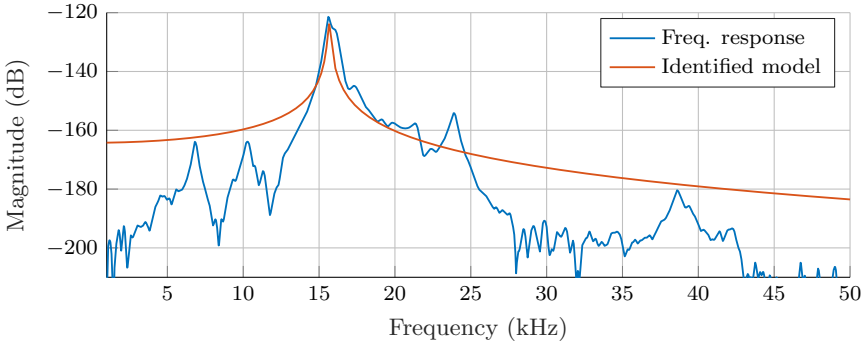

(b)

Figure 8.7: System identification. (a) Cantilever spring constant calibration. (b) Cantilever frequency response and approximated second-order model, from piezo modulator to deflection.

8.5.2 Estimator Tuning

The parameter estimator needs to be appropriately tuned for the experimental conditions. The main tunables are β and $\mathbf{P}_0$. Here, β determines the bandwidth of the estimator, with very high values resulting in noisy estimates. The $\mathbf{P}_0$ matrix determines the level of trust in the initial conditions of the parameter estimates, with large values meaning low trust, and thus fast initial convergence.

The following values were determined which provided a reasonable bandwidth with low noise:

$$\beta = 50, \quad \mathbf{P}_0 = \mathrm{diag}(5 \times 10^7, 1 \times 10^{18}).$$

Additionally, α was set to unity.

8.5.3 Estimation Time Interval

By using the results from Corollary 8.1, the estimation time during each indentation, for which the parameter error is guaranteed to be sufficiently small, can be found. However, the PE properties of the signal vector need to be known in order to apply the results. In the following, it is demonstrated how to find the desired time interval when using sample model $\mathcal{A}$, and the estimator tuning from the previous section.

Consider the applied sinusoidal cantilever modulation force (8.26). Assuming that the resulting cantilever deflection is dominated by a linear response, and that the cantilever is in contact with the sample, we have

$$\delta = A \sin(\omega_0 t + \varphi) + \bar{\delta} \tag{8.44}$$

for some amplitude A, phase φ, and mean depth $\bar{\delta} \geq A$. While nonlinear tip-sample interaction forces can induce a response at other frequencies, they would be substantially attenuated due to the strong resonance effect of the cantilever near ω_0. Thus, (8.44) should be a close approximation to the experimental situation. Inserting (8.44) into $\boldsymbol{\phi}_{\mathcal{A}}$ from (8.14) gives the signal vector

$$\boldsymbol{\phi}_{\mathcal{A}} = \begin{bmatrix} A\omega \cos(\omega_0 t + \varphi) & A \sin(\omega_0 t + \varphi) + \bar{\delta} \end{bmatrix}^T. \tag{8.45}$$

Next, consider the PE expression from Definition 2.3, and define

$$\mathbf{S} \triangleq \frac{1}{T_\mathrm{p}} \int_t^{t+T_\mathrm{p}} \boldsymbol{\phi}_{\mathcal{A}} \boldsymbol{\phi}_{\mathcal{A}}^T d\tau. \tag{8.46}$$

By choosing

$$T_\mathrm{p} = 2\pi\omega_0^{-1} \tag{8.47}$$

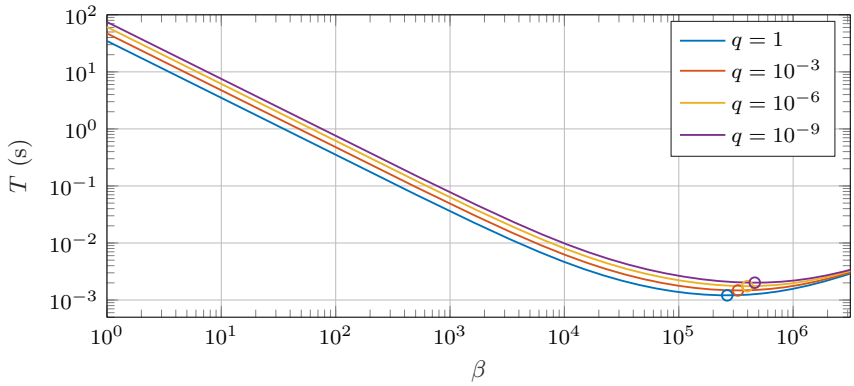

Figure 8.8: Minimum estimation time T which guarantees convergence of the parameter estimate error to within q fraction of the initial error.

and using (8.45), it can be shown that the solution to (8.46) is given by

$$\mathbf{S} = \begin{bmatrix} \frac{1}{2}A^2\omega_0^2 & 0 \\ 0 & \frac{1}{2}A^2 + \bar{\delta}^2 \end{bmatrix}. \tag{8.48}$$

Thus, $\boldsymbol{\phi}_{\mathcal{A}}$ is PE with level of excitation α_0 and α_1 given by

$$\alpha_0 = \min\left\{\tfrac{1}{2}A^2\omega_0^2,\ \tfrac{1}{2}A^2 + \bar{\delta}^2\right\} \tag{8.49}$$

$$\alpha_1 = \max\left\{\tfrac{1}{2}A^2\omega_0^2,\ \tfrac{1}{2}A^2 + \bar{\delta}^2\right\} \tag{8.50}$$

which satisfy the PE condition

$$\alpha_0\mathbf{I} \leq \mathbf{S} \leq \alpha_1\mathbf{I}. \tag{8.51}$$

Thus, with the PE condition found, Corollary 8.1 can then be used to find the time interval T, within which the parameter error is guaranteed to be desirably small. First, the following properties can be determined by considering $\boldsymbol{\phi}_{\mathcal{A}}$ from (8.45)

$$\bar{\phi}_{\mathcal{A}}^2 = A^2\omega^2 + \left(A + \bar{\delta}\right)^2, \quad \bar{m}_{\mathcal{A}}^2 = 1 + \bar{\phi}_{\mathcal{A}}^2, \tag{8.52}$$

Using (8.28)-(8.33), the time interval can be plotted as a function of β at various values of q, as seen in Fig. 8.8.

By using the tuned value of β, it was found that the time interval which guarantees that the estimator error has been reduced to $q = 0.001\%$ of the initial value is given by

$$T = 1.13\,\text{s}. \tag{8.53}$$

For the actual implementation, the time interval was rounded up to 1.2 s. This value was used as the time spent in the *Stationary* state during each indentation, see Fig. 8.6.

8.6 Experimental Results

The method was implemented on the commercial AFM (Park Systems XE-70) employed in the previous section, using the same cantilever (B40_CONTR). The AFM was connected to an embedded computer (dSpace DS1103) controlling all aspects of the operation. A Simulink program implements the necessary equations from the previous sections, as well as the scanning logic. The program was transferred to the embedded computer before operation.

The parameter estimator and demodulator was implemented online at a sampling rate of 200 kHz. The state machine and XYZ controller was run at a separate sampling rate of 1 kHz. This separation allows for faster sampling speed for the estimator. The XYZ controller was tuned for relatively low bandwidths, and its sampling rate was thus sufficient.

8.6.1 Two-Component Polymer Film Sample

The first experiment was performed to demonstrate the normal operating procedure of DIVE mode AFM, revealing spatially varying viscoelastic properties of the sample. A total of 30×30 indentations into a PS-LDPE-12M film sample were performed. This two-component polymer sample has specified elastic moduli of around 0.1 GPa and 2 GPa for the two components. The sample is especially suitable for measuring variations in elasticity due to its clear contrast between the two polymer components.

In this experiment, sample model $\mathcal{A}$ was used for online estimation of spring constants and damping coefficients. In order to find the elastic modulus, equation (8.8) was used offline. The results of the scan can be seen in Fig. 8.9. The contrast in elasticity between the two polymer components is clearly visible.

For each pixel in the scan results, the online estimator recursively estimates the spring constant and the damping coefficient. The vertical tip position and corresponding parameter estimates in the time-domain, during two subsequent indentations, are shown in Fig. 8.10. It can be seen that the first indentation is located in the softer region of the sample, while the second indentation near the stiffer region. This results in the first indentation going deeper, as seen in Fig. 8.10(a). Since the second indentation does not reach deep into the sample, it is consequently more prone to noise in the depth estimate, resulting in somewhat more noisy parameter estimates as seen in Fig. 8.10(b). To mitigate such noise, it is emphasized that the spring constant and tip radius of the cantilever used, need to be suitable for the sample being investigated. A very soft cantilever will deflect too much before it sufficiently indents the sample, while a very stiff cantilever will

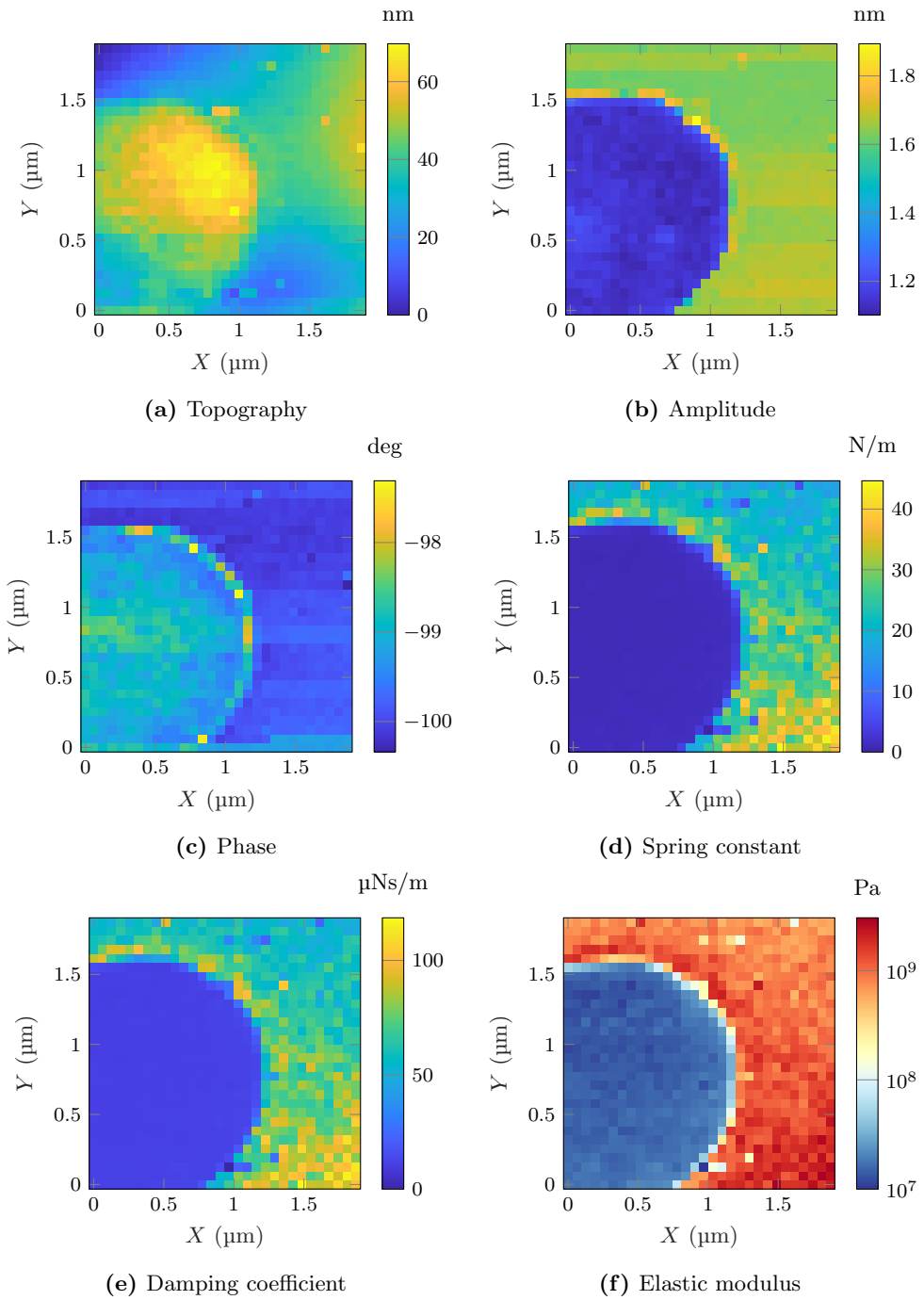

(a) Topography **(b)** Amplitude

(c) Phase **(d)** Spring constant

(e) Damping coefficient **(f)** Elastic modulus

Figure 8.9: AFM experiment for a two-component polymer sample.

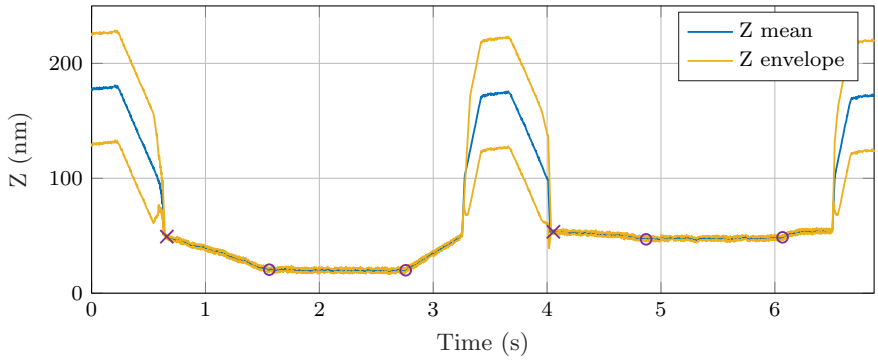

(a) Vertical tip position

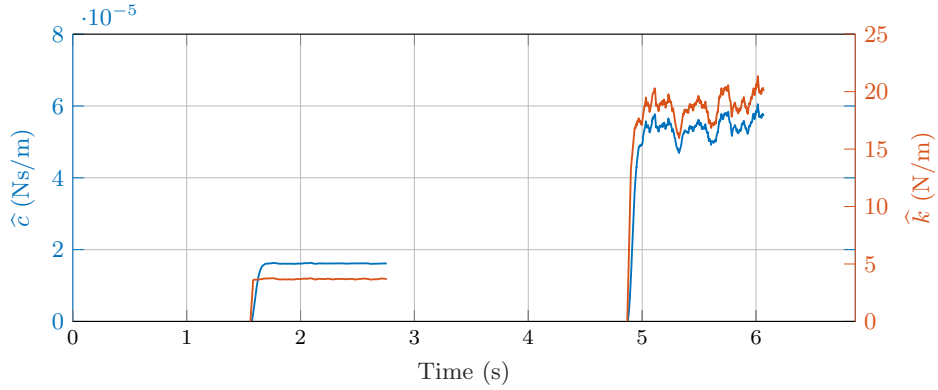

(b) Parameter estimates

Figure 8.10: Tip position (a) and parameter estimation (b) during two subsequent indentations into the two-component polymer sample. In (a), crosses '×' mark contact detection point (topography), while within the circles '○' the stationary state is active and sample parameters are estimated.

Table 8.1: Depth versus elasticity.

Indentation	Spring constant	Elastic modulus
100 nm	0.335 N/m	2.73 MPa
250 nm	0.435 N/m	2.31 MPa
Difference	26.0 %	16.7 %

indent the sample without sufficiently deflecting and can cause damage.

8.6.2 Homogeneous Gel Sample

In the second set of experiments, a soft gel sample (PDMS-SOFT-1-12M) was used with a specified elastic modulus of about 2.5 MPa. Four experiments at 20×20 resolution were performed in order to compare sample model $\mathcal{A}$ and $\mathcal{B}$ at different indentation depths, 100 nm and 250 nm, respectively. The resulting identified spring constants (sample model $\mathcal{A}$) and elastic moduli (sample model $\mathcal{B}$) are shown in Fig. 8.11.

The mean of the identified parameters from each experiment is given in Table 8.1. The identified elastic modulus is close to the specified value of 2.5 MPa. If the sample perfectly complies with the Hertz model, then the elastic modulus should be invariant with regards to the indentation depth. However, the results indicate some difference at the two depths. This suggests that the Hertz model is not completely descriptive for the experimental setup. In particular, the indentation is large compared to the radius of the cantilever, which violates the assumption of small indentations. This could be mitigated by using a cantilever with a larger tip radius, or lower spring constant. Additionally, adhesion effects could be large, something which is further discussed in the next experiment.

Note that the difference in the mean spring constant is larger than for the elastic modulus. This can be used as an argument in favor of implementation of the Hertz sample model $\mathcal{B}$, and demonstrates the necessity of a nonlinear sample model.

For many soft, biological materials it is not possible to calculate the elastic modulus [96], as they do not even approximately behave in accordance with Hooke's law or its nonlinear variants, which is the basis of the elastic models presented in this chapter. For such materials, a more suitable sample model could be developed, and used in the modeling and identification approach as presented.

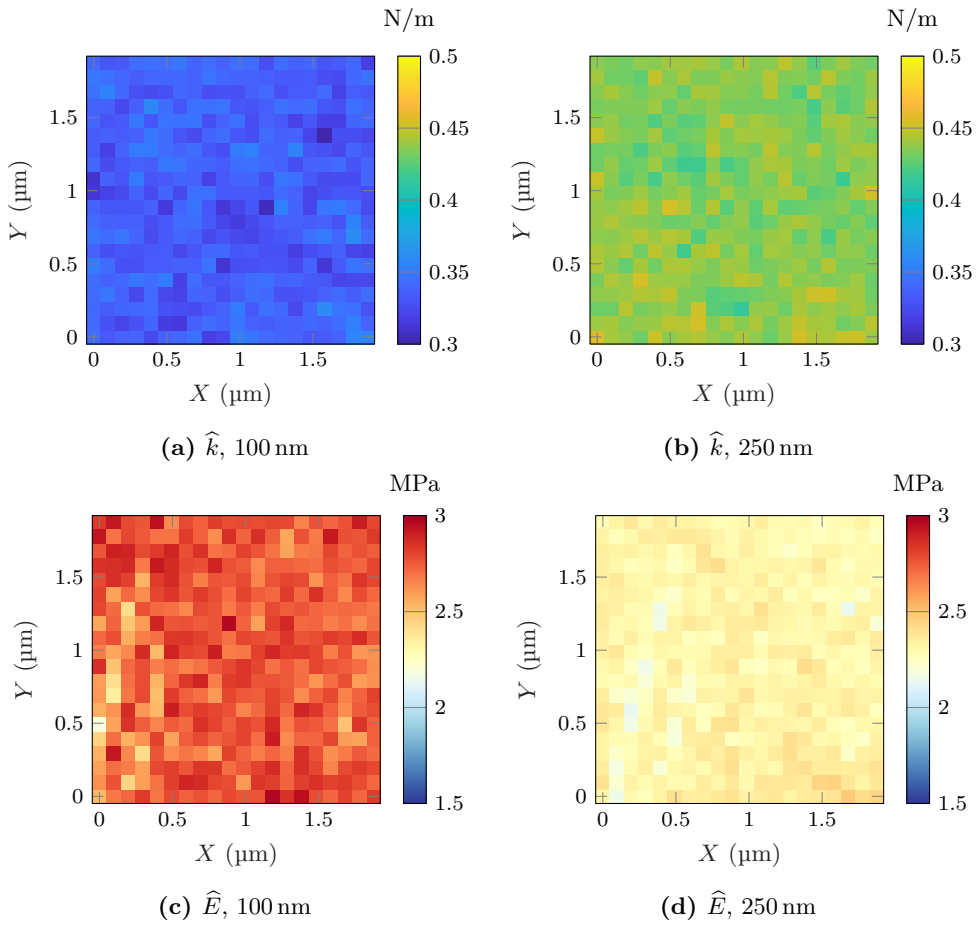

(a) $\widehat{k}$, 100 nm **(b)** $\widehat{k}$, 250 nm

(c) $\widehat{E}$, 100 nm **(d)** $\widehat{E}$, 250 nm

Figure 8.11: Four AFM experiments demonstrating identification of (a)-(b) spring constants (sample model $\mathcal{A}$), versus (c)-(d) elastic moduli (sample model $\mathcal{B}$), at different indentation depths on a homogeneous gel sample.

8.6.3 Time-Varying Estimation

Since the presented approach uses a recursive parameter estimation scheme, the time-varying nature of the parameters can be recorded. This can be demonstrated by performing a single indentation into a soft sample. If the sample complies with the Hertz model, then the spring constant from sample model $\mathcal{A}$ should increase with increasing indentation depth. Thus, if the cantilever tip is lowered and raised again, experimental results should demonstrate time-varying parameters.

This experiment was performed on the same gel sample as previous (PDMS-SOFT-1-12M). During the experiment, the cantilever was lowered until it reached some specified depth into the sample, then raised again. Throughout the whole procedure, while the tip was in contact with the sample, the parameter estimator was enabled. The experiment was implemented at a slow vertical speed, to make sure that the parameter estimates were accurate. The cantilever and experimental setup from the previous experiments have otherwise been used.

The results of the experiment are given in Fig. 8.12. The parameter estimates as shown in Fig. 8.12(a) demonstrate that the spring constant generally increases with increasing indentation depth as expected, and decreases as the tip is raised again. Thus, proper estimation of time-varying parameters by using the presented approach is demonstrated.

The results also demonstrate several effects due to *adhesion and deformation* that should be considered when performing experiments:

After initial contact. Initially after contact, the spring constant estimates become negative. Negative spring constants make little physical sense unless one considers the effect of adhesion. As the tip approaches the sample, attractive adhesion forces pull the tip onto the sample, resulting in a negative cantilever deflection (Fig. 8.12(b)) which is interpreted as negative interaction forces by the parameter estimator. The best fit of the positive indentation depth signal onto the negative cantilever deflection using the sample models implemented, results in negative parameter estimates.

Raising the cantilever. A similar effect is seen towards the end of the experiment, just before the tip is freed from the sample. As the tip is raised, adhesion forces will make the sample stick to the cantilever tip. This could also result in deformation of the sample, by raising it towards the tip as it is lifted. For these reasons, in the experiment, at some point the indentation depth becomes zero and then negative. As it approaches zero depth, the spring constant estimate grows toward either positive or negative infinity, depending on the net force experienced by the cantilever. Generally, the sample model and estimates in the adhesive regime is thus invalid.

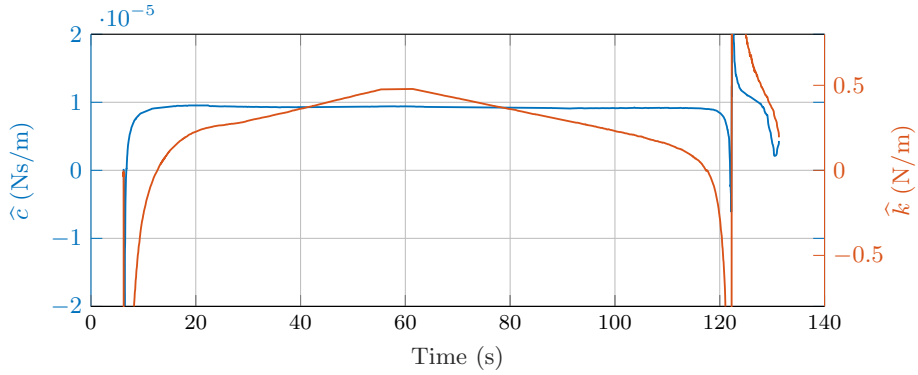

(a) Parameter estimates

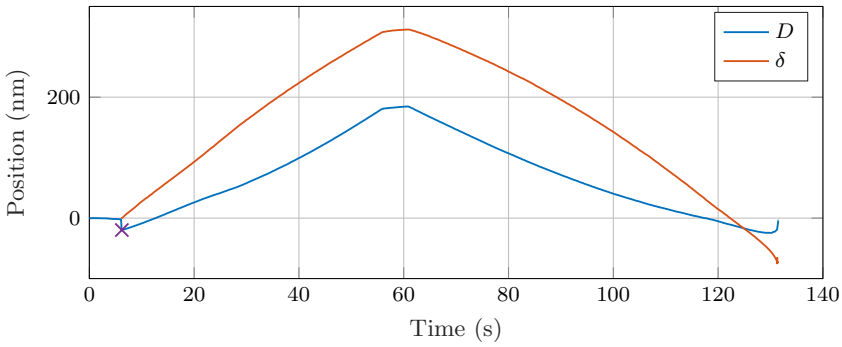

(b) Deflection and depth

Figure 8.12: Time-varying parameter estimates. The estimated spring constant is shown to change with the indentation depth. Unmodeled adhesion effects give rise to unreliable results at the start and end of the experiment.

These effects could explain the difference of the elastic modulus at different depths in the previous experiment. To mitigate the effect of adhesion, the sample model could be modified to include adhesion, such as by employing the Johnson-Kendall-Roberts (JKR) or Derjaguin-Muller-Toporov (DMT) contact models [195].

8.7 Conclusions

A model-based identification technique is presented for determining spatially resolved nanomechanical properties in AFM. Both the cantilever and sample behavior is described by dynamic models. The cantilever dynamics are assumed known by identifying its parameters before performing the experiments, while the sample dynamics incorporate the unknown parameters to be identified. A recursive least squares estimator is used for identification of the sample parameters.

Employing a recursive estimator has several advantages over comparable techniques. First, it allows online identification of the nanomechanical properties, enabling the operator to see real-time conditions. Secondly, it allows the determination of time-varying changes of the parameters as demonstrated by the experiments. This could be useful by itself, such as for observing changing conditions in cells or other biological material. Finally, observing such time-varying changes could reveal erroneous conditions or unmodeled dynamics, as this could dramatically affect the estimated parameters. An example of this is seen in the last experiment, where negative and diverging spring constant estimates are seen near the beginning and end of the experiment. This is believed primarily to occur due to unmodeled adhesion effects.

Furthermore, the use of an analytical expression for the estimation time interval of the recursive least squares estimator is demonstrated. Within this time interval, the parameter error is guaranteed to have been reduced to any given fraction of the initial error. The time interval can be determined a priori, and spending this length of time at each indentation point then guarantees that the parameters will converge to any desired accuracy. This is verified by the experiments, where the parameters are seen to converge within the determined time interval.

Two sample models are developed and implemented for this approach – a linear spring-damper model and a nonlinear Hertz model. It is demonstrated that only minor modifications are needed to switch between the models. The experiments show the Hertz model to be a better match. However, some materials may not be well described by this model, and it is then a clear advantage of the proposed modeling and identification approach that the sample model can be exchanged for a more suitable dynamic model.

Chapter 9

Conclusions and Future Work

This thesis consists of three parts mainly concerning performance improvements, and novel methodologies for revealing nanomechanical sample properties in AFM. Conclusive remarks to each part are given here, with suggestions for future work.

9.1 Part I

In Part I, a technique is developed for simultaneous estimation of the true topography and the tip-sample interaction force, in noncontact dynamic mode AFM. The cantilever dynamics are considered linear, while the distance between the tip and the sample appears nonlinearly in the tip-sample interaction force considered. Thus, in order to resolve the tip-sample distance and consequently, the true topography, a nonlinear estimation problem must be solved. Two distinct observers are designed to solve this problem, one of which guarantees near-global exponentially stable error dynamics. Numerical results are given in this work, while experimental implementations of this approach remain to be performed.

Several extensions to this approach can be considered for future work. The simultaneous estimation of the Lennard-Jones parameters would increase the practicality of the approach; and since they appear linearly in the tip-sample interaction force, they should be identifiable under normal PE conditions. Since the approach only considers the attractive force regime, it may be sufficiently accurate to only consider the van der Waals term of the force model (the distance squared term), resulting in a much simpler system to be observed. Otherwise, the method could be extended to tapping mode, where both attractive and repulsive forces are considered. Finally, the robustness of the approach to modeling errors or disturbances should be investigated. In particular, the tip-sample interaction force may not be

as smooth as considered, and the cantilever model contains higher modes which may need to be included for accurate representation of real world conditions.

9.2 Part II

In Part II, the demodulator in dynamic mode AFM is considered. A comparison of state-of-the-art techniques for demodulation in AFM is presented. Furthermore, the Lyapunov estimator is introduced for demodulation of amplitude and phase. Numerical and experimental results demonstrate that the Lyapunov estimator achieves a particularly attractive combination of (i) performance in terms of bandwidth and noise attenuation, (ii) low implementation complexity, and (iii) rejection of frequency components away from the carrier frequency. Compared to the widely used lock-in amplifier, the Lyapunov estimator demonstrates a better performance at higher bandwidths, but is somewhat more sensitive to noise at lower bandwidths and to other frequency components. This can mainly be attributed to the usage of a fourth-order low-pass filter in the lock-in amplifier. In future work, it could be investigated how the Lyapunov estimator performs when augmented with an equivalent filter, and whether the $W(s)$ pre-filter could be utilized for increased noise attenuation without sacrificing performance. Compared to the peak hold method used in some of the major high-speed AFM results, the Lyapunov estimator performs similarly or better in terms of bandwidth, is vastly improved in terms of sensitivity to noise, and can be used in multifrequency AFM applications. However, it is somewhat more complicated in terms of implementation complexity. A future challenge is to investigate whether it can be implemented at sampling times near those achieved with the peak hold method. If successfully implemented as such, high-speed AFM imaging may be improved in terms of noise and possibly better resolution or contrast.

9.3 Part III

Part III introduces the model-based identification approach for resolving nanomechanical properties in AFM. This approach is particularly attractive compared to recent multifrequency AFM approaches for determination of such properties, since it avoids complicated relationships between the observables and the properties to be determined. Furthermore, the demodulation of the deflection signals at multiple frequencies is completely avoided, as the model-based identification approach directly uses the measured signals.

Two modes of operation are developed for the model-based identification ap-

proach, DIVE mode and SVE mode. A numerical simulation environment is developed to investigate the performance of the two modes. Furthermore, DIVE mode is implemented experimentally and successfully resolves the mechanical properties of the samples investigated, including online identification of elastic moduli. SVE mode remains to be experimentally implemented. A particular challenge for samples of highly varying elasticity is the use of the constant-depth controller. However, the mode should be able to be adapted to avoid this component, and rather rely on typical amplitude signals or similar for feedback control. SVE mode is likely to produce vastly improved imaging rates compared to DIVE mode, and rather comparable to those of recent multifrequency AFM approaches. It can even be argued that it can be improved over multifrequency AFM, as the presented approach does not rely on stationary signals such as amplitude and phase, but rather uses the entire transient information of the signals.

In future work, the sample model can be augmented to include additional properties. The presented approach is easily extended for parameters that appear linearly in the signals, the only requirement is then to ensure PE conditions. Such properties may include the depth-gradients of elasticity and viscosity. Then, one only needs to ensure that additional sinusoids appear in the cantilever deflection signal to ensure PE conditions. Single frequency excitation may be sufficient if the higher harmonics are detectable, otherwise the cantilever can be excited at multiple frequencies. Parallels to multifrequency AFM then start to become apparent.

This brings an interesting viewpoint, or insight, into multifrequency AFM. The ability to measure the properties that are measured in existing methods, can essentially be considered a problem of ensuring persistency of excitation. That is, the information in the recorded signals needs to be sufficiently rich to ensure that the properties can be uniquely determined. This insight may be used as a guideline for future research. Instead of pursuing complicated relationships between the observables and the multifrequency components, rather pursue PE conditions using the model-based identification approach.

Other improvements to the sample model would be highly attractive, such as including adhesion effects. However, depending on how adhesion is modeled, its parameters may not appear linearly in the model. It is also possible that such a property cannot be uniquely determined without completely retracting from the sample and approaching it again, such that it can only be determined in DIVE mode. These efforts may not be as easy as ensuring PE conditions. However, for some problems with nonlinearly parametrized properties, a solution may be found by employing approaches such as the nonlinear state- and parameter-estimator used in Chapter 3.

For simulation purposes, one could consider replacing the grid of spring-damper elements, and rather directly use a contact model with varying parameters. This approach might lead to more physically accurate simulations, while being simpler numerically.

Finally, this part also introduces upper bounds on the convergence rate of the least squares estimator in the general sense. This makes it possible to guarantee convergence of the parameters to any desired accuracy after a given time interval, and was exploited during the experiments performed in DIVE mode. In future work, it would be helpful to additionally develop a lower bound on the convergence rate. Such a result could aid in tuning of the estimator, as the upper bound may be rather conservative.

Appendix A

Total Integrated Noise

This chapter discusses total integrated noise (TIN), used to measure the noise performance of various demodulation schemes given in Chapter 4 and Chapter 5. The TIN given white noise filtered through a system $G(s)$ is given by [49]

$$\sigma(G) = \sqrt{\int_0^{f_{bw}} A|G(j2\pi f)|^2 df} \tag{A.1}$$

where f_{bw} is the measurement bandwidth, and A is the power spectral density of the white noise. Consider the first order and second order low-pass filters

$$G_1(s) = \frac{1}{(2\pi f_c)^{-1}s + 1}, \quad G_2(s) = \frac{1}{((2\pi f_c)^{-1}s + 1)^2},$$

for some cut-off frequency $f_c > 0$. Using (A.1) the TIN for each system is given by

$$\sigma(G_1) = \sqrt{A}\sqrt{f_c \operatorname{atan}\left(\frac{f_{bw}}{f_c}\right)} \tag{A.2}$$

$$\sigma(G_2) = \sqrt{A}\sqrt{\frac{1}{2}f_c \operatorname{atan}\left(\frac{f_{bw}}{f_c}\right) + \frac{1}{2}\frac{f_{bw}f_c^2}{f_{bw}^2 + f_c^2}}. \tag{A.3}$$

It can be shown that $\sigma(G_1) > \sigma(G_2)$ for all $f_{bw}, f_c > 0$. Furthermore, consider the case where the measurement bandwidth is much greater than the cut-off frequency, $f_{bw} \gg f_c$. Then, the ratio between the TIN of each system is given by

$$\lim_{f_{bw}\to\infty} \frac{\sigma(G_2)}{\sigma(G_1)} = 1/\sqrt{2}.$$

Table A.1: TIN Ratio for nth vs. first order low-pass filter.

n	$\sigma(G_n)/\sigma(G_1)$
2	0.7071
3	0.6124
4	0.5590
5	0.5229

Thus, the TIN of the second-order filter is a factor ~ 0.71 the TIN of the first-order low-pass filter. By following the above procedure for the higher order filters

$$G_n(s) = \frac{1}{((2\pi f_c)^{-1}s + 1)^n}, \tag{A.4}$$

the TIN ratio between an nth order and a first order low-pass filter can be found. Results are summarized in Table A.1. Note that the TIN is reduced with increasing filter order.

Bibliography

[1] D. Y. Abramovitch. "Low latency demodulation for Atomic Force Microscopes, Part I efficient real-time integration." In *American Control Conference*, 2011.

[2] D. Y. Abramovitch. "Low latency demodulation for Atomic Force Microscopes, Part II: Efficient Calculation of Magnitude and Phase." In *American Control Conference*, 2011.

[3] D. Y. Abramovitch, S. B. Andersson, L. Y. Pao, and G. Schitter. "A Tutorial on the Mechanisms, Dynamics, and Control of Atomic Force Microscopes." In *American Control Conference*, New York, USA, 2007.

[4] B. D. O. Anderson and R. M. Johnstone. "Adaptive systems and time varying plants." *International Journal of Control*, 37(2):367–377, 1983.

[5] T. Ando. "High-speed atomic force microscopy coming of age." *Nanotechnology*, 23(6):062001, 2012.

[6] T. Ando, N. Kodera, E. Takai, D. Maruyama, K. Saito, and A. Toda. "A high-speed atomic force microscope for studying biological macromolecules." *Proceedings of the National Academy of Sciences*, 98(22):12468–12472, 2001.

[7] T. Ando, T. Uchihashi, and T. Fukuma. "High-speed atomic force microscopy for nano-visualization of dynamic biomolecular processes." *Progress in Surface Science*, 83(7-9):337–437, 2008.

[8] T. Ando, T. Uchihashi, and N. Kodera. "High-speed AFM and applications to biomolecular systems." *Annual review of biophysics*, 42:393–414, 2013.

[9] S. S. Aphale, B. Bhikkaji, and S. O. R. Moheimani. "Minimizing scanning errors in piezoelectric stack-actuated nanopositioning platforms." *IEEE Transactions on Nanotechnology*, 7(1):79–90, 2008.

[10] G. Bar, Y. Thomann, R. Brandsch, H.-J. Cantow, and M.-H. Whangbo. "Factors Affecting the Height and Phase Images in Tapping Mode Atomic Force Microscopy. Study of Phase-Separated Polymer Blends of Poly(ethene-co-styrene) and Poly(2,6-dimethyl-1,4-phenylene oxide)." *Langmuir*, 13(14):3807–3812, 1997.

[11] A. R. Bausch, F. Ziemann, A. A. Boulbitch, K. Jacobson, and E. Sackman. "Local measurements of viscoelastic parameters of adherent cell surfaces by magnetic bead microrheometry." *Biophysics*, 75(4):2038–2049, 1998.

[12] A. Bazaei, Y. K. Yong, and S. O. R. Moheimani. "High-speed Lissajous-scan atomic force microscopy: Scan pattern planning and control design issues." *Review of Scientific Instruments*, 83(6):063701, 2012.

[13] R. Benitez and J. L. Toca-herrera. "Looking at cell mechanics with atomic force microscopy: Experiment and theory." *Microscopy Research and Technique*, 77(11):947–958, 2014.

[14] B. Bhushan, ed. "Springer handbook of nanotechnology." Springer, 2010.

[15] B. Bhushan and O. Marti. "Scanning Probe Microscopy - Principle of Operation, Instrumentation, and Probes." In B. Bhushan, editor, *Springer Handbook of Nanotechnology*, pp. 573–617. Springer Berlin Heidelberg, 2010.

[16] G. Binnig, C. F. Quate, and C. Gerber. "Atomic Force Microscope." *Physical Review Letters*, 56(9):930–933, 1986.

[17] G. Binnig, H. Rohrer, C. Gerber, and E. Weibel. "Surface Studies by Scanning Tunneling Microscopy." *Physical Review Letters*, 49(1):57–61, 1982.

[18] B. Brogliato, B. Maschke, R. Lozano, and O. Egeland. "Dissipative Systems Analysis and Control." Springer, London, UK, 2007.

[19] B. R. Brückner, H. Nöding, and A. Janshoff. "Viscoelastic Properties of Confluent MDCK II Cells Obtained from Force Cycle Experiments." *Biophysical Journal*, 112(4):724–735, 2017.

[20] N. A. Burnham, O. P. Behrend, F. Oulevey, G. Gremaud, P.-J. Gallo, D. Gourdon, E. Dupas, A. J. Kulik, H. M. Pollock, and G. A. D. Briggs. "How does a tip tap?" *Nanotechnology*, 8(2):67–75, 1997.

[21] H.-J. Butt, B. Cappella, and M. Kappl. "Force measurements with the atomic force microscope: Technique, interpretation and applications." *Surface Science Reports*, 59(1-6):1–152, 2005.

[22] H.-J. Butt and M. Jaschke. "Calculation of thermal noise in atomic force microscopy." *Nanotechnology*, 6(1):1–7, 1995.

[23] H.-J. Butt, P. Siedle, K. Seifert, K. Fendler, T. Seeger, E. Bamberg, A. L. Weisenhorn, K. Goldie, and A. Engel. "Scan speed limit in atomic force microscopy." *Journal of Microscopy*, 169(1):75–84, 1993.

[24] P. Carl and H. Schillers. "Elasticity measurement of living cells with an atomic force microscope: data acquisition and processing." *Pflügers Archiv - European Journal of Physiology*, 457(2):551–559, 2008.

[25] A. Cartagena and A. Raman. "Local Viscoelastic Properties of Live Cells Investigated Using Dynamic and Quasi-Static Atomic Force Microscopy Methods." *Biophysical Journal*, 106(5):1033–1043, 2014.

[26] A. X. Cartagena-Rivera, W.-H. Wang, R. L. Geahlen, and A. Raman. "Fast, multi-frequency, and quantitative nanomechanical mapping of live cells using the atomic force microscope." *Scientific Reports*, 5:11692, 2015.

[27] G. M. Clayton, S. Tien, K. K. Leang, Q. Zou, and S. Devasia. "A Review of Feedforward Control Approaches in Nanopositioning for High-Speed SPM." *Journal of Dynamic Systems, Measurement, and Control*, 131(6):061101, 2009.

[28] A. Della Pia and G. Costantini. *Scanning Tunneling Microscopy*. In. *Encyclopedia of Nanotechnology*. B. Bhushan, editor. Springer Netherlands, Dordrecht, 2012, pp. 2301–2313.

[29] B. V. Derjaguin, V. M. Muller, and Y. U. P. Toporov. "Effect of contact deformation on the adhesion of particles." *Journal of colloid and interface science*, 52(3):105–108, 1975.

[30] S. Devasia. "Should model-based inverse inputs be used as feedforward under plant uncertainty?" *IEEE Transactions on Automatic Control*, 47(11):1865–1871, 2002.

[31] S. Devasia, E. Eleftheriou, and S. O. R. Moheimani. "A Survey of Control Issues in Nanopositioning." *IEEE Transactions on Control Systems Technology*, 15(5):802–823, 2007.

[32] E. K. Dimitriadis, F. Horkay, J. Maresca, B. Kachar, and R. S. Chadwick. "Determination of Elastic Moduli of Thin Layers of Soft Material Using the Atomic Force Microscope." *Biophysical Journal*, 82(5):2798–2810, 2002.

[33] F. Ding and T. Chen. "Performance bounds of forgetting factor least-squares algorithms for time-varying systems with finite measurement data." *IEEE Transactions on Circuits and Systems I: Regular Papers*, 52(3):555–566, 2005.

[34] D. E. Discher, D. H. Boal, and S. K. Boey. "Simulations of the erythrocyte cytoskeleton at large deformation. II. Micropipette aspiration." *Biophysics*, 75(3):1584–1597, 2008.

[35] M. E. Dokukin and I. Sokolov. "Quantitative Mapping of the Elastic Modulus of Soft Materials with HarmoniX and PeakForce QNM AFM Modes." *Langmuir*, 28(46):16060–16071, 2012.

[36] Y. F. Dufrêne, T. Ando, R. Garcia, D. Alsteens, D. Martinez-Martin, A. Engel, C. Gerber, and D. J. Müller. "Imaging modes of atomic force microscopy for application in molecular and cell biology." *Nature Nanotechnology*, 12(4):295–307, 2017.

[37] Y. M. Efremov, D. V. Bagrov, M. P. Kirpichnikov, and K. V. Shaitan. "Application of the Johnson-Kendall-Roberts model in AFM-based mechanical measurements on cells and gel." *Colloids and Surfaces B: Biointerfaces*, 134:131–139, 2015.

[38] Y. M. Efremov, W.-H. Wang, S. D. Hardy, R. L. Geahlen, and A. Raman. "Measuring nanoscale viscoelastic parameters of cells directly from AFM force-displacement curves." *Scientific Reports*, 7(1):1541, 2017.

[39] O. Egeland and J. T. Gravdahl. "Modeling and Simulation for Automatic Control." Marine Cybernetics, Trondheim, Norway, 2002.

[40] A. A. Eielsen, M. Vagia, J. T. Gravdahl, and K. Y. Pettersen. "Damping and Tracking Control Schemes for Nanopositioning." *IEEE/ASME Transactions on Mechatronics*, 19(2):432–444, 2013.

[41] A. A. Eielsen. "Topics in Control of Nanopositioning Devices." PhD thesis, Norwegian University of Science and Technology, Department of Engineering Cybernetics, 2012.

[42] A. A. Eielsen, J. T. Gravdahl, and K. Y. Pettersen. "Adaptive feed-forward hysteresis compensation for piezoelectric actuators." *Review of Scientific Instruments*, 83(8):085001, 2012.

[43] R. Enning, D. Ziegler, A. Nievergelt, R. Friedlos, K. Venkataramani, and A. Stemmer. "A high frequency sensor for optical beam deflection atomic force microscopy." *Review of Scientific Instruments*, 82(4):043705, 2011.

[44] S. Eslami and N. Jalili. "A comprehensive modeling and vibration analysis of AFM microcantilevers subjected to nonlinear tip-sample interaction forces." *Ultramicroscopy*, 117:31–45, 2012.

[45] M. W. Fairbairn, S. O. R. Moheimani, and A. J. Fleming. "Q Control of an Atomic Force Microscope Microcantilever : A Sensorless Approach." *Journal of Microelectromechanical Systems*, 20(6):1372–1381, 2011.

[46] A. J. Fleming and A. G. Wills. "Optimal Periodic Trajectories for Band-Limited Systems." *IEEE Transactions on Control Systems Technology*, 17(3):552–562, 2009.

[47] A. J. Fleming. "Nanopositioning system with force feedback for high-performance tracking and vibration control." *Mechatronics, IEEE/ASME Transactions on*, 15(3):433–447, 2010.

[48] A. J. Fleming, S. S. Aphale, and S. O. R. Moheimani. "A New Method for Robust Damping and Tracking Control of Scanning Probe Microscope Positioning Stages." *IEEE Transactions on Nanotechnology*, 9(4):438–448, 2010.

[49] A. J. Fleming and K. K. Leang. "Design, Modeling and Control of Nanopositioning Systems." Springer, Cham, Switzerland, 2014.

[50] J. Fraxedas, S. Garcia-Manyes, P. Gorostiza, and F. Sanz. "Nanoindentation: Toward the sensing of atomic interactions." *Proceedings of the National Academy of Sciences*, 99(8):5228–5232, 2002.

[51] T. Fukuma. "Wideband low-noise optical beam deflection sensor with photothermal excitation for liquid-environment atomic force microscopy." *Review of Scientific Instruments*, 80(2):023707, 2009.

[52] T. Fukuma and S. P. Jarvis. "Development of liquid-environment frequency modulation atomic force microscope with low noise deflection sensor for cantilevers of various dimensions." *Review of Scientific Instruments*, 77(4):043701, 2006.

[53] Y. Gan. "Atomic and subnanometer resolution in ambient conditions by atomic force microscopy." *Surface Science Reports*, 64(3):99–121, 2009.

[54] R. Garcia and A. S. Paulo. "Attractive and repulsive tip-sample interaction regimes in tapping-mode atomic force microscopy." *Physical Review B*, 60(7):4961–4967, 1999.

[55] R. Garcia and R. Perez. "Dynamic atomic force microscopy methods." *Surface science reports*, 47(6-8):197–301, 2002.

[56] R. Garcia. "Amplitude Modulation Atomic Force Microscopy." Wiley-VCH Verlag GmbH & Co. KGaA, Weinheim, Germany, 2010.

[57] R. Garcia. "Multifrequency Atomic Force Microscopy." In, *Amplitude Modulation Atomic Force Microscopy*, pp. 117–128. Wiley-VCH Verlag GmbH & Co. KGaA, Weinheim, Germany, 2010.

[58] R. Garcia and E. T. Herruzo. "The emergence of multifrequency force microscopy." *Nature Nanotechnology*, 7(4):217–226, 2012.

[59] R. Garcia and R. Proksch. "Nanomechanical mapping of soft matter by bimodal force microscopy." *European Polymer Journal*, 49(8):1897–1906, 2013.

[60] S. Garcia-Manyes, G. Oncins, and F. Sanz. "Effect of Ion-Binding and Chemical Phospholipid Structure on the Nanomechanics of Lipid Bilayers Studied by Force Spectroscopy." *Biophysical Journal*, 89(3):1812–1826, 2005.

[61] M. Geradin and D. J. Rixen. "Continuous Systems." In, *Mechanical Vibrations: Theory and Application to Structural Dynamics*, pp. 444–543. John Wiley & Sons, New York, USA, 2014.

[62] F. J. Giessibl. "Advances in atomic force microscopy." *Reviews of Modern Physics*, 75(3):949–983, 2003.

[63] F. J. Giessibl. "Higher-harmonic atomic force microscopy." *Surface and Interface Analysis*, 38(12-13):1696–1701, 2006.

[64] G. C. Goodwin and K. Sang Sin. "Adaptive Filtering Prediction and Control." Dover Publications, Mineola, New York, 1984.

[65] S. Gould, O. Marti, B. Drake, L. Hellemans, C. E. Bracker, P. K. Hansma, N. L. Keder, M. M. Eddy, and G. D. Stucky. "Molecular resolution images of amino acid crystals with the atomic force microscope." *Nature*, 332(6162):332–334, 1988.

[66] H. F. Grip. "Topics in State and Parameter Estimation for Nonlinear and Uncertain Systems." PhD Thesis, Norwegian University of Science and Technology, 2010.

[67] H. F. Grip and A. Saberi. "Structural decomposition of linear multivariable systems using symbolic computations." *International Journal of Control*, 83(7):1414–1426, 2010.

[68] H. F. Grip, A. Saberi, and T. A. Johansen. "Estimation of states and parameters for linear systems with nonlinearly parameterized perturbations." *Systems & Control Letters*, 60(9):771–777, 2011.

[69] G.-Y. Gu, L.-M. Zhu, C.-Y. Su, H. Ding, and S. Fatikow. "Modeling and Control of Piezo-Actuated Nanopositioning Stages: A Survey." *IEEE Transactions on Automation Science and Engineering*, 13(1):313–332, 2016.

[70] J. Guck, R. Ananthakrishnan, C. C. Cuningham, and J. Kas. "Stretching biological cells with light." *Journal of Physics: Condensed Matter*, 14(19):4843–4856, 2002.

[71] N. Guz, M. Dokukin, V. Kalaparthi, and I. Sokolov. "If Cell Mechanics Can Be Described by Elastic Modulus: Study of Different Models and Probes Used in Indentation Experiments." *Biophysical Journal*, 107(3):564–575, 2014.

[72] K. M. Haase, D. Tremblay, and A. E. Pelling. "Mechanotransduction." In, *Atomic Force Microscopy in Nanobiology.* Vol. 5, pp. 379–422. Pan Stanford Publishing, 2014.

[73] K. Haase and A. E. Pelling. "Investigating cell mechanics with atomic force microscopy." *Journal of The Royal Society Interface*, 12(104), 2015.

[74] D. M. Harcombe, M. G. Ruppert, M. R. P. Ragazzon, and A. J. Fleming. "Higher-harmonic AFM Imaging with a High-Bandwidth Multifrequency Lyapunov Filter." In *IEEE International Conference on Advanced Intelligent Mechatronics*, Munich, Germany, 2017.

[75] D. M. Harcombe, M. G. Ruppert, M. R. P. Ragazzon, and A. J. Fleming. "Lyapunov estimation for high-speed demodulation in multifrequency atomic force microscopy." *Beilstein Journal of Nanotechnology*, 9(1):490–498, 2018.

[76] F. M. Hecht, J. Rheinlaender, N. Schierbaum, W. H. Goldmann, B. Fabry, and T. E. Schäffer. "Imaging viscoelastic properties of live cells by AFM: power-law rheology on the nanoscale." *Soft Matter*, 11(23):4584–4591, 2015.

[77] E. T. Herruzo, A. P. Perrino, and R. Garcia. "Fast nanomechanical spectroscopy of soft matter." *Nature communications*, 5:3126, 2014.

[78] R. Hillenbrand, M. Stark, and R. Guckenberger. "Higher-harmonics generation in tapping-mode atomic-force microscopy: Insights into the tip-sample interaction." *Applied Physics Letters*, 76(23):3478–3480, 2000.

[79] H. Hölscher. "Quantitative measurement of tip-sample interactions in amplitude modulation atomic force microscopy." *Applied Physics Letters*, 89(12):123109, 2006.

[80] S. Hu and A. Raman. "Inverting amplitude and phase to reconstruct tip-sample interaction forces in tapping mode atomic force microscopy." *Nanotechnology*, 19(37):375704, 2008.

[81] Y. Huang, P. Cheng, and C.-H. Menq. "Dynamic Force Sensing Using an Optically Trapped Probing System." *Mechatronics, IEEE/ASME Transactions on*, 16(6):1145–1154, 2011.

[82] J. L. Hutter and J. Bechhoefer. "Calibration of atomic-force microscope tips." *Review of Scientific Instruments*, 64(7):1868, 1993.

[83] IBM Research. "A Boy And His Atom." 2013. URL: `https://www.research.ibm.com/articles/madewithatoms.shtml` (visited on 2017-11-23).

[84] P. A. Ioannou and J. Sun. "Robust adaptive control." Prentice Hall, Upper Saddle River, NJ, 1996.

[85] J. N. Israelachvili. "Intermolecular and surface forces." Academic Press, 2011.

[86] K. Iversen. "Biological Cell Models and Atomic Force Microscopy: A Literature Review." Master's thesis, NTNU, Norwegian University of Science and Technology, 2015.

[87] N. Jalili and K. Laxminarayana. "A review of atomic force microscopy imaging systems: application to molecular metrology and biological sciences." *Mechatronics*, 14(8):907–945, 2004.

[88] F. Javadpour, M. Moravvej Farshi, and M. Amrein. "Atomic-Force Microscopy: A New Tool for Gas-Shale Characterization." *Journal of Canadian Petroleum Technology*, 51(04):236–243, 2012.

[89] Y. Jeong, G. R. Jayanth, S. M. Jhiang, and C.-H. Menq. "Direct tip-sample interaction force control for the dynamic mode atomic force microscopy." *Applied Physics Letters*, 88(20):204102, 2006.

[90] S. Jesse, S. V. Kalinin, R. Proksch, A. P. Baddorf, and B. J. Rodriguez. "The band excitation method in scanning probe microscopy for rapid mapping of energy dissipation on the nanoscale." *Nanotechnology*, 18(43):435503, 2007.

[91] K. L. Johnson. "Contact mechanics." Cambridge University Press, Cambridge, 1985.

[92] K. L. Johnson, K. Kendall, and A. D. Roberts. "Surface Energy and the Contact of Elastic Solids." *Proceedings of the Royal Society A: Mathematical, Physical and Engineering Sciences*, 324(1558):301–313, 1971.

[93] K. S. Karvinen and S. O. R. Moheimani. "A high-bandwidth amplitude estimation technique for dynamic mode atomic force microscopy." *Review of Scientific Instruments*, 85(2):023707, 2014.

[94] K. S. Karvinen. "Control and Estimation Techniques for High-Bandwidth Dynamic Mode Atomic Force Microscopy." PhD thesis, University of Newcastle, 2014.

[95] K. S. Karvinen, M. G. Ruppert, K. Mahata, and S. O. R. Moheimani. "Direct Tip-Sample Force Estimation for High-Speed Dynamic Mode Atomic Force Microscopy." *IEEE Transactions on Nanotechnology*, 13(6):1257–1265, 2014.

[96] S. Kasas and G. Dietler. "Probing nanomechanical properties from biomolecules to living cells." *Pflügers Archiv - European Journal of Physiology*, 456(1):13–27, 2008.

[97] A. J. Katan, M. H. v. Es, and T. H. Oosterkamp. "Quantitative force versus distance measurements in amplitude modulation AFM: a novel force inversion technique." *Nanotechnology*, 20(16):165703, 2009.

[98] B. J. Kenton, A. J. Fleming, and K. K. Leang. "Compact ultra-fast vertical nanopositioner for improving scanning probe microscope scan speed." *Review of Scientific Instruments*, 82(12):1–8, 2011.

[99] R. Knoll, K. Magerle, and G. Krausch. "Tapping Mode atomic force microscopy on polymers: Where is the true sample surface?" *Macromolecules*, 34(12):4159–4165, 2001.

[100] N. Kodera, M. Sakashita, and T. Ando. "Dynamic proportional-integral-differential controller for high-speed atomic force microscopy." *Review of Scientific Instruments*, 77(8):083704, 2006.

[101] N. Kodera, D. Yamamoto, R. Ishikawa, and T. Ando. "Video imaging of walking myosin V by high-speed atomic force microscopy." *Nature*, 468(7320):72–6, 2010.

[102] J. Kokavecz, Z. Tóth, Z. L. Horváth, P. Heszler, and Á. Mechler. "Novel amplitude and frequency demodulation algorithm for a virtual dynamic atomic force microscope." *Nanotechnology*, 17(7):S173–S177, 2006.

[103] M. Krstic, I. Kanellakopoulos, and P. Kokotovic. "Nonlinear and adaptive control design." John Wiley & Sons, Inc., New York, NY, 1995.

[104] S. Kuiper and G. Schitter. "Model-based feedback controller design for dual actuated atomic force microscopy." *Mechatronics*, 22(3):327–337, 2012.

[105] T. G. Kuznetsova, M. N. Starodubtseva, N. I. Yegorenkov, S. A. Chizhik, and R. I. Zhdanov. "Atomic force microscopy probing of cell elasticity." *Micron*, 38(8):824–833, 2007.

[106] K. K. Leang and S. Devasia. "Feedback-Linearized Inverse Feedforward for Creep, Hysteresis, and Vibration Compensation in AFM Piezoactuators." *IEEE Transactions on Control Systems Technology*, 15(5):927–935, 2007.

[107] S. Lee, S. Howell, A. Raman, and R. Reifenberger. "Nonlinear dynamics of microcantilevers in tapping mode atomic force microscopy: A comparison between theory and experiment." *Physical Review B*, 66(11):115409, 2002.

[108] F. L. Leite, C. C. Bueno, A. L. Da Róz, E. C. Ziemath, and O. N. Oliveira. "Theoretical Models for Surface Forces and Adhesion and Their Measurement Using Atomic Force Microscopy." *International Journal of Molecular Sciences*, 13(10):12773–12856, 2012.

[109] M. Lekka. "Atomic force microscopy: A tip for diagnosing cancer." *Nature nanotechnology*, 7(11):691–2, 2012.

[110] M. Lekka, D. Gil, K. Pogoda, J. Dulińska-Litewka, R. Jach, J. Gostek, O. Klymenko, S. Prauzner-Bechcicki, Z. Stachura, J. Wiltowska-Zuber, K. Okoń, and P. Laidler. "Cancer cell detection in tissue sections using AFM." *Archives of Biochemistry and Biophysics*, 518(2):151–156, 2012.

[111] M. Lekka, K. Pogoda, J. Gostek, O. Klymenko, S. Prauzner-Bechcicki, J. Wiltowska-Zuber, J. Jaczewska, J. Lekki, and Z. Stachura. "Cancer cell recognition - Mechanical phenotype." *Micron*, 43(12):1259–1266, 2012.

[112] T. Li and Q. Zou. "Simultaneous topography imaging and broadband nanomechanical mapping on atomic force microscope." *Nanotechnology*, 28(50):505502, 2017.

[113] D. C. Lin, E. K. Dimitriadis, and F. Horkay. "Robust Strategies for Automated AFM Force Curve Analysis—II: Adhesion-Influenced Indentation of Soft, Elastic Materials." *Journal of Biomechanical Engineering*, 129(6):904, 2007.

[114] L. Ljung. "System Identification: Theory for the User." Prentice Hall, Upper Saddle River, NJ, 2nd ed., 1999.

[115] L. Ljung and S. Gunnarsson. "Adaptation and tracking in system identification-A survey." *Automatica*, 26(1):7–21, 1990.

[116] J. R. Lozano and R. Garcia. "Theory of Multifrequency Atomic Force Microscopy." *Physical Review Letters*, 100(7):076102, 2008.

[117] R. G. Lyons. "Understanding Digital Signal Processing." Prentice Hall, Upper Saddle River, NJ, 3rd ed., 2010.

[118] I. A. Mahmood and S. O. R. Moheimani. "Fast spiral-scan atomic force microscopy." *Nanotechnology*, 20(36):365503, 2009.

[119] S. R. Manalis, S. C. Minne, A. Atalar, and C. F. Quate. "High-speed atomic force microscopy using an integrated actuator and optical lever detection." *Review of Scientific Instruments*, 67(9):3294–3297, 1996.

[120] N. F. Martínez, J. R. Lozano, E. T. Herruzo, F. Garcia, C. Richter, T. Sulzbach, and R. Garcia. "Bimodal atomic force microscopy imaging of isolated antibodies in air and liquids." *Nanotechnology*, 19(38):384011, 2008.

[121] N. F. Martinez, S. Patil, J. R. Lozano, and R. Garcia. "Enhanced compositional sensitivity in atomic force microscopy by the excitation of the first two flexural modes." *Applied Physics Letters*, 89(15):1–4, 2006.

[122] M. F. d. Mathelin and R. Lozano. "Robust adaptive identification of slowly time-varying parameters with bounded disturbances." In *European Control Conference*, 1997.

[123] C. T. McKee, J. A. Last, P. Russell, and C. J. Murphy. "Indentation versus tensile measurements of Young's modulus for soft biological tissues." *Tissue engineering. Part B, Reviews*, 17(3):155–164, 2011.

[124] J. Mertz, O. Marti, and J. Mlynek. "Regulation of a microcantilever response by force feedback." *Applied Physics Letters*, 62(19):2344, 1993.

[125] S. Messineo, M. R. P. Ragazzon, F. Busnelli, and J. T. Gravdahl. "Nonlinear Analysis of PI-control for Atomic Force Microscopy in Contact Mode," 2018. In writing.

[126] B. Mokaberi and A. A. G. Requicha. "Compensation of Scanner Creep and Hysteresis for AFM Nanomanipulation." *IEEE Transactions on Automation Science and Engineering*, 5(2):197–206, 2008.

[127] M. Morgenstern, A. Schwarz, and U. D. Schwarz. "Low-Temperature Scanning Probe Microscopy." In B. Bhushan, editor, *Springer Handbook of Nanotechnology*, pp. 663–709. Springer Berlin Heidelberg, 2010.

[128] D. J. Müller and Y. F. Dufrêne. "Atomic force microscopy: a nanoscopic window on the cell surface." *Trends in cell biology*, 21(8):461–469, 2011.

[129] K. S. Narendra and L. S. Valavani. "Stable Adaptive Controller Design–Direct Control." *IEEE Transactions on Automatic Control*, 23(4):570–583, 1978.

[130] R. B. Northrop. "Introduction to instrumentation and measurements." CRC Press, Boca Raton, FL, 2nd ed., 2005.

[131] F. Ohnesorge and G. Binnig. "True Atomic Resolution by Atomic Force Microscopy Through Repulsive and Attractive Forces." *Science*, 260(5113):1451–1456, 1993.

[132] A. F. Payam, D. Martin-Jimenez, and R. Garcia. "Force reconstruction from tapping mode force microscopy experiments." *Nanotechnology*, 26(18):1–12, 2015.

[133] D. Platz, E. A. Tholén, D. Pesen, and D. B. Haviland. "Intermodulation atomic force microscopy." *Applied Physics Letters*, 92(15):153106, 2008.

[134] M. Plodinec, M. Loparic, C. A. Monnier, E. C. Obermann, R. Zanetti-Dallenbach, P. Oertle, J. T. Hyotyla, U. Aebi, M. Bentires-Alj, R. Y. H. Lim, and C.-A. Schoenenberger. "The nanomechanical signature of breast cancer." *Nature Nanotechnology*, 7(11):757–765, 2012.

[135] P. Polyakov, C. Soussen, J. Duan, J. F. L. Duval, D. Brie, and G. Francius. "Automated Force Volume Image Processing for Biological Samples." *PLOS ONE*, 6(4):1–19, 2011.

[136] Precision Mechatronics Lab at the University of Newcastle. URL: `http://www.precisionmechatronicslab.com/` (visited on 2017-12-12).

[137] J. G. Proakis and D. G. Manolakis. "Digital signal processing: Principles, algorithms, and applications." Prentice Hall, Upper Saddle River, NJ, 3rd ed., 1996.

[138] R. Proksch. "Multi-Frequency Atomic Force Microscopy." In S. V. Kalinin and A. Gruverman, editors, *Scanning Probe Microscopy of Functional Materials*, pp. 125–151. Springer New York, New York, NY, 2011.

[139] R. Proksch. "Multifrequency, repulsive-mode amplitude-modulated atomic force microscopy." *Applied Physics Letters*, 89(11):1–4, 2006.

[140] U. Rabe, K. Janser, and W. Arnold. "Vibrations of free and surface-coupled atomic force microscope cantilevers: Theory and experiment." *Review of Scientific Instruments*, 67(9):3281–3293, 1996.

[141] M. Radmacher, R. W. Tillmann, and H. E. Gaub. "Imaging viscoelasticity by force modulation with the atomic force microscope." *Biophysical journal*, 64(3):735–742, 1993.

[142] M. R. P. Ragazzon and J. T. Gravdahl. "Imaging Topography and Viscoelastic Properties by Constant Depth Atomic Force Microscopy." In *IEEE Multi-Conference on Systems and Control*, Buenos Aires, Argentina, 2016.

[143] M. R. P. Ragazzon, J. T. Gravdahl, and A. J. Fleming. "On Amplitude Estimation for High-Speed Atomic Force Microscopy." In *American Control Conference*, Boston, USA, 2016.

[144] M. R. P. Ragazzon, J. T. Gravdahl, and K. Y. Pettersen. "Exponential Convergence Bounds in Least Squares Estimation: Identification of Viscoelastic Properties in Atomic Force Microscopy." In *IEEE Conference on Control Technology and Applications*, Kohala Coast, Hawai'i, USA, 2017.

[145] M. R. P. Ragazzon, J. T. Gravdahl, K. Y. Pettersen, and A. A. Eielsen. "Topography and force imaging in atomic force microscopy by state and parameter estimation." In *American Control Conference*, Chicago, USA, 2015.

[146] M. R. P. Ragazzon, J. T. Gravdahl, and M. Vagia. "Viscoelastic properties of cells: Modeling and identification by atomic force microscopy." *Mechatronics*, 2017. In press, available online.

[147] M. R. P. Ragazzon, J. T. Gravdahl, and K. Y. Pettersen. "Model-Based Identification of Nanomechanical Properties in Atomic Force Microscopy: Theory and Experiments." *IEEE Transactions on Control Systems Technology*, 2018. Provisionally accepted.

[148] M. R. P. Ragazzon, M. G. Ruppert, D. M. Harcombe, A. J. Fleming, and J. T. Gravdahl. "Lyapunov Estimator for High-Speed Demodulation in Dynamic Mode Atomic Force Microscopy." *IEEE Transactions on Control Systems Technology*, 26(2):765–772, 2018.

[149] M. R. P. Ragazzon, M. Vagia, and J. T. Gravdahl. "Cell Mechanics Modeling and Identification by Atomic Force Microscopy." In *7th IFAC Symposium on Mechatronic Systems*, Loughborough, UK, 2016.

[150] M. R. P. Ragazzon, A. A. Eielsen, and J. T. Gravdahl. "H∞ Reduced Order Control for Nanopositioning: Numerical Implementability." In *19th IFAC World Congress*, Cape Town, South-Africa, 2014.

[151] A. Raman, S. Trigueros, A. Cartagena, A. P. Z. Stevenson, M. Susilo, E. Nauman, and S. A. Contera. "Mapping nanomechanical properties of live cells using multi-harmonic atomic force microscopy." *Nature nanotechnology*, 6(12):809–14, 2011.

[152] S. S. Rao. "Mechanical Vibrations." Prentice Hall Upper Saddle River, 5th ed., 2011.

[153] B. Rateesh and S. Esmita. "Atomic Force Microscopy: A Source of Investigation in Biomedicine." *International Journal of Electronic and Electrical Engineering*, 11(23):4553–4732, 2014.

[154] T. R. Rodriguez and R. Garcia. "Theory of Q control in atomic force microscopy." *Applied Physics Letters*, 82(26):4821–4823, 2003.

[155] M. G. Ruppert, D. M. Harcombe, and S. O. R. Moheimani. "High-Bandwidth Demodulation in MF-AFM: A Kalman Filtering Approach." *IEEE/ASME Transactions on Mechatronics*, 21(6):2705–2715, 2016.

[156] M. G. Ruppert, D. M. Harcombe, and S. O. R. Moheimani. "State Estimation for High-Speed Multifrequency Atomic Force Microscopy." In *American Control Conference*, Boston, USA, 2016.

[157] M. G. Ruppert, D. M. Harcombe, M. R. P. Ragazzon, S. O. R. Moheimani, and A. J. Fleming. "A review of demodulation techniques for amplitude-modulation atomic force microscopy." *Beilstein Journal of Nanotechnology*, 8(1):1407–1426, 2017.

[158] M. G. Ruppert, D. M. Harcombe, M. R. P. Ragazzon, S. O. R. Moheimani, and A. J. Fleming. "Frequency Domain Analysis of Robust Demodulators for High-Speed Atomic Force Microscopy." In *American Control Conference*, Seattle, USA, 2017.

[159] M. G. Ruppert, K. S. Karvinen, S. L. Wiggins, and S. O. R. Moheimani. "A Kalman Filter for Amplitude Estimation in High-Speed Dynamic Mode Atomic Force Microscopy." *IEEE Transactions on Control Systems Technology*, 24(1):276–284, 2016.

[160] M. G. Ruppert and S. O. R. Moheimani. "Multimode Q Control in Tapping-Mode AFM: Enabling Imaging on Higher Flexural Eigenmodes." *IEEE Transactions on Control Systems Technology*, 24(4):1149–1159, 2016.

[161] S. Rutzel, S. I. Lee, and A. Raman. "Nonlinear dynamics of atomic-force-microscope probes driven in Lennard-Jones potentials." *Proceedings of the Royal Society A: Mathematical, Physical and Engineering Sciences*, 459(2036):1925–1948, 2003.

[162] O. Sahin, S. Magonov, C. Su, C. F. Quate, and O. Solgaard. "An atomic force microscope tip designed to measure time-varying nanomechanical forces." *Nature nanotechnology*, 2(8):507–14, 2007.

[163] O. Sahin, C. F. Quate, O. Solgaard, and F. J. Giessibl. "Higher Harmonics and Time-Varying Forces in Dynamic Force Microscopy." In B. Bhushan, editor, *Springer Handbook of Nanotechnology*, pp. 711–729. Springer Berlin Heidelberg, 2010.

[164] D. R. Sahoo, P. Agarwal, and M. V. Salapaka. "Transient Force Atomic Force Microscopy: A New Nano-Interrogation Method." In *2007 American Control Conference*, 2007.

[165] D. R. Sahoo, T. De, and M. V. Salapaka. "Observer based imaging methods for Atomic Force Microscopy." In *44th IEEE Conference on Decision and Control*, Seville, Spain, 2005.

[166] D. R. Sahoo, A. Sebastian, and M. V. Salapaka. "An ultra-fast scheme for sample-detection in dynamic-mode atomic force microscopy." In *2004 NSTI Nanotechnology Conference and Trade Show*, vol. 3, 2004.

[167] D. R. Sahoo, A. Sebastian, and M. V. Salapaka. "Harnessing the transient signals in atomic force microscopy." *International Journal of Robust and Nonlinear Control*, 15(16):805–820, 2005.

[168] D. R. Sahoo, A. Sebastian, and M. V. Salapaka. "Transient-signal-based sample-detection in atomic force microscopy." *Applied Physics Letters*, 83(26):5521–5523, 2003.

[169] S. Salapaka, A. Sebastian, J. P. Cleveland, and M. V. Salapaka. "High bandwidth nano-positioner: A robust control approach." *Review of Scientific Instruments*, 73(9):3232, 2002.

[170] S. M. Salapaka, T. De, and A. Sebastian. "A robust control based solution to the sample-profile estimation problem in fast atomic force microscopy." *International Journal of Robust and Nonlinear Control*, 15(16):821–837, 2005.

[171] S. M. Salapaka, T. De, and A. Sebastian. "Sample-profile estimate for fast atomic force microscopy." *Applied Physics Letters*, 87(5):053112, 2005.

[172] S. Santos, C.-Y. Lai, T. Olukan, and M. Chiesa. "Multifrequency AFM: from origins to convergence." *Nanoscale*:5038–5043, 2017.

[173] D. Sarid. "Scanning force microscopy." Oxford University Press, New York, 1994.

[174] A. Schirmeisen, B. Anczykowski, H. Hölscher, and H. Fuchs. "Dynamic Modes of Atomic Force Microscopy." In B. Bhushan, editor, *Springer Handbook of Nanotechnology*, pp. 731–761. Springer Berlin Heidelberg, 2010.

[175] G. Schitter, P. Menold, H. F. Knapp, F. Allgöwer, and A. Stemmer. "High performance feedback for fast scanning atomic force microscopes." *Review of Scientific Instruments*, 72(8):3320–3327, 2001.

[176] G. Schitter, K. J. Astrom, B. E. DeMartini, P. J. Thurner, K. L. Turner, and P. K. Hansma. "Design and modeling of a high-speed AFM-scanner." *IEEE Transactions on Control Systems Technology*, 15(5):906–915, 2007.

[177] G. Schitter, P. J. Thurner, and P. K. Hansma. "Design and input-shaping control of a novel scanner for high-speed atomic force microscopy." *Mechatronics*, 18(5-6):282–288, 2008.

[178] A. Sebastian, D. R. Sahoo, and M. V. Salapaka. "An observer based sample detection scheme for atomic force microscopy." In *42nd IEEE International Conference on Decision and Control*, vol. 3, Maui, HI, USA. IEEE, 2003.

[179] A. Sebastian, M. V. Salapaka, D. J. Chen, and J. P. Cleveland. "Harmonic analysis based modeling of tapping-mode AFM." In *American Control Conference*, 1999.

[180] A. Sebastian and S. M. Salapaka. "Design methodologies for robust nano-positioning." *IEEE Transactions on Control Systems Technology*, 13(6):868–876, 2005.

[181] A. Sebastian, A. Gannepalli, and M. V. Salapaka. "A Review of the Systems Approach to the Analysis of Dynamic-Mode Atomic Force Microscopy." *IEEE Transactions on Control Systems Technology*, 15(5):952–959, 2007.

[182] D. Simon. "Optimal State Estimation." Wiley, New York, 2006.

[183] I. N. Sneddon. "The relation between load and penetration in the axisymmetric boussinesq problem for a punch of arbitrary profile." *International Journal of Engineering Science*, 3(1):47–57, 1965.

[184] I. Sokolov. "Atomic Force Microscopy in Cancer Cell Research." *Cancer Nanotechnology*, 1:1–17, 2007.

[185] I. Sokolov, M. E. Dokukin, and N. V. Guz. "Method for quantitative measurements of the elastic modulus of biological cells in AFM indentation experiments." *Methods*, 60(2):202–213, 2013.

[186] I. Sokolov, S. Iyer, V. Subba-Rao, R. M. Gaikwad, and C. D. Woodworth. "Detection of surface brush on biological cells in vitro with atomic force microscopy." *Applied Physics Letters*, 91(2):2–5, 2007.

[187] J. Å. Stakvik, M. R. P. Ragazzon, A. A. Eielsen, and J. T. Gravdahl. "On Implementation of the Preisach Model: Identification and Inversion for Hysteresis Compensation." *Modeling, Identification and Control*, 36(3):133–142, 2015.

[188] M. Stark, R. W. Stark, W. M. Heckl, and R. Guckenberger. "Inverting dynamic force microscopy: from signals to time-resolved interaction forces." *Proceedings of the National Academy of Sciences of the United States of America*, 99(13):8473–8, 2002.

[189] R. W. Stark and W. M. Heckl. "Fourier transformed atomic force microscopy: tapping mode atomic force microscopy beyond the Hookian approximation." *Surface Science*, 457(1-2):219–228, 2000.

[190] R. W. Stark and W. M. Heckl. "Higher harmonics imaging in tapping-mode atomic-force microscopy." *Review of Scientific Instruments*, 74(12):5111–5114, 2003.

[191] R. W. Stark, G. Schitter, M. Stark, R. Guckenberger, and A. Stemmer. "State-space model of freely vibrating and surface-coupled cantilever dynamics in atomic force microscopy." *Physical Review B*, 69(8):085412, 2004.

[192] P. Stoica, H. Li, and J. Li. "Amplitude estimation of sinusoidal signals: Survey, new results, and an application." *IEEE Transactions on Signal Processing*, 48(2):338–352, 2000.

[193] T. Sulchek, R. Hsieh, J. D. Adams, G. G. Yaralioglu, S. C. Minne, C. F. Quate, J. P. Cleveland, A. Atalar, and D. M. Adderton. "High-speed tapping mode imaging with active Q control for atomic force microscopy." *Applied Physics Letters*, 76(11):1473, 2000.

[194] A. Surendiran, S. Sandhiya, S. C. Pradhan, and C. Adithan. "Novel applications of nanotechnology in medicine." *Indian Journal of Medical Research*, 130(6):689–701, 2009.

[195] K. K. M. Sweers, M. L. Bennink, and V. Subramaniam. "Nanomechanical properties of single amyloid fibrils." *Journal of Physics: Condensed Matter*, 24(24):243101, 2012.

[196] Y. R. Teo, Y. Yong, and A. J. Fleming. "A comparison of scanning methods and the vertical control implications for scanning probe microscopy." *Asian Journal of Control*, 19(2):1–15, 2016.

[197] T. Uchihashi, H. Watanabe, S. Fukuda, M. Shibata, and T. Ando. "Functional extension of high-speed AFM for wider biological applications." *Ultramicroscopy*, 160:182–196, 2016.

[198] M. Vagia, A. A. Eielsen, J. T. Gravdahl, and K. Y. Pettersen. "Design of a Nonlinear Damping Control Scheme for Nanopositioning." In *IEEE/ASME International Conference on Advanced Intelligent Mechatronics*, Wollongong, NSW, Australia, 2013.

[199] M. Vagia, A. A. Eielsen, J. T. Gravdahl, and K. Y. Pettersen. "Nonlinear tracking control scheme for a nanopositioner." In *24th Mediterranean Conference on Control and Automation*, 2016.

[200] S. Vahabi, B. Nazemi Salman, and A. Javanmard. "Atomic force microscopy application in biological research: a review study." *Iranian journal of medical sciences*, 38(2):76–83, 2013.

[201] A. Vahidi, A. Stefanopoulou, and H. Peng. "Recursive least squares with forgetting for online estimation of vehicle mass and road grade: theory and experiments." *Vehicle System Dynamics*, 43(1):31–55, 2005.

[202] D. Wang, S. Fujinami, K. Nakajima, and T. Nishi. "True surface topography and nanomechanical mapping measurements on block copolymers with atomic force microscopy." *Macromolecules*, 43(7):3169–3172, 2010.

[203] Y. K. Yong, S. O. R. Moheimani, B. J. Kenton, and K. K. Leang. "Invited Review Article: High-speed flexure-guided nanopositioning: Mechanical design and control issues." *Review of Scientific Instruments*, 83(12):121101, 2012.

[204] Y. K. Yong and S. O. R. Moheimani. "Collocated Z-axis Control of a High-Speed Nanopositioner for Video-rate Atomic Force Microscopy." *IEEE Transactions on Nanotechnology*, 2015.

[205] Y. K. Yong, S. P. Wadikhaye, and A. J. Fleming. "High speed single- and dual-stage vertical positioners." *Review of Scientific Instruments*, 87(8):085104, 2016.

[206] Y. K. Yong, K. Liu, and S. O. R. Moheimani. "Reducing cross-coupling in a compliant XY nanopositioner for fast and accurate raster scanning." *IEEE Transactions on Control Systems Technology*, 18(5):1172–1179, 2010.

[207] X. Zhu, E. Siamantouras, K. K. Liu, and X. Liu. "Determination of work of adhesion of biological cell under AFM bead indentation." *Journal of the Mechanical Behavior of Biomedical Materials*, 56:77–86, 2016.

[208] Y. Zhu and P. R. Pagilla. "Adaptive Estimation of Time-Varying Parameters in Linearly Parametrized Systems." *Journal of Dynamic Systems, Measurement, and Control*, 128(3):691, 2006.